Schlussbericht vom 30.08.2023

zu IGF-Vorhaben Nr. 294 EN

Thema

Predictability of long-term refractoriness of refractory high alumina monolithics under high thermal load with special regard to impurities introduced by secondary raw materials

Berichtszeitraum

01.01.2021 - 30.06.2023

Forschungsvereinigung

Forschungsgemeinschaft Feuerfest e. V.

Forschungseinrichtung(en)

1. Forschungseinrichtung: Forschungsgemeinschaft Feuerfest e. V.

2. Forschungseinrichtung: Hochschule Koblenz, Fachbereich bauen-kunst-werkstoffe, Fachrichtung Werkstofftechnik Glas und Keramik

3. Łukasiewicz - Instytut Ceramiki i Materiałów Budowlanych, Gliwice, Polen

Gefördert durch:

Bundesministerium für Wirtschaft und Klimaschutz

aufgrund eines Beschlusses des Deutschen Bundestages

Vorwort

Das vorliegende Dokument stellt den gemeinsamen Schlussbericht für das IGF-Vorhaben 294 EN und für das CORNET-Gesamtprojekt aller drei beteiligter Forschungseinrichtungen dar.

Aus Deutschland wirkten die Forschungsgemeinschaft Feuerfest e. V. und die Hochschule Koblenz an dem CORNET-Gesamtprojekt mit. An dem CORNET-Gesamtprojekt war außerdem das Łukasiewicz - Instytut Ceramiki i Materiałów Budowlanych in Polen beteiligt, gefördert durch das National Centre for Research and Development (NCBR).

Table of Contents

1. Scientific-technical and economical scope of work

1.1 Motivation

Refractory linings are essential for many important industrial processes, e.g. production of iron and steel, glass, cement, ceramics, or energy generation etc., and are exposed to severe working conditions. Two general types of refractory linings can be realised: Bricks (shaped products) or monolithic (typically castables) linings. Historically, refractory linings were done by means of brickwork. Over the past few decades, monolithic linings gained in popularity, as they were increasingly used by refractory users industries, and were thus asked from refractory producers.

Since refractory materials are consumables, they have to be re-installed periodically in the refractories users industries (“relining”). Their lifetimes vary between hours and several years. Especially the main refractory consumer industries, e.g. the iron and steel industry or the non-ferrous metallurgy, relining periods are short (for example every 1 to 2 weeks). The ultimate objective of the refractory sector is to provide refractories suitable for demanding environments with a good lifetime. The ability for refractory materials to achieve this is driven by the sort and quality of the raw materials. Knowledge about the influence that different choices of raw materials show on the said objective is scarce, however. Raw materials are furthermore a major concern for the EU refractory industry, as many high-quality raw materials are sourced from China and their availability is becoming increasingly uncertain.

Refractory producers want to, need or must increase the use of secondary raw materials. They may be forced to do so by economic, ecologic or even legal causes. It is unclear, however, how impurities which are being carried over into refractory materials from secondary raw materials influence the behaviour of those refractory materials, either during the processing state or during their use in high temperature environments.

The research objective of this CORNET project was to increase the knowledge about the influence of small amounts of impurities ($\Sigma < 2$ wt.-%) from secondary raw materials onto the processing behaviour (workability, setting, hardening) and the high temperature behaviour/performance of monolithics.

1.2 General description of the issue addressed

The overall problem addressed by this CORNET project was the requirement to predict and guarantee a reliable performance of refractory materials in high temperature applications even if impurities are introduced by the use of secondary (recycled) raw materials. Refractory user industries do not tolerate increased downtime due to failure or accelerated wear of refractories, which significantly concerns the refractory producers, e.g. SMEs. Therefore, the high-temperature performance of refractories needs to be guaranteed.

The key elements to enable systematic development of refractories tailored to specific applications by SMEs are 1) the comprehensive understanding of the high temperature thermomechanical performance of refractory materials by 2) practical testing methods (“practical” meaning that the methods are able to submit the refractory materials to the conditions close to industrial applications/use during the tests, mostly specific combinations of changing mechanical and non-linear thermal load) and investigation strategies. Very few publications and thus very little knowledge is available to guide SMEs towards systematic approaches concerning the relation between composition and the high temperature behaviour of monolithics; and this is especially true for (very) small quantities of impurities introduced by secondary raw materials. Impurities, as termed by the refractory industry, are components that reduce the maximum service due to the formation of liquid phases that lead to a material softening during its use. However, as addressed in this CORNET project, very small amounts of liquid may even be beneficial for the thermo-mechanical properties of refractories, because the typical brittleness of ceramic refractory structures may turn to a more ductile state that potentially relieves thermo-mechanic stress. Furthermore, it is unclear how impurities present in refractory systems behave and affect the refractory under the dual influence of mechanical loading and thermal gradient, as it is the case for refractory in use.

SMEs in the sector identified that the information available on the relation between composition and the high temperature behaviour of refractories is insufficient and hinders the development of new and improved refractories containing recycled raw materials. The subsequently defined needs were thus derived from the shortcomings of the present state of art.

1.3 Innovation targets

Based on the overall issue addressed, the **first innovation target** was to develop and produce high alumina raw materials with defined amounts of impurities and prepare refractory model castables, as well as to investigate any eventual influence of impurities on the drying and setting properties of the monolithics. In order to achieve a better understanding of how critical impurities (in terms of nature and concentration) affect the thermomechanical stability at high temperature is critical to have a well-defined model system with a controlled manufacturing process to ensure that effects measured at high temperature are not the simple consequence of the manufacturing process or be able to disentangle the impact of the impurities during the manufacturing process from their impact on the high temperature thermomechanical behaviour of the refractory castable.

The **second innovation target** was to establish a reliable testing strategy to determine the maximum service temperature of refractories so that refractory producers can communicate and guarantee the thermomechanical stability to users of their refractories. At present, the refractory industry is still unable to determine the maximum service temperature of refractory materials. It is still not clear how refractory materials perform if impurities are present in low concentration (< 2 wt.-%) from raw materials (the overall problem). This is especially important when refractory materials operate close to their maximum service temperatures, and even small changes in the grade of raw materials may cause severe degradation and subsequent damages.

The **third innovation target** was to investigate the high temperature performance of refractories close to service conditions and break out of the quasi-static and isothermal testing conditions paradigm, which do not take into consideration temperature gradients or realistic mechanical loading during testing. To address this, an innovative testing procedure that caters for dynamic real-life in-use conditions is proposed. With this achieved the effect of impurities from secondary raw materials on the high-temperature behaviour of refractories can be investigated under close to service conditions.

Within the framework of the CORNET collaboration, each single innovation target was addressed by one of the research performers. For the sake of clarity, the project work that was linked to a specific innovation target is referred to in this report to as “subproject”. Hochschule Koblenz, Germany, worked on the first innovation target (subproject I), while Łukasiewicz - Instytut Ceramiki i Materiałów Budowlanych, Poland dealed with the second innovation target (subproject II). Forschungsgemeinschaft Feuerfest e. V. (Germany) was responsible for the third innovation target and a small part of the second innovation target (subproject III).

1.4 Summary of the results

1.4.1 Subproject I – Development of high alumina raw materials with defined amounts of impurities as well as preparation refractory model castables using these impurified raw materials and characterization of their setting behaviour.

The impurification (2 wt.-%) of the raw material fraction 0-45 µm had no significant effects on the workability, curing and setting behaviour and drying strength (110 °C) of the refractory model castables (spinel-free/spinel-forming) using these impurified raw material. The water-soluble ions (impurities) were bound by the sintering process during the production process of the impurified raw materials at 1600 °C. This was confirmed by the slump flow and ultrasonic velocity measurements, which showed comparable results for all model castables using impurified raw materials when compared the reference castables using no impurified raw materials. Slight deviations of the flow behaviour and drying strength can be explained by the small differences in the particle size distribution and d_{50} values of the impurified raw materials.

The comparable processing properties and setting and curing behaviour guaranty the very similar initial situation for casting/molding and demolding test pieces made of model castables using impurified raw materials, as well as for the high temperature investigations performed by the project partners. Constant flow during a sufficient working window is necessary for proper molding, but thereafter a rapid increase in strength is inevitable for adequate demolding properties of the test pieces. This is the case for all model refractory model castables developed. Effects that may be seen in the high temperature characterization (subprojects II and III) can therefore be attributed solely to the presence of impurities in the raw material fraction 0-45 µm.

Selected impurity compositions were the most unfavourable cases from the point of view of thermomechanical properties due to formation of liquid phase. The results show that for refractory producers it carries the risk of not detecting impurities which might be critical for the high temperature behaviour already in the processing state of the refractory castables.

In subproject I, a systematic approach was designed and successfully implemented. This approach can be used or serve as an example for further investigations, also to figure out proportions of impurities that are not critical for the hot properties.

1.4.2 Subproject II – Establishment of a reliable testing strategy to determine the maximum service temperature of refractories

The introduction of impurities in the raw materials of model high alumina refractory castables affected the mechanics of cracking and facilitate the sintering at lower temperature by forming of small amounts of liquid phase. This also affects the thermomechanical properties of the investigated materials.

Thanks to high temperature x-ray diffraction investigations, it could be highlighted that the impurified raw materials (precursors) used to produce the model refractory castables were in an equilibrium state, which is probably also the case for secondary raw materials recovered from refractory linings that experienced extended service life. This equilibrium state resulted in the limitation of chemical reactions and phase transformations in the model castable's matrix. Among the identified phase transformations occurring at higher temperatures, the spinel formation in the model refractory castables containing the spinel forming agent (MgO) played the most crucial role in the development of an advantageous microstructure and driven improvements of thermomechanical properties while mitigating the negative effect of the presence of impurities.

The used hydratable alumina binder greatly affected the sintering behaviour of the model refractory castable, allowing them to sinter at relatively low temperatures. The castables were in a viscoplastic state during the sintering process. This had consequences for the thermomechanical properties of this type of castables and was clearly visible, among others, in creep measurements on these model castables. Under the conditions of the experiments, no material destruction stage was observed, even after a hundred-hour test.

Most observed changes of thermomechanical properties are likely to be associated with the appearance of a liquid phase in the model refractory castables and the formation of a microstructure specific to each model castables. The observed microstructural changes of the model refractory castables were related to the sintering of the matrix, grain growth and the formation of microcracks derived by differences in thermal expansion of phases, and in the case of the model spinel forming castables MHA-S, the formation of spinel solid solutions.

One important conclusion is that processes such as grain growth in the material matrix and the formation of ceramic bonds, which increase the thermomechanical strength of the investigated materials, do not keep up with the effects caused by the applied load (i.e. creep). This is a valuable clue that materials of this type, namely bonded with hydratable alumina, should not be use in applications where there is a high mechanical load during initial heating. However, after the first heating, significantly higher resistance to deformation were assessed according to refractoriness under load measurements.

It is important to bear in mind that the combination of impurities selected for the preparation of the impurified raw materials used to prepare the investigated model refractory castables, represented the most unfavourable cases in terms of thermomechanical properties as the formation of liquid phase formation was specifically maximized. This in turn highlighted that these model castables, and, by extension, refractory products using secondary raw materials, could still be used for tailored applications with defined application temperature. Finally, it should be possible to deduce mutual proportions of impurities for which the deterioration of thermomechanical properties should not be that critical, or even beneficial for some applications.

1.4.3 Subproject III – Investigation of the high temperature performance of refractories close to service conditions

Thanks to wedge splitting tests (WSTs), the stabile fracture process of test pieces was monitored and quantified, hence their ability to resist damaging assessed. The reference model castable (high alumina cement-free model refractory castables) display a relative moderate strength and specific fracture energy that get weakened by increasing temperature. The addition of spinel precursors to the castable promote an increase of the material strength and specific fracture energy as well as reduction of its brittleness. The impurification of the raw materials (2 % additional impurities in the fraction 0-45 µm) almost systematically resulted in the deterioration of the mechanical properties of the model castable and enhancement of their brittleness. One notable exception in the spinel free formulations was the combination of Fe and Ca that apparently toughen the material and reduce its brittleness, which corelates with the combination of impurities that is expected to form the lowest amount of liquid at the testing temperature. Spinel forming formulation were much more tolerant to impurities, which corelates again with their tendency to form low amount of liquid at the testing temperature. This seems to indicate that a small amount of liquid phase could also be beneficial, especially increasing the ductility of the material without impacting its mechanical strength to extensively.

Despite its ability to detect different microstructural changes, such phase transformation, the method of the monotonic heating (MMH) was not sensitive enough to detect the formation of the liquid in the model castables with impurified raw materials. However, MMH measurements on the impurified raw materials helped to classify the raw materials by identifying at which temperature should the formation occurred.

A new testing system was developed to simulate the thermal gradient and compressive loading that refractory materials experience as a part of linings in industry furnaces and vessels in service. The thermal gradient resulted from the heating of a prismatic test piece from one side (hot face). The loading was applied through refractory plungers connected with servomotors, either by restricting the free thermal expansion or applying a constant load. Stress levels of up to 30 MPa were assessed or applied near to the hot face, in either one or the two directions perpendicular to the thermal gradient. Such level of stress should be expected near to the hot face of refractory linings.

High load and high temperatures promoted specific microstructural changes in the test piece near to the hot face, especially a densification of the matrix that cannot be achieved by a simple prefiring or moderate load as prescribed in the standards EN ISO 1893: Determination of refractoriness under load, and EN 993-9: Determination of creep in compression. Similarly, the addition of impurities in the model refractory castable led to increase of the level of deformations and apparent creep rates under bi-directional loading condition. In combination with high load and high temperature, impurified raw materials that tend to form liquid phases earlier and in higher amount promoted microstructural changes that make the material more resistance to erosion during cutting at room temperature. The high temperature properties of materials with these microstructural changes should now be investigated to improve our understanding on the behaviour of the hot face of refractory linings as well as to push forward our ability to predict its performance.

Overall, a better insight into the behaviour of refractory materials exposed to thermal gradient and high compressive stresses as occurring in refractory linings was gained and should open up new perspectives for material development.

2. Subproject I – Development of high alumina raw materials with defined amounts of impurities as well as preparation refractory model castables using these impurified raw materials and characterization of their setting behaviour.

2.1 Need #1: Establish how critical impurities, namely Na, Ti, Si, Ca and Fe, affect the high temperature performance of refractories / developing a model castable including this impurities in a well-controlled way

Even in low concentrations, impurities significantly influence the thermal behaviour of high alumina monolithics. The way such impurities in traces change the high temperature performance of refractories is however not fully understood and was never investigated systematically. Clues that even relatively high concentrations of impurities may yet improve the thermomechanical properties of high alumina monolithics are present in the literature, especially depending on whether the critical impurities are present in the coarse grains or the matrix.

However, it still remains unclear how impurities from secondary raw materials affect the high temperature performance of refractories, as no publications exist that address this issue with a systematic approach. It is also unclear which reactions lead to a change in the high temperature performance, as determined by means of refractoriness under load, Creep in compression, Resonance-Frequency-Damping Analysis and hot wedge splitting tests. Therefore, it is impossible to predict the performance of refractory materials in high temperature applications if a distinct amount of impurities is introduced by the use of secondary (recycled) raw materials.

Finally the research institution involved in the present project strongly believe that the use of refractories in a highly industrialises society, and the increasing use of secondary raw materials to produce those refractories in a circular economy, is without technological alternatives.

Accordingly, the first need (need #1) that was addressed in the present CORNET project was to develop a model castable including selected impurities and their critical combination in a well-controlled way, to establish how critical impurities, namely Na, Ti, Si, Ca and Fe, affect the high temperature performance of refractories. With this need fulfilled, secondary raw materials can be introduced into refractories with significantly higher confidence and refractory producers can offer reliably performing monolithics, even if recycled raw materials are used.

2.2 State of the art

The ultimate goal of the refractory industry is to provide refractories that are suitable for demanding environments with a good service life. The ability of refractories to achieve this is influenced by the nature and quality of the raw materials. Raw materials are a major concern for the EU refractory industry as many high-quality raw materials are sourced from China and their availability is becoming increasingly uncertain. This is just one reason why refractory manufacturers need to use, or are already using, secondary materials. The service life and high temperature performance of refractory materials is mainly determined by their high temperature thermo-mechanical behavior and mechanical stability. Little is known about the influence of different raw material choices in this respect. A better understanding of the relationship between the composition of raw materials and the thermomechanical behavior of the refractories made from them should lead to better raw material selection and promote the increased use of secondary raw materials. For users of refractory materials, knowledge of their high temperature performance is of great value. Such knowledge leads to stability, reliability, and profitability of processes in their industries, as well as improved cost management.

However, the use of secondary raw materials in the processing of new refractory materials is very risky. Refractories can be costly and any failure result in significant losses in production time, equipment, and in some cases, the product itself. It is crucial to maintain premium quality and monitor the refractories for optimal performance. There are numerous applications for refractory materials and at least an equal number of varying types and compositions available. As a result, secondary raw materials may also comprise different compositions and new developed mineralogical phases due to the previous use. Several researchers investigated the impact of naturally occurring impurities (B_2O_3 and CaO) in varying concentrations on the oxidation resistance of carbon bonded magnesia refractory bricks. They found that even slight changes significantly affect the reaction between carbon and magnesia [*1*-3].

Due to a lack of publications that take a systematic approach, it remains unclear how impurities from secondary raw materials affect the high temperature performance of refractories, in particular monolithics. It is not clear which processes cause changes in high temperature performance. Therefore, when a significant amount of impurities are introduced through the use of secondary (recycled) raw materials, it is impossible to predict the performance of refractories in high temperature applications.

Through the production process of raw materials, iron, titanium and silicon are typically and already present in concentrations below 0.1 wt% (traces). Generally, Fe contaminations promote carbon-bursting as Fe or oxidic Fe acts like a catalyst in CO or CH_4 atmospheres. SiO_2 is particularly sensitive to H_2 corrosion due to the reduction of the oxidic component by H_2 [4]. Liu et al. [5] demonstrate through their research comparing two conventional raw materials for high purity corundum bricks that even for primary raw materials applies the purer the raw material, the better and more balanced the performance of the material. Frulli [6] reports similar findings for andalusite and mullite raw materials. Secondary high alumina raw materials are expected to contain higher levels of impurities due to previous industrial use. E.g. calcium is significantly enriched in secondary raw materials, as Ca is a major component of metallurgical slags.

Refractory castables in particular have many adjusting screws that can be positively or negatively influenced by impurities deriving from the raw materials. The properties of the castables are set with high precision for the molding of special shapes and parts on location site. They can form entire furnace linings and other unique shapes and are applicable through pouring, pumping, troweling, gunning, and shotcreting. The rheology, processability and setting behavior needed for the relevant installation method are crucial. For highly resistant castables, a high alumina (corundum) content is utilized due to its high melting point of 2050°C, chemical resistance, and mechanical durability. Fluxes in the primary impure refractory product and/or encountered in use can considerably decrease the melting point. Refractory products in use can withstand only minimal melting (1-5 %) before their essential structural properties are lost [7]. Further literature indicates that impurities even at low concentrations, have a significant effect on the thermal behavior of high alumina monolithic materials [8-9]. A first attempt to assess the effect of sodium on high alumina calcium aluminate cement-bonded refractories was made by Alex et al. [8]. Their finding was that monolithics spiked with up to 1 wt% sodium by the addition of sodium acetate show significant changes in the thermal evolution of calcium aluminate phases, causing increased expansion of the materials that significantly deteriorate the properties of the castables. Möhmel [9] shows that considerably higher impurity concentrations can actually improve the thermal stability and thermo-mechanical properties of high alumina monolithics, depending on whether the critical impurities are present in the coarse grains or in the matrix.

Following, the investigation of the effect of minor concentration of impurities that should simulate impurities in secondary raw materials on the processing behavior (workability, setting, hardening) of high alumina castables is described in detail. It will provide a basis for systematic investigation of the effect of impurities in refractory castables, ultimately facilitating the use of secondary raw materials in the production of high performance castables.

2.3 Research strategy

The major aim of Hochschule Koblenz was to develop two kinds of high alumina cement free castables (spinel-free / spinel-forming) with a systematically impurified matrix for the development of knowledge base about the influence of impurities in minor concentrations ($\Sigma < 2$ wt.-%) on the working and setting properties of said castables.

The challenge and intention were to spike the model refractory castables with impurities in the way like they occur in recycled raw materials, but in a controlled scientific procedure. During the previous use(s) impurities in recycled high alumina raw materials can form mixed oxides, such as hibonite in the presence of Ca, beta-alumina in the presence of Na, or melt/glassy phases when impurities are present in higher concentrations. The targeted reactions will be replicated in a controlled laboratory setting by mixing pure fine primary alumina (< 45 µm) with different amounts of impurities (Na, Ti, Si, Ca and Fe in oxidic form up to 2 wt.-%), homogenizing and pelletizing the mixtures and sintering them at 1600 °C. It's essential to highlight that the sintering temperature represents the standard operating conditions during steel production. After milling the sintered materials, a fraction of 0 to 45 µm is obtained, which is typically the open fine grain fraction in the matrix composition.

The goal was to develop spiked raw materials (precursors) that cover a wide range of mineralogical conditions but achieving this required significant effort. To determine critical amounts and combinations of impurities and to forecast reactions that take place within the stated concentration range, FactSage® was employed. Chemical (XRF) and particle size distribution (laser granulometry) characterization were performed on all precursors from Hochschule Koblenz and the mineralogical analysis (X-ray diffractometry) was performed by the polish project partner. Finally, tabular alumina (0-45 µm) from either spinel-free or spinel-forming cement free model refractory castables was substituted by the spiked precursors. Said castables were processed in sufficient amounts for the needs of all project partners in the course of the project.

The impact of spiked precursors on the model refractory castables working and setting properties (as determined through slump flow testing and ultrasonic velocity measurement) was investigated, as well as on their cold modulus of rupture by means of the cold bending strength testing. The results deepened our understanding of the correlations and helped to generate additional knowledge.

2.4 Materials and methods

2.4.1 Analytical methods

For the development of the model castables an extensive set of investigations were performed, which allows to determine the workability, the setting velocity, and the strength evolution of the developed castables:

2.4.1.1. Slump-flow

The rheological properties of the resulting self-flowing castables were analysed by applying the slump flow test. The use of a digital camera during the measurement allows a time-dependent investigation of the traditional slump flow test setup based on ISO 1927-4 as reported by L. Klein and O. Krause [10]. The slump flow measurement was started within 2 minutes after the mixing time to ensure a similar initial situation for all castables.

2.4.1.2. Ultrasonic velocity

The time-dependent curing and setting behaviour of the different refractory castables were investigated by means of ultrasonic velocity measurements according to the IP8-measuring system of the company UltraTest GmbH - Dr. Steinkamp & Büssenschütt, Germany.

An ultrasonic signal is transmitted through the test piece and the transmission-time is analysed. An increase of the sonic velocity indicates a physical change in the castable that typically correlates with the stiffening due to hydration in case of cement containing or a gelation in case of sol/gel bonded castables. For proper moulding a sufficient working window is necessary but thereafter a rapid gain in strength is inevitable for sufficient demoulding properties of the test pieces.

2.4.1.3. Cold Modulus of Rupture

The Cold Modulus of Rupture (CMoR, 3-point bending strength) was measured on dried and tempered test pieces in accordance with DIN EN ISO 1927-6.

2.4.2 Raw material selection and preparation of spiked raw materials

Refractory products are coarse ceramic materials that display a broad spectrum of grain sizes. Impurities tend to accumulate in the fine (matrix) fractions, which behave distinctly from the coarser-grained fractions. The matrix predominantly dictates the properties of a high-performing refractory material, with particularly crucial implications for refractory castables (unshaped refractory products), which have typically a higher matrix share than shaped refractory products [11]. Therefore, a matrix component material was chosen as the basis material to be spiked with impurities. Reactive and calcined alumina were found to be unsuitable for the mixing with the impurity raw materials in preliminary tests due to their extreme fineness (d50 < 2 µm). Finally, the tabular alumina (T60/64) corresponding to the matrix fraction of 0-45 µm (d50 = 10 µm) from Almatis GmbH in Germany was selected. The spiked materials, or precursors, were composed of 98 weight percent as delivered tabular alumina in the 0-45 µm fraction and 2 weight percent added impurifications. The, in this manner introduced impurities, were tailored in terms of the type and quantity. Common impurities, including Na, Ti, Si, Ca, and Fe, were identified as particularly relevant, either by being impurities already found during the production process of refractory raw materials and/or or residue from previous industrial use (secondary raw materials) and accordingly selected for the present research.

FactSage was utilized to ascertain the critical concentration and mixing ratios of the oxidic components of the selected impurities, especially utilizing ternary or four component systems, with alumina as the primary component. An illustration is presented in the following two figures, revealing the N/S ratio for the precursor identified as 2NS. Figure I.1 presents a binary phase diagram of an alumina system making 98% of the total composition and the remaining 2% a combination of SiO_2 and Na_2O. The phase diagram was generated using the FactSage® software. The temperature is plotted in °C against the ratio of SiO_2 and Na_2O. SiO_2 is represented at 100% when the x-axis value is 0, while Na_2O is represented likewise when the x-axis value is 0.02. The values are normalized to 1.0 and result in 0.98 alumina and a range of 0 - 0.02 for the sum of SiO_2 and Na_2O. The eutectic at an approximate N/S ratio of 1/4 with a temperature of 1068 °C, as confirmed by the ternary phase diagram of Na_2O, Al_2O_3, and SiO_2, provided in the figure I.2. This methodological approach was used to calculated further four additional precursor compositions (2CS, 2FC, 2FCS, and 2TCS) listed in the table I.1, which served as the foundation for the ensuing production process. The calculation was adjusted to determine the optimal ratio for maximum liquid phase formation at temperatures exceeding 1600 °C. The sintering temperature of the precursors was set to this value to mimic the conditions of a practical application, thereby ensuring comparable phase transformations with secondary raw materials.

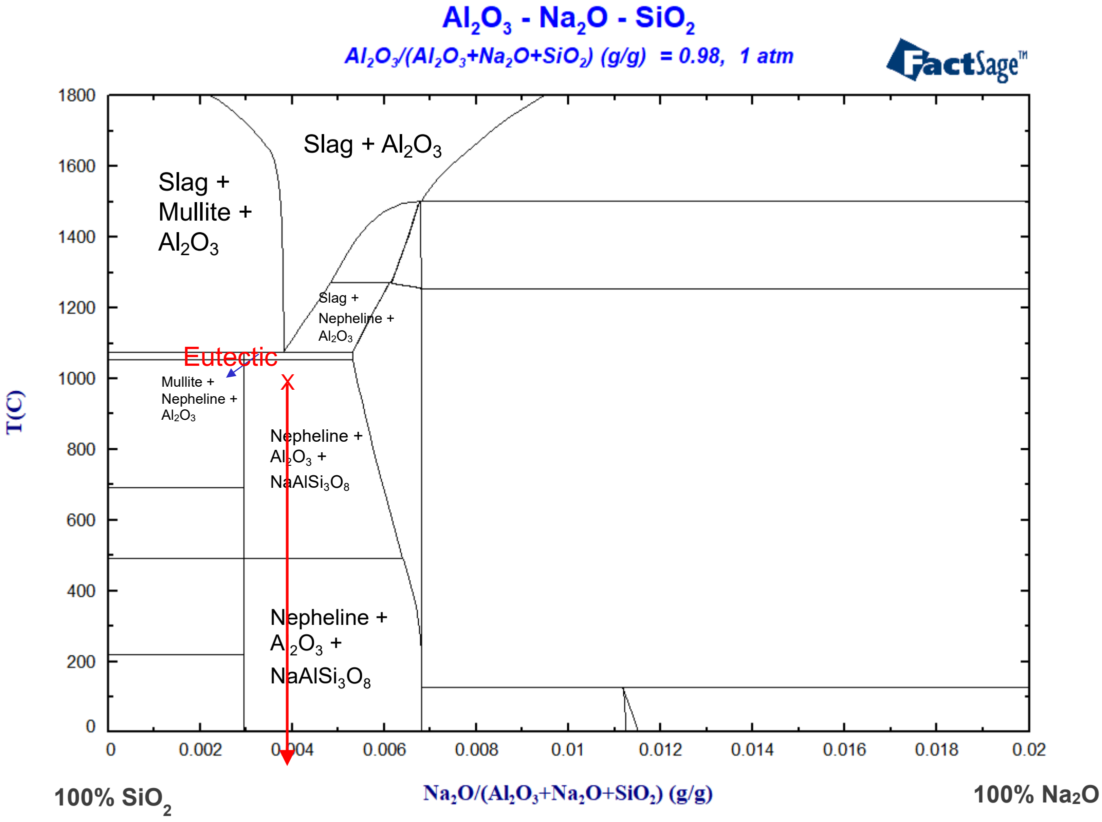

Fig. I.1: Binary component system of SiO_2 and Na_2O in the presence of 98 % of Al_2O_3 to determine the N/S ratio at the eutectic point (about 1/4).

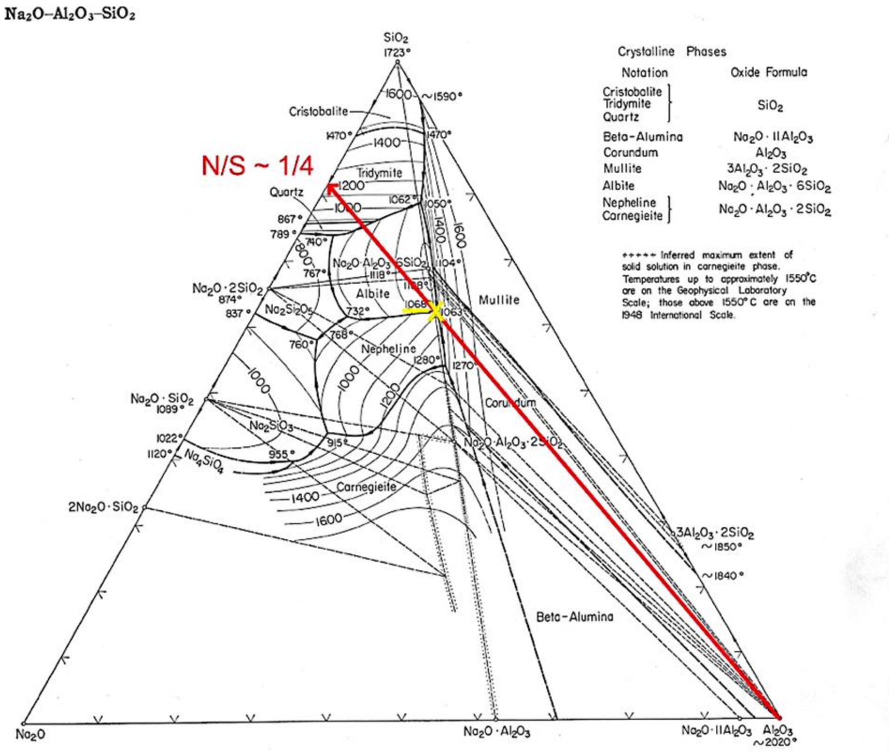

FIG. 501.—System Na_2O–Al_2O_3–SiO_2; composite.

E. F. Osborn and Arnulf Muan, revised and redrawn "Phase Equilibrium Diagrams of Oxide Systems," Plate 4, published by the American Ceramic Society and the Edward Orton, Jr., Ceramic Foundation, 1960.

Fig. I.2: System Na_2O - Al_2O_3 - SiO_2. [12]

Tab. I.1: Calculated composition (highest amount of liquid phase at 1600 °C) of selected five precursors; 98 wt.% Al_2O_3 and 2 wt.-% in total of two or three of the oxides of the selected impurities (Na_2O, TiO_2, SiO_2, CaO and Fe_2O_3).

Component / wt%	**2CS**	**2NS**	**2FC**	**2FCS**	**2TCS**
Al_2O_3	98	98	98	98	98
CaO	1,0	-	0,7	0,7	0,9
SiO_2	1,0	1,6	-	0,3	0,8
Na_2O	-	0,4	-	-	-
Fe_2O_3	-	-	1,3	1,0	-
TiO_2	-	-	-	-	0,3
Sum	**100**	**100**	**100**	**100**	**100**

Figure 3 illustrates the production process of the precursors. The resulting mixture was granulated for further processing. Highly refined alumina powder (particle size < 45 µm) was mixed with powder of the oxide or carbonate form of the impurities (Na_2CO_3, TiO_2, SiO_2, $CaCO_3$, and Fe_2O_3) and homogenized in an intensive countercurrent mixer using a granulation tool from Maschinenfabrik Gustav Eirich GmbH & Co KG, Germany. Granulation was necessary to achieve sufficient bonding between the raw materials and impurities, and accordingly the desired phase transformations during subsequent sintering at 1600°C. Subsequently, the materials were ground to a fraction of 0-45 µm using opposed fluidized bed jet mills (Hosokawa Micron Powders GmbH, Germany).

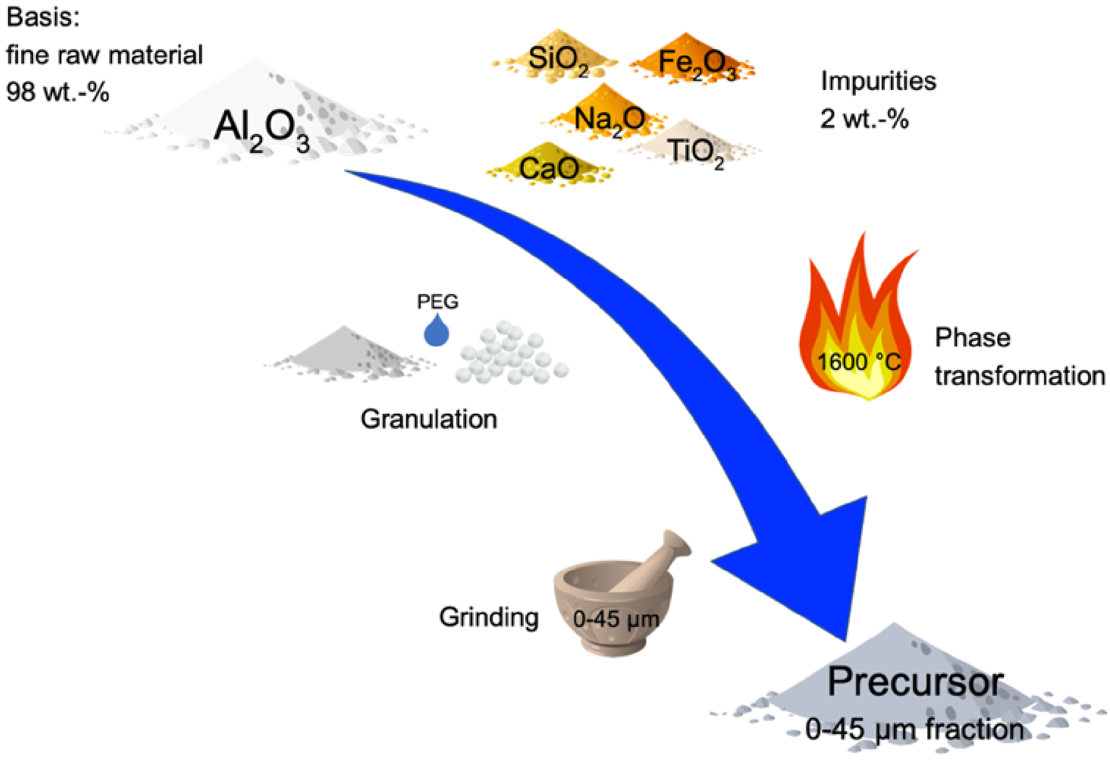

Fig. I.3: Flow-chart of the production process of the precursors.

Figure I.4 shows the resulting particle size distributions (PSD) of the milled precursors compared to the reference 0-45 µm tabular alumina from Almatis measured with laser granulometry (Saturn DigiSizer II, Micromeritics Corporate, GA, USA). The obtained PSD of the precursor looked relatively similar to the PSD of the precursors to the reference alumina but show a narrower particle size range in their distribution and a nearly double as high d_{50} value (Tab. I.2). In the case of 2CS there is even a bimodal distribution but a d_{50} value (14,88 µm) closer to the reference (10,39 µm). It should be noted that this value does not perfectly comply with the values from the datasheet of Almatis (26 µm), however, as all analysis were performed with the same equipment, the measured values were deemed suitable for a direct comparison of the results. The precursor 2FC has the highest d_{50} value of 22,03 µm, which is slightly over twice as much as the reference value.

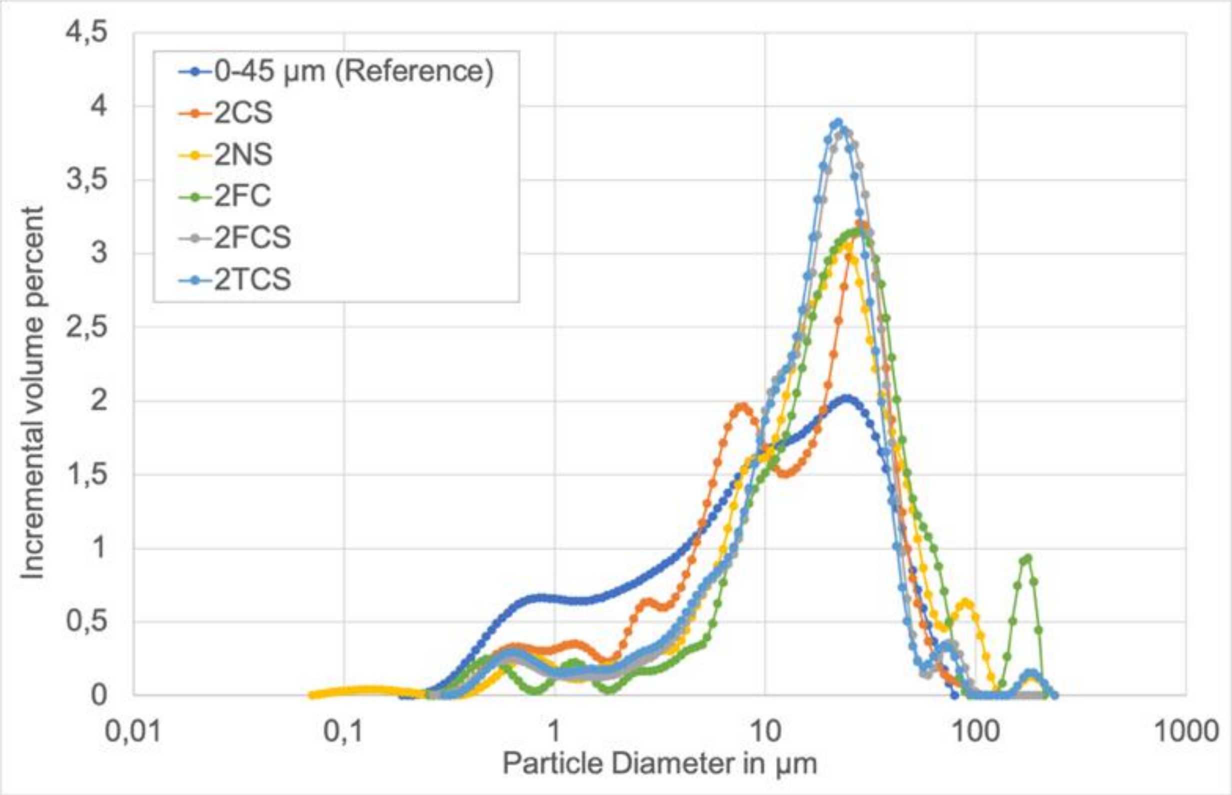

Fig. I.4: PSD of the prepared precursors (2CS, 2NS, 2FC, 2FCS and 2TCS) compared to the 0-45 µm reference fraction of tabular alumina material measured by laser granulometry.

Tab. I.2: d_{50} values of the prepared precursors (2FC, 2NS, 2FC, 2FCS and 2TCS) compared to the 0-45 µm reference fraction of tabular alumina material measured by laser granulometry.

Material	0-45 µm	2CS	2NS	2FC	2FCS	2TCS
d_{50} in µm	10,39	14,88	18,87	22,03	18,64	17,77

The distribution of impurities in the prepared precursors and the pure 0-45 µm alumina was checked by X-ray fluorescence analysis (XRF- spectrometer Axios max 2,4 kW, Malvern Panalytical, Kassel, Germany) (Fig. I.5). The total amount of impurities within the precursors is 2 wt.-%. The other 98 wt.-% of the precursor is alumina. The amount of the individual impurities (aimed and measured) as well as the measured deviation of the measured (real) values are provided on the left of the figure 5. For each batch of precursor powder, five samples were taken and measured to check the number of impurities. The slight elevation of almost all values in comparison to the aimed values (bars in the figure 5) may be the result of the presence from the minor impurities in the basis alumina material (Fig. I.5 – left diagram).

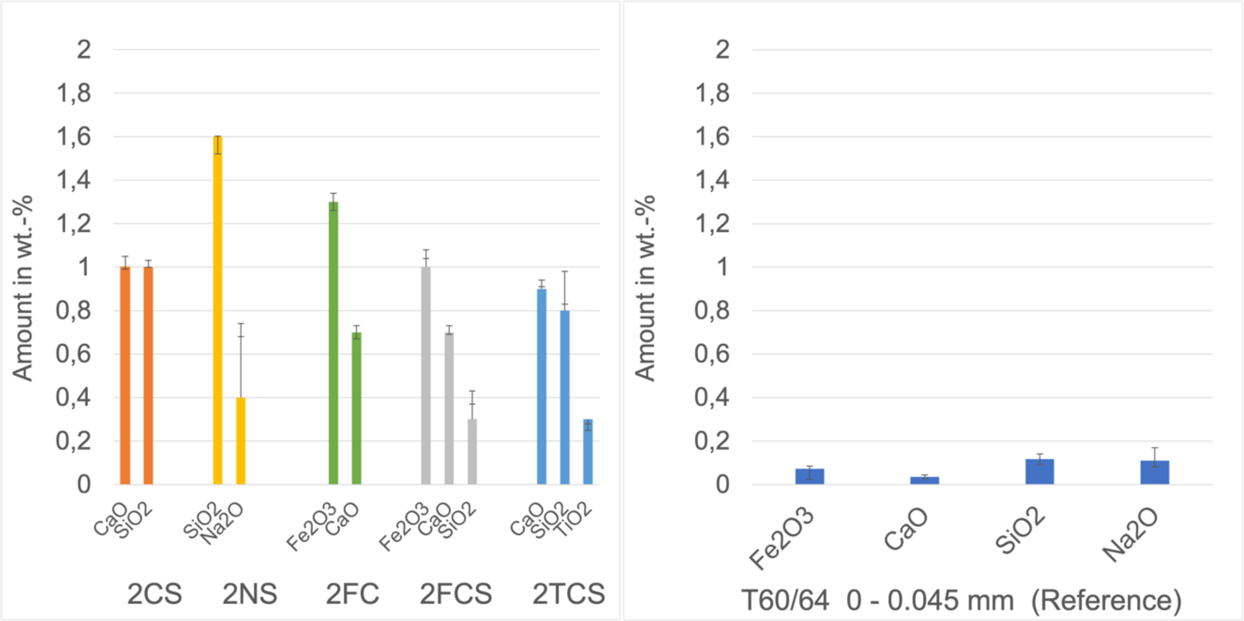

Fig. I.5: Left: oxidic ratio of impurities in the prepared precursors (2CS, 2NS, 2FC, 2FCS and 2TCS) and the deviation of the measured (real) values to the aimed values (bars); Right: oxidic ratio of impurities in the pure alumina T60/64 0-0.045 mm, measured by X-ray fluorescence analysis; each material measured five times.

2.4.3 Raw materials and additives

The physical and chemical properties of the raw materials used for the preparation of the model castables are listed in the tables I.3 and I.4. The alumina raw materials and a hydratable alumina binder Alphabond 300 were provided by Almatis GmbH, Ludwigshafen, Germany.

A poylcarboxylate ether Castament FS60 from BASF SE, Ludwigshafen, Germany was used as dispersing agent.

The following materials were used as impurities:

- Calcium carbonate (min. 99 %), sodium carbonate (min. 99.5 %) and Kieselgel 60 (0.02 – 0.045 mm) from Carl Roth GmbH & Co. KG, Karlsruhe, Germany
- Nano Titanium dioxide (anatase, min 99 %)
- Iron oxide from ThyssenKrupp Steel Europe AG, Duisburg, Germany

As spinel-forming agent NedMag 99-170 mesh, a high-purity synthetic Dead Burned Magnesia (DBM) from Nedmag B.V., Veendam, Netherlands was used. This material was chosen for its elevated MgO concentration and minimal impurities.

Tab. I.3: Specific surface area, particle size and chemical analysis (producer's specifications) for the fine alumina raw materials.

		Alphabond 300		**RG4000**	**CTC20**	**T60 0-0,045**	
Properties/ method		min.	max.	typ.	typ.	typ.	max.
Specific surface area/ BET	m^2/g			7.2	2.0		
Particle size / d_{50}	µm	4	8	0.6	1.8		
Particle size / d_{90}	µm		30	3.0	4.5		0.045
Chemical analysis							
Al_2O_3	%	88		99.8	99.7	99.10	
Na_2O	%		0.5	0.08	0.12		0.60
Fe_2O_3	%			0.02	0.03		0.30
SiO_2	%		0.3	0.03	0.03		0.12
CaO	%		0.1	0.03	0.03		
MOI (% loss 25 – 250 °C)			4.1				
LOI (% loss 250 – 1000°C)		5.0	7.0				

Tab. I.4: Specific surface area, particle size and chemical analysis (producer's specifications) for the coarse alumina raw materials.

		T60 0-0,2		**T60 0,2-0,6**		**T60 0,5-1,0**		**T60 1,0-3,0**	
Properties / method		typ.	max.	typ.	max.	typ.	max.	typ.	max.
Particle size	mm		0.2		0.6		1.0		3.0
Chemical analysis									
Al_2O_3	%	99.50		99.50		99.50		99.50	
Na_2O	%		0.40		0.40		0.40		0.40
Fe_2O_3	%		0.02		0.02		0.02		0.02
SiO_2	%		0.09		0.09		0.09		0.09
CaO	%								

2.4.4 Castable and test piece preparation

The reference refractory model castable (MHA-REF) is a self-flowing, cement-free, tabular alumina castable based with a maximum grain size of 3 mm. The formulation contains different types of alumina raw materials supplied by Almatis GmbH, Germany. Using the prepared precursors, five corresponding unpurified model castables were developed by substituting the 0-45 mm tabular alumina grain fraction delivered by Almatis 1:1 with one of the precursors (Tab. I.5). Calculated on the basis of the composition the resulting amount of impurities brought in the castable by the precursor is 0,18 wt.-%. All developed castables were bonded with 5.0 wt.-% of Alphabond 300 (Hydratable Alumina), an amorphous alumina forming hydraulic bonds, from Almatis GmbH, Germany and dispersed with 0,15 wt.-% Castament FS60 a PCE from BASF SE, Germany. High alumina cement-free refractory castables have the advantage of being a relatively simple and convenient model with a well-defined and homogeneous composition, so that the effect of the impurities should be easy to detect and investigate. Additionally, a matching set of spinel-forming castables was prepared using NedMag 99-170 mesh, a dead burned MgO, to trigger the spinel-formation at high temperature (Tab. I.6). 2 wt.-% of NedMag were added and substituted 2 wt.-% of the alumina grain fraction 0 – 0,2 mm which is comparable in the average particle size of approx. 70 µm.

To ensure a proper mixing, an intensive mixer (type R02, Eirich GmbH & Co. KG, Germany) was used. For mixtures ≤ 4 kg a stick agitator and simultaneous rotation was selected, while a star stirrer with counter rotation was used for mixes ≥ 4 kg. All castable formulations were prepared with A mixing speed of 450 rpm was used, applying 1 min dry mixing and 4 min wet mixing time.

Besides bars for CMoR measurements, several test pieces of various shapes were casted for the project partners' high temperature investigations. After casting the test pieces, they were cured for 48 h (demoulded after 24 h) in a climatic cabinet at 20 °C and 95 % rh. Afterwards they were dried at 110 °C for further 24 h.

Tab. I.5: Recipes of the reference model refractory castable MHA-REF and the impurified formulations MHA-2CS, MHA-2NS, MHA-2FC, MHA-2FCS and MHA-2TCS, where the TA fraction 0-45 µm has been replaced by the precursors 2CS, 2NS, 2FC, 2FCS and 2TCS.

Component	**wt.-%**					
	MHA[1)]-REF	**MHA-2CS**	**MHA-2NS**	**MHA-2FC**	**MHA-2FCS**	**MHA-2TCS**
Tabular alumina (T60/64)						
0,2-3 mm	57	57	57	57	57	57
0-0,2 mm	12	12	12	12	12	12
0-0,045 mm	9	-	-	-	-	-
Precursor 0-0,045 mm	-	9	9	9	9	9
Calcined alumina (CTC20)	10	10	10	10	10	10
Reactive alumina (RG4000)	7	7	7	7	7	7
Binder (Alphabond 300)	5	5	5	5	5	5
Sum	**100**	**100**	**100**	**100**	**100**	**100**
Water	6,3	6,3	6,3	6,3	6,3	6,3
Dispersing agent (PCE) Castament FS60	0,15	0,15	0,15	0,15	0,15	0,15

[1] MHA: MonolithicHydratableAlumina

Tab. I.6: Recipes of the reference model refractory castable MHA-S-REF and the impurified formulations MHA-S-2CS, MHA-S-2NS, MHA-S-2FC, MHA-S-2FCS and MHA-S-2TCS, where the TA fraction 0-45 µm has been replaced by the precursors 2CS, 2NS, 2FC, 2FCS and 2TCS and MgO was added for the spinel-formation during at high temperature.

Component	**wt.-%**					
	MHA-S[2)]-REF	**MHA-S-2CS**	**MHA-S-2NS**	**MHA-S-2FC**	**MHA-S-2FCS**	**MHA-S-2TCS**
Tabular alumina (T60/64) 0,2-3 mm	57	57	57	57	57	57
0-0.2 mm	10	10	10	10	10	10
0-0,045 mm	9	-	-	-	-	-
Precursor 0-0.045 mm	-	9	9	9	9	9
Calcined alumina (CTC20)	10	10	10	10	10	10
Reactive alumina (RG4000)	7	7	7	7	7	7
Binder (Alphabond 300)	5	5	5	5	5	5
MgO (nedMag 99-170 mesh)	2	2	2	2	2	2
Sum	**100**	**100**	**100**	**100**	**100**	**100**
Water	6,3	6,3	6,3	6,3	6,3	6,3
Dispersing agent (PCE) Castament FS60	0,15	0,15	0,15	0,15	0,15	0,15

[2] MHA-S: MonolithicHydratableAlumina-Spinelforming

2.4.4.1. Test pieces for Subproject II (L-ICiMB)

To obtain a quantitative and reliable finding of the effect of the impurities on the behaviour of the refractory castable at high temperature, the model refractory castables have undergo intense thermo-mechanical investigations using standardized methods with extended testing conditions (Subproject II). The testing methods ICiMB used, and the correspondent test piece formats produced by HSKO are as follows:

Creep in Compression (CiC) according to DIN EN 993-9 and **developed testing procedure of creep investigations based on Northon Bailey creep parameters** to reveal the creep mechanism by identifying stages of creep process as well as **Refractoriness under Load (RuL)** acc. to DIN EN ISO 1893:2008:

- Format B to drill ∅35 x 50 mm^3 cylinders (Fig. I.6 (a)),
- Cylinders format ∅50 x 120 mm to cut two ∅50 x 50 mm^3 cylinders (Fig. I.6 (c)),
- Bars format 20 x 20 x 160 mm^3 to drill ∅14 x 20 mm^3 cylinders

Resonant frequency and damping analysis (RFDA) to determine changes in stiffness (Young's modulus) at high temperature and therefore to detect structural changes like cracks or grain growth as well as to assess the temperature range of the elasticity of the monolithics developed:

- Bars special format 25 x 45 x 150 mm^3 to be cut in 25 x 25 x 150 mm^3 (Fig. I.6 (b)),
- Plates to cut bars 12/24 x 65 x 140 mm^3

All these measurements were carried out by partner L-ICiMB in Poland.

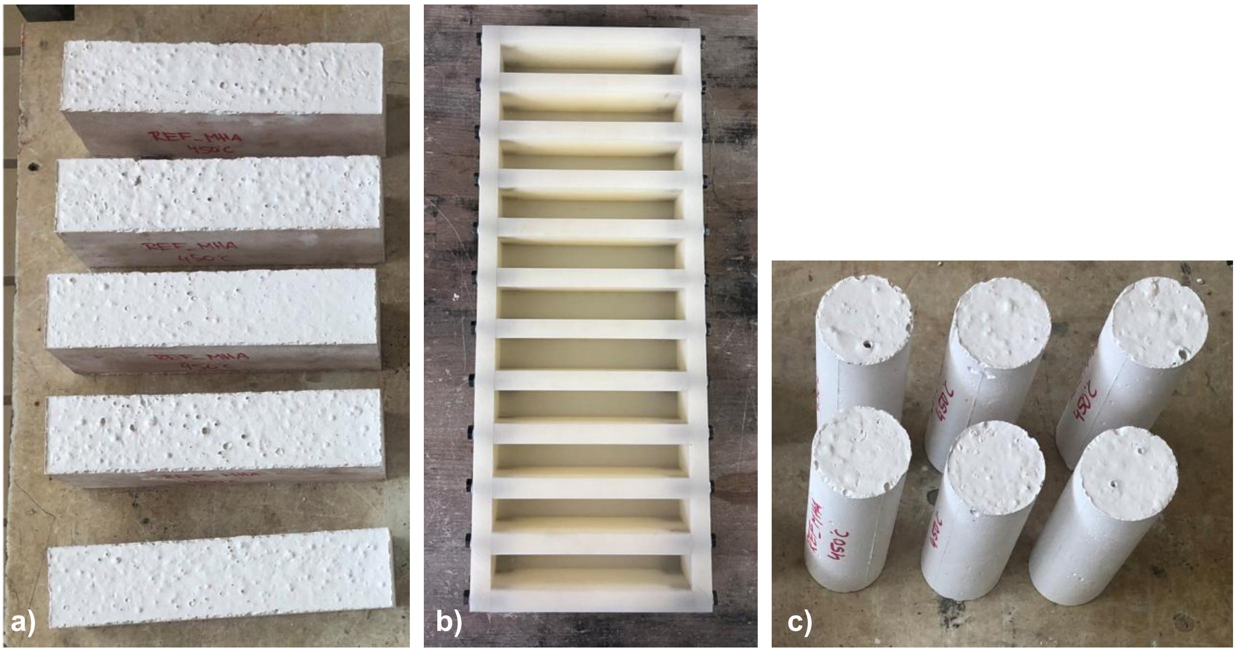

Fig. I.6: ***a)*** *Format B test pieces after drying,* ***b)*** *Casting mould for bars in format 25 x 45 x 150* mm^3*,* ***c)*** *cylindric test pieces with the dimension ∅50 x 120* mm^3 *after drying.*

2.4.4.2. Test pieces for Subproject III (FGF)

For the **newly developed innovative testing device** that allows investigation of the combined effect of temperature gradient and load (Subproject III), test pieces with the dimensions of Format B bars, but casted in a specially designed upend Format B mould (Fig. I.7 (a) und (b)) to avoid the presence of casting skin on the long sides of the test pieces, were prepared. Furthermore, HSKO produced the refractory plungers necessary for the new testing device (see section 4.3.3), by casting a cement bonded high alumina castable (a refractory castable well studied from Hochschule Koblenz side) into a special mould provided by FGF (Fig. I.7 (c)).

In addition, to support the thermo-mechanical investigations performed within the Subproject II by the polish partner L-ICiMB, high-temperature fracture characterisation of the two sets of developed impurified model castables was performed using the **wedge splitting method** (see section 4.3.2.1). To this end on cubic samples 100 x 100 x 75 mm^3 (Fig. I.7 (d)) were casted, as well as cylinders with the dimensions ∅ 46 x 100 mm^3 to perform **Monotonic Heating Method (MMH)** measurements (see section 4.3.2.2).

All these measurements were carried out by partner FGF in Germany.

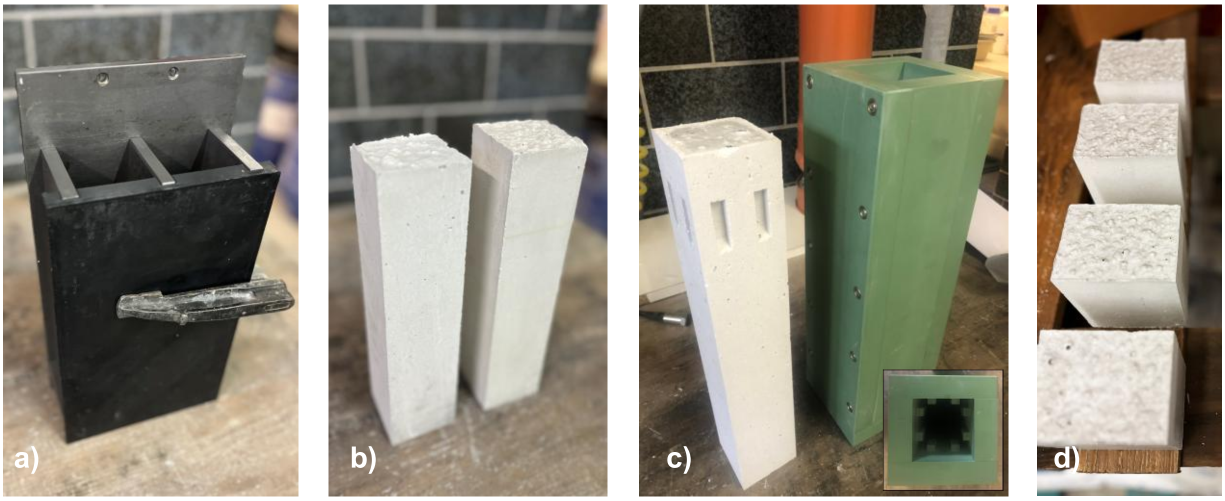

Fig. I.7: ***a)** upend mould to cast Format B test piece without casting skin on their long sides, **b)** Format B test piece without casting skin on their long sides after drying, **c)** Refractory plunger of the new testing device of FGF after drying and its mould including a top view of the mould in the small picture, **d)** WST cubes after drying before machining.*

2.5 Results and discussion

2.5.1 Slump flow measurements

The slump flow area was calculated using top view pictures taken from the digital camera during the slump flow test, which were converted to black and white shadow pictures. The area of the spreading slump flow is set in relation to the area of the cone (0,01 m^2). The measurement is typical performed for 10 min (600 s), which is significantly longer than recommended by DIN EN ISO 1927-4 (60 s). Figures I.8 and I.989 show the resulting time resolved curves of the evolution of the slump flow area in m^2 for the six spinel-free and six spinel-forming model refractory castables. This highlights well why a measurement period 10 times longer than recommended by the standard was selected, the spread flow is not terminated after 60 s.

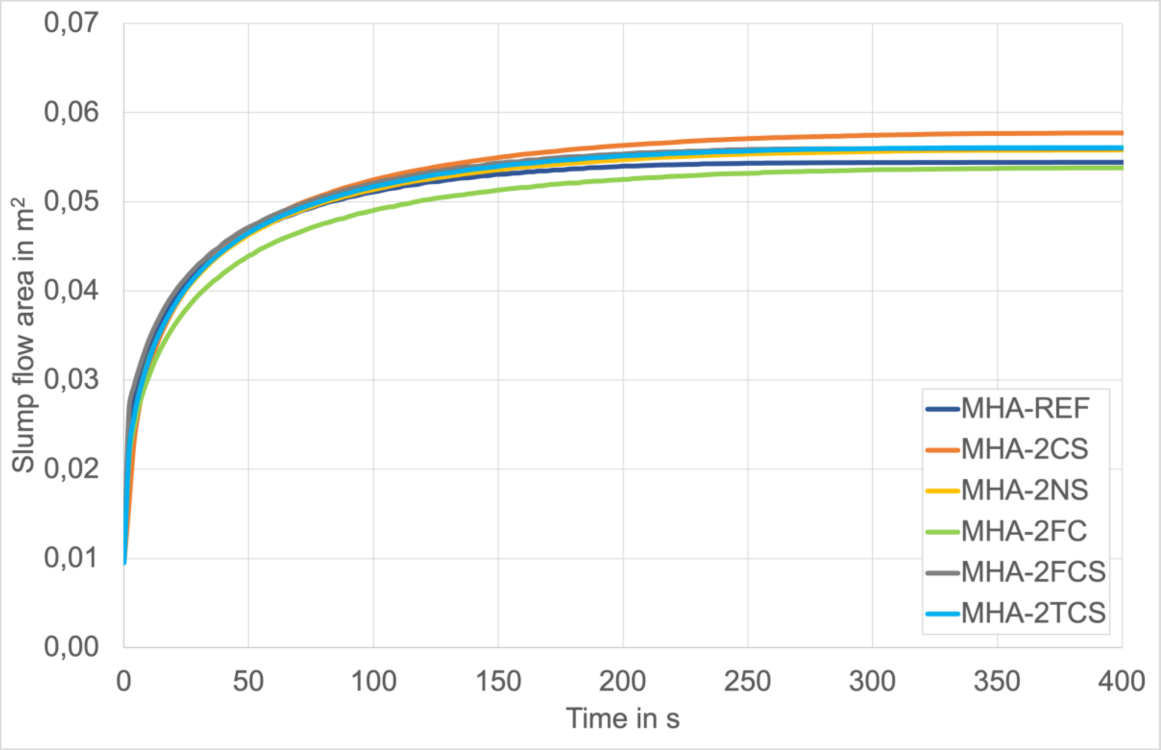

Fig. I.8: *Time dependent evolution of the slump flow area for the reference model castable (MHA-REF) and the model castables after substitution of the TA fraction 0-45 µm by the different precursors (MHA-2FCS, -2NS, -2CS, -2TCS and -2FC).*

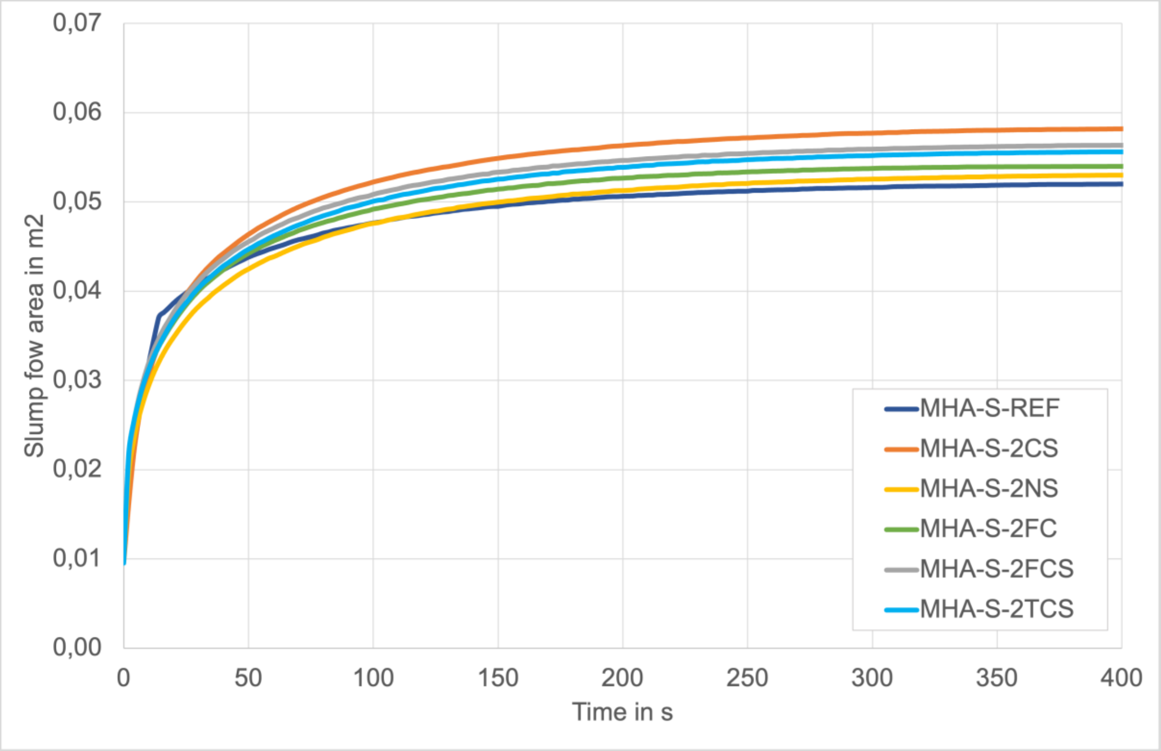

Fig. I.9: *Time dependent evolution of the slump flow area for the spinel-forming reference model castable (MHA-S-REF) and the spinel-forming model castables after substitution of the TA fraction 0-45 µm by the different precursors (MHA-S-2FCS, -2NS, -2CS, -2TCS and -2FC).*

The diameters in mm were calculated from the final slump flow areas in m^2, namely as the flow stopped. The values for the spinel-free model castables are listed in table 7 together with the time in seconds when the final spread was reached. With an average of 266 mm the values of the diameters are comparable and characteristic for self-flowing castables. MHA-2CS showed the largest final spread with a value of 271 mm in combination with the longest flow time (306 s) before a constant slump flow area was reached. The lowest final spreads were observed for MHA-REF and MHA-2FC with values of respectively 263 mm and 262 mm. MHA-2FC reached this final spread much slower (292 s) than the reference material which was the fastest (172 s) to stop flowing. The final spread of mixtures MHA-2NS, MHA-2FCS and MHA-2TCS were very similar. With values of respectively 267 mm, 266 mm and 267 mm, they all showed a slightly lower final spread and with values of 272 s / 212 s / 230 s and stopped to flow significantly later than MHA-REF, but earlier than MHA-2CS.

Tab. I.7 Diameter of the final spread of the slump flow measurement for the cement-free self-flowing high alumina castable reference model material (MHA-REF) and the five cement-free self-flowing high alumina model castables with substitution of the TA fraction 0-45 µm by the different precursors (2FCS, 2NS, 2CS, 2TCS and 2FC).

Castable	**Ø final spread in mm**	**Stoppage time (end of flow) in s**
MHA-REF	263	172
MHA-2CS	271	306
MHA-2NS	267	272
MHA-2FC	262	292
MHA-2FCS	266	212
MHA-2TCS	267	230

The spinel-forming castables and their corresponding final spreads and time in seconds to reach them are listed in table 8. The final spreads had an average value of 264 mm which was accordingly comparable between the spinel-forming and spinel-free model castables. Like for the spinel-free formulations, MHA-S-2CS displayed the largest final spread with 272 mm, while MHA-S-REF presented the lowest with 258 mm. The bimodal PSD of the 2CS precursor seems to promote the flow behavior. MHA-2FCS achieved its final spread, namely 268 mm, in the shortest time, namely 256 s, while MHA-S-2TCS had a similar final spread (266 mm), but it took 356 s, making it the slowest. On average, the spinel-forming castables flowed for over half a minute longer (288 s), compared to the spinel-free castables (247 s) to reach similar spread values. This may be attributed to the spinel-forming agent MgO in the castable formulation that seemed increase the viscosity of the castable. A higher water demand for spinel-forming MgO containing castables to maintain the flow properties similar to those of spinel-free castables was even identify in other research projects.

Tab. I.8 Diameter of the final spread of the slump flow measurement for the cement-free, self-flowing, high alumina spinel-forming reference model castable (MHA-S-REF) and the five cement-free, self-flowing, high alumina , spinel-forming model castables with substitution of the TA fraction 0-45 µm by the different precursors (2FCS, 2NS, 2CS, 2TCS and 2FC).

Castable	**Ø final spread in mm**	**Stoppage time (end of flow) in s**
MHA-S-REF	258	280
MHA-S-2CS	272	280
MHA-S-2NS	260	294
MHA-S-2FC	262	266
MHA-S-2FCS	268	256
MHS-S-2TCS	266	356

As reported by Klein [10], the end of flow (stoppage time) correlates with the slump flow diameter. Figure Fig. I.10 shows this correlation when plotting the stoppage time against the final spread. The only exception is the mixture MHA-2FC that displayed the smallest spread and took longest to stop flowing. Mixtures with lower viscosity will show a higher flow rate if the PSD is properly adjusted. Since it is assumed that all ions from the added impurities are bound in the raw material, they should not influence the flow behaviour. It is therefore much more likely that the variations could be attributed to the different PSD of the spiked precursors (Fig. I.4). The much higher d_{50} value of the MHA-2FC precursor (Tab. I.2) could be an explanation for this deviating final spread of 262 mm. As indicated in the figure 11, with increasing d_{50} the final spread almost systematically decreased and thus indicates an increase in the viscosity of the mixture.

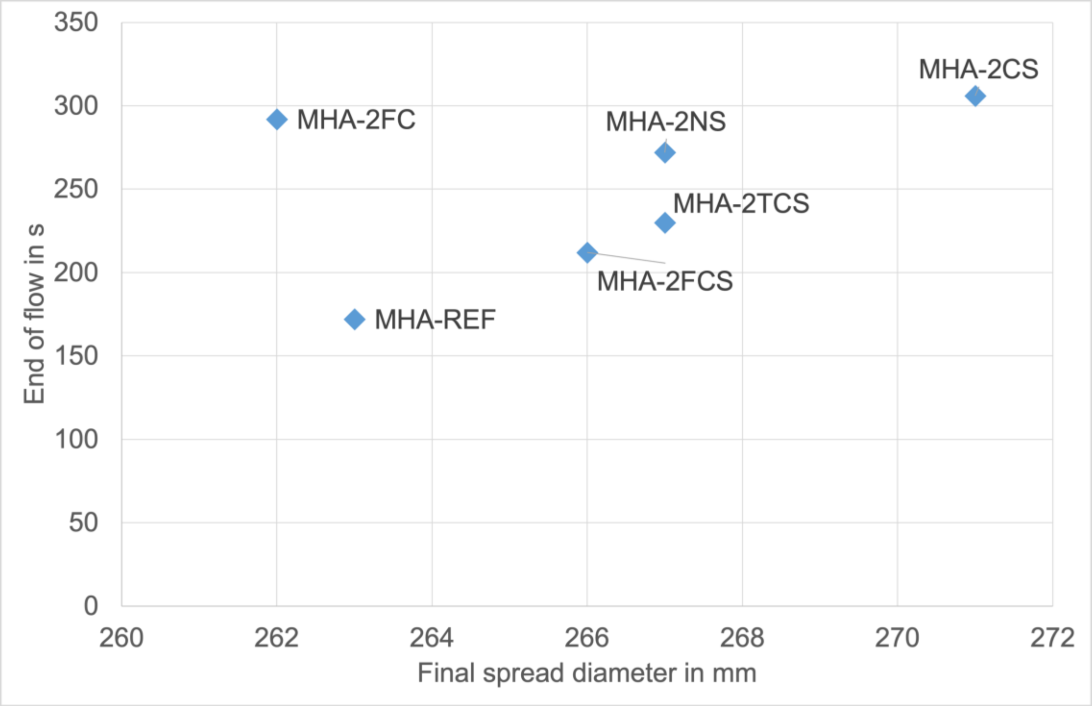

Fig. I.10: End of flow against the final spread in diameter of the slump flow test for the cement-free, self-flowing, high alumina, spinel-free reference model castable (MHA-REF) and the five cement-free, self-flowing, high alumina, spinel-free model castables with substitution of the TA fraction 0-45 µm by the different precursors (MHA-2FCS, -2NS, -2CS, -2TCS and -2FC).

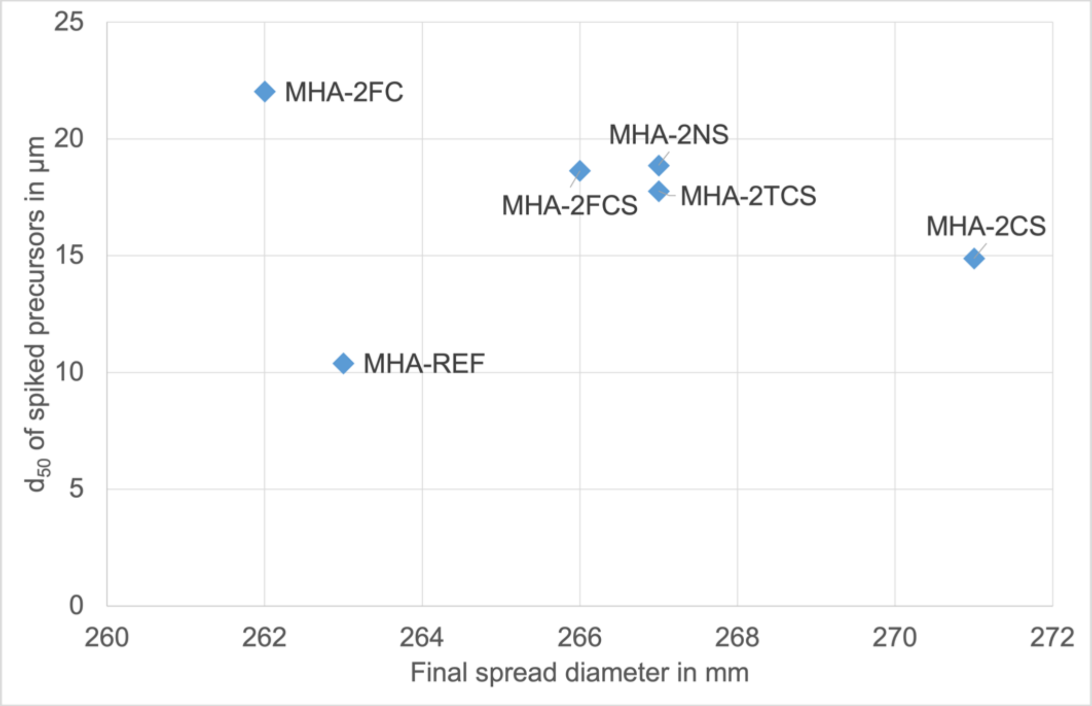

Fig. I.11: d_{50} of spiked precursors against the final spread diameter of the slump flow test for the cement-free, self-flowing, high alumina, spinel-free reference model castable (MHA-REF) and the five cement-free self-flowing, high alumina, spinel-free model castables with substitution of the TA fraction 0-45 µm by the different precursors (MHA-2FCS, -2NS, -2CS, -2TCS and -2FC).

The before described correlation between end of flow and final spread is not observable for the spinel-forming castables (Fig. I.12), but the d_{50} value of the spiked precursors (Tab. I.2) may still influence the final spread (Fig. I.13).

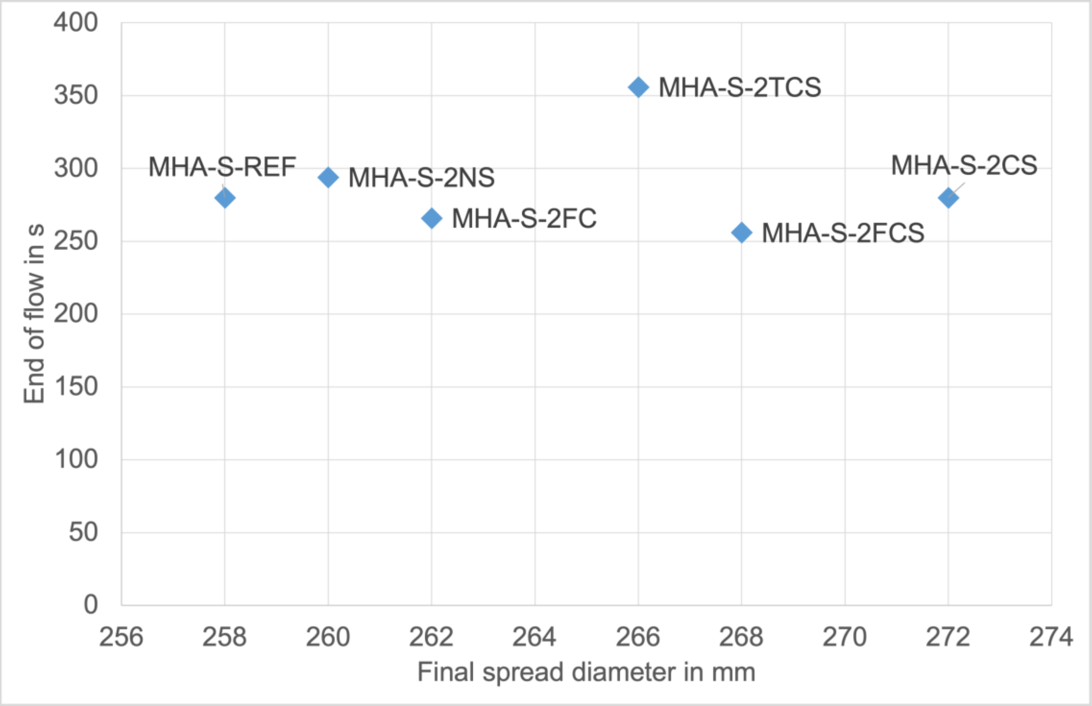

Fig. I.12: End of flow against the final spread in diameter of the slump flow test for the cement-free, self-flowing, high alumina, spinel-forming reference model castable (MHA-S-REF) and the five cement-free, self-flowing, high alumina, spinel-forming model castables with substitution of the TA fraction 0-45 µm by the different precursors (2FCS, 2NS, 2CS, 2TCS and 2FC).

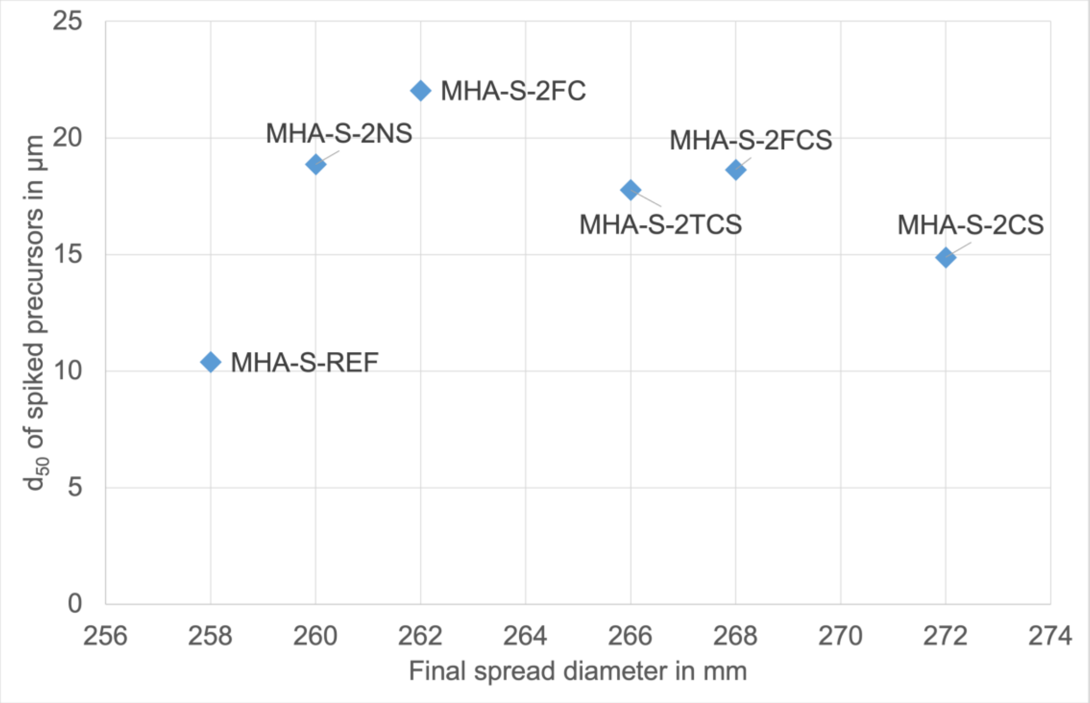

Fig. I.13: d_{50} of spiked precursors against the final spread diameter of the slump flow test for the cement-free, self-flowing, high alumina, spinel-forming reference model castable (MHA-S-REF) and the five cement-free, self-flowing, high alumina, spinel-forming model castables with substitution of the TA fraction 0-45 µm by the different precursors (2FCS, 2NS, 2CS, 2TCS and 2FC).

2.5.2 Investigation of the setting and curing behaviour

The setting and curing behaviour assessed by the ultrasonic velocity measurements (figures I.14 and I.15) was comparable for all castables, spinel-free and spinel-forming, and has no technological impact on the castables preparation. These results tend to confirm the assumption that the ions, added as impurities, were no longer water-soluble and were bound in the raw material by sintering. The increase in ultrasonic velocity began for all castables after approximately 4 hours of cure and indicates a physical change in the castable that typically correlates first with the coagulation of the castable and then with the hydration-induced stiffening. At the end of the measurements similar values of ultrasonic velocity were obtained.

All in all, the impact of the addition of impurities in the 0-45 µm fraction of the model castables on their workability and their moldability was negligeable and all test pieces could be casted properly.

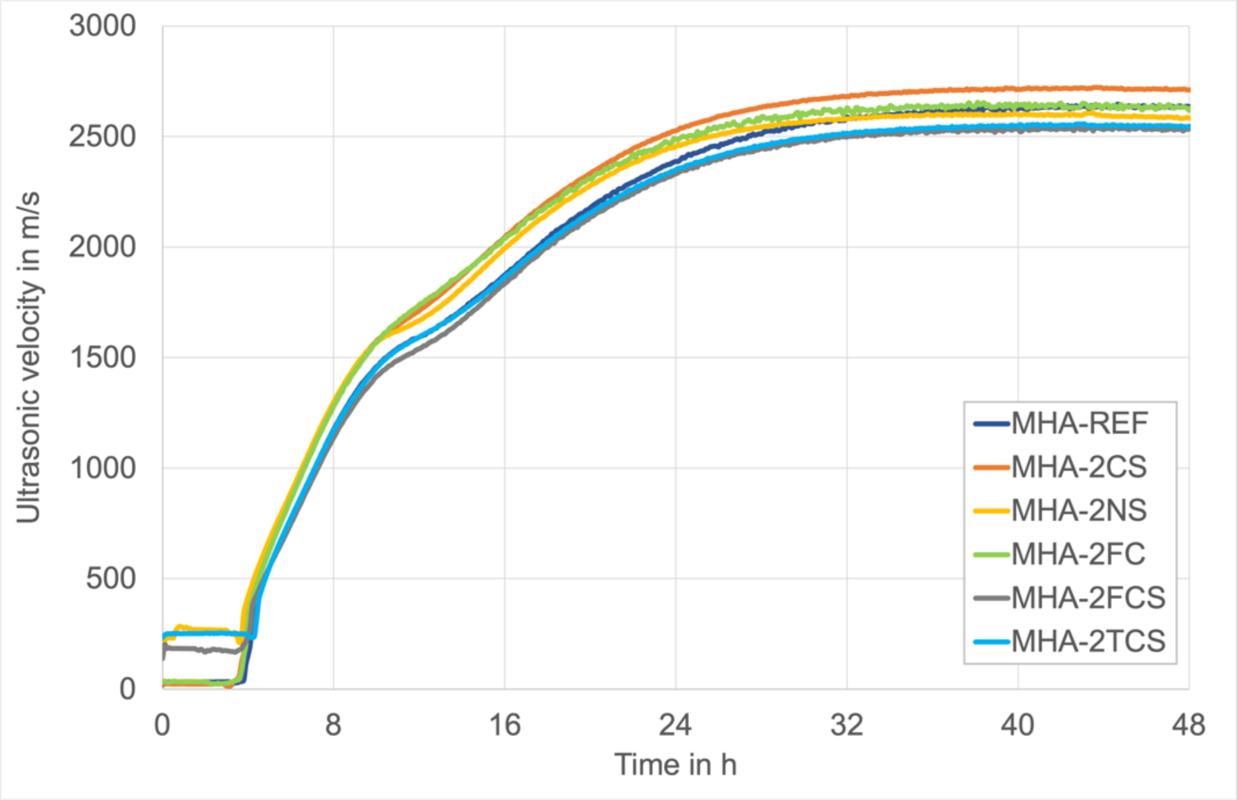

Fig. I.14: Time dependent evolution of the ultrasonic velocity for the cement-free, self-flowing, high alumina, spinel-free reference model castable (MHA-REF) and the five cement-free, self-flowing, high alumina, spinel-free model castables with substitution of the TA fraction 0-45 µm by the different precursors (MHA-2FCS, -2NS, -2CS, -2TCS and -2FC), curing conditions: 20 °C and 95 % relative humidity. MHA-2NS, -2FCS, and -2TCS show at the beginning a higher initial sonic velocity that is attributed to a measuring device related erroneous zero value definition.

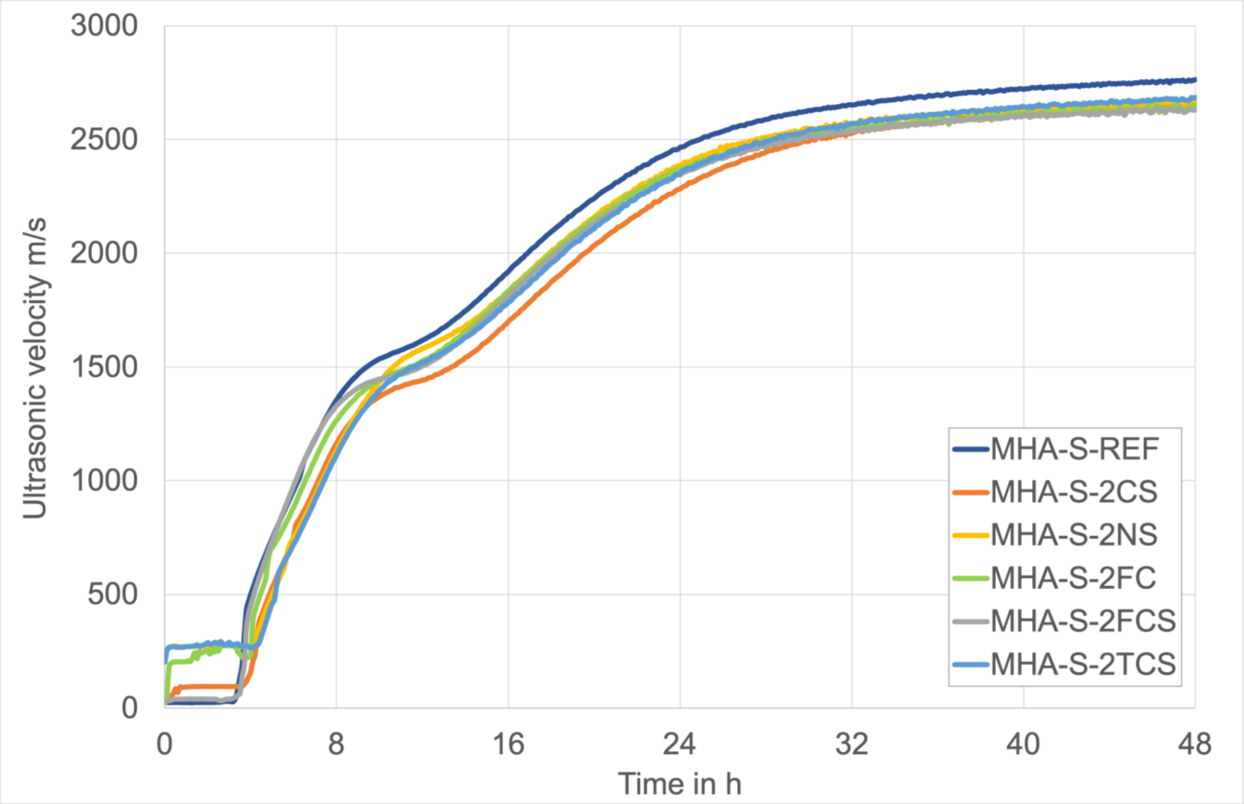

Fig. I.15: Time dependent evolution of the ultrasonic velocity for the cement-free, self-flowing, high alumina, spinel-forming reference model castable (MHA-S-REF) and the five cement-free, self-flowing, high alumina, spinel-forming model castables with substitution of the TA fraction 0-45 µm by the different precursors (MHA-S-2FCS, -2NS, -2CS, -2TCS and -2FC), curing conditions: 20 °C and 95 % relative humidity. MHA-S-2CS, -2FC and -2TCS show at the beginning a higher initial sonic velocity that is attributed to a measuring device related erroneous zero value definition.

Fig. I.16 shows the results of the Cold Modulus of Rupture (CMoR) measurements of the spinel free test pieces after drying for 24 h at 110 °C. The average values are comparable and vary only between 7,6 and 9,2 MPa, which are not a significant deviation for the CMoR. The CMoR of the spinel-forming test piece is 10 MPa higher on average (Fig. I.17). The average values are comparable within the set of model castables and ranged between 15,3 and 20,9 MPa, which is slightly higher than for the spinel-free test pieces, but still not significant.

An explanation for the higher CMoR of the spinel-forming model castables could be a deviation in the PSD of the castables due to the substitution of 2 wt.-% of the 0-0,2 mm alumina fraction by MgO. A deviation in the particle size and/or distribution of the two materials could have resulted in a slightly higher packing density of the spinel-forming material and thus a higher strength after casting. It is also conceivable that the strength could be increase by the formation of finely distributed brucite particles resulting from the hydration of MgO. In this case, the volume expansion induced by the brucite formation would stay uncritical and accordingly do not cause visible cracks that could lead to early structural failure but rather enhanced the castable’s strength..

In summary, the comparable processing properties and setting and curing behavior provide the same initial situation for casting/molding and demolding test pieces as well as for the high temperature analysis of the project partners. Constant flow during a sufficient working window is necessary for proper molding, but thereafter a rapid increase in strength is inevitable for adequate demolding properties of the test pieces. This is the case for all model refractory castables. Effects that may be seen in the high temperature characterization (subprojects II and III of L-ICiMB and FGF) can therefore be attributed solely to the presence of impurities in the precursors.

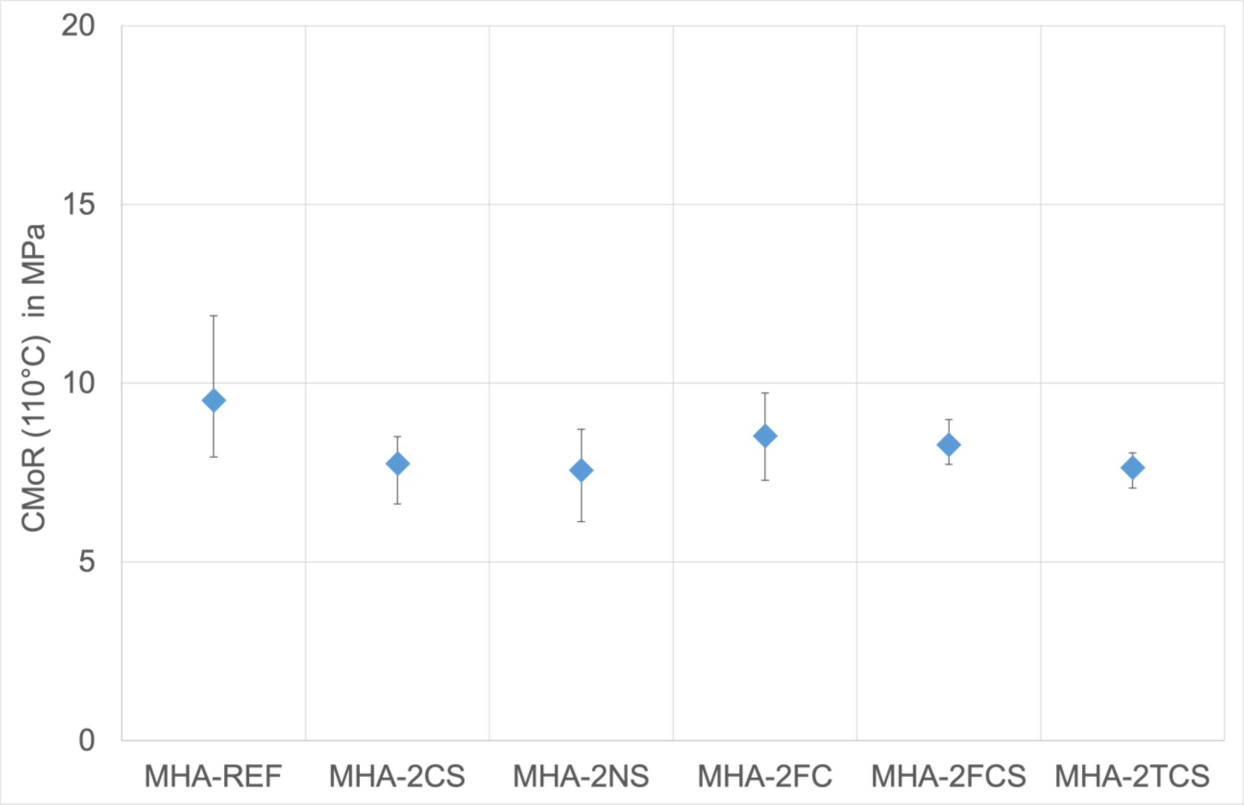

Fig. I.16: Cold modulus of rupture after drying at 110 °C of the cement-free, self-flowing, high alumina, spinel-free reference model castable (MHA-REF) and the five cement-free, self-flowing, high alumina, spinel-free model castables with substitution of the TA fraction 0-45 µm by the different precursors (MHA-2FCS, -2NS, -2CS, -2TCS and -2FC).

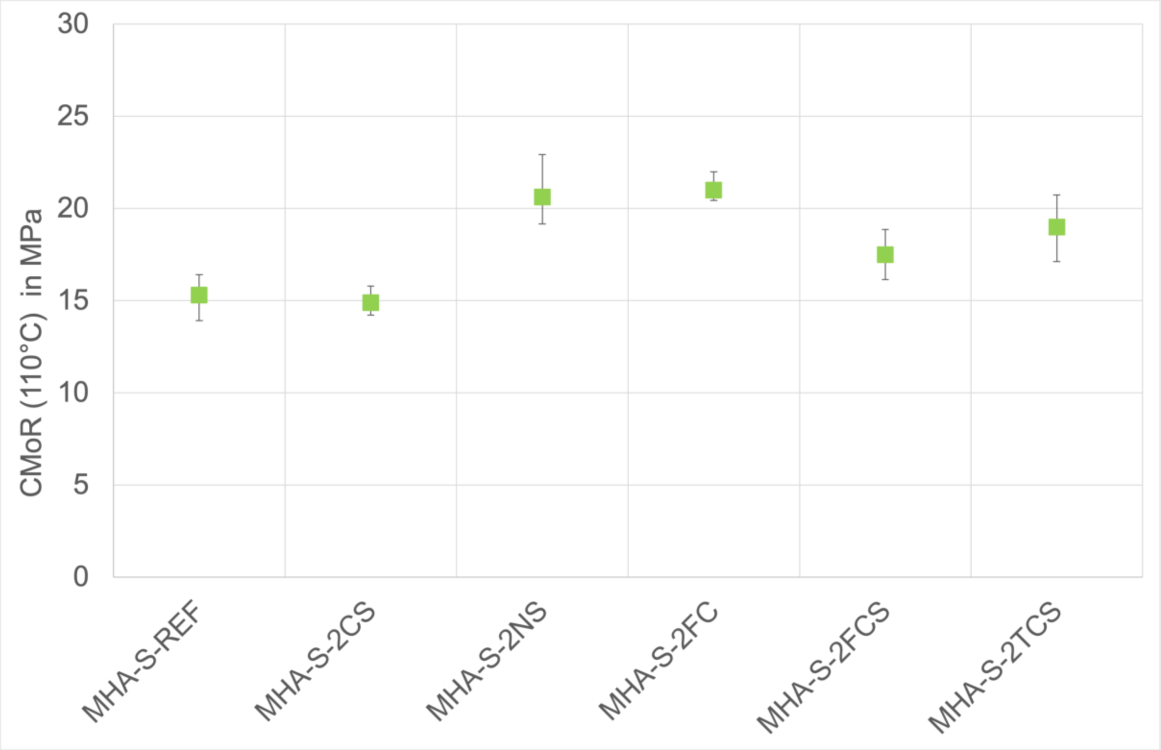

Fig. I.17: Cold modulus of rupture after drying at 110 °C of the cement-free, self-flowing, high alumina, spinel-forming reference model castable (MHA-S-REF) and the five cement-free, self-flowing, high alumina, spinel-forming model castables with substitution of the TA fraction 0-45 µm by the different precursors (MHA-S-2FCS, -2NS, -2CS, -2TCS and -2FC).

2.6 Conclusions

Tailored impurified raw materials (precursors) that simulate secondary raw material (recycled raw materials) were successfully produced and used to produce model castables. No significant effects on the working properties and curing behaviour of the investigated refractory model castables using impurified raw materials were found.

Because of the sintering of the precursors at 1600 °C, all ions (impurities) were bound and were no longer water-soluble and therefore had no significant influence on the castable flow and setting properties.

The slight deviations in the Cold Modulus of Rupture are most likely due to the different grain size distributions of the precursors and or the castable formulations, which in turn have a significant influence on the flow behaviour, as can be clearly seen in the case of MHA-2FC, MHA-2CS and MHA-S-2CS. Nevertheless, the workability and setting behaviour were comparable to the pure high alumina reference model castable. This provides the same starting situation for all model refractory castables for the thermos-mechanical investigations. Accordingly, all deviations that can be measured during high temperature investigations should be attributable to the presence of impurities in the model castable and not to the test pieces preparation.

Unfortunately, it also means that there is a risk for refractory manufacturers to not detecting impurities in the processing state that could be critical for the hot properties of the products.

2.7 References

[1] Maekawa, A.; Geji, M.; Tanaka, M.: Influence of impurities in fused magnesia on properties of MgO-C bricks, in Taikabutsu Overseas - Journal of the Technical Association of Refractories, Japan 17 (4), (1997) p. 74.

[2] Matsui, K.: Effect of impurities in magnesia on reaction between magnesia and carbon, in Taikabutsu 43 (11), (1991) p. 660.

[3] Matsui, K.; Kawano, F.: Effect of impurities in magnesia on reaction between magnesia clinker and carbon, in Taikabutsu 45 (6), (1993) p. 355–366.

[4] Sax, A.: Verschleißmechanismen Feuerfester Erzeugnisse; Seminar „Feuerfest – Schlüsseltechnologie und ihre Anwendungen“, Höhr-Grenzhausen (2014).

[5] Liu, X.; Yanqing, X.; Keming, G.; Buhr, A.; Büchel, G.: Tabular Alumina for High Purity Corundum Brick, in Proceedings of The Fifth International Symposium on Refractories, ISR'2007, (2007).

[6] Frulli, D.: Production and Properties of Refractory Raw Materials Based on Andalusite and Mullite – Influence of Impurities in the Refractory Behavior, in refractories Worldforum 8, (3), (2016).

[7] Hubble, D. H.: Chapter 3 – Steel Plant Refractories, in Ironmaking, 1999 the AISE Steel Foundation, Pittsburgh, PA (1999).

[8] Alex, J.; Vandeperre, L.; Touzo, B.; Parr, C.; Lee, W. E.: Effect of Sodium on Microstructures and Thermoelastic Properties of Calcium Aluminate Cement–Bonded Refractories, in the Journal of the American Ceramic Society 99 (3), (2016), p. 1079–1085.

[9] Möhmel, S.; Weissenbacher, M.; Kurz, B., Joubert, O.: The influence of different raw materials on the behaviour of low cement castables, in Proceedings of UNITECR 2015, Wien (2015).

[10] Klein L, Krause O.: Automatic Image Analysis of the Slump Flow and Comparison to Rheometrical Measurements with the Ball Measuring System, in Proceedings of the 59th International Colloquium on Refractories 2016, Aachen (2016), p. 155-158.

[11] Samanta, A. K.; Sathpathy, S.; Arimitsu, E.; Tsuyuguchi, K.; Panda, P. B.; Shankha Chatterjee: The Role of Matrix Aluminas on the Properties of High Performing Refractory Castables, in Proceedings of UNITECR 2017, Wien (2017).

[12] Osborn, E. F.; Muan A., revised and redrawn “Phase Equilibrium Diagrams of Oxide Systems,” Plate 4, published by the American Ceramic Society and the Edward Orton Jr., Ceramic Foundation, (1960).

3. Subproject II – Establish a reliable testing strategy to determine the maximum service temperature of refractories.

3.1 Need #2: Understand and define the maximum service temperature ("refractoriness")

The refractory industry was still unable to determine the maximum service temperature of refractory materials. The behaviour of refractory materials is typically characterized by standardised tests, e.g. mechanical strength or Young's modulus, in cold state or at isothermal high temperature. More dynamic tests are performed to study the softening behaviour such as "refractoriness under load" and "creep in compression". Said tests define a bulk "refractoriness" and deliver results for the bulk composition of a refractory system, but do not explain why the materials show their characteristic thermomechanical behaviour which is mainly determined by the matrix composition (including impurities therein). If impurities in secondary raw materials are being considered, comprehensive investigations on the measurement of the resulting high temperature behaviour are almost absent in literature.

Currently, the definition of the maximum service temperature is correlated with the $T_{0,5}$-value obtained from standardised tests for "refractoriness under load" (RuL, ISO 1893). However, recent research shows that $T_{0,5}$ values corelate with the complete structural breakdown of the ceramic structure, but major and critical thermo-mechanical changes that will strongly influence the high temperature behaviour of refractory castables are happening at temperatures below $T_{0,5}$, opening a gap of more than 100 K in which the high temperature behaviour of refractories is not well understood.

Accordingly, the second need (need #2) that has been addressed in this CORNET project is to better understand and define the maximum service temperature ("refractoriness") in order to fairly assess the impact of raw materials with impurities. With this need fulfilled, refractory producers can define, communicate and guarantee the "refractoriness" of their products and the effect of impurities from secondary raw materials on the "refractoriness" can be thoroughly investigated to support need #1.

3.2 State of the art

Due to the depletion of natural resources and an overall endeavour to manage natural resources sustainably, there is a need to increasingly use recycled materials. In the case of refractory materials, which are used in various industries, the reuse of refractory materials after decommissioning of worn refractory linings as secondary raw materials is not easy. Refractory producers face a classic and basic dilemma to have to select between high purity, usually more expensive and less available raw materials that are expected to promote high temperature performance, or lower grad, less expensive raw materials, including secondary sources (i.e. recycled materials) but deem to lead to lower refractoriness. More broadly, refractory producers need reliable data on the influence of impurities on the high temperature performance of refractory products in order to develop formulations suitable for specific applications with targeted refractoriness and tailored admissible level of impurities and hence promote the use of recycled raw materials.

Within this work, high alumina castables made from high alumina raw materials were investigated. Due to their outstanding thermal stability and corrosion resistance, those raw materials as derived and purified by the Bayer process are broadly used in the refractory industry. Due to the production process, iron, titanium and silicon are typically present in concentrations lower than 0.1 wt.-% (traces). The nature of bond of those traces is unclear, as X-ray powder diffraction is unsuitable to analyse them because of the very low concentration [1-2]. In secondary high alumina raw materials, higher degrees of impurities are expected stemming from the previous industrial use. Especially Ca is enriched significantly in secondary raw materials, as they are often derived from Ca-containing castables and Ca is a major component in metallurgical slags

Even in low concentrations, impurities/traces significantly influence the thermal behaviour of high alumina castables [3,4]. The way such impurities in traces change the high temperature performance of monolithics is however not fully understood. Said traces of sodium, titanium, silicon and iron are typically addressed as impurities that diminish the refractory performance of the castable made of these raw materials. However, mentioned authors shows that distinct higher concentrations of impurities may even improve the thermal stability and the thermo-mechanic properties of high alumina castables, depending on whether the critical impurities are present in the coarse grains or the matrix [4].

If impurities in secondary raw materials are being considered, comprehensive investigations on the measurement of the resulting high temperature behaviour are rare in literature [5]. This is because of the typical structure of refractory materials that consist of a broad range of particle sizes, and where impurities are being enriched in the fine (matrix) fractions and are predominantly build into hibonite and β-alumina or create further phases like e. g. gehlenite or feldspars (mainly anorthite (Ca) or albite (Na) or their solid solutions) with low melting temperatures. Therefore, the matrix behaves differently compared to the coarse-grained fractions and mainly controls the high temperature properties of a refractory material. This is especially critical for castables where the share of matrix is higher compared to shaped materials. Widely used testing methods however do not allow to analyse and understand these processes, as their results mainly reflect the behaviour of the coarse-grained bulk fractions. Usually, refractory materials behave rather brittle at room temperature and low temperatures, yet many authors report or assume a much more ductile behaviour, even yield, at high temperature [6,7]. Finally, at their maximal service temperature, refractory materials tend even to experience a soft (ductile) failure as they start to creep massively and progressively lose their capacity to sustain load without experiencing catastrophic failure. More recently, a direct proof of brittle-ductile transition (BDT) in refractory castable was established [8].

3.3 Investigated materials

For the needs of the project. synthetic materials (precursors) imitating secondary raw materials with specific compositions, or more precisely, mutual proportions of impurity oxides were produced and sintered at 1600 °C by partner Hochschule Koblenz (see Subproject I). The compositions of the precursors were chosen regarding their melting behaviour. More precisely, the most unfavourable combinations, from the point of view of the temperature of formation of the liquid phase in the material, as well as its quantity and viscosity, were selected.

3.3.1 Thermochemical predictions

Thermodynamic simulation calculations were carried out by partner L-ICiMB using FactSage 6.4 engineering software and the "Equilib" module, which allows for the calculation of the equilibrium composition of a multi-component material in the temperature range up to 1800 °C with steps of 100 degrees. The purpose of the calculations was to determine the temperature of the liquid phase formation and its amount depending on the CaO to SiO_2 (C/S) or Na_2O to SiO_2 (N/S) ratio, with the initial assumption that the added impurities represent 2% of the mass of the simulated system (the rest being Al_2O_3). The viscosity of the liquid phase being formed was calculated using the “Viscosity” module in FactSage software. The obtained calculation results were used to select the compositions of precursors imitating raw materials.

The following pure three-component systems were simulated: Al_2O_3-CaO-SiO_2, Al_2O_3-Na_2O-SiO_2 and Al_2O_3-CaO-Fe_2O_3 and two four-component systems: Al_2O_3-CaO-SiO_2-Fe_2O_3 and Al_2O_3-CaO-SiO_2-TiO_2.

In the Al_2O_3-CaO-SiO_2 system (Fig. II.1), the liquid phase appears between 1400 and 1500 °C. Its amount depends on the mutual share of contaminating components CaO and SiO_2 (A = CaO/SiO_2). At a temperature of 1500 °C, the liquid phase in the system occurs when A is less than approx. 1.35. Considering a system rich in silica. there is no liquid phase at this temperature. Increasing the temperature contributes to the appearance of the liquid phase in the entire range of impurities share considered. The obtained results also show the variability of the composition (value of A) that generates the maximum amount of the liquid phase. With the increase in the considered temperature. the composition that promotes the formation of the largest amount of the liquid phase shifts to compositions rich in CaO, from A = 1,06 for 1500 °C to A = 0,36 for 1800 °C.

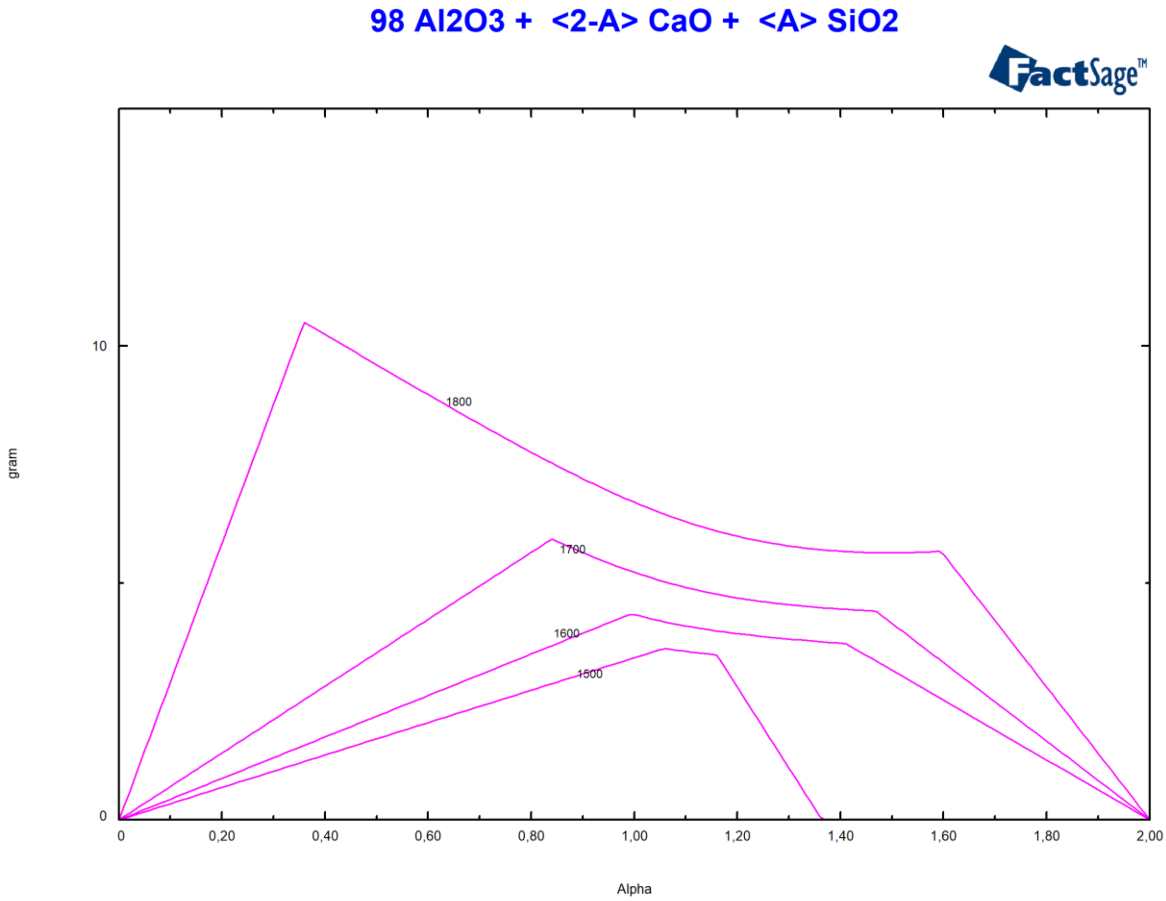

Fig. II.1: Results of the calculation for the formation of liquid phase in the Al_2O_3-CaO-SiO_2 system with a variable share of CaO and SiO_2.

The analysis of the system with sodium oxide as an impurity (Al_2O_3-Na_2O-SiO_2 system, Fig. II.2) showed clearly different behaviour. The admixture of alkali oxides led to the apparition of liquid phase in the system already for a temperature of 1100 °C. Up to a temperature of 1400 °C, its amount is limited by its composition (A greater than approx. 1,35). From a temperature of 1500 °C. the liquid phase is present in the entire range of impurities composition. For this Al_2O_3-Na_2O-SiO_2 system, the maximum of the liquid phase occurs for compositions where the weight ratio of Na_2O and SiO_2 is close to 1,0.

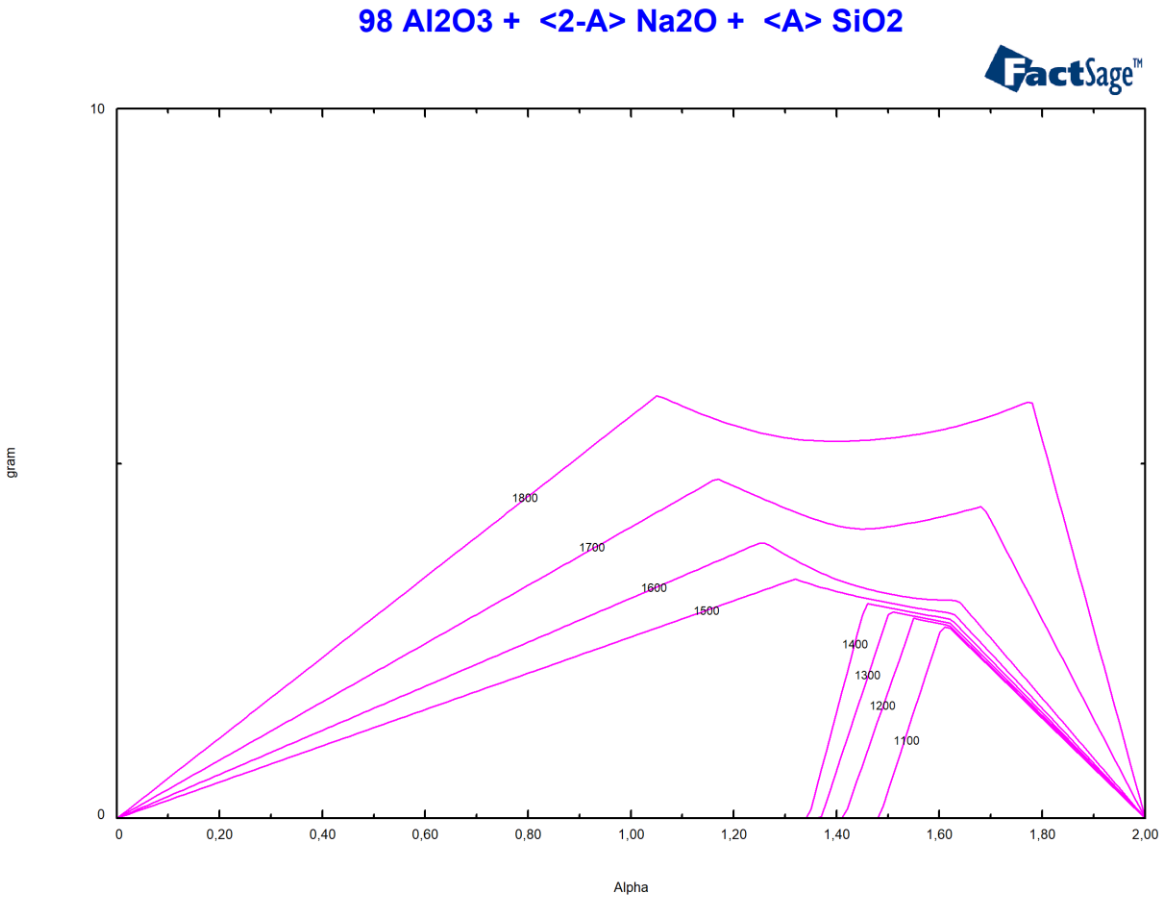

Fig. II.2: Results of the calculation for the formation of liquid phase in the Al_2O_3- Na_2O-SiO_2 system with a variable share of Na_2O and SiO_2.

The Al_2O_3-CaO-Fe_2O_3 system was analysed in a similar way (Fig. II.3). The clear presence of the liquid phase is observed for temperatures above 1400 °C and occurs over the entire range of investigation compositions. The largest amount of the liquid phase also depends on the temperature and composition. As the temperature increases, the maximum amount of liquid phase shifts to compositions rich in CaO. The maximum occurs for A = 0,46 (at 1800 °C).

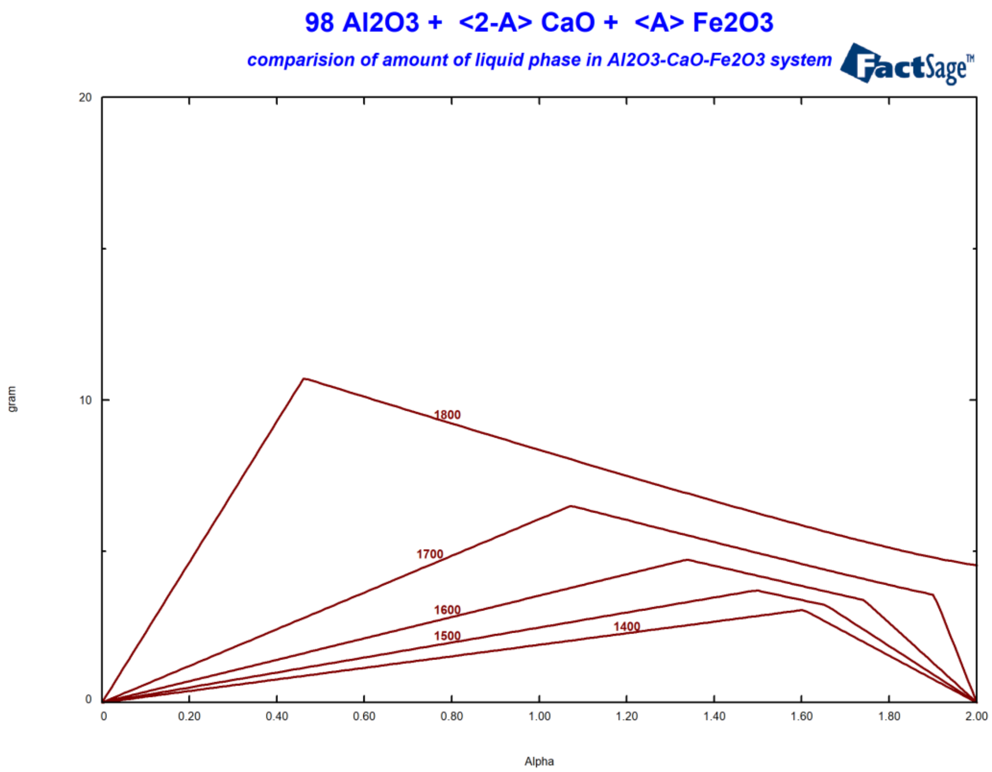

Fig. II.3: Results of the calculation for the formation of liquid phase in the Al_2O_3-CaO-Fe_2O_3 system with a variable share of CaO and Fe_2O_3.

In four-component systems, calculations were carried out depending on the C/S ratio with different shares of Fe_2O_3 and TiO_2, looking for the composition that would generate the maximum amount of liquid phase in the system for a temperature of 1600 °C. In the case of the system with iron oxide, it turned out to be $98Al_2O_3$-0,81CaO-$0,30SiO_2$-$0,89Fe_2O_3$, and it was $98Al_2O_3$-0,97CaO-$0,73SiO_2$-$0,30TiO_2$ for the titanium containing composition.

In a second implementation of the thermochemical calculation, the actual chemical composition of the raw materials used to produce the samples was considered (i.e. taking into account the innate presence of impurities in the tabular alumina / as delivered by the supplier). Additionally, the calculation of the viscosity of the melts in the analysed systems were performed in order to facilitate the interpretation of the results obtained in later stages of work. The combination of impurities had a significant impact on the formation of the liquid phase in the considered systems and contributed to shifts the composition generating the maximum amounts of the liquid phase. Thus, for the Al_2O_3-CaO-SiO_2 system (Fig. II.4), the first liquid phase is formed already at 1100 °C, while the maximal formed amount varies for the composition from A = 1,64/2,00 at 1100 °C to A = 0,32 at 1800 °C. Similar changes were observed for the all considered systems. Especially the appearance of the liquid phase occurred systematically at a lower temperature in comparison to "pure" systems (i.e. without considering the innate presence of impurities in the tabular alumina). For the Al_2O_3-Na_2O-SiO_2 system considering the actual chemical composition of the raw materials (Fig. II.5), the maximum of the liquid phase is observed for compositions where the weight fraction of SiO_2 is high and ranges from A = 1,2 to approximately A = 1,9 at 1800 °C. For the Al_2O_3-CaO-Fe_2O_3 system (Fig. II.6), the maximum corresponds to the composition for which A = 0,25 (at 1800 °C). A summary of viscosity changes is shown in the figure II.7. Within the considered systems, several groups, which displayed similar viscosity behaviour depending on temperature, can be distinguished. Sodium containing compositions, besides promoting the formation of a liquid phase at a relatively lower temperature, are characterized by the presence of a liquid phase with a relatively high viscosity. However, the liquid phase formed in Al_2O_3-CaO-Fe_2O_3 systems is characterized by very low viscosity over its entire temperature range of existance. Also noteworthy is the increase in viscosity for some of the compositions from the Al_2O_3-Na_2O-SiO_2 system.

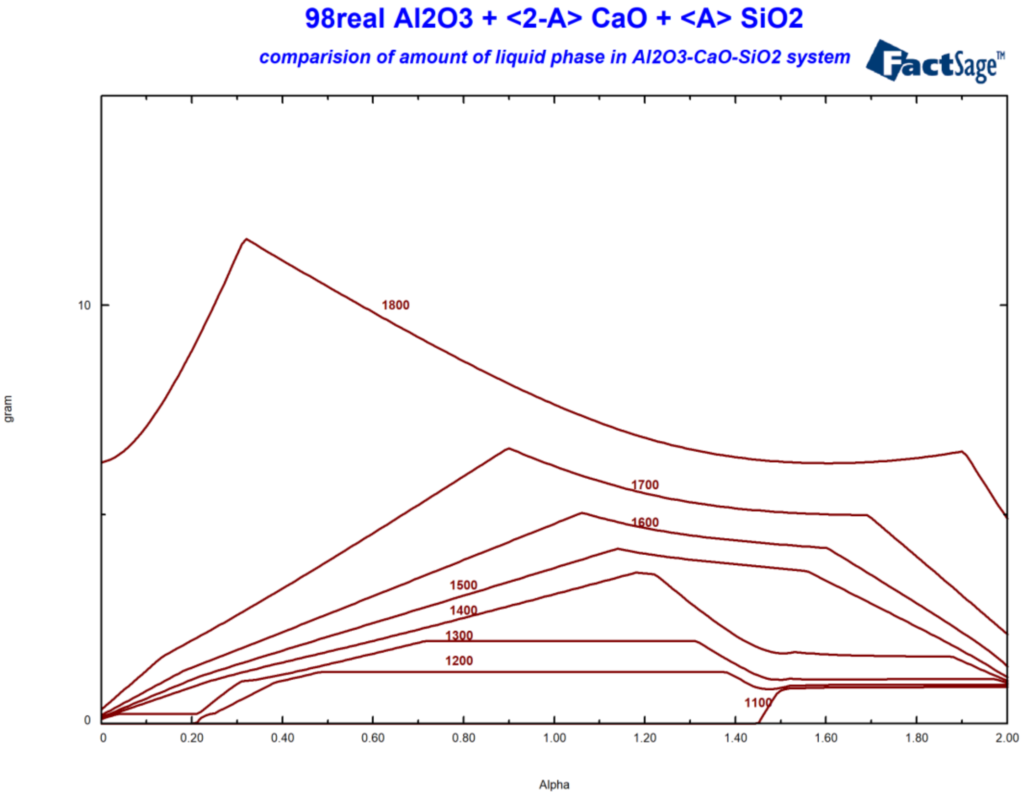

Fig. II.4: *Results of the calculation for the formation of liquid phase in the actual Al_2O_3-CaO-SiO_2 system (including impurities already present in the raw material) with a variable share of CaO and SiO_2.*

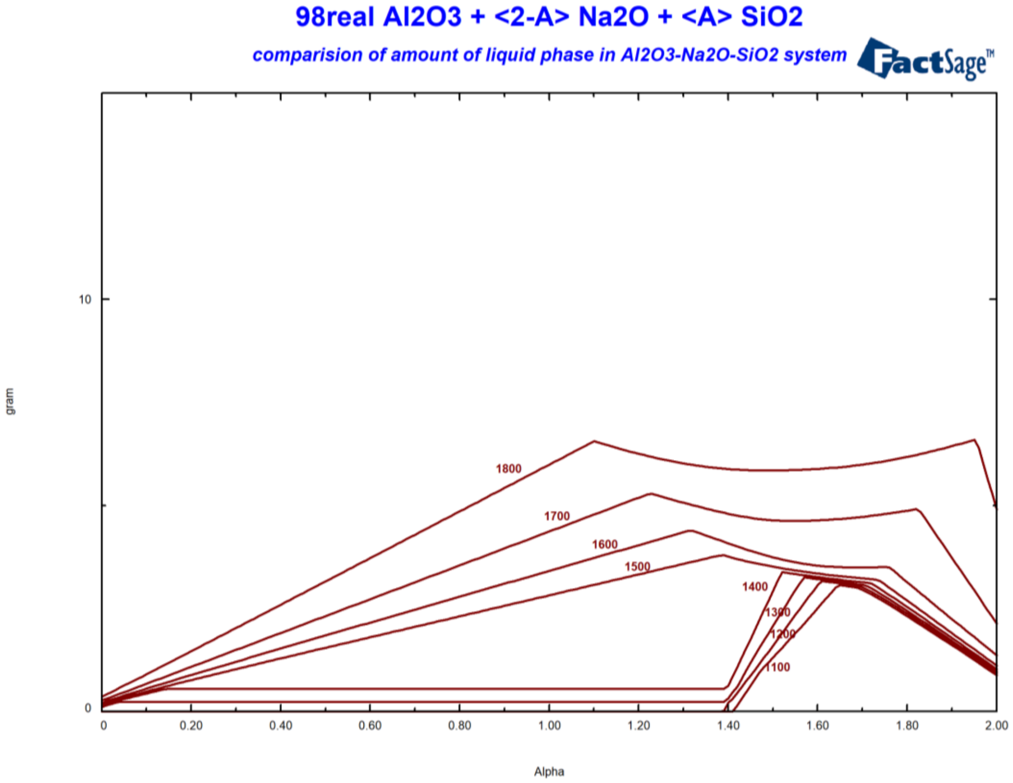

Fig. II.5: Results of the calculation for the formation of liquid phase in the actual the Al_2O_3-Na_2O-SiO_2 system with a variable share of Na_2O and SiO_2.

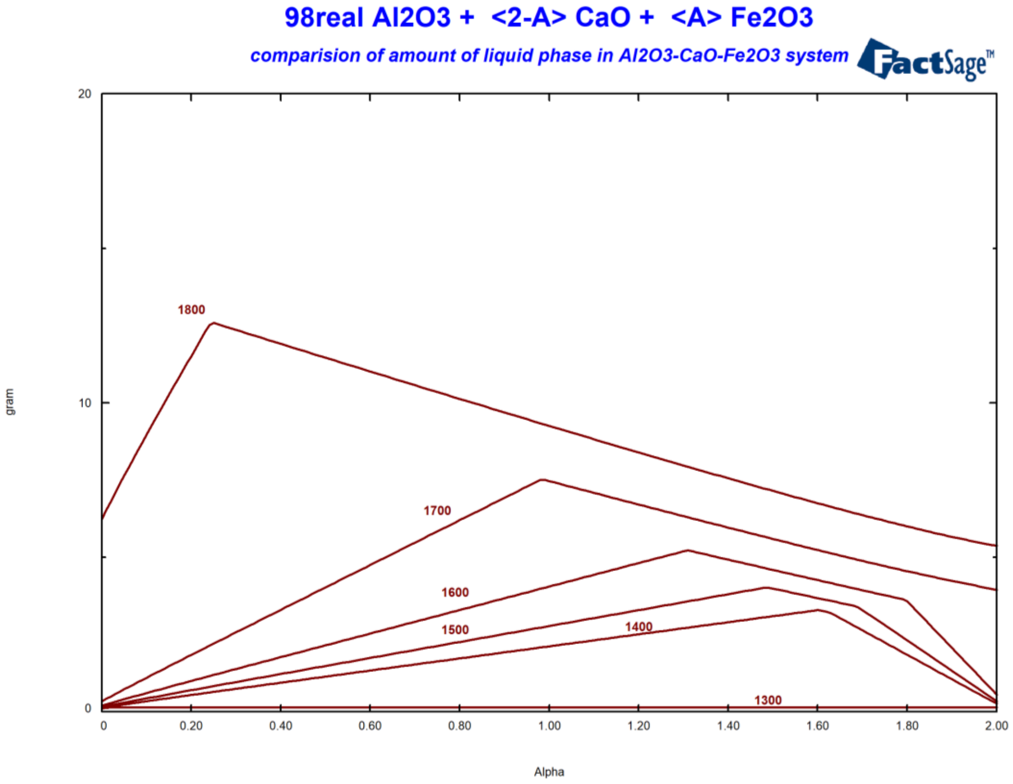

Fig. II.6: Results of the calculation for the formation of liquid phase in the actual the Al_2O_3-CaO-Fe_2O_3 system with a variable share of CaO and Fe_2O_3.

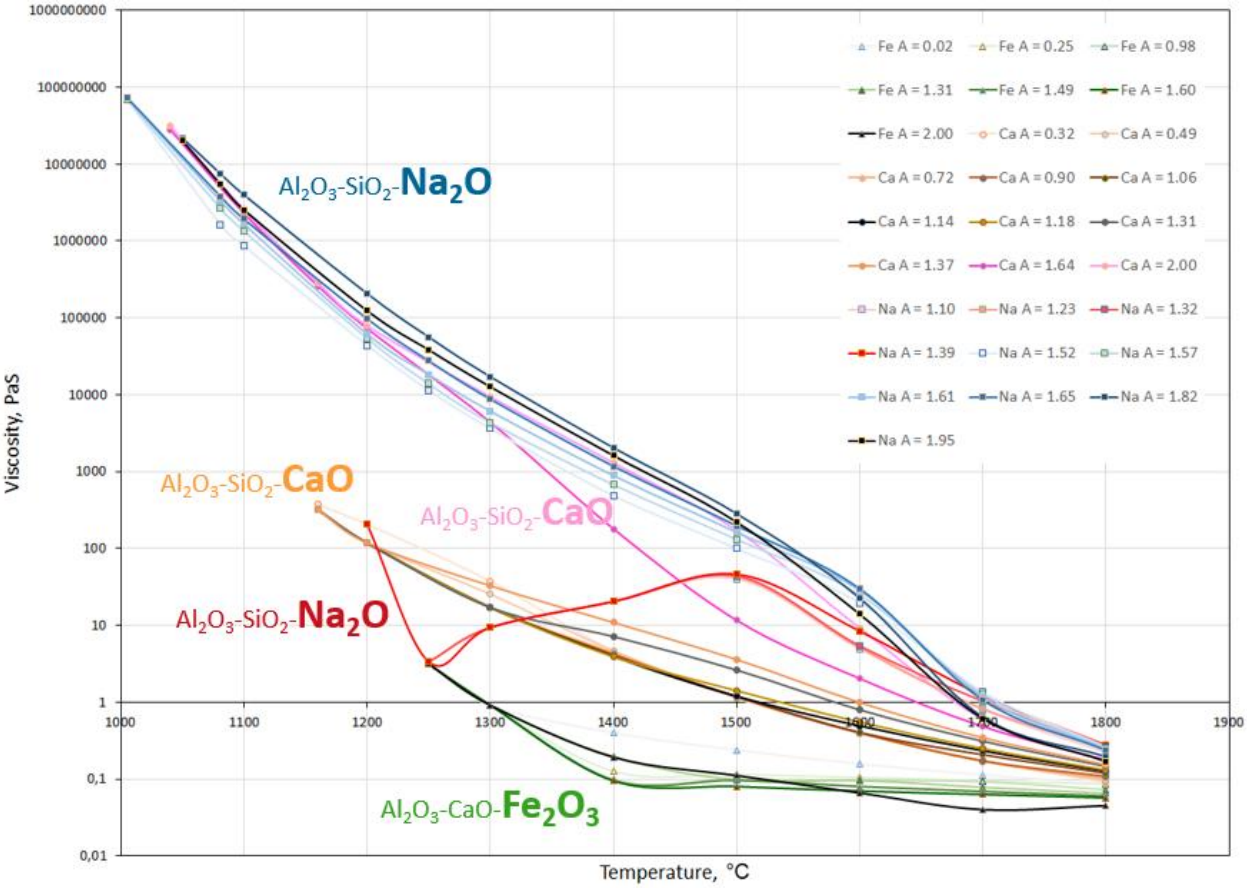

Fig. II.7: Evolution of the viscosity of the liquid phase with increasing temperature for actual chemical compositions of the considered systems.

In the course of the research project implementation, some concerns were raised regarding the phenomenon of sodium evaporation from the raw material that could led to undesirable compositions lacking of the aimed sodium share. Accordingly, an attempt was made to assess the thermodynamic stability of the β-Al_2O_3, which primarily contained sodium, phase using FactSage 6.4. The amount of sodium in the liquid and gas phase at specific temperatures were calculated in order to assess the expected amount of sodium in the gas phase in the closed pores of the material. The calculation results showed that this problem can be neglected.

3.3.2 Selection of the precursor composition

Based on these calculations, 5 precursors were prepared (compositions listed in Table I.1), which were then introduced into the reference material MHA-REF (chemical composition provided in Table II.1), as described in the sections 2.4.2 “Raw material selection and preparation of spiked raw materials” and 2.4.4 “Castable and test piece preparation”. These were the compositions with the most unfavourable shares of individual oxides regarding the temperature of formation of the liquid phase and the amount formed according to the performed calculations. The matrix fraction 0-45 µm (tabular alumina) with the amount of 9 wt.-% was substituted 1:1 by the precursor material. The sum of impurity oxides in these spiked alumina’s fraction was 2 wt.-% and resulted in a share of 0,18 wt.-% relative to the whole castable formulation. The phase compositions of the reference material and the precursors measured by X-ray diffractometry are presented in the table 2 and the figures II.8-13.

Tab. II.1: Chemical composition of reference material MHA-REF in wt.-%.

Component	wt.-%
SiO_2	0.02
Al_2O_3	98.59
Fe_2O_3	0.04
TiO_2	< 0.01
MnO	0.01
CaO	0.04
MgO	0.02
Na_2O	0.21
K_2O	< 0.01
P_2O_5	< 0.01
Loss of Ignition	0,80

Tab. II.2: Phase compositions of the reference material MHA-REF (without active alumina) and the 5 precursors (XRD).

Material	wt.-%
MHA-REF	Al_2O_3 (corundum) – 97.1 %. β-Al_2O_3 – 2.9 %
2CS	Al_2O_3 (corundum) – 92.5 %. β-Al_2O_3 – 0.1 %. $CaAl_{12}O_{19}$ (hibonite) – 5.4 %. $NaAlSiO_4$ (nepheline) – 2.0 %
2NS	Al_2O_3 (corundum) – 96.6 %. β-Al_2O_3 – 0.1 %. $NaAlSiO_4$ (nepheline) – 0.7 %. $NaAlSiO_4$ – 2.6%
2FC	Al_2O_3 (corundum) – 87.4 %. β-Al_2O_3 – 3.7 %. $CaAl_{12}O_{19}$ (hibonite) – 9.0 %
2FCS	Al_2O_3 (corundum) – 90.2 %. β-Al_2O_3 – 2.6 %. $CaAl_{12}O_{19}$ (hibonite) – 6.6 %. $NaAlSiO_4$ (nepheline) – 0.6 %
2TCS	Al_2O_3 (corundum) – 92.5 %. $CaAl_{12}O_{19}$ (hibonite) – 6.1 %. $NaAlSiO_4$ (nepheline) – 1.3 %. $CaTiO_3$ (perovskite) – 0.1 %

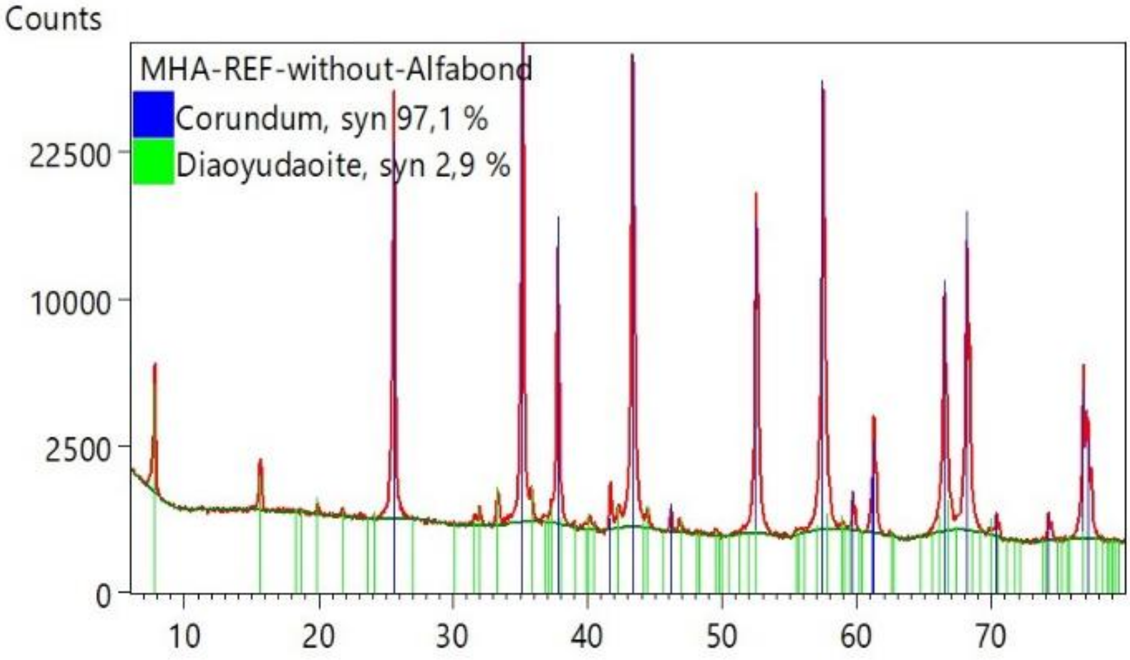

Fig. II.8: *X-ray diffraction pattern of the reference material MHA-REF without the addition of a binder - active alumina.*

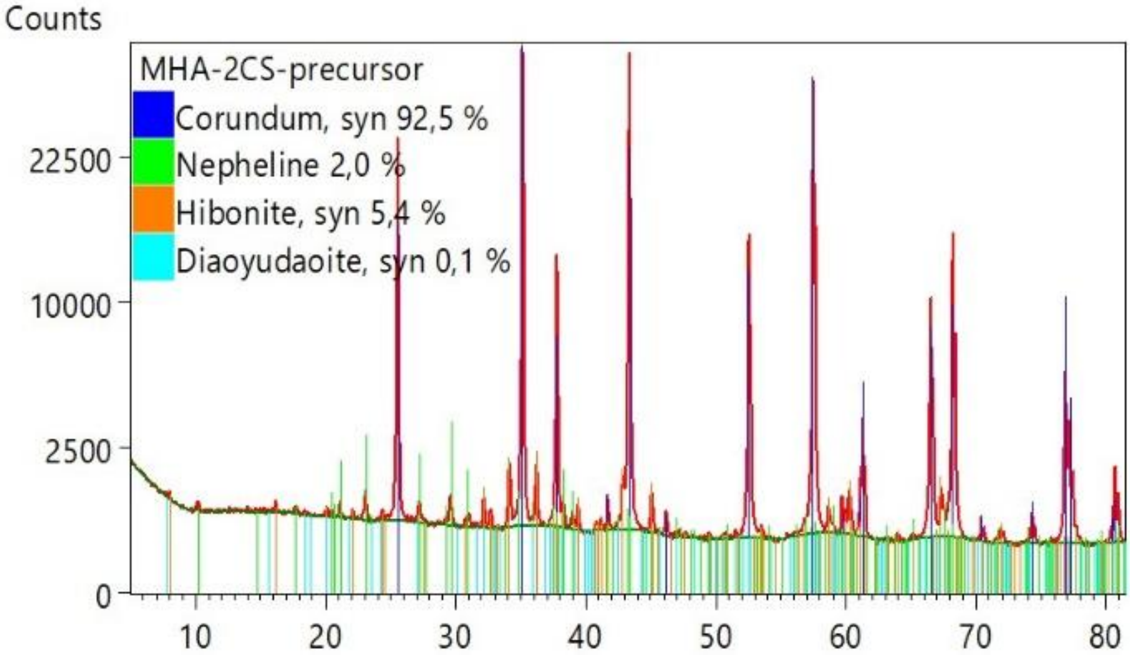

Fig. II.9: *X-ray diffraction pattern of the MHA-2CS precursor.*

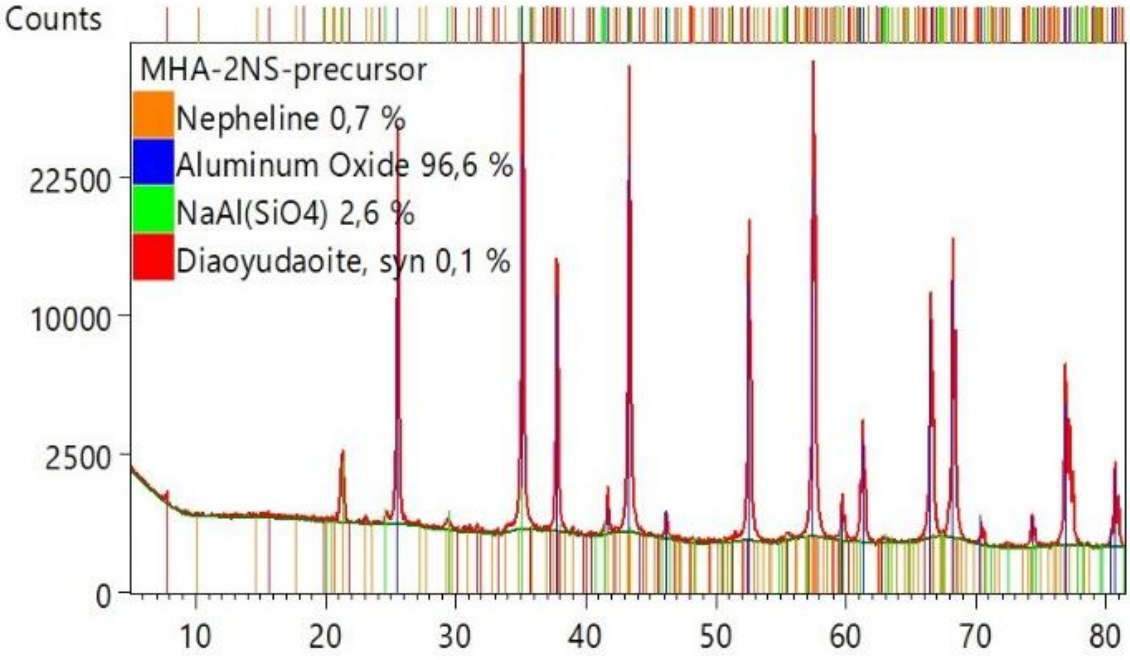

Fig. II.10: X-ray diffraction pattern of the MHA-2NS precursor.

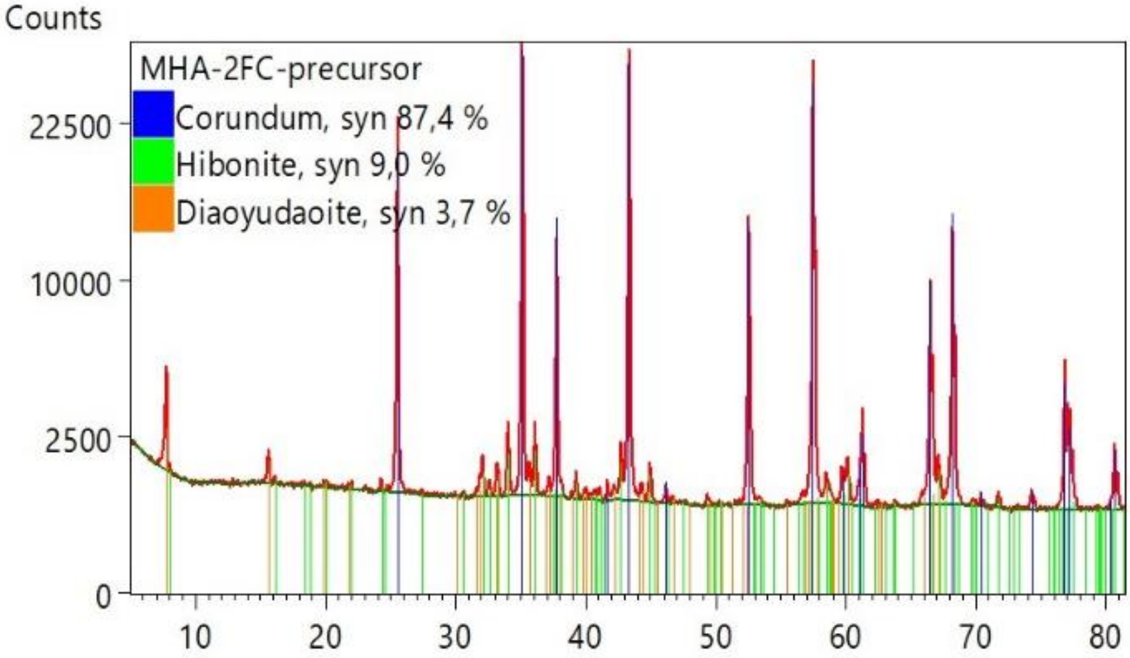

Fig. II.11: X-ray diffraction pattern of the MHA-2FC precursor.

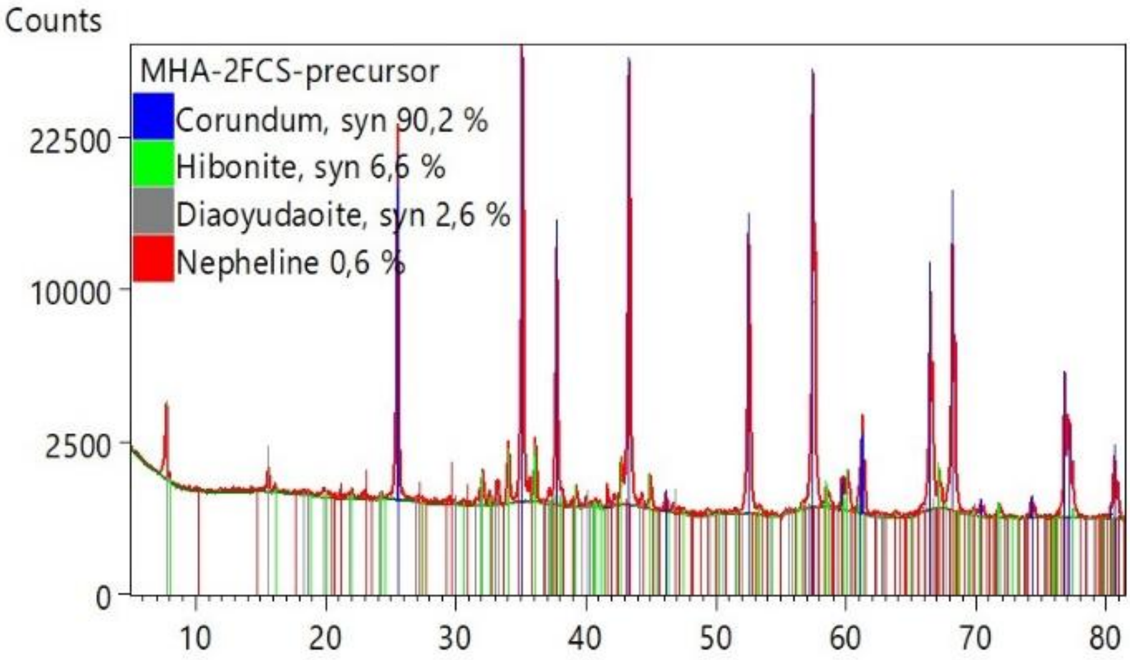

Fig. II.12: X-ray diffraction pattern of the MHA-2FCS precursor.

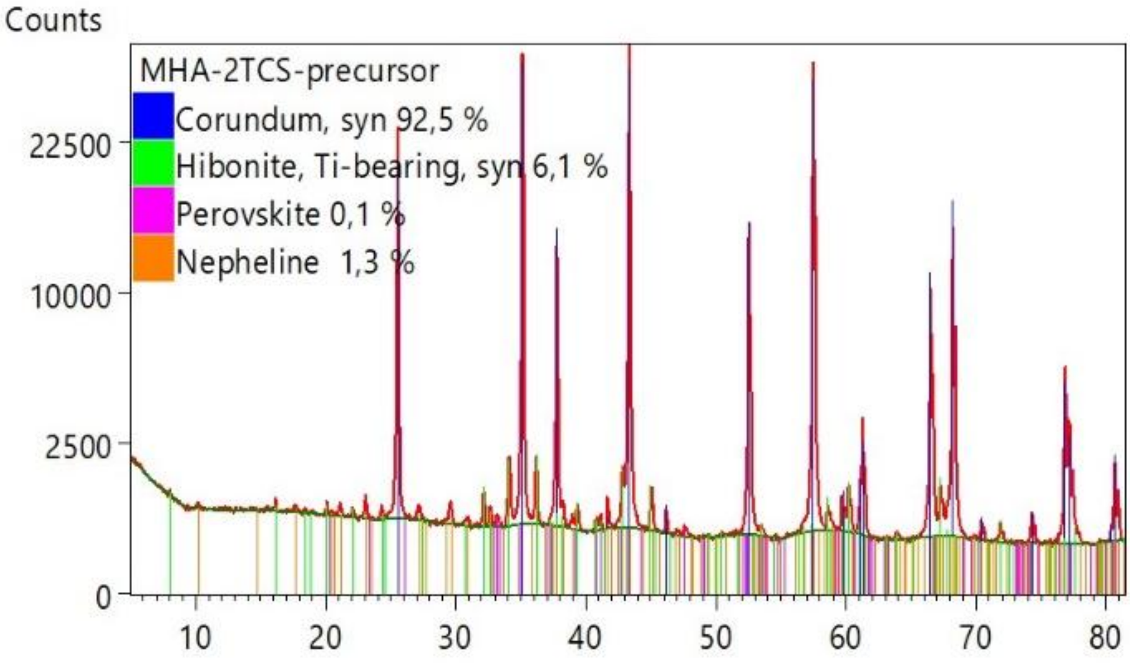

Fig. II.13: X-ray diffraction pattern of the MHA-2TCS precursor.

3.4 Testing methods

3.4.1 Refractoriness under Load (RuL) and Creep in Compression (CiC)

The high temperature performance of refractory products is basically assessed using the testing standards EN ISO 1893: Determination of refractoriness under load. and EN 993-9: Determination of creep in compression. Both testing standards are carried out with the same testing equipment and similar testing procedure. A cylindrical refractory test piece is subjected to a constant load (0,2 MPa) while increasing the temperature (5 °C.min^{-1}) in air. The deformation (height) of the sample is recorded continuously, usually with the differential method. For the determination of refractoriness under load (RuL), the test is stopped once a prescribed deformation is attained, typically 5 % of its initial length ($T_{0.5}$). For the determination of creep in compression (CiC), once a specified temperature of the sample has been reached, the temperature is maintained constant for a given time. The deformation of the test piece at this constant temperature over time is then recorded. In both tests. temperatures corresponding to a characteristic degree of deformation are identified from the deformation against temperature/time curves.

In the present study, the testing conditions specified in the standards were extended. Variable load conditions were selected and applied on cylinders (Ø 35 x 50 mm) with an axial hole with a diameter of 12 mm. The measurements were performed in a NETZSCH 421 device heated by an electric furnace.

3.4.2 Creep in Compression (CiC) based on the Norton-Bailey concept

Creep rate ware measured using a newly developed method based on the Norton-Bailey concept and works from Jin [9] et al as well as Samadi et al [10] to identify the different stages of creep. According to this concept, the creep of the material should take place in three stages as shown in figure II.14. In the initial primary creep stage (also called time-hardening) the creep strain rate decreases with time to a minimum steady-state value. In the secondary creep regime, the creep strain rate is almost constant. This is also called steady-state creep and in the third creep stage the creep strain increases with time until a failure occurs.

Measurements under variable load conditions in a NETZSCH 421 device. The test pieces were heated to $T_{0.5}$ - 100 K; $T_{0.5}$;. $T_{0.5}$ + 100 K at a rate of 5 K/min and three different loading forces (0,2. 0,8 and 1,2 MPa). In the tests performed, the maximum loading force of 1,2 MPa was a compromise between the size of the measuring chamber of the apparatus, the grain size of the coarsest grain fraction of the tested materials and the slenderness of the test piece determined by the ratio of diameter to height. In some cases, when using a heavy load at $T_{0.5}$ and $T_{0.5}$ +100 °C, the tests had to be stopped due to excessive strain beyond the measuring range of the device. Measurements were also made under a load of 1,2 MPa of two selected test piece with extending the holding time to 100 h.

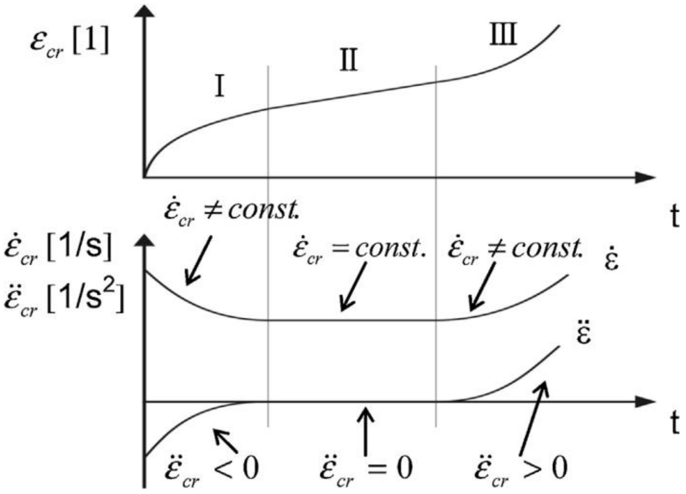

Fig. II.14: Complete strain/time curve for creep in compression. I – primary creep. II – secondary creep. III - tertiary creep.

3.4.3 High temperature X-ray diffraction

To identify the chemical reactions and phase change transformations in the precursors and matrixes of high alumina and high alumina spinel-forming model castables, the high-temperature diffraction method was applied. A high-temperature chamber - Anton-Paar HT2000, coupled with a PANalytical X'Pert MPD diffractometer equipped with Cu radiation tube were used. The investigations were performed at temperatures ranging from 25 °C to $T_{0,5}$- 100 °C temperature (determined by RuL measurements). Specific test temperatures for individual test pieces were selected based on the evolution of the Young's modulus and damping with temperature in the RFDA measurements. The heating rate between each measuring temperature was 10 °C per minute. Before taking measurements at a given temperature. the test piece was thermostated during 2 minutes and, then, the X-ray patterns were collected at an angular range of 5 to 70°2Θ. Afterwards. for each collected diffraction pattern, phase identification and quantification were based on the Rietveld method. The phase composition of the investigated test pieces was determined using the ICDD PDF 4+ database and HighScorePlus.

3.4.4 Resonance Frequency Damping Analysis (RFDA)

The non-destructive technique IET (Impulse Excitation Technique) was used to investigate the elastic properties of the produced test pieces. Dynamic method for the determination of the Young's modulus (E-modulus) by means of resonance method according to ASTM E1876-15, ISO 12680-1 or EN 843-2 was applied up to different temperature depending on refractoriness of the investigated model castable. Equipment based on the IET method, such as RFDA (Resonant Frequency Damping Analyser), induces vibrations in a test piece through light mechanical impulse and then analyses the spectrum of vibrations. The method allows to directly determine the frequency *f* as well as damping parameters of vibration, namely the loss rate parameter *k* and internal friction Q^{-1} (damping), which represents the energy absorption and dispersion by the material. As mentioned earlier, there are different standards available that described different resonant frequencies, which can be excited dependent on the position of the support wires and the microphone of the testing system. The two most important resonant frequencies are the flexural which is controlled by the Young's modulus of the test piece and the torsional which is controlled by the shear modulus for isotropic materials. For predefined shapes like rectangular bars. discs. rods and grinding wheels, a dedicated software calculates the test piece's elastic properties using the test piece dimensions, weight and resonant frequency (ASTM E1876-15).

The young's modulus is calculated based on equation presented in the figure II.2.2 and internal friction based on equation presented in the figure Fig. II.2.3.

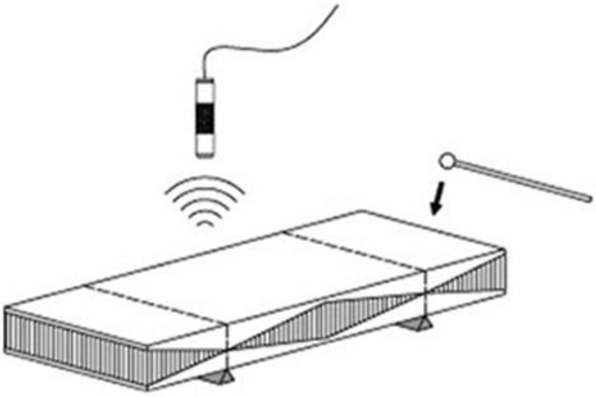

$$E = 0.9465\left(\frac{m\,f_f^{2}}{w}\right)\left(\frac{L^3}{t^3}\right)T$$

with **E** the Young's modulus
f_f the flexular frequency
m the mass
L the length
w the width
t the thickness
T the correction factor

Fig. II.15: Operating principles of Young's modulus determination by means of RFDA.

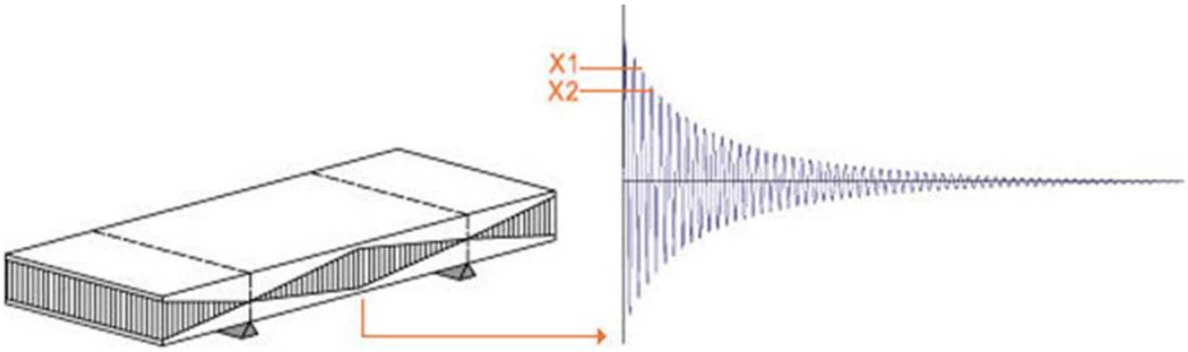

$$\text{Internal friction} = Q^{-1} = \frac{\text{energy dissipated as heat per unit volume over one cycle}}{\text{energy stored per unit volume}} = \frac{1}{\pi}\ln\left(\frac{X_1}{X_2}\right)$$

Fig. II.16: Operating principles of internal friction (damping) determination by means of RFDA.

To determine the Young's modulus, the equipment measures the flexural vibration frequency (Fig. II.15) and calculates the Young's modulus using the mass and dimensions of the test piece according to the different standards (ASTM E1876-15. ISO 12680-1. EN 843-2).

Material damping or internal friction characterize the decay of the vibration amplitude in the test piece while free vibrating as the logarithmic decrement (Fig. II.16). The damping behaviour originates from inelastic processes occurring in a strained solid i.e. thermo-elastic damping, magnetic damping, viscous damping, defect damping etc. For example, different materials defects (dislocations. vacancies. etc.) and running phase transformation or chemical reactions can contribute to an increase in the internal friction.

The relationship between the Young's modulus and temperature in the cycling process of heating and cooling has been determined between room temperature and different temperatures depending on refractoriness of the investigated model castable, namely $T_{0,5}$ -100 C. Above this temperature, the investigated model castables were already in a viscoplastic state and measurements at a higher temperature did not make physical sense. The dimensions of the specimens were 25 x 35 x 150 mm. The heating and cooling rate was set at 3 K/min and a dwell time of 2 hours at the maximum temperature ($T_{0.5}$ – 100 °C) was applied to achieve an equilibrium state. Each test was repeated twice.

3.4.5 Fracture energy by means of static method (three point bending test)

Fracture energy measurements were performed using the method of three-point bending on 25 x 25 x 150 mm beam with a notch having a depth of 7 mm and a width of 0,5 mm, loading rate of 20 µm/min, bending force up to 2500 N and a measuring system deformation correction (equipment-Netzsch HMOR422). Total deformation of the measuring system and the test piece is measured by means of an extensometer. The thermal expansion of the measuring system was corrected by experimental determination of the latter. The fracture energy G_F has been calculated from the following formula:

$$G_F = \frac{\int F(dx)}{2A} \qquad \text{(II.1)}$$

Where F is the force in Newtons, x is the deformation in metres and A is the specimen cross-sectional area in square metres.

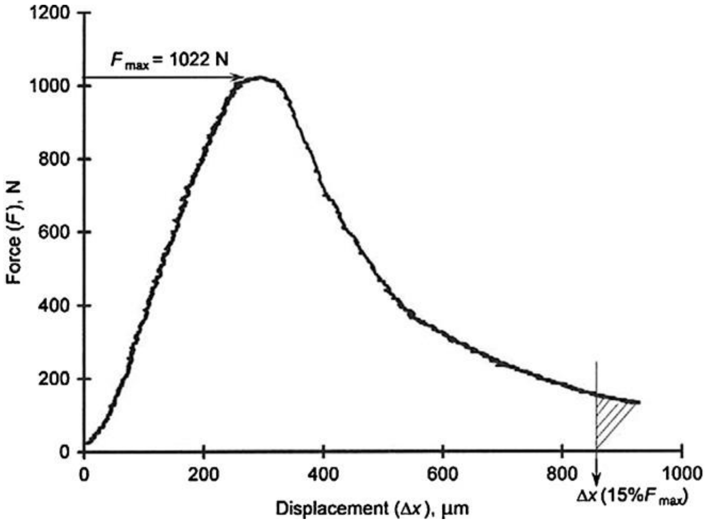

Fig. II.17: Illustration of the WOF determination method — Load F(x)-Displacement (Δx) diagram [15].

In order to avoid the influence of compressive stresses in the upper part of the test piece, the area under the curve was measured until a value of deformation corresponding to 15 % maximal force.

The results of WOF (work of fracture) measurements on refractory materials have been published since the early 1960s [11-16]. There are many varieties of WOF determination methods. An example of the force versus deformation dependence is shown in Figure II.17.

3.4.6 Modulus of rupture

Modulus of rupture at elevated temperature was made in accordance to the standard EN 993-7:2001. The maximum stress that a bar shaped test piece with dimensions of 25±1 x 25±1 x 150±1 mm place on supports spaced 125±1 mm apart and subjected to three-point bending just before failing was determined (Fig. II.18). The test pieces were loaded vertically until they broke, using a stress increase rate of 0,15 ± 0.015 MPa/s (shaped refractory products). The test pieces were heated at different rates depending on the temperature range: up to 600°C – 10,0 K/min, from 600 °C to 1200 °C - 5.0 K/min, from 1200 °C to 1450 °C - 2.5 K/min. At a given temperature, the measurements were performed three times and the average modulus of rupture was determined. The testing temperature were selected according to results of the refractoriness under load measurements. The following temperatures were used: T_0, $T_{0.5}$, $T_{0.5}$-100°C. In the case of the high alumina spinel forming model castables MHA-S, no measurements were performed at temperature $T_{0.5}$ exceeding 1450 °C due to equipment limitations.

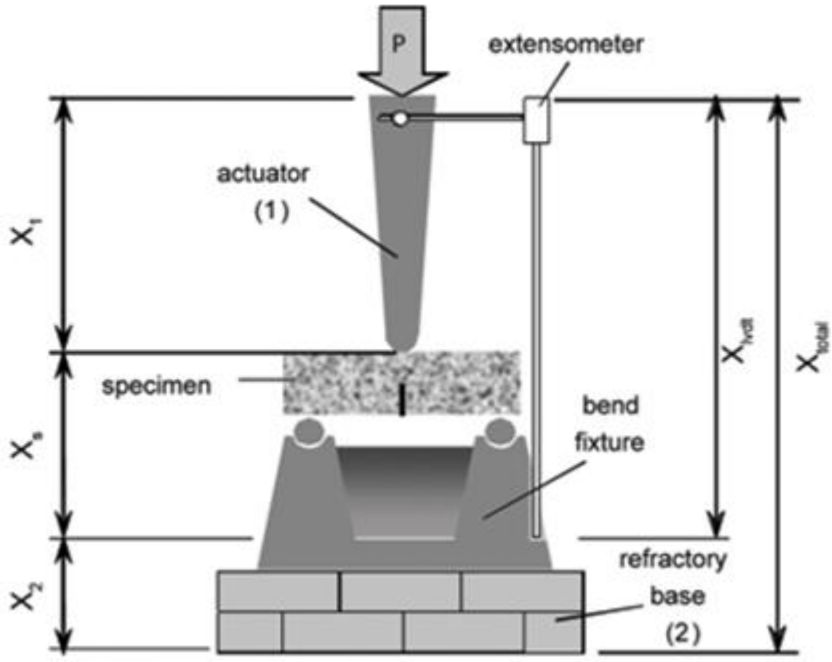

Fig. II.18: Principle of determination of the modulus of rupture in the three-point bending test.

The modulus of rupture *S_F* is calculated from the formula given in the standards EN 993-6:1998 and EN 993-7:2001:

$$\sigma_F = \frac{M_{\max}}{W} = \frac{3}{2}\cdot\frac{F_{\max}\cdot L_s}{b\cdot h^2} \quad / \text{ MPa} \qquad \text{(II.2)}$$

Where:

M_{max} is bending moment,
W is section index,
F_{max} is maximum force exerted on the test piece, in newtons,
Ls is distance between the support points of the test piece, in millimeters,
b is width of the test piece, in millimeters,
h is height of the test piece, in millimeters.

3.4.7 High temperature microscopy

The high-temperature microscopy method (microscopic-photographic) allows to determine characteristic temperatures connected with sintering process of the tested material during heating, such as: sintering temperature T_S, softening temperature T_A, melting temperature T_B and flow temperature T_C. Due to its role in the technological processes of ceramic materials, sintering is the most important factor in the firing process. This process takes place at a temperature lower than the melting point of the main component of the ceramic material. The sintering process is often accompanied by chemical reactions and phase transformations leading to changes in the volume of the material. In measurements using a high-temperature microscope, linear changes of the test piece are examined during heating. The measurement used a high-temperature microscope from Leitz. The test pieces were prepared in the form of a cube with dimensions of 3 mm. As a binder PVA were used. The test pieces were then placed on corundum pads and heated to 1600 °C at a rate of 7 K/min, without the use of a protective atmosphere. During heating, changes in test piece's volume were photographically recording. Using microscopic image analysis, the relative change in the test piece cross-sectional area δ(T) as a function of temperature and characteristic temperatures accompanying the sintering of the material were determined.

Characteristic temperatures were determined in accordance with the criteria given in the PN-82/G-04535 standard, point 1.4., based on the calculated relative change in the test piece cross-sectional area δ(T) according to the formula:

$$\delta(T) = \frac{\mathrm{P}(T) - \mathrm{P}_0}{\mathrm{P}_0} \;/\,\% \tag{II.3}$$

Where:

P_o is a number of black pixels in the test piece area at room temperature,
P(T) is a number of black pixels in the test piece area at the measurement temperature.

3.4.8 Scanning electron microscopy (SEM/EDS)

Microstructure analysis was performed using TESCAN Mira 3 scanning electron microscope with field emission equipped with an Energy Dispersive Spectrometer (EDS) system with AZtec Automated software (Oxford Instruments). The microstructure was observed at an accelerating voltage of 15 kV in the backscattered electron mode (BSE) or secondary electron mode (SE). The measurements were carried out on the polished cross-sections of test pieces covered by a conductive layer of chromium by using a Quorum Q150R ES device (Quorum Technologies). Images were collected at different magnifications.

3.5 Results and discussion

3.5.1 Thermochemical predictions

In order to facilitate the interpretation of the thermomechanical simulation results for the model castable's compositions, the amount and viscosity of the liquid phase formed at the temperature close or below $T_{0.5}$ were calculated. The temperature of the formation of the first drop of liquid for each of these compositions as well as the formed amount and its viscosity are presented in Table II.3. These results are for the compositions with the most unfavourable shares of individual oxides from the point of view of temperature and the amount of liquid phase formation. as was presented I chapter II.1. These calculations were performed for reference compositions and precursor compositions. It was assumed that the precursors introduced into the castable matrix would be the weakest part of the material.

Tab. II.3: Summary of the temperature of the formation of the first drop of liquid for the investigated the model castable's compositions as well as the formed amount and its viscosity.

	First drop of liquid phase / °C	**Amount of liquid phase / g**	**Viscosity of liquid phase / P**		
		1250 °C	**1200 °C**	**1250 °C**	**1300 °C**
Real composition (taking in account the innate presence of impurities in the raw materials)					
MHA_REF	1249	0,10024	-	3,127	1,598
2CS	1087	1,6260	93,76	35,68	15,50
2NS	920	3,2011	48879,2	13595,2	4917,3
2FC	1217	0,19066	1,916	0,315	0,161
2FCS	1087	1,6446	53,38	2,071	0,695
2TCS	1082	1,9777	50,27	16,08	6,65
Real composition, spinel forming formulation					
MHA_REF-S	1183	0,04469	0,22	0,555	1,865
2CS-S	1081	1,8090	16143,5	4160,8	1068,3
2NS-S	1086	2,447	15269,0	4016,3	1340,4
2FC-S	1058	0,0524	0,16	0,073	0,151
2FCS-S	1074	0,0483	0,186	0,049	0,173
2TCS-S	1083	1,8082	9205,9	1262,7	99,28

3.5.2 Refractoriness under load of the model castables MHA and MHA-S

Each of the model castables was tested first after drying, followed by a second measurement on the same cylinders, namely having experience high temperatures. The test pieces were heated up to 1700 °C or $T_{0,1}$. The obtained results are presented in table II.II. and figures II.19-30. It was found that during the first heating all materials displayed significantly lower refractoriness under load (Tab. II.4) compared to high alumina cement bonded refractory castables, even the reference material which contained no impurities (fluxes) and consisted mainly of alumina (Tab. II.1). The repetition of the RuL measurements on the same test pieces (second heating) showed that the refractoriness under load, in each case, increased by up to several hundred degrees (Table II.II. and figures II.19-30). This indicates that the amount of the liquid phase was not the only or main factor influencing the thermomechanical properties of these materials. Reactive alumina and its sinterability played an equally important role in this type of material. The observed phenomenon is discussed in more detail later in the report.

Tab. II.4: Refractoriness under load for the two times heated reference castables and series of MHA and MHA-S castables.

Material	**$T_{0.5}$ in °C First heating**	**$T_{0.5}$ in °C Second heating**
MHA-REF	1410	>1700
MHA-2CS	1360	1690
MHA-2NS	1360	1630
MHA-2FC	1420	>1700
MHA-2FCS	1360	1600
MHA-2TCS	1370	1630
MHA-REF-S	1560	>1700
MHA-2CS-S	1420	1580
MHA-2NS-S	1490	>1700
MHA-2FC-S	1540	1660
MHA-2FCS-S	1520	>1700
MHA-2TCS-S	1500	1630

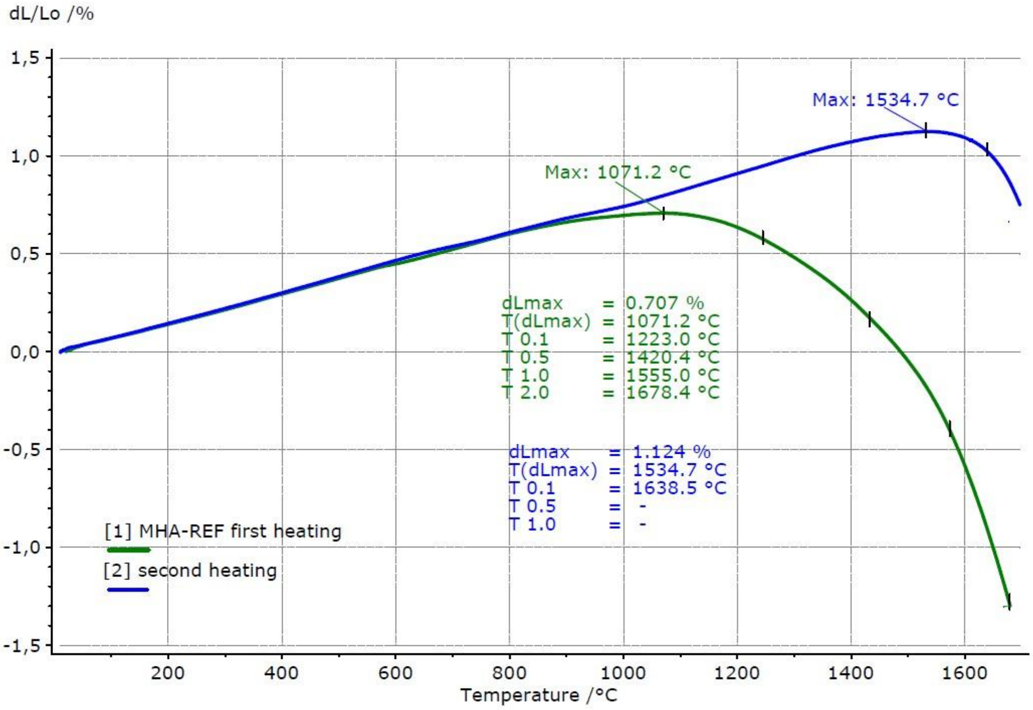

Fig. II.19: Refractoriness under load curves after the first and the second heating of the same test piece; reference model castable MHA-REF.

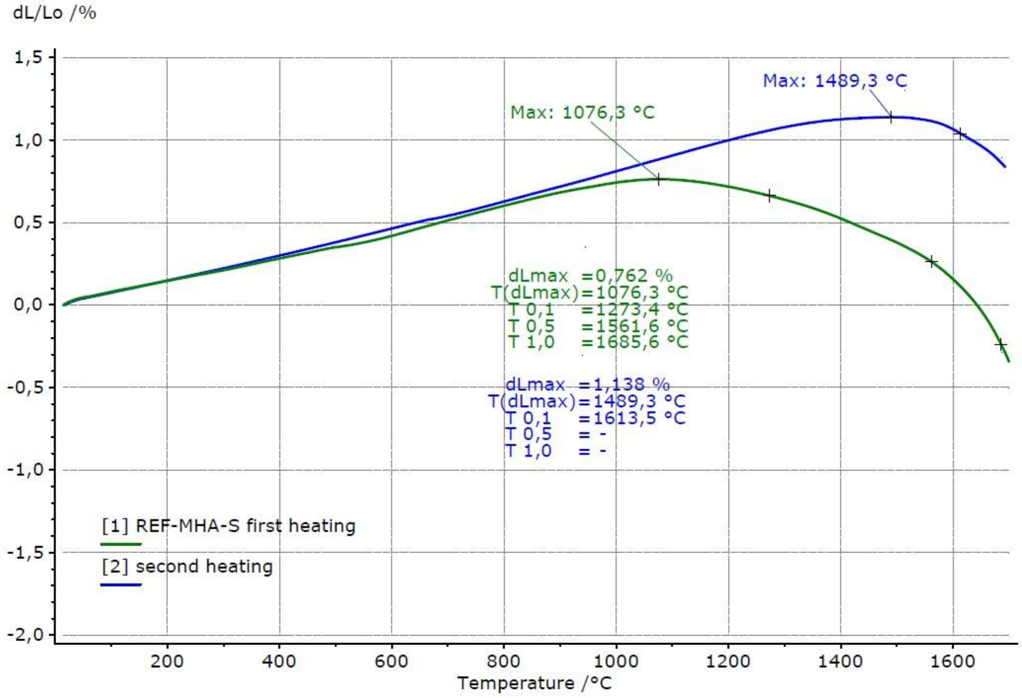

Fig. II.20: Refractoriness under load after first and second heating on the test piece sample; reference model castable MHA-S-REF.

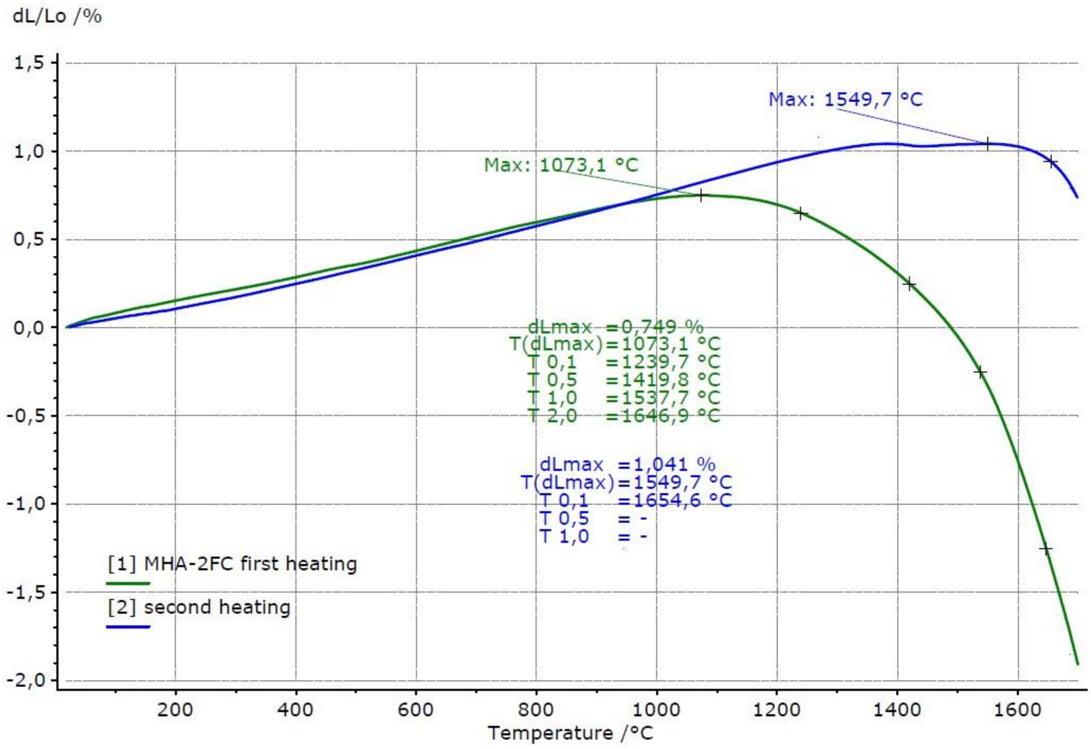

Fig. II.21: Refractoriness under load after first and second heating on the same test piece; impurified model castable MHA-2FC.

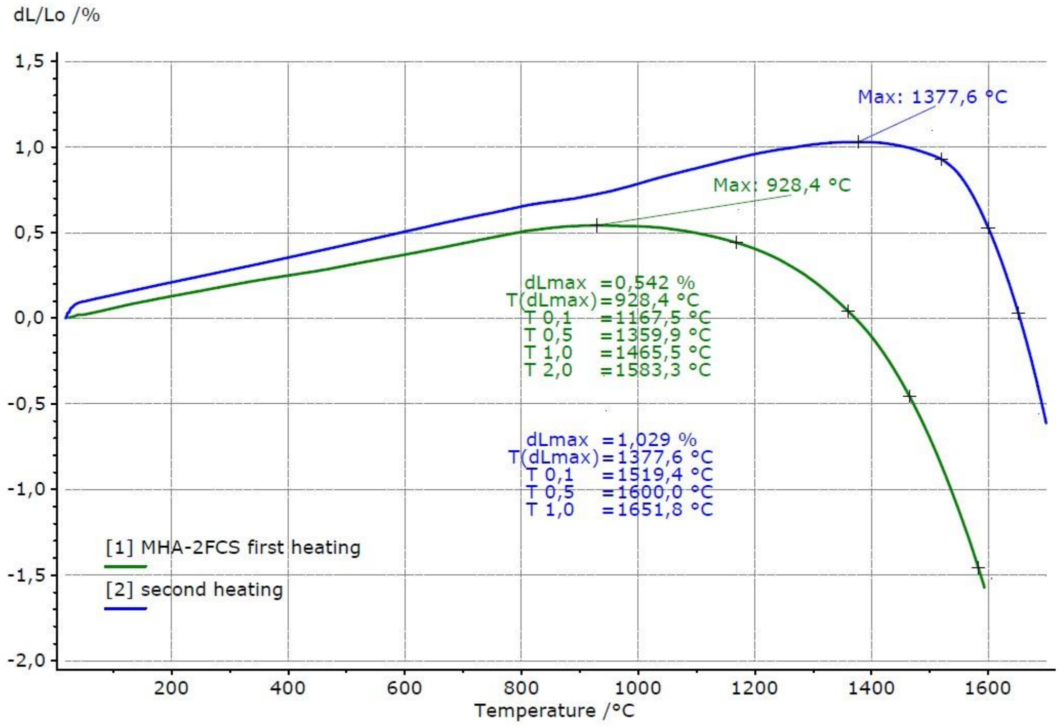

Fig. II.22: Refractoriness under load after first and second heating on the same test piece; impurified model castable MHA-2FCS.

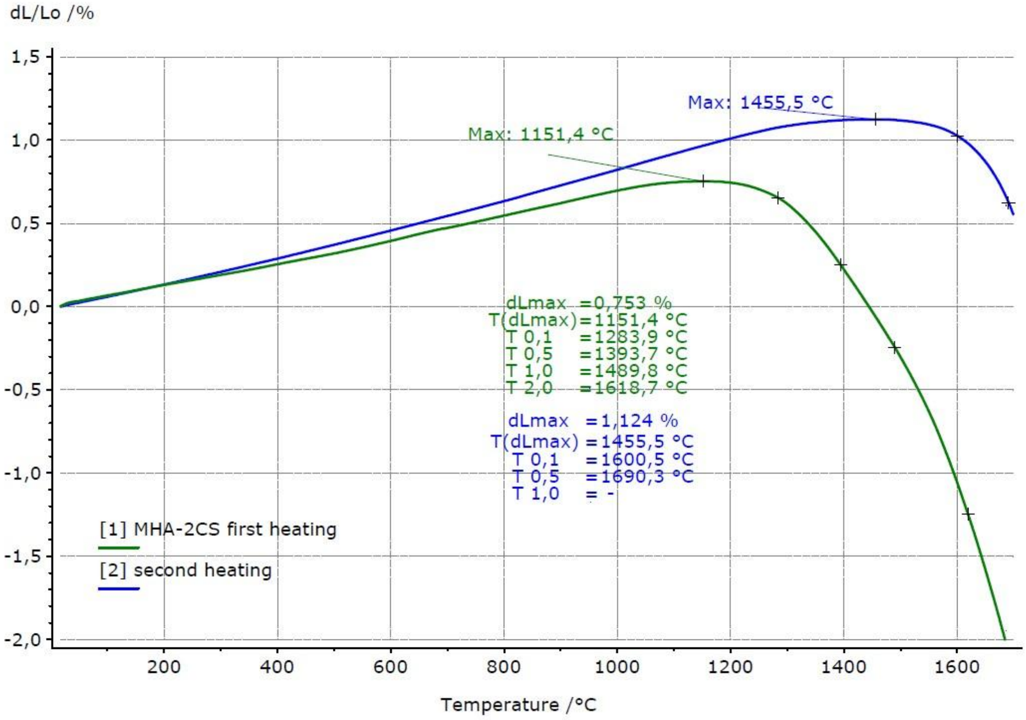

Fig. II.23: Refractoriness under load after first and second heating on the same test piece; impurified model castable MHA-2CS.

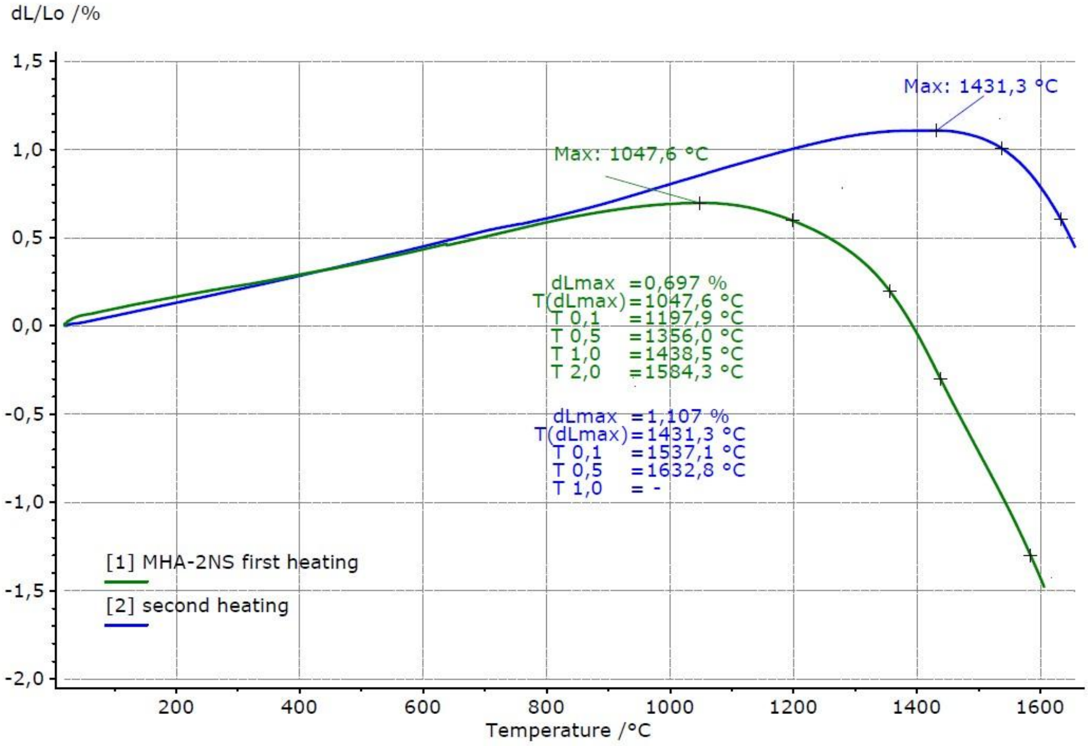

Fig. II.24: Refractoriness under load after first and second heating on the same test piece; impurified model castable MHA-2NS.

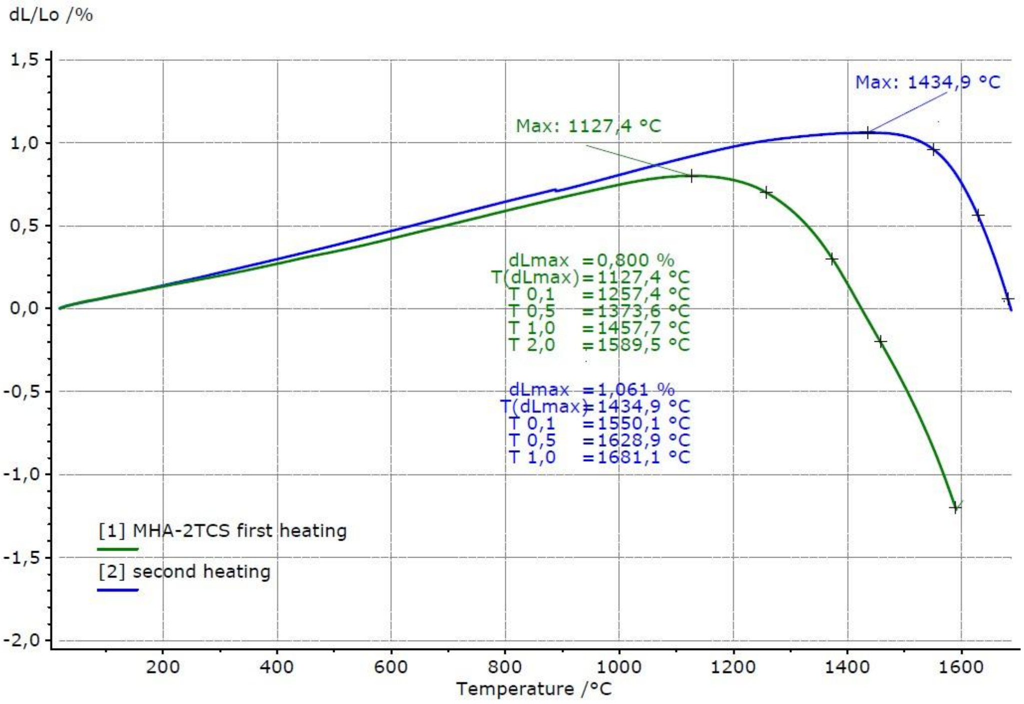

Fig. II.25: Refractoriness under load after first and second heating on the same test piece; impurified model castable MHA-2TCS.

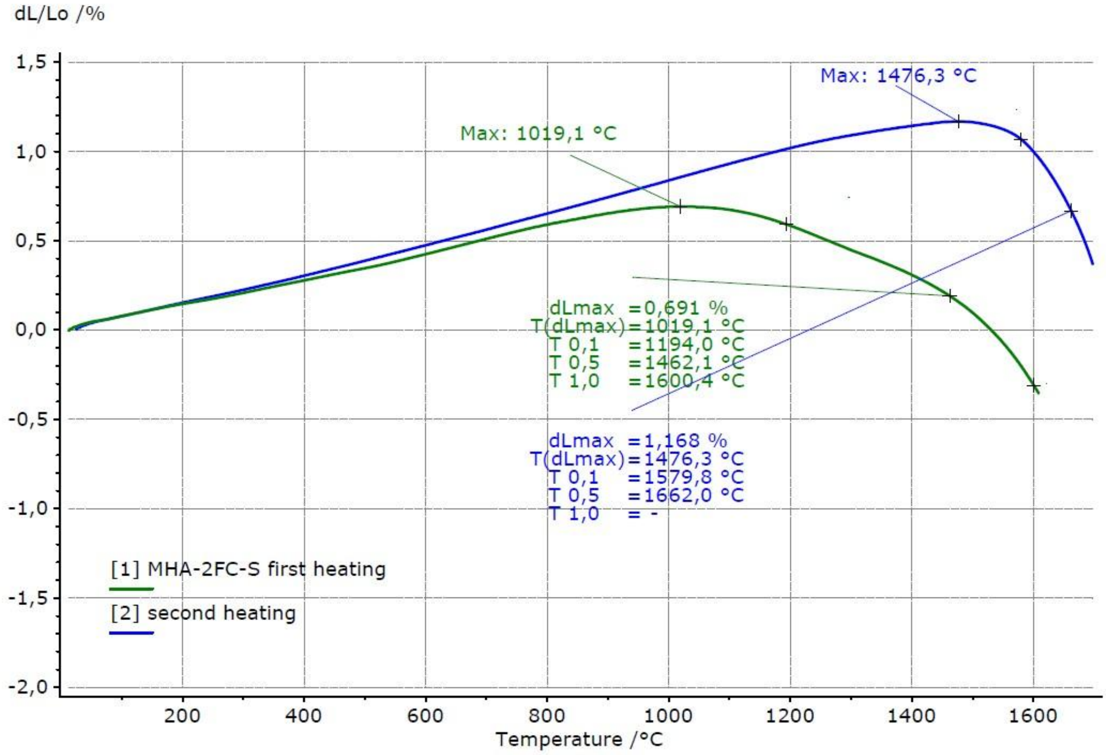

Fig. II.26: Refractoriness under load after first and second heating on the same test piece; impurified model castable MHA-2FC-S.

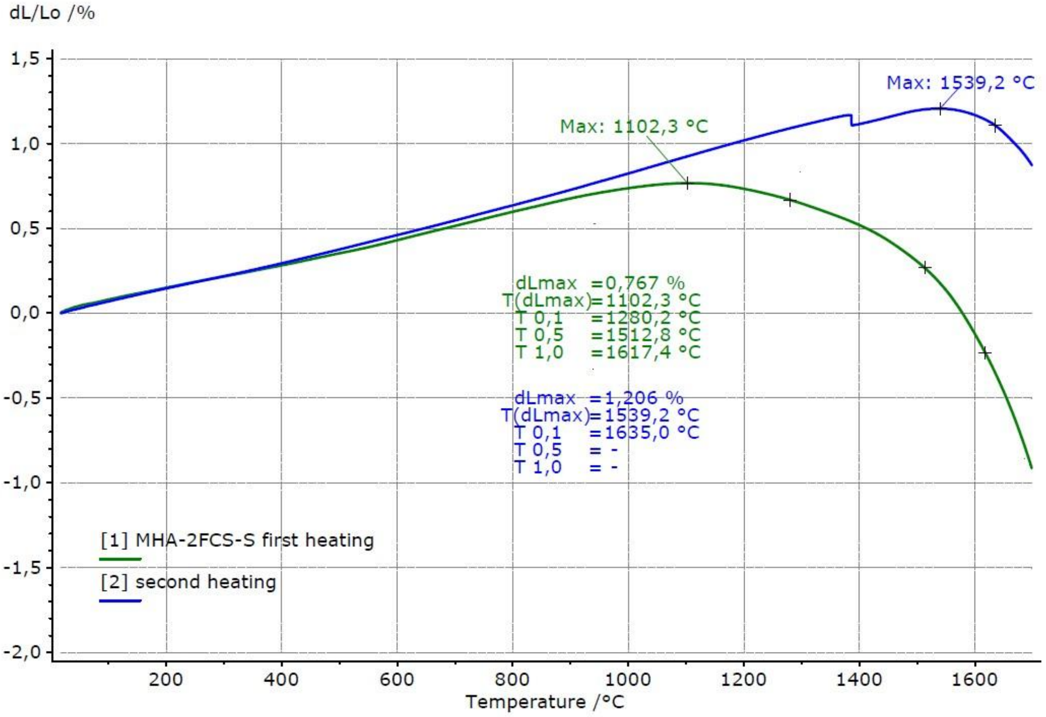

Fig. II.27: Refractoriness under load after first and second heating on the same test piece; impurified model castable MHA-2FCS-S.

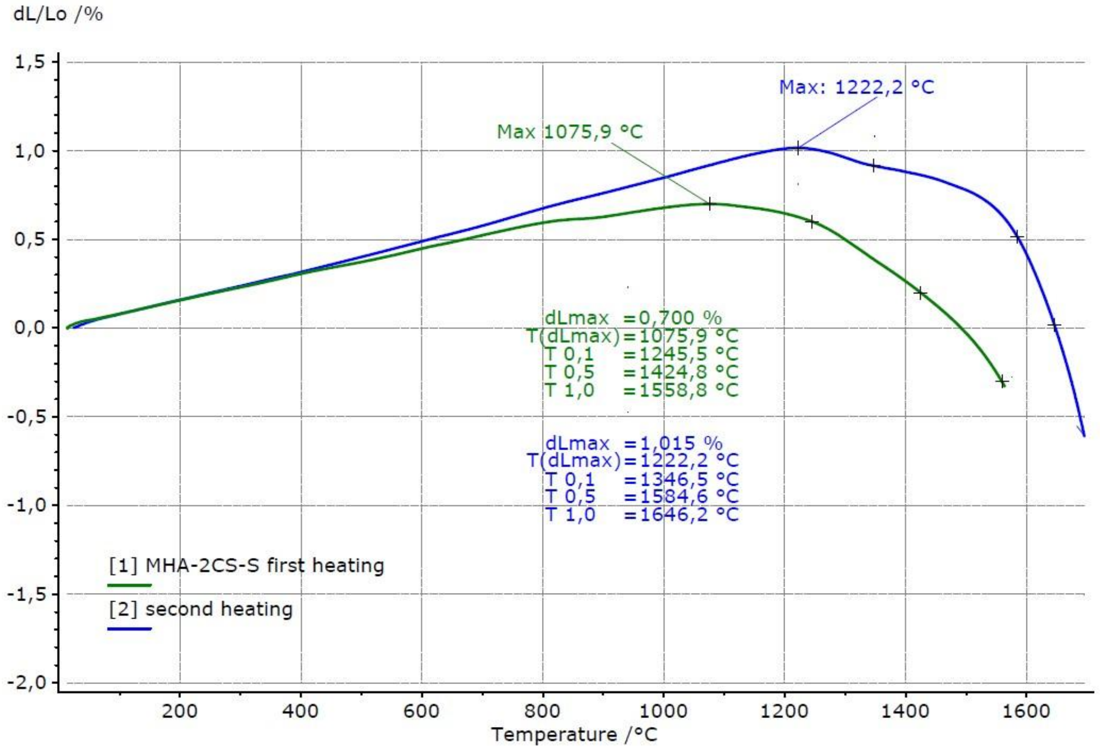

Fig. II.28: Refractoriness under load after first and second heating on the same test piece; impurified model castable; MHA-2CS-S.

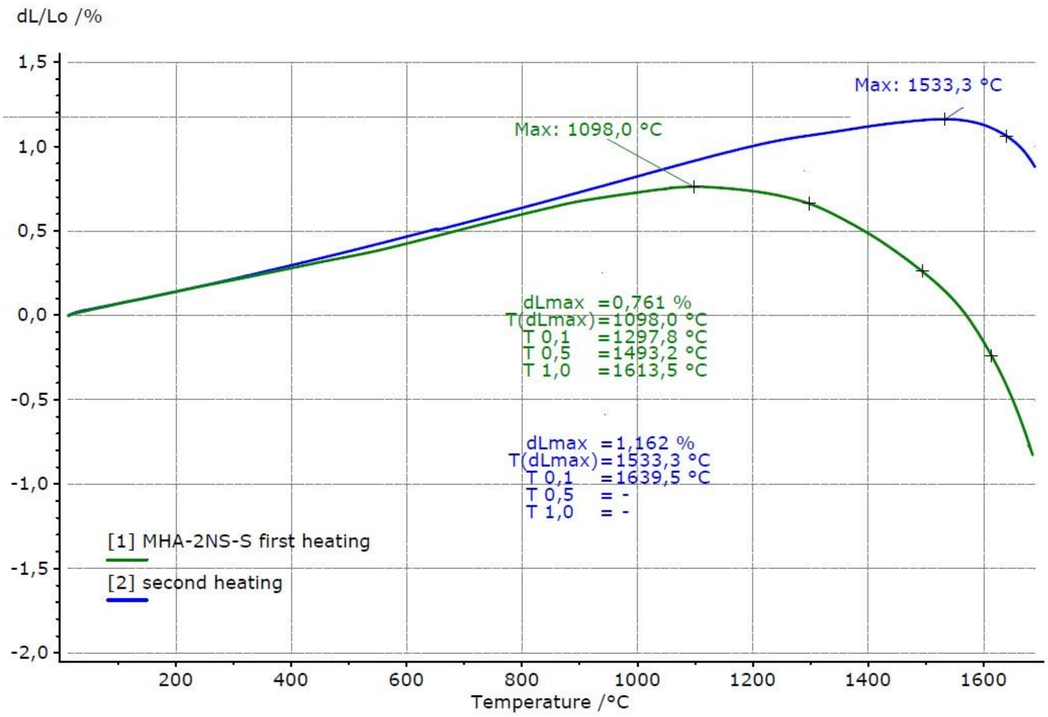

Fig. II.29: Refractoriness under load after first and second heating on the same sample; MHA-2NS-S.

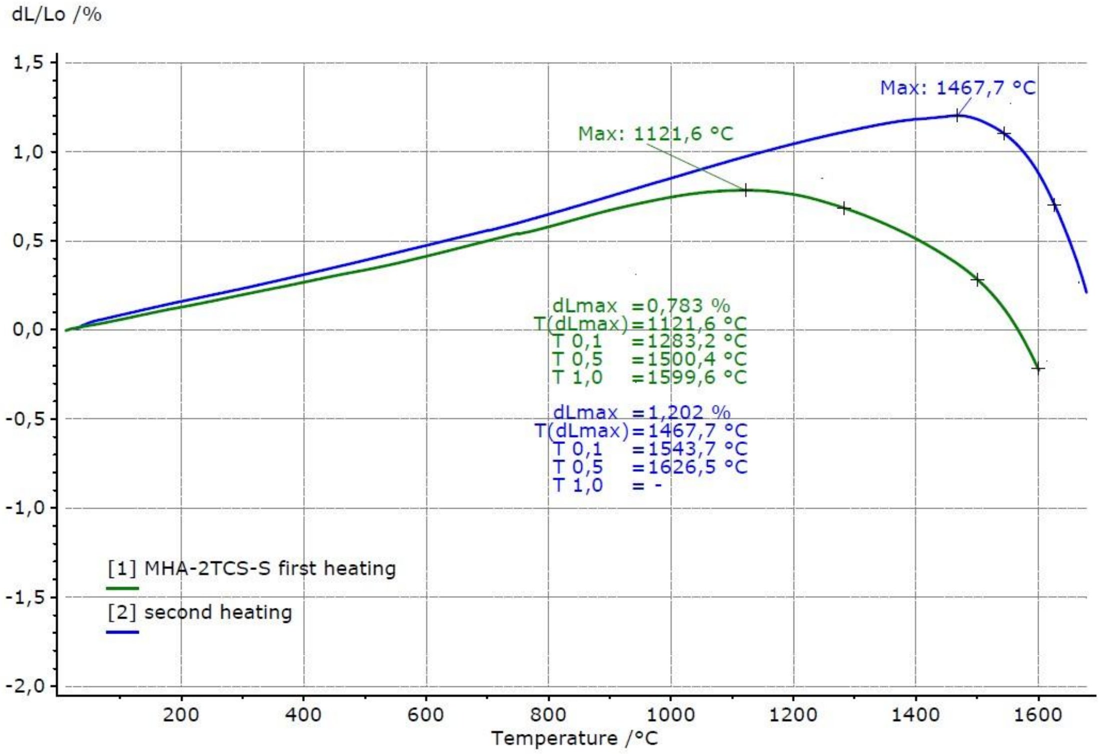

Fig. II.30: Refractoriness under load after first and second heating on the same test piece; impurified model castable MHA-2TCS-S.

3.5.3 Sinterability studies in a high-temperature microscope

Sinterability measurements performed in a high-temperature microscope enabled to estimate the rate of linear changes in the cross-sectional area of test pieces examined in a high-temperature microscope. Photographs of the test piece for selected temperatures are shown in the figures II.31 to 33. The graphical course of linear changes in heated test pieces is displayed in the figure II.34. The determined sintering temperatures (Ts) are presented in Tab. II.5.

The obtained results showed that the spinel-forming additive (MgO) increases the spatial stability of the model spinel forming refractory castables MHA-S in comparison to the model refractory castables MHA. Actually, both formulations (spinel free and spinel forming) probably started to sinter at similar temperatures, however, the formation the formation of spinel, which is accompanied with a volume expansion, compensate the shrinkage observed in the spinel free formulation. This is visible in castables with compositions 2FCS, 2CS, 2NS and 2TCS. Only in the case of the model castables 2FC, the same result was obtained.

a) **REF-MHA-**matrix

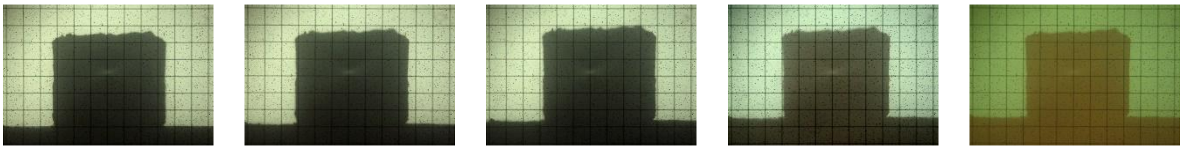

22°C 500°C 1200°C 1500°C 1600°C

b) **REF-MHA**

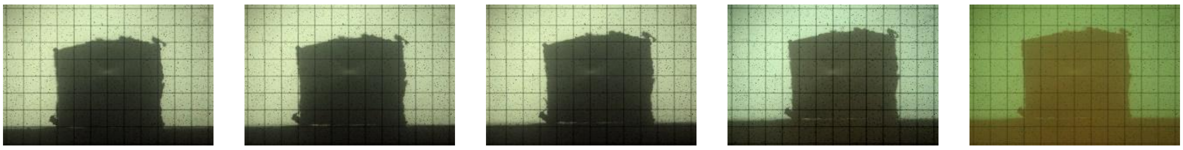

22°C 500°C 1200°C 1500°C 1600°C

Fig. II.31: Photos of a) REF-MHA-matrix. b) REF-MHA cube test pieces during the measurement in the high-temperature microscope.

a) ***MHA-2FC***

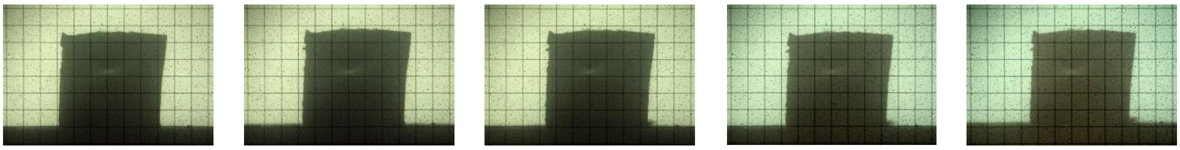

22°C 500°C 1200°C 1500°C 1600°C

b) ***MHA-2TCS***

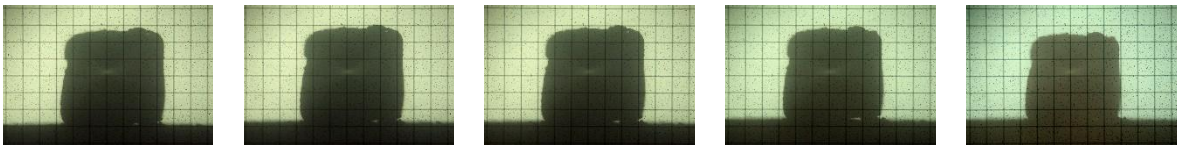

20°C 500°C 1200°C 1400°C 1600°C

c) ***MHA-2CS***

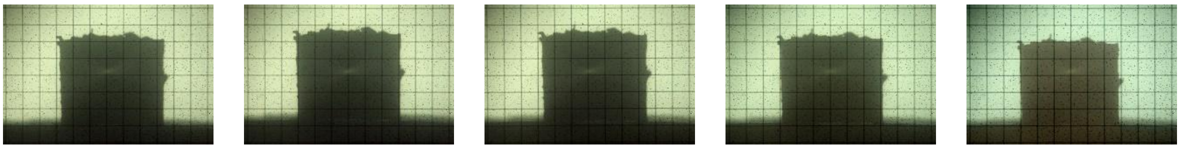

20°C 500°C 1200°C 1400°C 1600°C

d) *MHA-2FCS*

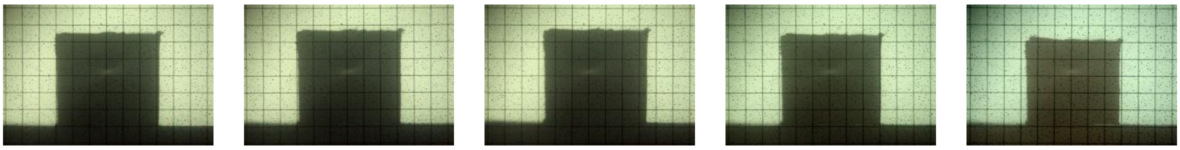

21°C 500°C 1200°C 1400°C 1600°C

e) *MHA-2NS*

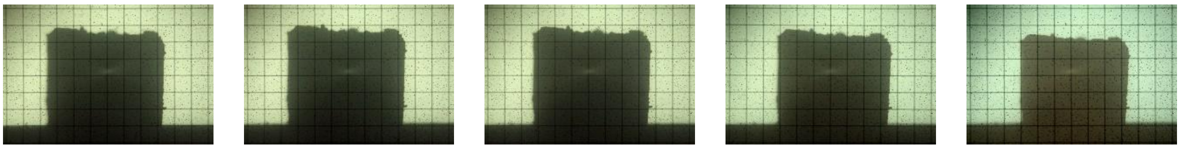

21°C 500°C 1200°C 1400°C 1600°C

Fig. II.32: Photos of a) MHA-2FC. b) MHA-2TCS. c) MHA-2CS. d) MHA-2FCS. e) MHA-2NS cube test pieces during the measurement in the high-temperature microscope.

a) *MHA-2FC-S*

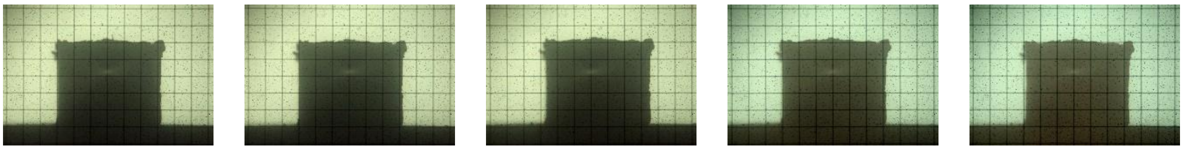

21°C 500°C 1200°C 1500°C 1600°C

b) *MHA-2TCS-S*

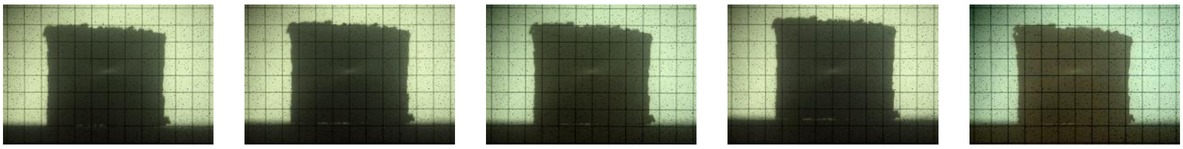

22°C 500°C 1200°C 1400°C 1600°C

c) *MHA-2CS-S*

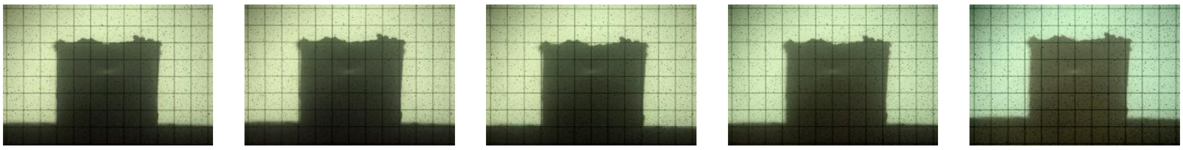

21°C 500°C 1200°C 1400°C 1600°C

d) *MHA-2FCS-S*

21°C 500°C 1200°C 1400°C 1600°C

e) *MHA-2NS-S*

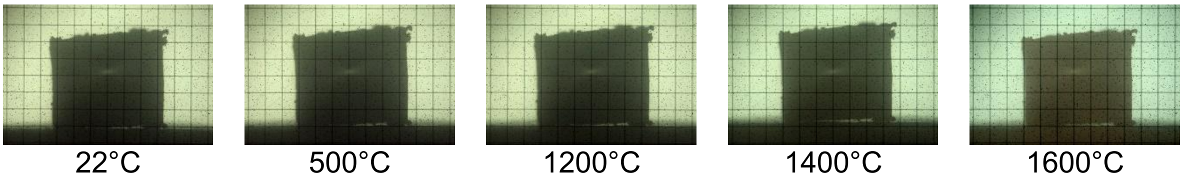

Fig. II.33: Photos of a) MHA-2FC-S. b) MHA-2TCS-S. c) MHA-2CS-S. d) MHA-2FCS-S. e) MHA-2NS-S cube sample during the test in the high-temperature microscope.

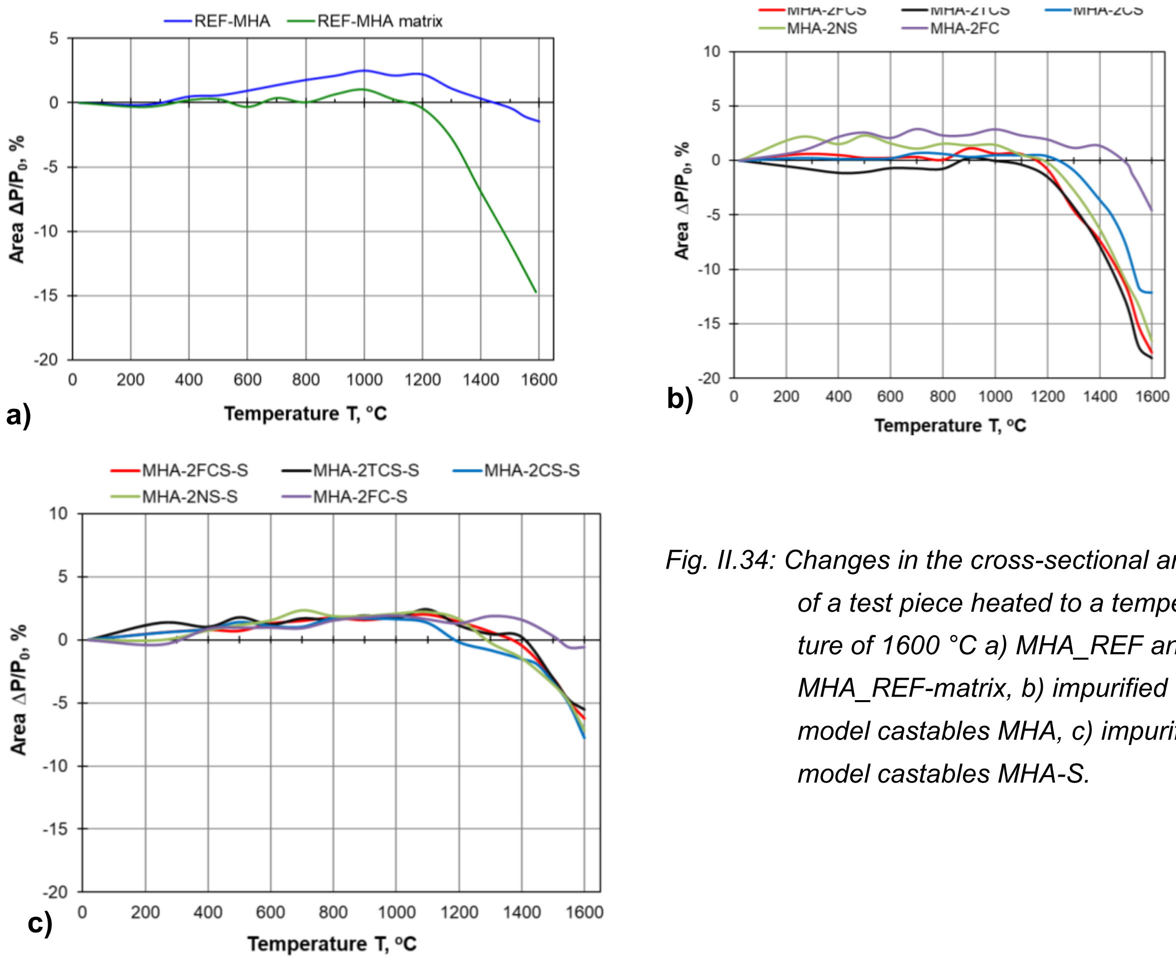

Fig. II.34: Changes in the cross-sectional area of a test piece heated to a temperature of 1600 °C a) MHA_REF and MHA_REF-matrix, b) impurified model castables MHA, c) impurified model castables MHA-S.

Tab. II.5: Sintering temperature Ts of model castables.

Model castable	**Ts / °C**	**Model castable**	**Ts / °C**
MHA-2FCS	1180	MHA-2FCS-S	1390
MHA-2TCS	1200	MHA-TCS-S	1410
MHA-2CS	1280	MHA-2CS-S	1450
MHA-2NS	1240	MHA-2NS-S	1300
MHA-2FC	1500	MHA-2FC-S	1500
MHA-REF matrix	1230		
MHA-REF	1350		

3.5.3.1. Creep in Compression (CiC) based on the Norton-Bailey concept

Creep rate ware measured using a newly developed method based on the Norton-Bailey concept [9-10] to identify the different stages of creep. According to this concept. the creep of the material should take place in three stages, as shown in figure II.14. The first two stages of creep described by the Norton-Bailey theory were identified in these studies. The results are presented in the figures II.35 to II.51. Despite the application of the maximum load allowed by the capabilities of the testing equipment, i.e. 1,2 MPa, the third stage of creep of the tested materials leading to their failing was never observed (Fig. II.37, II.40, II:43, II.46 and II.49). In some cases. when using this maximal load at the temperature $T_{0.5}$ and $T_{0.5}$ +100 °C, the tests had to be stopped due to excessive strain beyond the measuring range of the device (Fig. II.37 and II.48). The absence of the third stage of creep resulted in a change in the planning of the measurement campaign. It was decided not to perform some measurements at a temperature of $T_{0.5}$ +100 °C. Instead, the decision was made to check the assumption that at relatively low loads (up to a maximum of 1,2 MPa), the measurement time has a significant impact on the appearance of the third stage of creep, which lead to the failing of the test piece. Typically, the measurements were conducted for up to 25 hours. These additional measurements were carried out for 100 hours on reference model castable and the model castable MHA_2NS, in which it was expected that their strain after 100 hours would allow the measurements to be completed, while, at the same time, the creep would be greater than in the reference test piece. The results are presented in Fig. II.52 and II.53.

The fact that the material has not failed up to this point is indicative of the extensive thermoplastic properties of the refractory castables and is the most likely explanation for the lack of a failure step for the material subjected to mechanical stress.

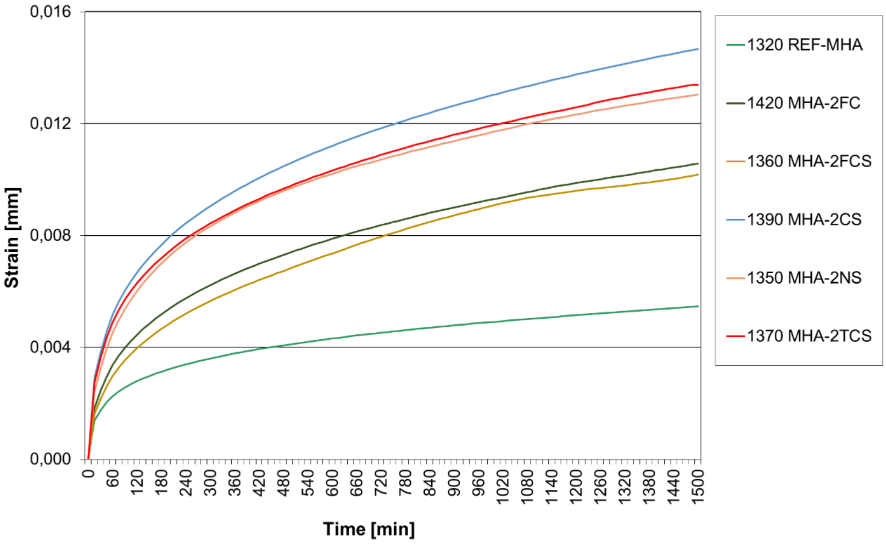

Fig. II.35: Deformation as function of time for the model castables MHA under a load of 0,2 MPa at a temperature of $T_{0,5}$.

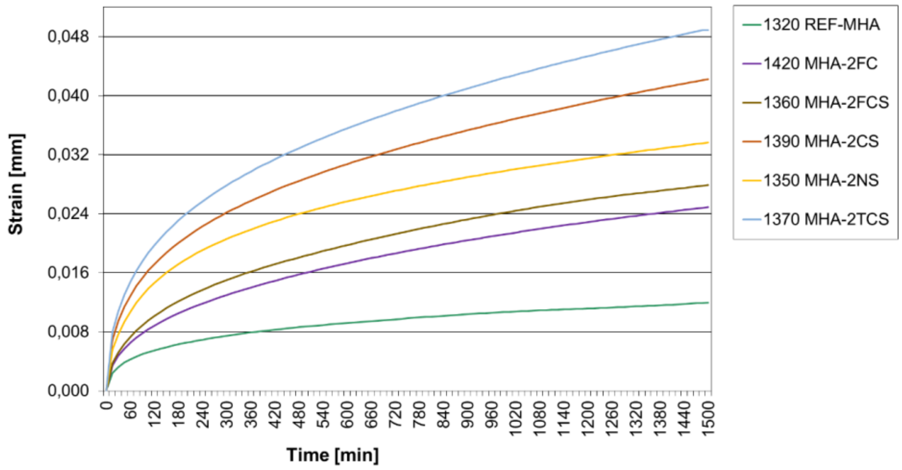

Fig. II.36: Deformation as function of time for the model castables MHA under a load of 0,8 MPa at a temperature of $T_{0,5}$.

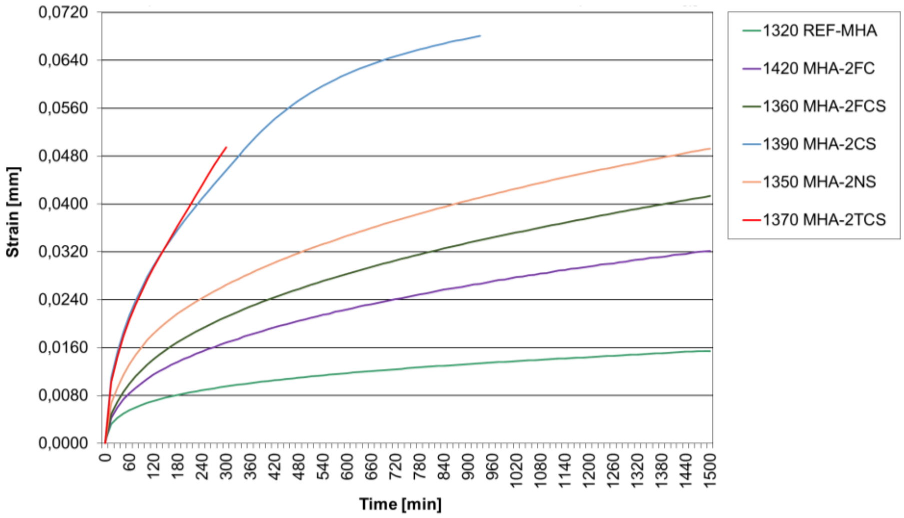

Fig. II.37: Deformation as function of time for the model castables MHA under a load of 1,2 MPa at a temperature of $T_{0,5}$.

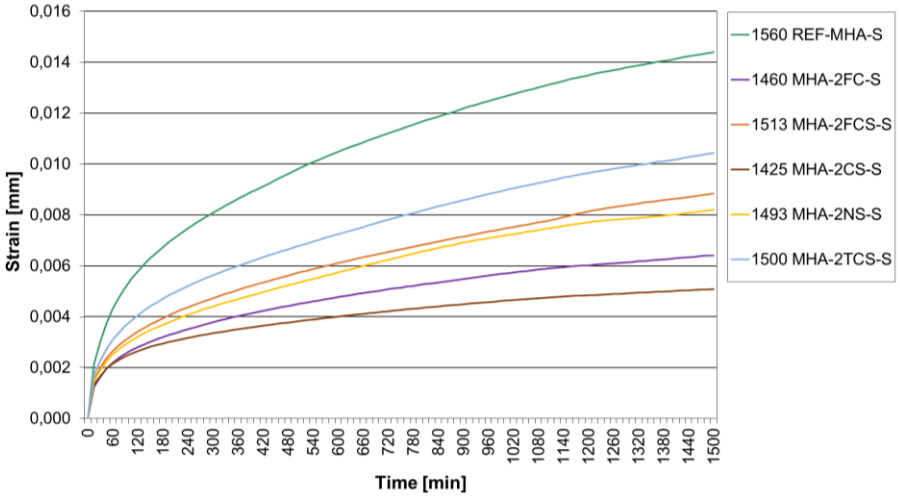

Fig. II.38: Deformation as function of time for the spinel forming model castables MHA-S under a load of 0,2 MPa at a temperature of $T_{0,5}$.

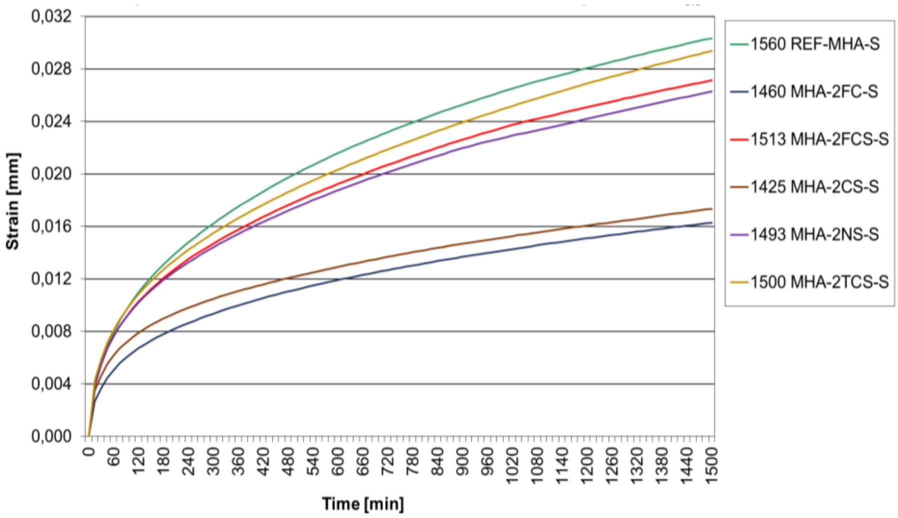

Fig. II.39: Deformation as function of time for the spinel forming model castables MHA-S under a load of 0,8 MPa at a temperature of $T_{0,5}$.

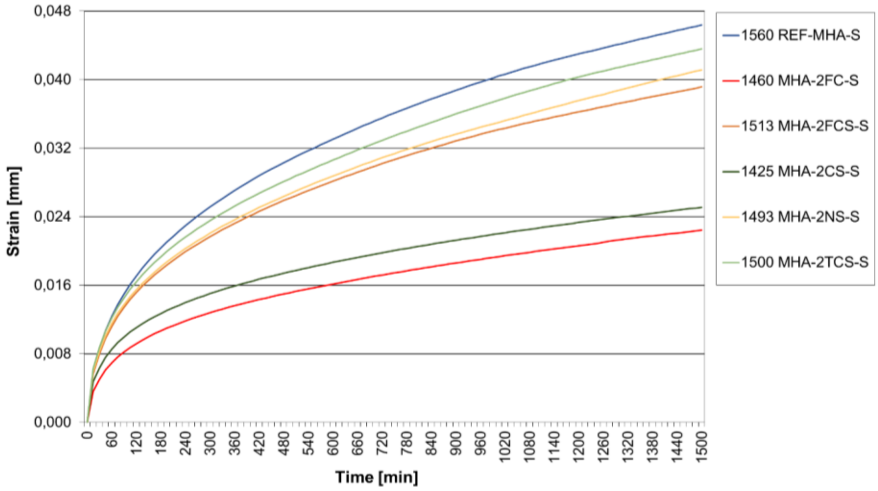

Fig. II.40: Deformation as function of time for the spinel forming model castables MHA-S under a load of 1,2 MPa at a temperature of $T_{0,5}$.

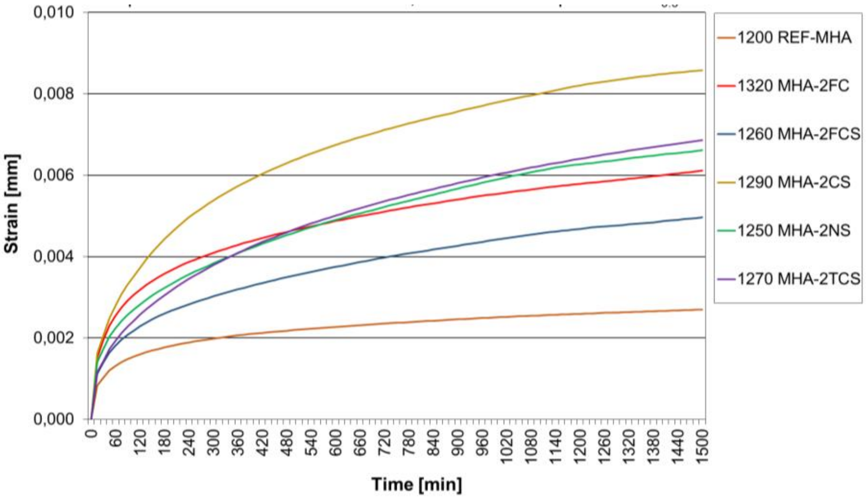

Fig. II.41: Deformation as function of time for the model castables MHA under a load of 0,2 MPa at a temperature of $T_{0,5}$-100 °C.

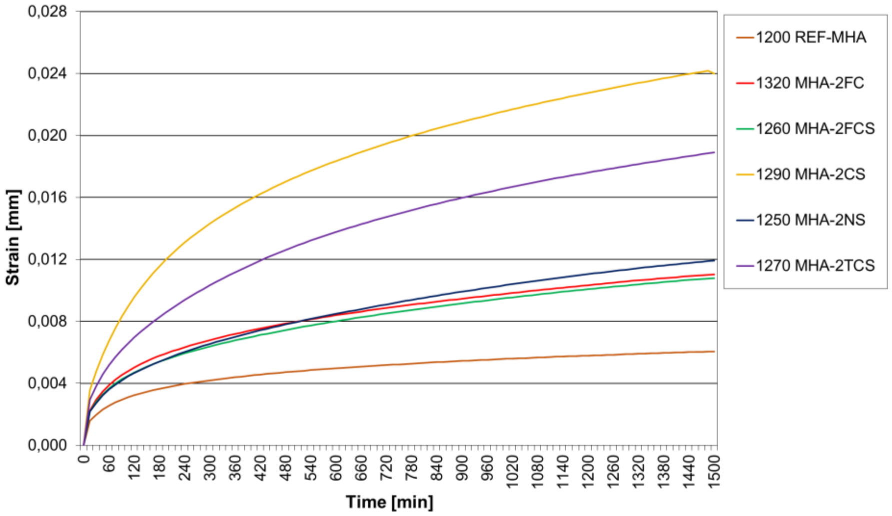

Fig. II.42: Deformation as function of time for the model castables MHA under a load of 0,8 MPa at a temperature of $T_{0,5}$-100 °C.

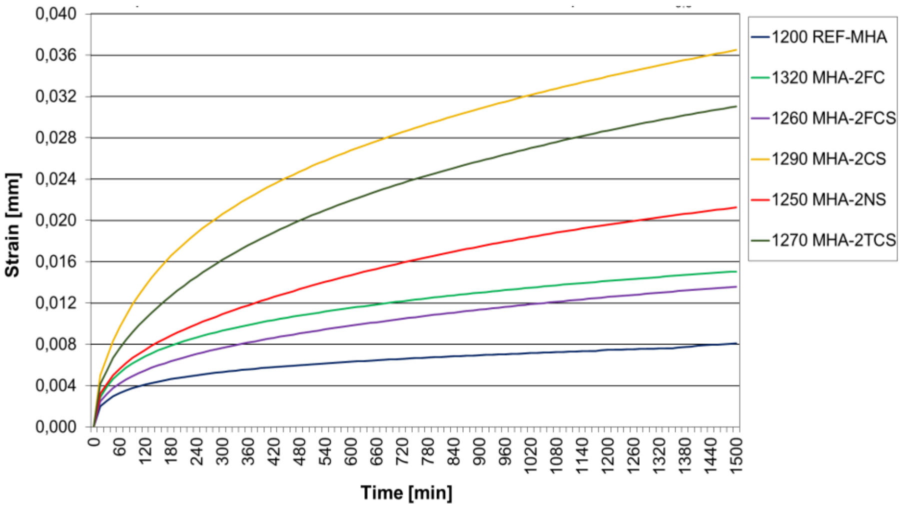

Fig. II.43: Deformation as function of time for the model castables MHA under a load of 1,2 MPa at a temperature of $T_{0,5}$-100 °C.

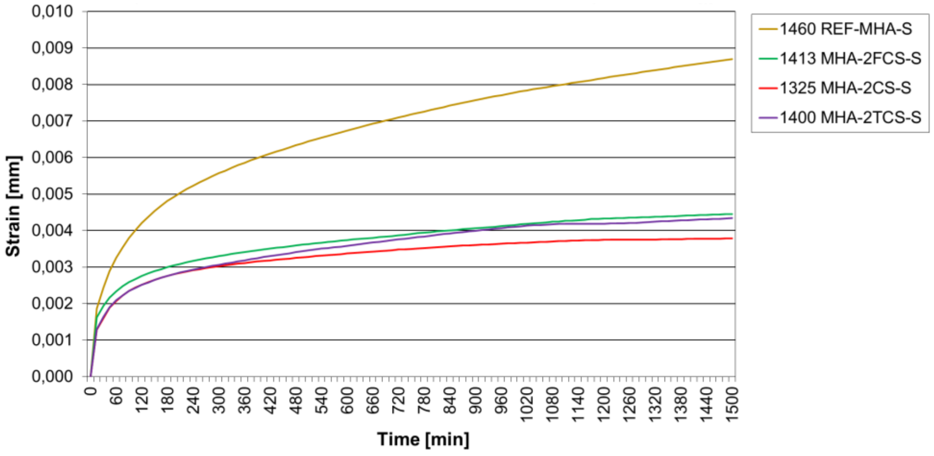

Fig. II.44: Deformation as function of time for the spinel forming model castables MHA-S under a load of 0,2 MPa at a temperature of $T_{0,5}$-100 °C.

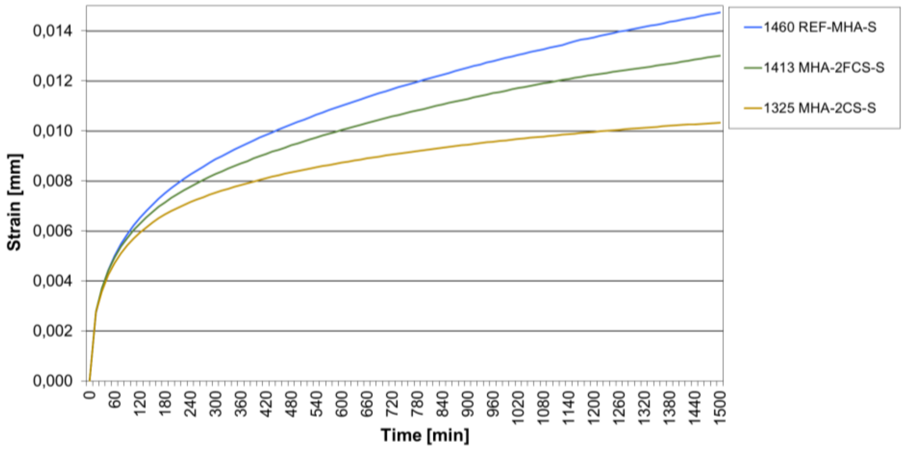

Fig. II.45: Deformation as function of time for the spinel forming model castables MHA-S under a load of 0,8 MPa at a temperature of $T_{0,5}$-100 °C.

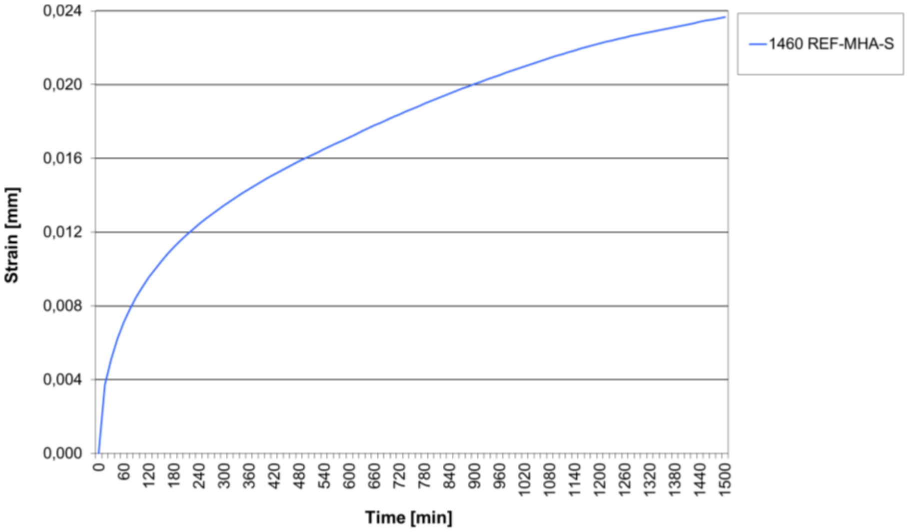

Fig. II.46: Deformation as function of time for the spinel forming model castables MHA-S under a load of 1,2 MPa at a temperature of $T_{0,5}$-100 °C.

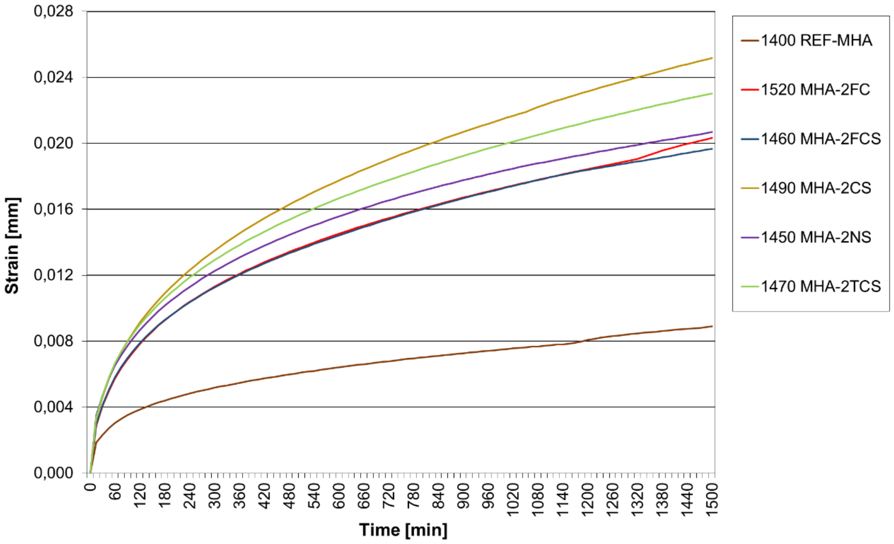

Fig. II.47: Deformation as function of time for the model castables MHA under a load of 0,2 MPa at a temperature of $T_{0,5}$+100 °C.

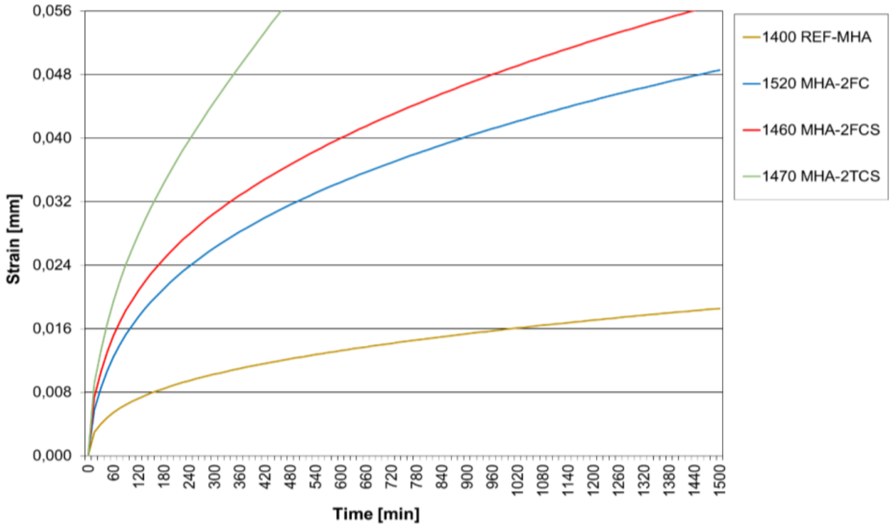

Fig. II.48: Deformation as function of time for the model castables MHA under a load of 0,8 MPa at a temperature of $T_{0,5}$+100 °C.

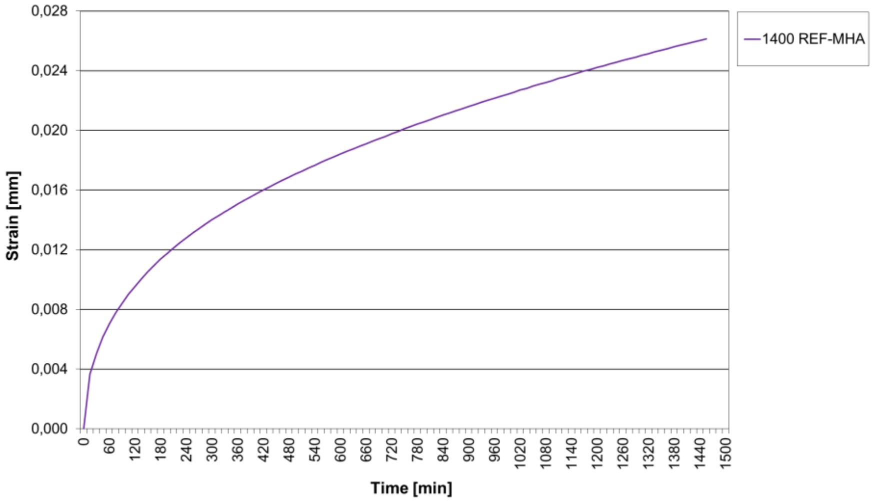

Fig. II.49: Deformation as function of time for the model castables MHA under a load of 1,2 MPa at a temperature of $T_{0,5}$+100 °C.

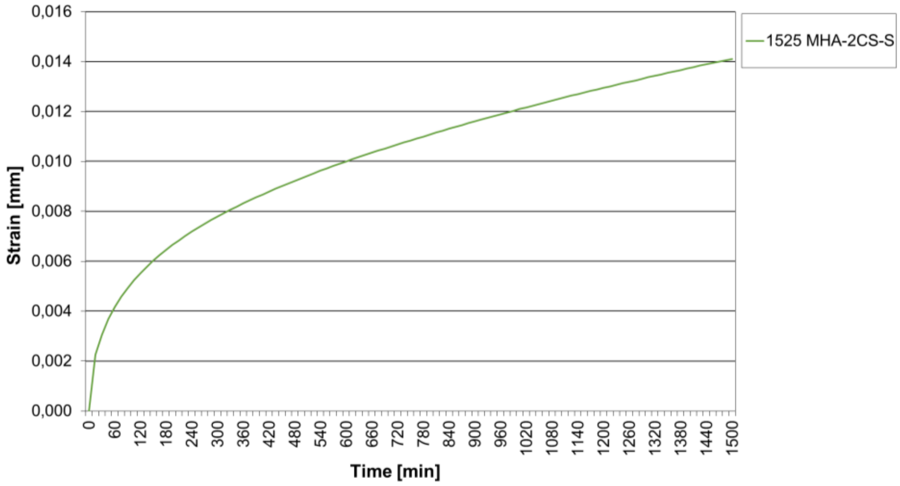

Fig. II.50: Deformation as function of time for the spinel forming model castables MHA-S under a load of 0,2 MPa at a temperature of $T_{0,5}$+100 °C.

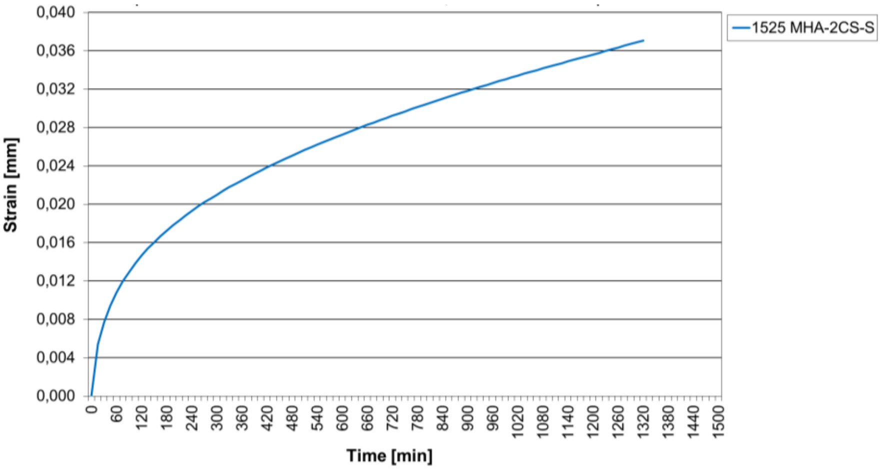

Fig. II.51: Deformation as function of time for the spinel forming model castables MHA-S under a load of 0,8 MPa at a temperature of $T_{0,5}$+100 °C.

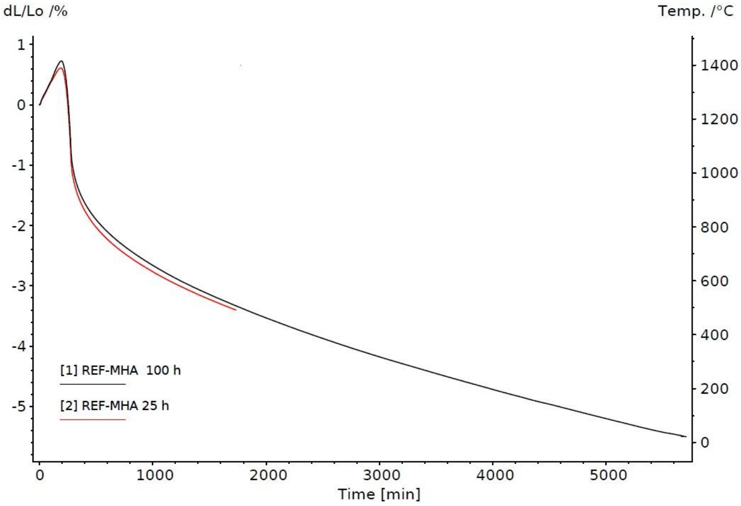

Fig. II.52: Comparison of creep in compression curves for the model castable REF_MHA assessed for 25 and 100 hours.

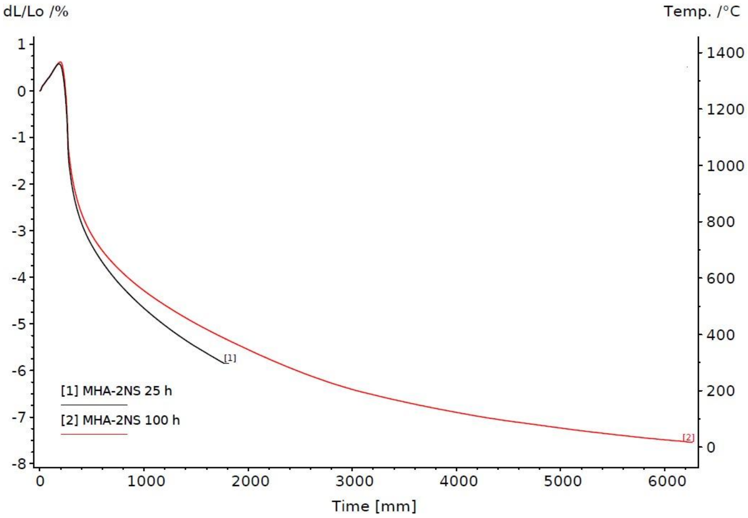

Fig. II.53: Comparison of creep in compression curves for the model castable MHA-2NS assessed for 25 and 100 hours.

3.5.4 Fracture energy by means of static method (three point bending test)

Changes in the evolution of force-strain relationships with temperature illustrate the thermoplastic transition of brittle to ductile state of the investigated model castables. At low temperatures, measured force-strain curves have typical characteristics of brittle materials, while at higher temperatures the force-strain curves developed characteristics closer to those of thermoplastic materials. This is illustrated with the reference model castables MHA-REF and MHA-S-REF (Fig. II.54). Using the values of the recorded force-strain curves for the test pieces presented in the figure II.54, the fracture energies were assessed and calculated at different temperatures based the results from the refractoriness under load measurements i.e. T_0-100 °C, T_0, $T_{0,1}$ or $T_{0,1}$ + 100 °C, $T_{0.5}$ - 100 °C, $T_{0,5}$. Measurements were not performed at temperature higher than 1450 °C since it exceeding the maximum temperature of the testing machine. The results are presented in the table II.6. and the figure II.55 for the model refractory castable MHA and the figure II.56 for spinel forming model refractory castable MHA-S.

The results of the determination of the fracture energy using the three-point bending method show that all the spiked model castables have inferior properties compared to the reference model castable at the temperature of $T_{0,5}$ (Figures II.55 and II.56). Below this temperature, the composition of the impurities regularly led to improvement of the thermomechanical properties. Considering that unfavourable combinations of impurities were introduced into the investigated castables in order to produce as much of the liquid phase as possible at high temperature (eutectic compositions), it is possible, that by moving the composition away from the eutectic, the detrimental effects of impurities near the working temperature will be much more limited.

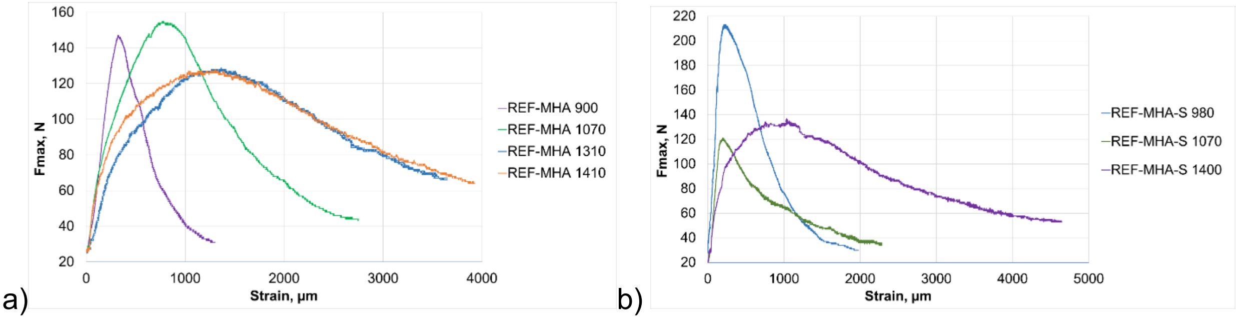

Fig. II.54: Force-strain curves for the three-point bending measurements of the reference model castables (a) MHA-REF and (b) MHA-S-REF, at different temperatures.

Tab. II.6: Fracture energy G and bending force F_{max} as a function of the temperature (the maximum temperature corresponds to $T_{0,5}$ for each castable) under three point bending configuration.

Model castable	Temp. / °C	G / J/m²	F_{max} / N	Model castable	Temp. / °C	G /J/m²	F_{max} / N
REF_MHA	900	86,9	147,0	**REF_MHA -S**	980	154,0	213
	980	110,6	128,0		1070	117,4	121
	1070	227,2	154		1400	333,8	137
	1310	283,1	128		1460	-	-
	1410	311,1	128		1560	-	-

MHA_2CS	1000	117,1	156				
	1150	102,4	85	**MHA_2CS-S**	1076	171,6	231
	1290	333,9	127		1320	261,0	130
	1390	127,8	73		1420	341,6	89
MHA_2NS	1050	151,3	139	**MHA_2NS-S**	1100	245,2	212
	1260	229,8	87		1390	226,9	85
	1360	120,2	55		1490	-	-
MHA_2FC	1070	191,1	200	**MHA_2FC- S**	1020	223,0	299
	1320	347,5	125		1440	447,8	165
	1420	240,2	94		1540	-	-
MHA_2FCS	800	138,1	409				
	930	133,1	219	**MHA_2FCS-S**	1100	339,5	192
	1260	165,9	130		1420	407,9	134
	1360	170,3	69		1520	-	-
MHA_2TCS	1060	95,5	175	**MHA_2TCS-S**	1120	207,1	172
	1270	174,1	80		1400	293	175
	1370	116,6	68		1500	-	-

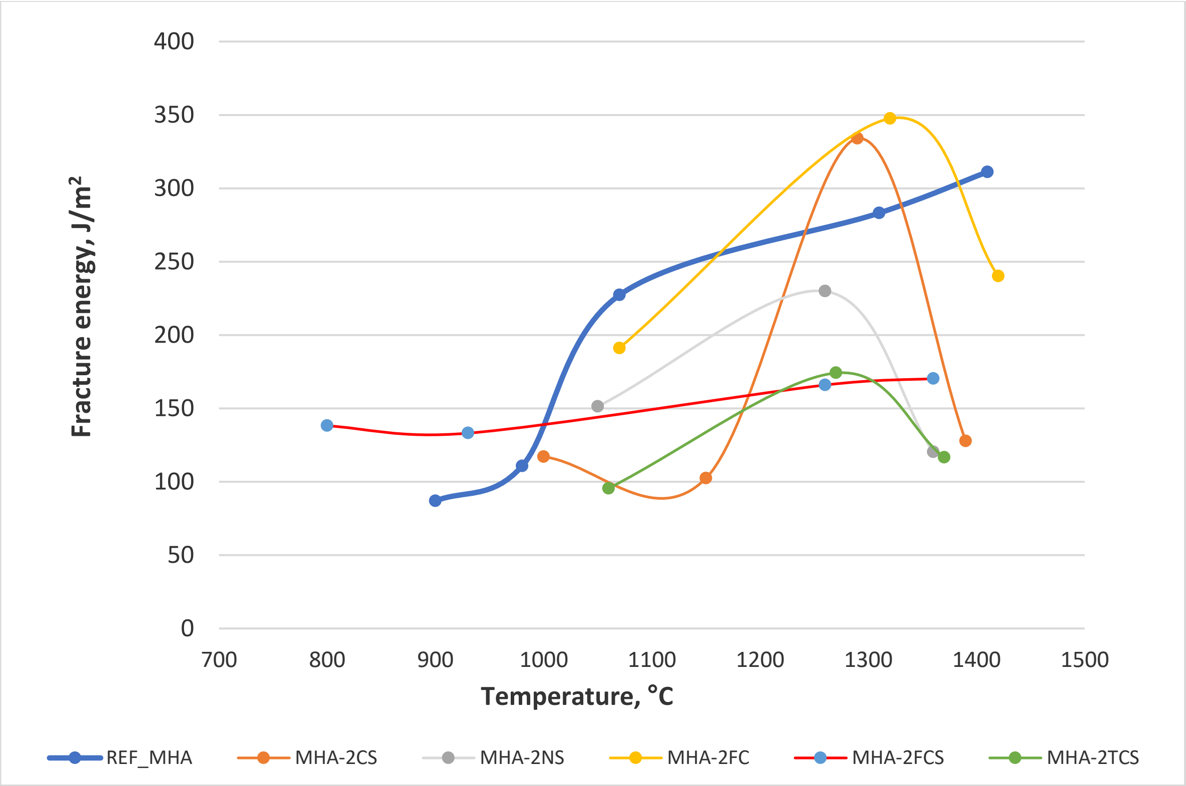

a)

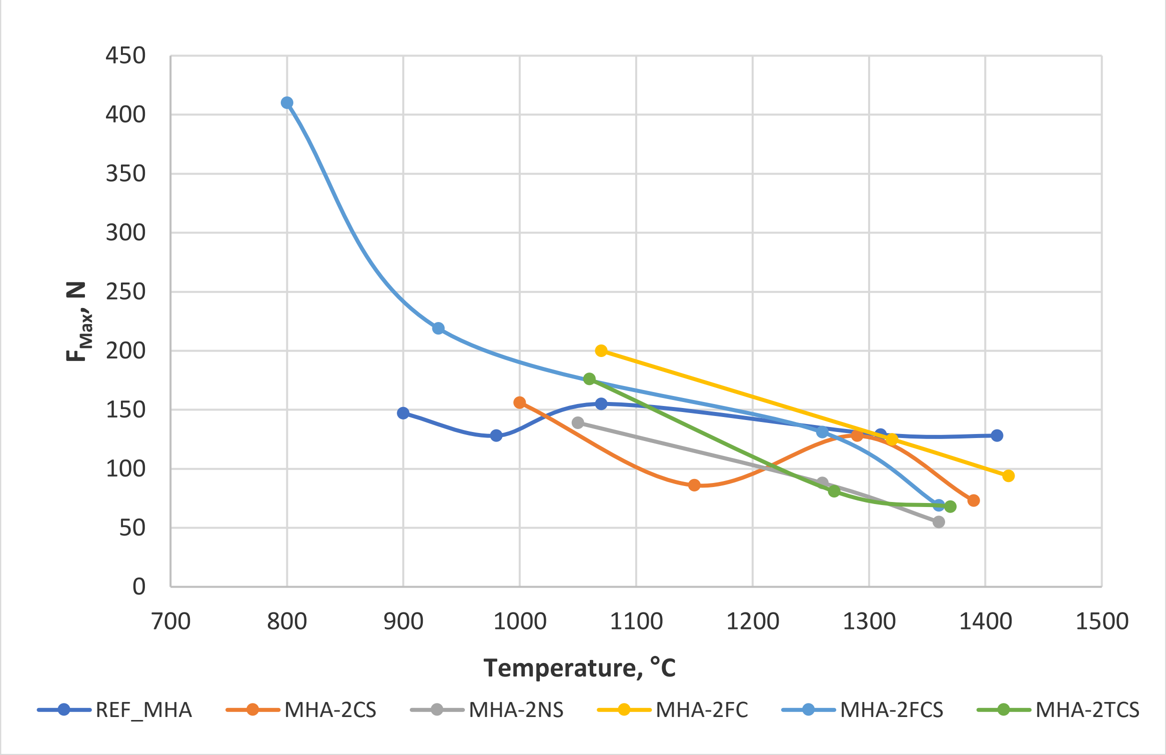

b)

Fig. II.55: Evolution of the (a) fracture energy G and (b) bending force F_{max} as a function of the temperature (the maximum temperature corresponds to $T_{0,5}$ for each material) for the model refractory castables MHA.

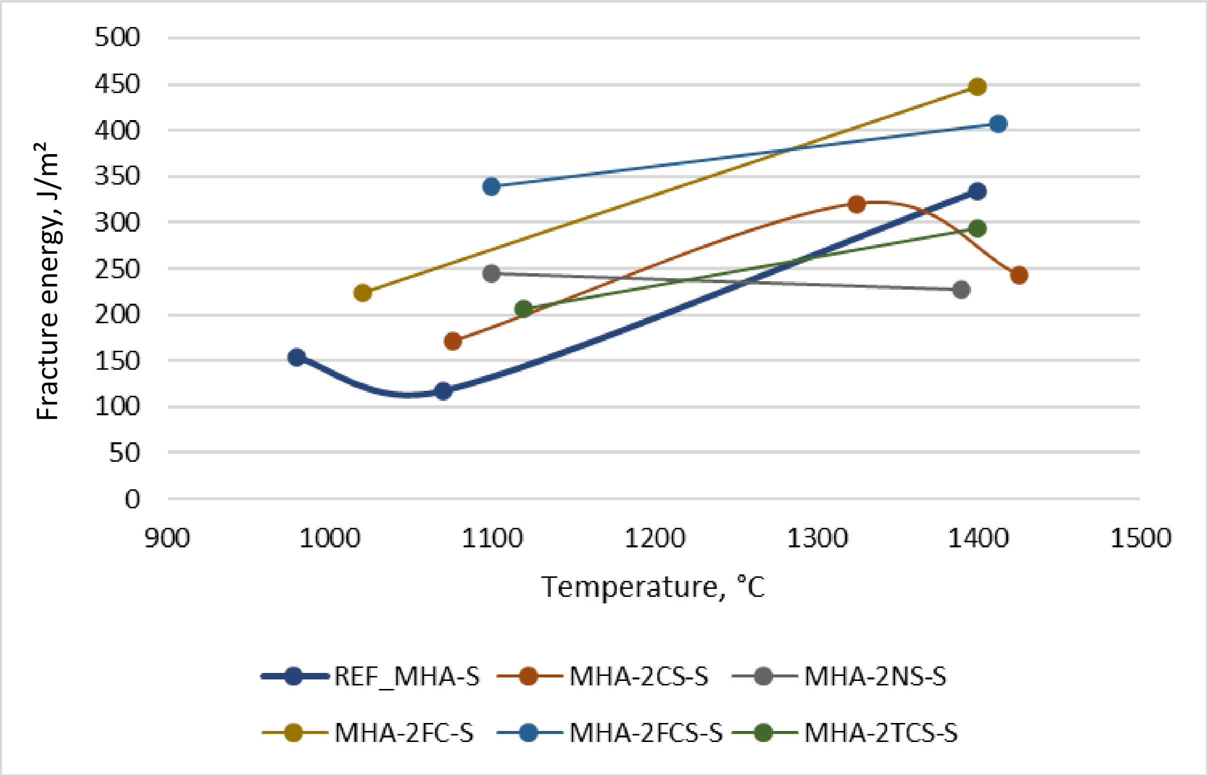

a)

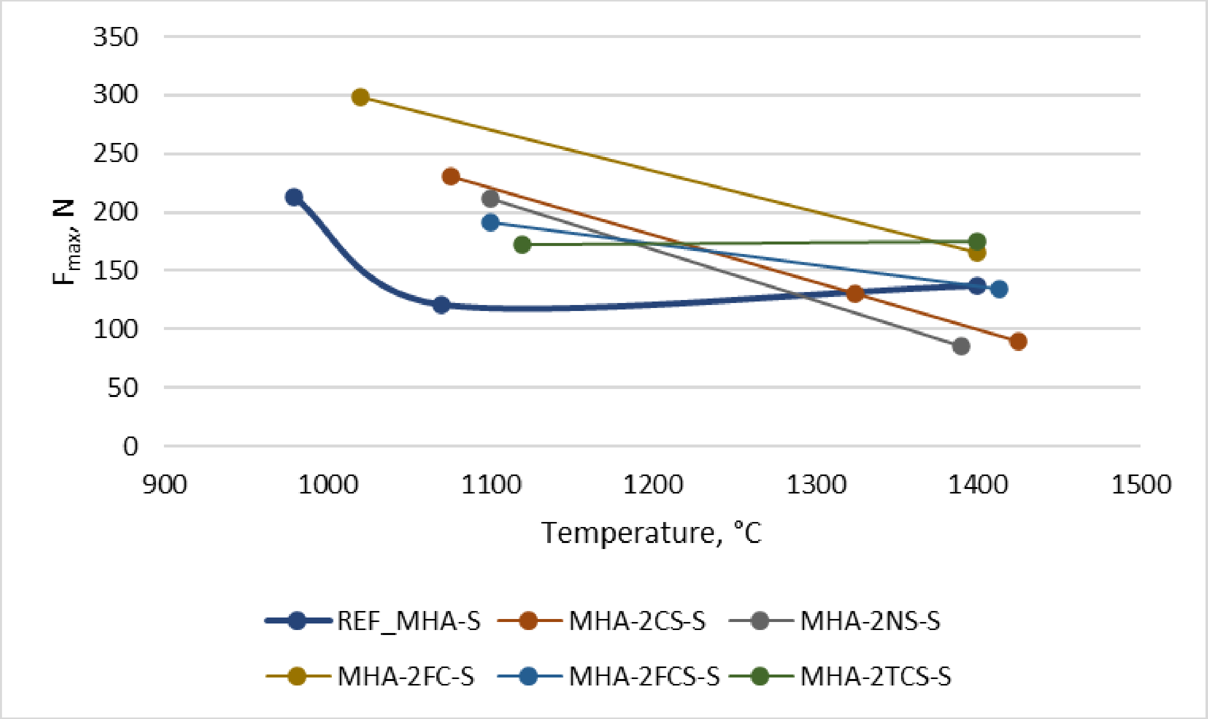

b)

Fig. II.56: Evolution of the (a) fracture energy G and (b) bending force F_{max} as a function of the temperature (the maximum temperature corresponds to $T_{0,5}$ for each material) for the spinel forming model refractory castables MHA-S.

3.5.5 Modulus of rupture

Measurements were performed at temperature selected according to the refractoriness under load measurements results. The following temperatures were accordingly implemented: T_0, $T_{0,5}$-100 °C, $T_{0.5}$. No measurements were performed for temperature $T_{0.5}$ higher than 1450 °C as it exceeded the maximum temperature allowed by the testing machine. The results are presented in Table II.7 and Figure II.57 for model refractory castables MHA and Figure II.58 for the spinel forming model refractory castables MHA-S.

The results of the modulus of rupture determination are consistent with the results obtained from fracture energy determination. For the model refractory castables MHA, only the model castable MHA-2FC achieved similar bending strength as the reference model refractory castable at $T_{0.5}$ temperature. The remaining results were systematically lower (Fig. II.57). In the case of the spinel forming model refractory castables MHA-S, measurements were made only up to the temperature $T_{0.5}$-100 °C (the temperature $T_{0.5}$ exceeded the maximal allowed temperature of the testing machine). Again, the findings from the fracture energy study were confirmed. Below temperature $T_{0.5}$, spinel forming refractory castable MHA-2FC-S was even characterized by a greater bending strength than the spinel forming reference refractory castable (Figure II.58). This represented an interesting indication that impurities could even improve the thermomechanical properties of refractory materials.

Tab. II.7: Modulus of rupture versus temperature.

Model castable	**Temperature. °C**	**Modulus of rupturę $\sigma_{Fśr.}$ MPa**	Model castable	**Temperature. °C**	**Modulus of rupture $\sigma_{Fśr.}$ MPa**
MHA_REF	1070	2,0	MHA_REF-S	900	3,7
	1310	1,9		1070	2,0
	1410	4,0		1400	5,3
MHA_2FCS	930	3,1	MHA_2FCS-S	1100	2,1
	1260	1,4		1413	4,3
	1370	2,7			
MHA_2NS	1050	2,1	MHA_2NS-S	1100	1,9
	1260	1,4		1393	3,3
	1370	1,4			
MHA_2CS	1150	1,2	MHA_2CS-S	1076	3,2
	1290	1,5		1325	3,2
	1390	2,2		1425	4,4
MHA_2TCS	1060	1,3	MHA_2TCS-S	1120	1,9
	1270	2,3		1400	3,4
	1370	2,1			
MHA_2FC	1070	1,7	MHA_2FC-S	1020	3,5
	1320	3,2		1400	5,7
	1420	4,2			

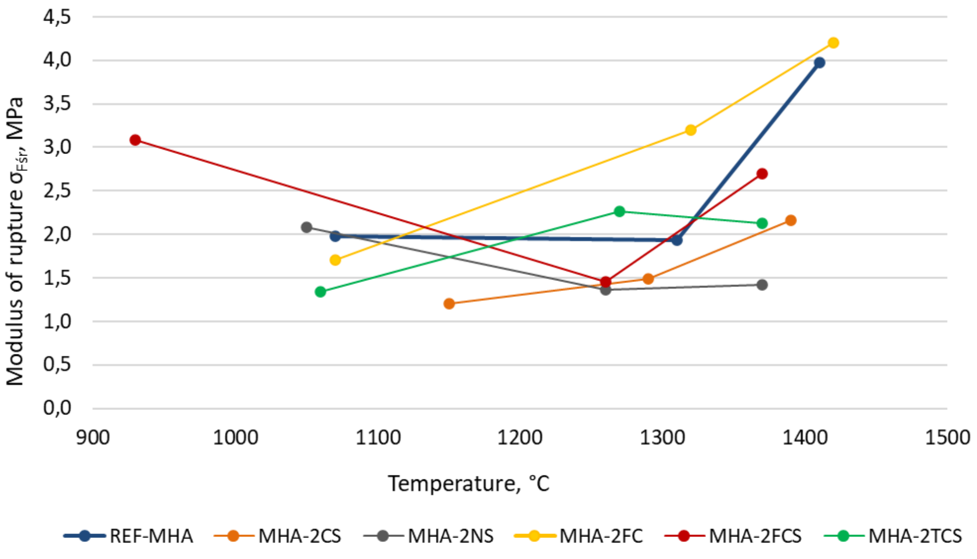

Fig. II.57: Modulus of rupture versus temperature (the maximum temperature corresponds to $T_{0,5}$) for the model refractory castables MHA.

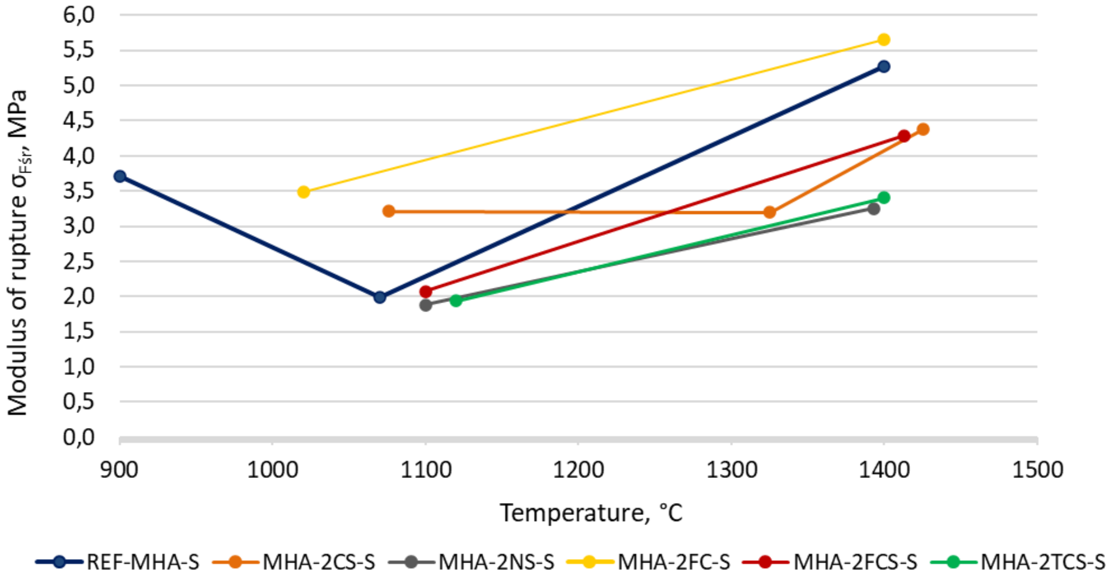

Fig. II.58: Modulus of rupture versus temperature (the maximum temperature corresponds to $T_{0.5}$ or $T_{0.5}$-100 °C) for the spinel forming model refractory castables MHA.

3.5.6 High temperature phase transformations

High-temperature diffractometry (HT-XRD) was performed on the precursors produced by Hochschule Koblenz (2CS, 2FC, 2FCS, 2NS, 2TCS) as well as on mixtures of precursors with spinel-forming additive (MgO) and Al_2O_3 fine fraction (2CS-S, 2FC-S, 2FCS-S, 2NS-S, 2TCS-S matrix) with compositions similar to those of the model refractory castables matrix. These samples were purposely not enriched with coarse Al_2O_3 fractions to avoid dilution and increase the detection of possible chemical reactions and phase changes. Incidentally, the coarse fraction of industrial refractory materials is less reactive, and microstructural changes tend to occur first within the matrix (fine fractions) in service. All investigated samples contained a large excess of free and active Al_2O_3, as in the composition of the model refractory castables themselves. The goal was to investigate thermochemical stability, identify chemical reactions and phase transformations occurring in the temperature range 25 °C to $T_{0,5}$- 100 °C (determined in RuL measurements as also applied during RFDA measurements). An equal step of temperature progression was not used in these studies. Instead, specific temperatures for producing diffractograms were selected based on the results of research on temperature changes in Young's modulus and damping presented in chapter 3.5.9 “Elastic properties under cyclic heating and cooling versus temperature by Resonant Frequencies and Damping Analysis (RFDA)”. This resulted in differences in the selection of individual temperatures for each sample. The observed changes, in particular damping, are assumed to be related to phase transformations taking place in the refractory castable’s matrix as well as other microstructural changes in the materials. Results from the HT-XRD investigations should hence help to explain the changes in damping and frequency of free vibrations (Young's modulus) with temperature during heating and cooling of the investigated test pieces. In RFDA measurements, test pieces were heated for 2 hours at the maximum test temperature before cooling. The same approach was used in HT-XRD investigations. Three diffractograms were taken at the maximum measurement temperature. The first one after reaching the maximum temperature, the second one after one hour and the third one after two hours, thus collecting kinetic data of the transformations taking place in the model refractory castables matrix.

3.5.6.1. Model refractory castables MHA

Changes in phase composition with temperature are shown in Figures II.59 to II.63.

No phase transitions were identified in the four precursors: 2CS, 2FC, 2FCS, 2TCS, which indicates good thermochemical stability of the precursors and that the thermodynamic equilibrium was reached at the stage of their production. Only for the precursor 2NS, at a temperature of approximately 900 °C, a polymorphic transformation of nepheline was observed. Napheline crystallizing in the P 32 space group (hexagonal), which was present in a larger share at low temperature, was transformed into the P 63 space group (also hexagonal). A trace amount of mullite was also identified in this precursor (less than 0,1% at all tested temperatures).

The MHA-REF reference refractory castable contained only alumina in the form of corundum (87,2 wt.-%) and β-Al_2O_3 (2.8 wt.-%). During heating to 1500 °C, the only change observed was the disappearance of β-Al_2O_3 at a temperature between 1150 °C and 1200 °C.

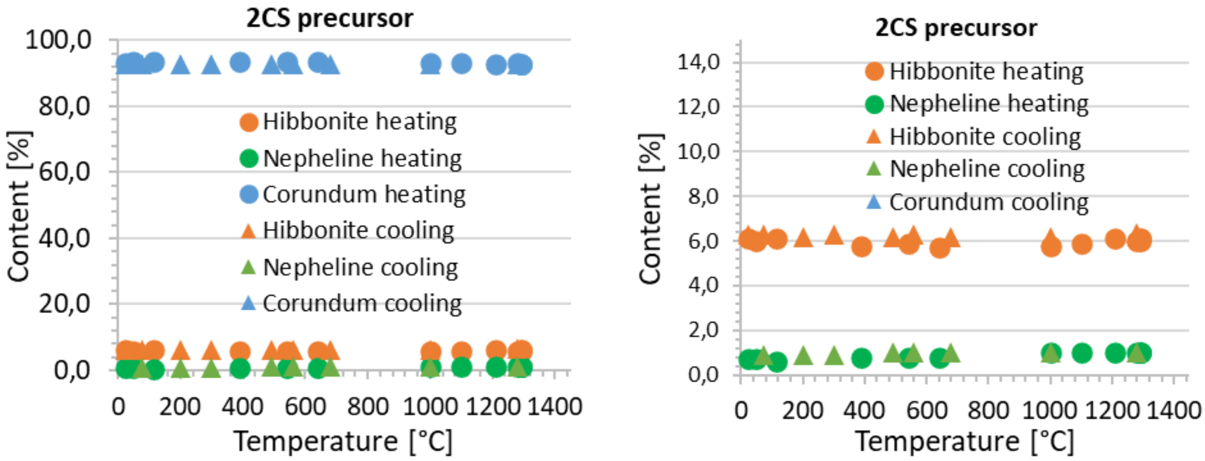

Fig. II.59: Evolution of the phase composition of the 2CS precursor up to a temperature of 1290 °C. The diagram on the right provides a zoom on the smaller shares.

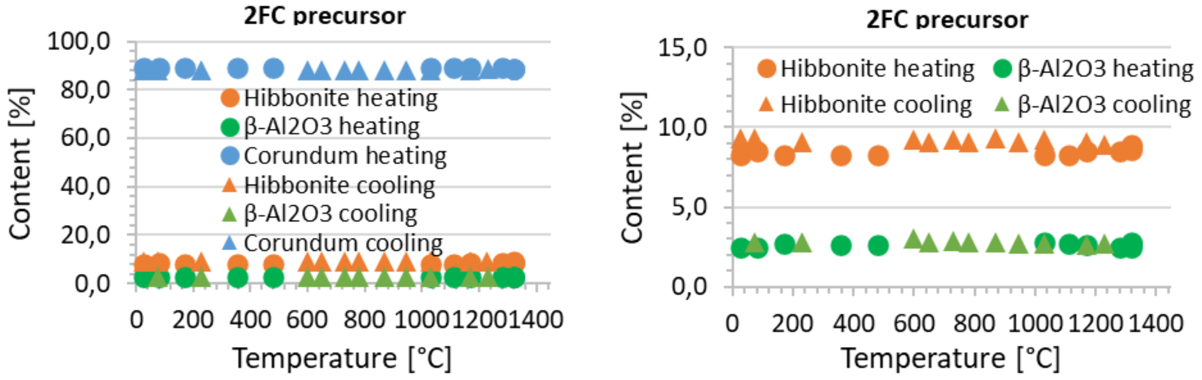

Fig. II.60: Evolution of the phase composition of the 2FC precursor up to a temperature of 1320 °C. The diagram on the right provides a zoom on the smaller shares.

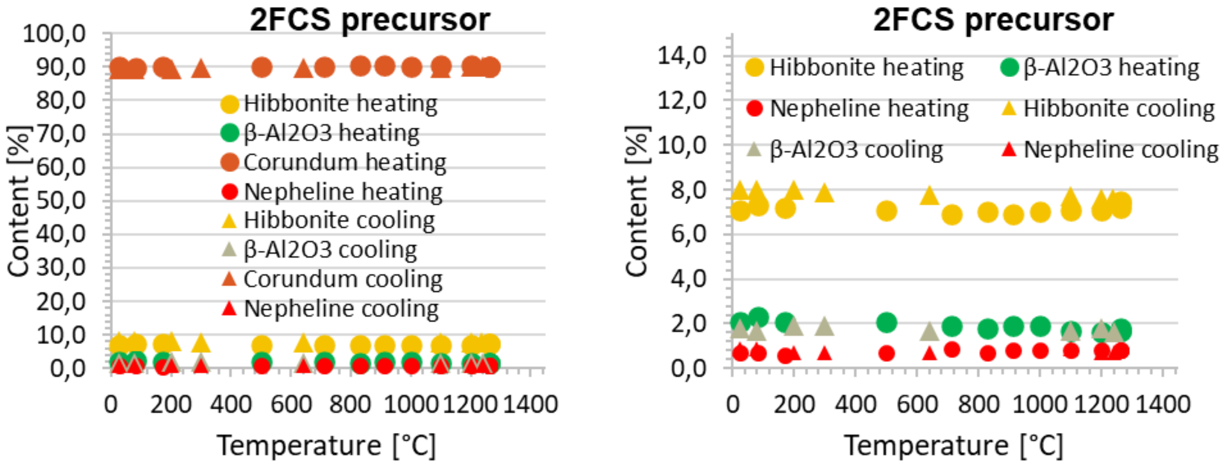

Fig. II.61: Evolution of the phase composition of the 2FCS precursor up to a temperature of 1260 °C. The diagram on the right provides a zoom on the smaller shares.

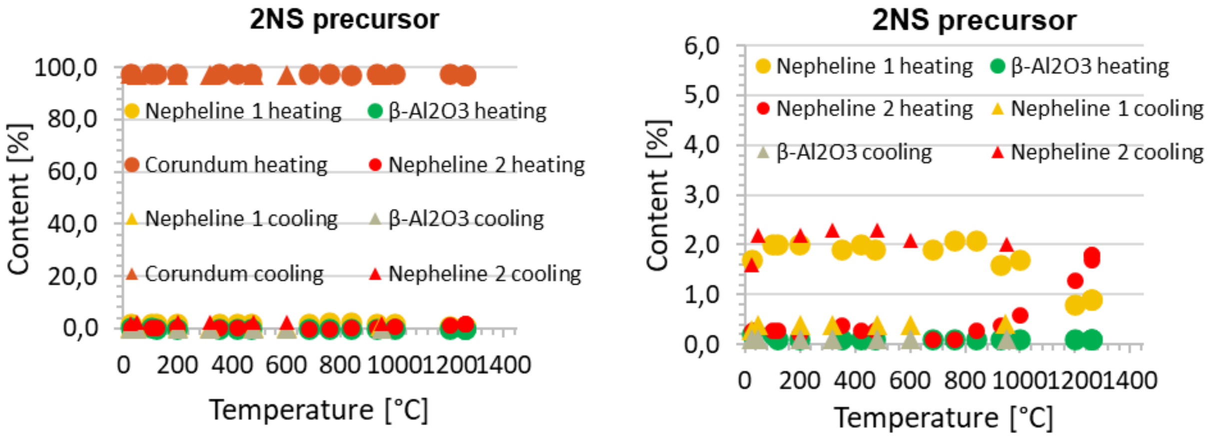

Fig. II.62: Evolution of the phase composition of the 2NS precursor up to a temperature of 1260 °C. The diagram on the right provides a zoom on the smaller shares.

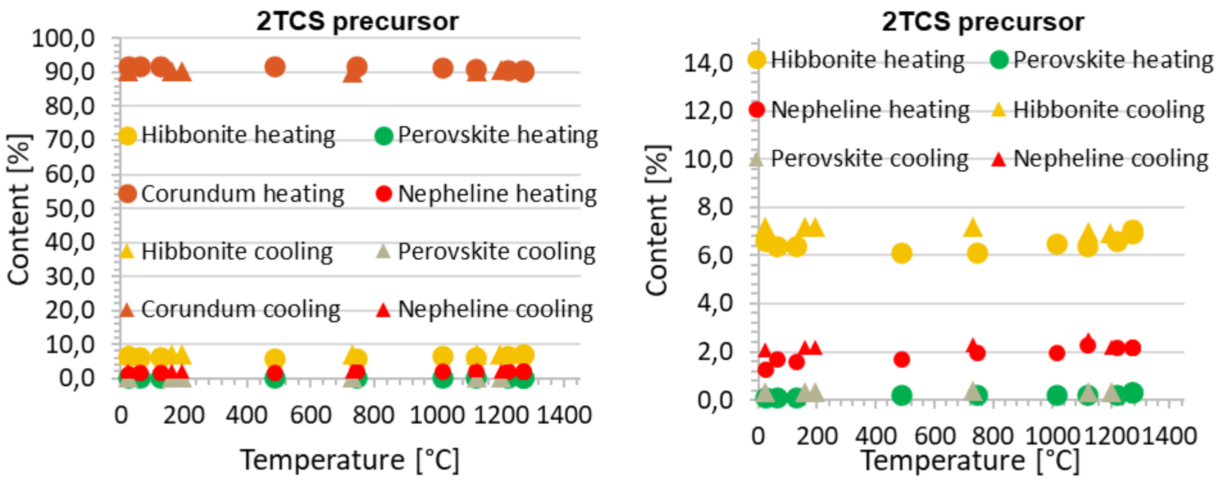

Fig. II.63: Evolution of the phase composition of the 2TCS precursor up to a temperature of 1270 °C. The diagram on the right provides a zoom on the smaller shares.

3.5.6.2. Model refractory castables MHA-S

For the model spinel forming refractory castable matrix composition (2CS-S, 2FC-S, 2FCS-S, 2NS-S, 2TCS-S matrix), mainly spinel synthesis was identified at temperatures from 1320 °C to 1420 °C, depending on the chemical composition of the matrix (Figures II.64 to II.69). For the 2CS-S matrix (Fig. II.64) and 2FC matrix (Fig. II.65), spinel was formed at 1320 °C, in 2FCS-S (Fig. II.66) matrix at 1420 °C, in 2NS-S (Fig. II.67) matrix at 1390 °C, and in 2TCS-S matrix at 1370 °C (Fig. II.68). Moreover, for all matrix composition, the XRD pics characteristic of the presence of corundum (corundum 2) were slightly shift towards low 2Θ angles. This is most likely related to differences in the grain size of corundum and the impurities dissolved in it. The samples were prepared by adding an appropriate amount of pure corundum raw material and active alumina to the precursors. The “added corundum” is visible at low temperatures, and in the 2CS, 2FC and 2FCS matrix, its disappearance correlates with the spinel formation temperatures. β-Al_2O_3 remains at a similar level over the entire range of investigated temperatures. In each case, the maximum test temperature did not exceed the stability range of β-Al_2O_3. For the 2NS-S matrix, similarly to the 2NS precursor, the Nepheline polymorphic transformation was identified. If hibonite (CA_6) was present in the investigated composition, its share did not change as a result of heating to the maximum test temperature.

In each case, despite being heated at the maximum measurement temperature (100 °C below $T_{0.5}$), the periclase had not fully reacted with Al_2O_3 and the maximum theoretical amount of spinel was not formed. This happened even for the 2FC-S matrix annealed at 1440 °C, the 2FCS-S matrix annealed at 1420 °C, and the 2TCS-S matrix annealed at 1400 °C for two hours. These temperatures were high enough to produce significant amounts of spinel. Meanwhile, for the 2FC-S matrix and 2FCS-S matrix, after two hours of heating, only 5 % of spinel was formed, and about 11 % of periclase remained unreacted. The highest amount of spinel was formed in the 2TCS-S matrix composition, with approximately 17 %, while the lowest amount of periclase remained, 2.5 %.

The in-situ formation of spinel without the involvement of impurities was followed with a measurement on the model reference spinel forming refractory castable MHA_REF-S matrix composition (Fig. II.69). Al-rich spinel begins to form at 1150 °C and is designated Spinel (Al rich). Mg-rich spinel begins to form at 1200 °C (Spinel (Mg rich)). At a temperature of 1500 °C, another Mg-rich spinel appears with a composition even richer in Mg. The composition of spinel enriched in Al or Mg is indicated by the unit cell parameters described in the next section. The mechanism of spinel formation in situ is a diffusion process well described in the literature [18-19]. According to described mechanism [18], the solid state spinel formation is carried out through the Al^{3+} and Mg^{2+} ions counter-diffusion which is well demonstrated in microscopic investigation described in chapter 3.5.8 “Microstructural investigation of model castables MHA and MHA-S”. The formation of spinels takes place at the MgO-$MgAl_2O_4$ and Al_2O_3-$MgAl_2O_4$ boundaries. In order to keep the electro-neutrality, Mg^{2+} ions diffuse to the alumina, whereas Al^{3+} ions diffuse to the magnesia grains. Due to this the reaction between MgO and Al_2O_3 results in the formation of Mg-rich $Mg_{1+x}Al_{2-x}O_4$ layer at the MgO- $MgAl_2O_4$ boundary, and Al-rich $Mg_{1-x}Al_{2+x}O_4$ layer at the Al_2O_3-$MgAl_2O_4$ boundary. Theoretically the layers thickness ratio between the formed spinel at the alumina and magnesia sides is 3:1, indicating a higher spinel formation rate at the alumina boundary. However, in the present investigation, the ratio of Al-rich to Mg-rich spinel was approximately 6:1 at 1500 °C (Fig. II.69).

This phenomenon was not observed in matrix compositions containing the precursors (2CS-S, 2FC-S, 2FCS-S, 2NS-S, 2TCS-S matrix). Probably because the measurements were carried out to a lower maximum temperature (corresponding to $T_{0.5}$-100 °C). The degree of reaction of MgO and Al_2O_3 under these measurement conditions was lower and only one type of spinel was formed, the most probably rich in Al.

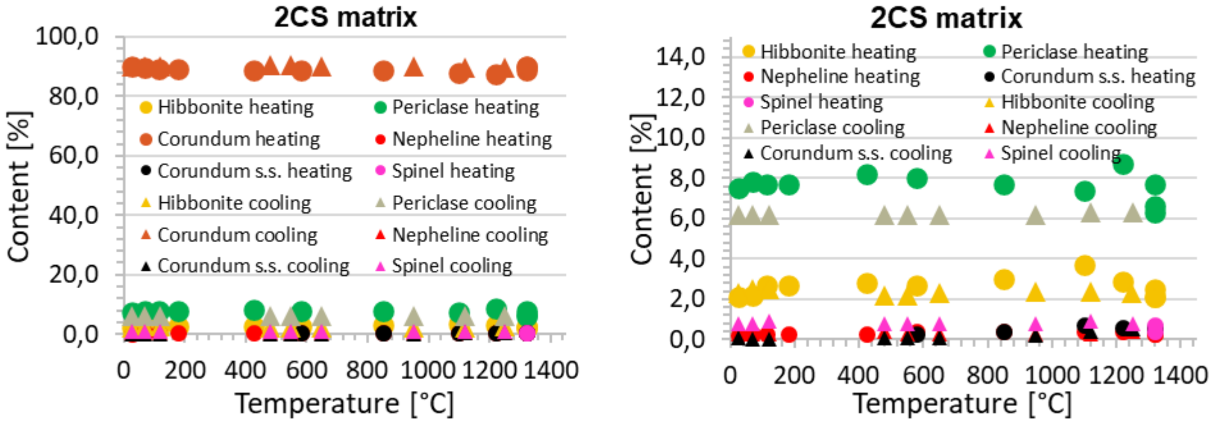

Fig. II.64: Evolution of the phase composition of 2CS-S matrix up to a temperature of 1320 °C. The diagram on the right provides a zoom on the smaller shares.

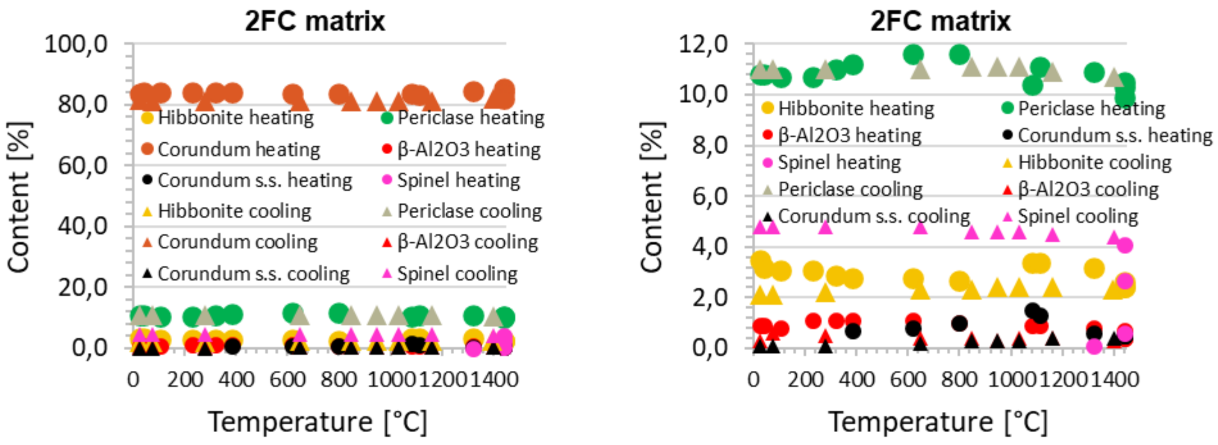

Fig. II.65: Evolution of the phase composition of 2FC-S matrix up to a temperature of 1440 °C. The diagram on the right provides a zoom on the smaller shares.

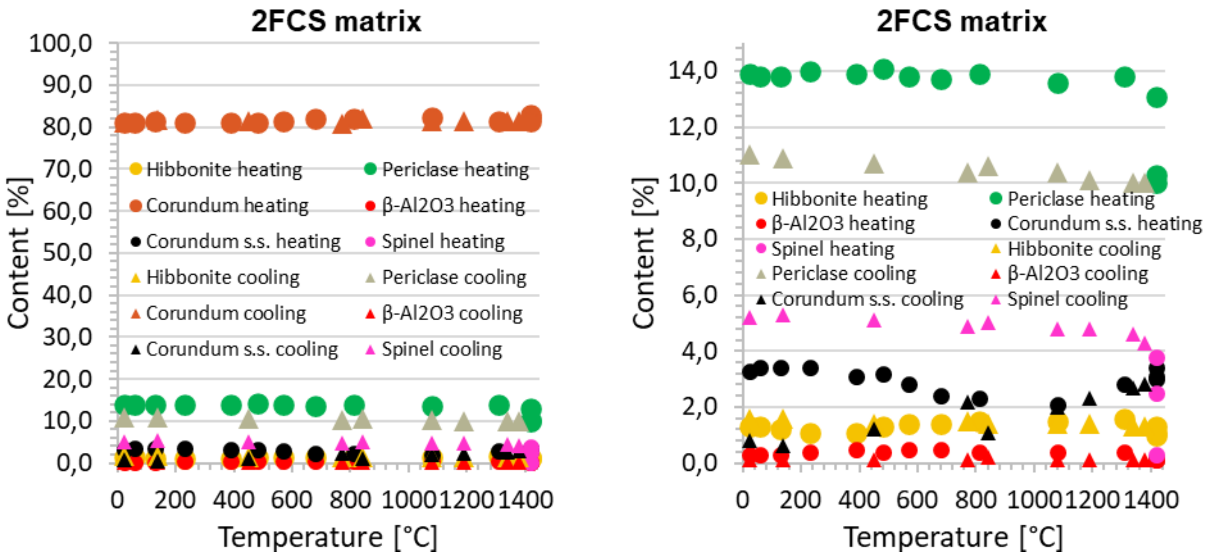

Fig. II.66: Evolution of the phase composition of 2FCS-S matrix up to a temperature of 1420 °C. The diagram on the right provides a zoom on the smaller shares.

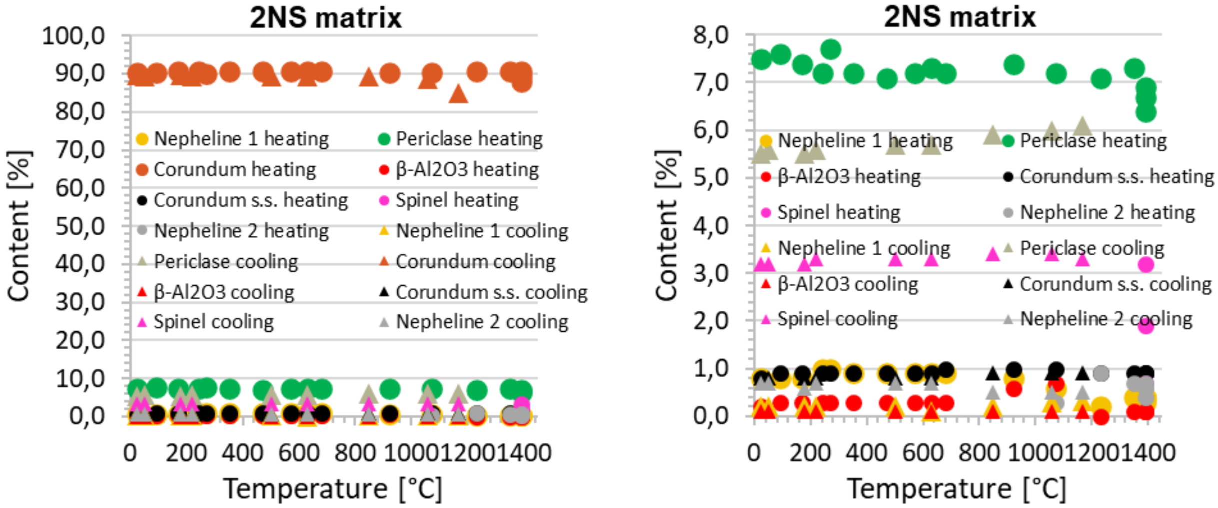

Fig. II.67: Evolution of the phase composition of 2NS-S matrix up to a temperature of 1390 °C. The diagram on the right provides a zoom on the smaller shares.

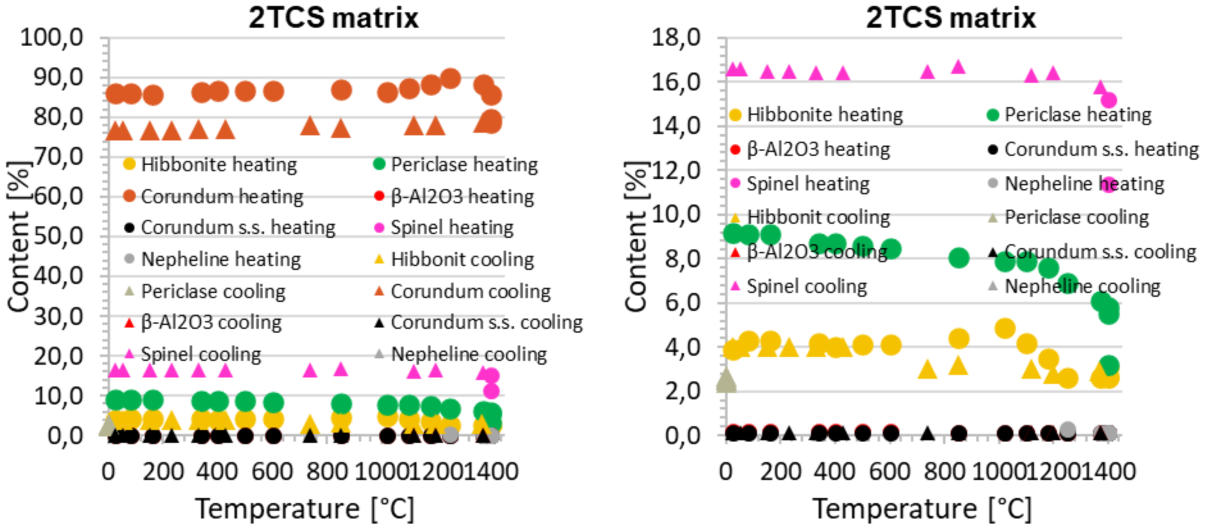

Fig. II.68: Evolution of the phase composition of 2TCS-S matrix up to a temperature of 1400 °C. The diagram on the right provides a zoom on the smaller shares.

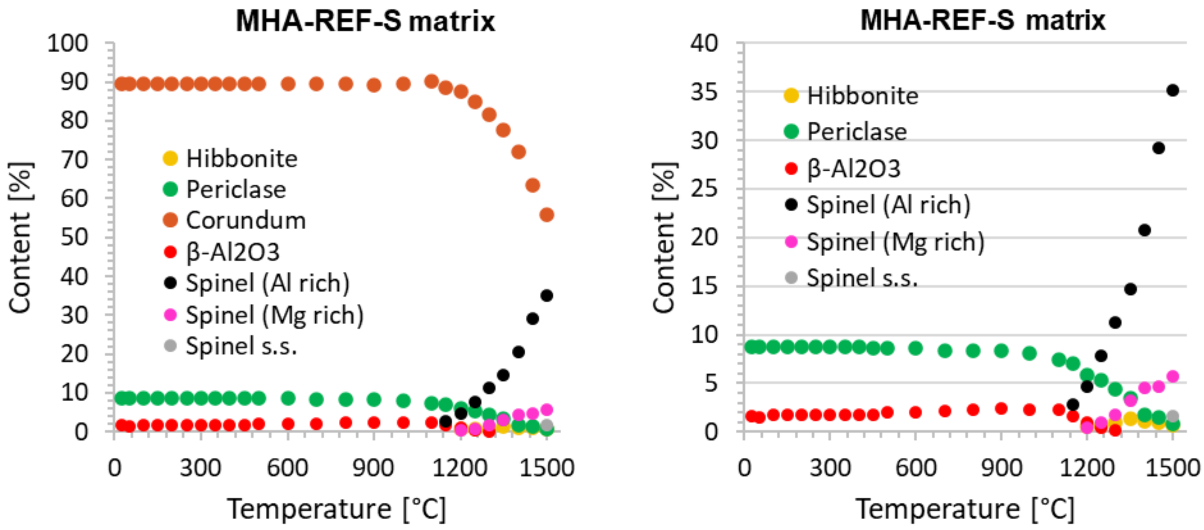

Fig. II.69: Evolution of the phase composition of the model spinel forming reference castable's matrix MHA-REF-S up to a temperature of 1500 °C. The diagram on the right provides a zoom on the smaller shares.

3.5.7 Thermal expansion of corundum. spinel and other identified phases

The thermal expansion of the phases identified during the HT-XRD measurements was determined. Because of the used method, based on the determination of unit cell parameters as a function of temperature (X-ray dilatometry) and Rietveld analysis, it was possible to investigate thermal expansion only in phases present in larger quantities. The advantage of the used method is the ability to determine the thermal expansion coefficients of individual phases constituting a given material separately, instead of the material as a whole, and thus refer to the mutual interactions of individual phases of the material with each other. Differences in the thermal expansion of individual phases are responsible for changing the state of internal stresses in the material as the temperature increases or decreases and may be the reason for the formation or closing of microcracks in the material, thus influencing the formation of the microstructure of the material. Disadvantage of this method is that phases occurring in trace could not be investigated due to the high measurement uncertainty and uncertainty of their identification. Unit cell parameters as a function of temperature were determined for: corundum, hibbonite, nepheline, periclase and spinel solid solutions. The parameters of the corundum unit cell and spinel solid solutions were determined on the reference spinel forming model refractory castable MHA-REF-S matrix formulation. For the other considered phases, formulation with the highest possible share were selected. For hibbonite and nepheline, it was the 2TCS precursor, for β-Al_2O_3 it was the 2FC precursor, and for periclase it was a 2CS matrix formulation. The results are presented in Figures II.70 to II.74.

For hibonite, corundum, nepheline and β-Al_2O_3, which belong to the hexagonal crystallographic system, the temperature dependencies of the a_0 and c_0 parameters were determined. For phases from the regular system: periclase and spinel, the parameter a_0 was assessed. The determined parameters of the corundum unit cell and thermal expansion are consistent with the literature data [19]. The thermal expansion of corundum in the temperature range of 25 °C to 1500 °C (close to

$T_{0.5}$-100 °C) varies from $4{,}2\cdot10^{-6}$ K^{-1} (25 °C) to $9{,}9\cdot10^{-6}$ K^{-1} for the a_0 parameter and in the range of $4{,}9\cdot10^{-6}$ K^{-1} (25 °C) to $11{,}0\cdot10^{-6}$ K^{-1} for parameter c_0. In hibonite, they vary in the temperature range 25 °C to $T_{0.5\text{-}100}$ from $4{,}9\cdot10^{-6}$ K^{-1} to $6{,}4\cdot10^{-6}$ K^{-1} for a_0 and from $8{,}6\cdot10^{-6}$ K^{-1} to $9{,}9\cdot10^{-6}$ K^{-1} for c_0. In nepheline from $6{,}4\cdot10^{-6}$ K^{-1} to $7{,}5\cdot10^{-6}$ K^{-1} for a_0 and $5{,}4\cdot10^{-6}$ K^{-1} to $10{,}7\cdot10^{-6}$ K^{-1} for c_0, and in β-Al_2O_3 from $2{,}2\cdot10^{-6}$ K^{-1} to $5{,}8\cdot10^{-6}$ K^{-1} for a_0 and $2{,}2\cdot10^{-6}$ K^{-1} to $2{,}9\cdot10^{-6}$ K^{-1} for c_0. In periclase, these changes varied between $9{,}5\cdot10^{-6}$ K^{-1} to $11{,}3\cdot10^{-6}$ K^{-1}, in the temperature range from 25 °C to 1500 °C, with values slightly lower than those given in the cited literature [19]. The Al-rich spinel that begins to form at a temperature of 1150 °C begins to shrink with temperature, which is related to the diffusion of Mg^{2+} ions into Al_2O_3. The effective ionic radius of Mg^{2+} is 1,95 Å and the ionic radius of Al^{3+} is 1,77 Å [20]. The deficit of Mg^{2+} ions in the spinel structure causes contraction of the crystal lattice. The difference in the radii of both ions and the amount of Mg deficit in the spinel structure have a stronger effect on the change of the unit cell parameter than thermal expansion. At 1200 °C, the formation of a second Mg-rich spinel was observed. This spinel should form at the MgO-$MgAl_2O_4$ boundary. Its unit cell parameter increases up to 1350 °C, in contrast to Al-rich spinel. This proves that Mg^{2+} ions dissolve in its structure. After exceeding 1350 °C, it also begins to shrink. This can be explained by the equalization of the concentrations of Mg^{2+} and Al^{3+} ions in spinel solid solutions. At 1500 °C, the formation of another solid spinel solution, most likely Mg-rich, was observed, with a unit cell parameter a_0 higher than in solid spinel solutions formed at a lower temperature.

In the light of these findings, changes in the thermal expansion of individual phases during heating and cooling influence the formation and nature of microcracks in the investigated castables.

Comparing the thermal expansion presented in Figures II.70 and II.73 for corundum and periclase it can be deducted that both expand similarly at temperatures close to $T_{0.5}$-100 °C. However, at lower temperatures, periclase is characterized by greater thermal expansion, which should result in an increase in internal stresses in its surroundings. The remaining identified phases: hibbonite, nepheline and β-Al_2O_3 expand at the investigated temperature in a much smaller extent compared to the main phase corundum. They occur in small amounts in the material matrix in a dispersed form. Surrounded by the main phase corundum, with greater thermal expansion, they undergo compression during heating, while during cooling tensile stresses appear at their boundaries.

Summarizing the results of HT-XRD investigations, it can be stated that changes in higher temperatures at which spinel formation in the model spinel-forming refractory castable MHA-S plays an important role in the development of the castables microstructure and affects the observed improvement in thermomechanical properties compared to the model refractory castable MHA without the spinel-forming additive. Due to the achievement of thermodynamic equilibrium for the produced precursors, no phase transformations that could significantly affect the thermomechanical properties were observed in the tested temperature range up to $T_{0.5}$-100 °C. The observed changes should be therefore associated with the appearance of a liquid phase in the investigated model refractory castables (small amounts, which are not visible in the diffractograms) and the formation of a microstructure specific to each of these materials. The observed changes in the microstructure of castables are related to the sintering of the matrix, grain growth and the formation of microcracks, and in the case of the model spinel-forming refractory castable MHA-S, the formation of spinel solid solutions.

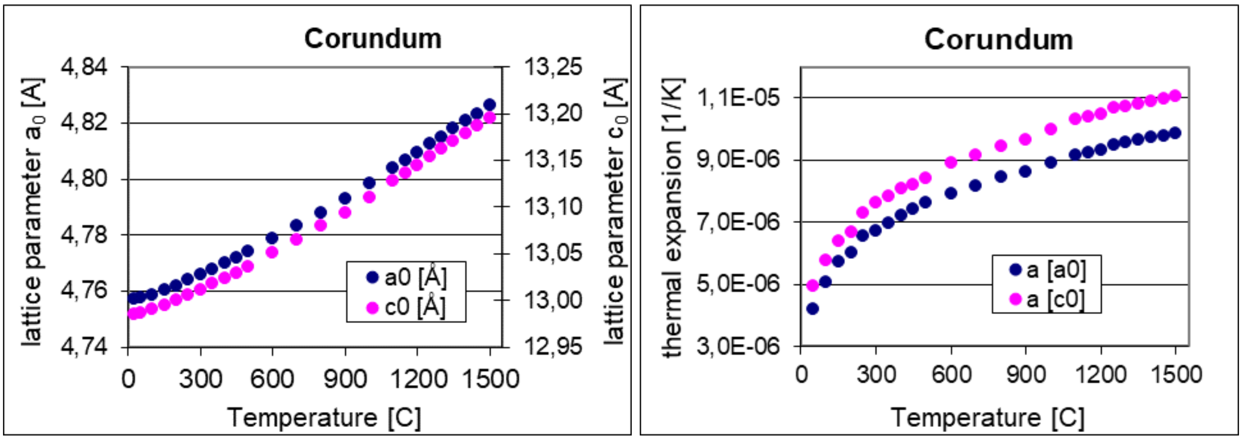

Fig. II.70: Temperature dependency of the corundum crystal lattice parameters a_0 and c_0 (left) and the corresponding thermal expansion (right) determined for the MHA-REF-S formulation.

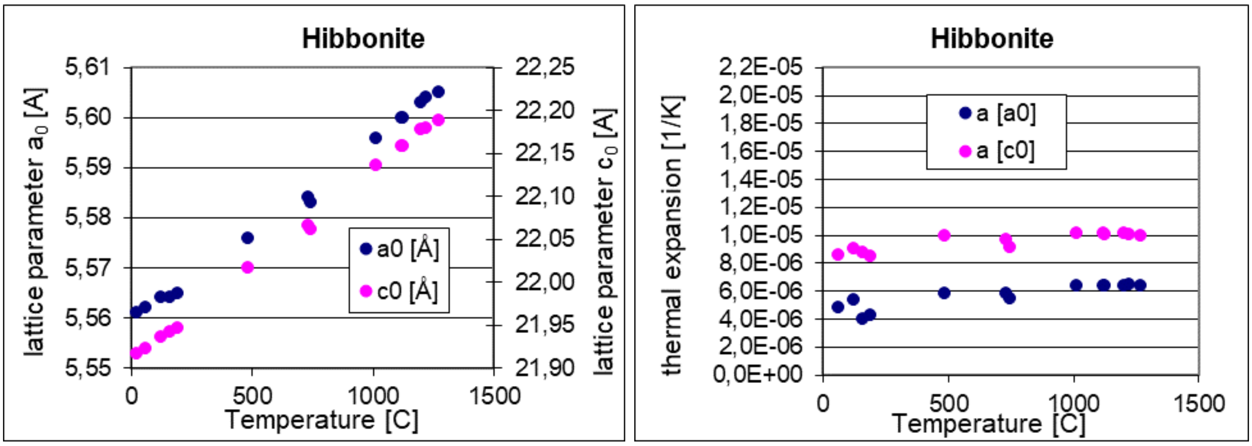

Fig. II.71: Temperature dependency of the hibbonite crystal lattice parameters a_0 and c_0 (left) and the corresponding thermal expansion (right) determined for the 2TCS precursor.

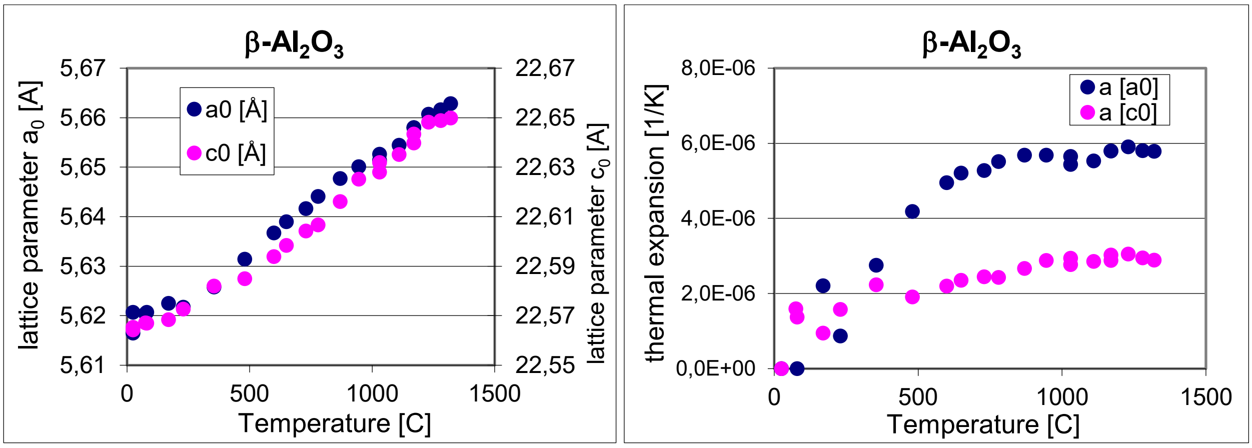

Fig. II.72: Temperature dependency of the β-Al_2O_3 crystal lattice parameters a_0 and c_0 (left) and the corresponding thermal expansion (right) determined for the 2FC precursor.

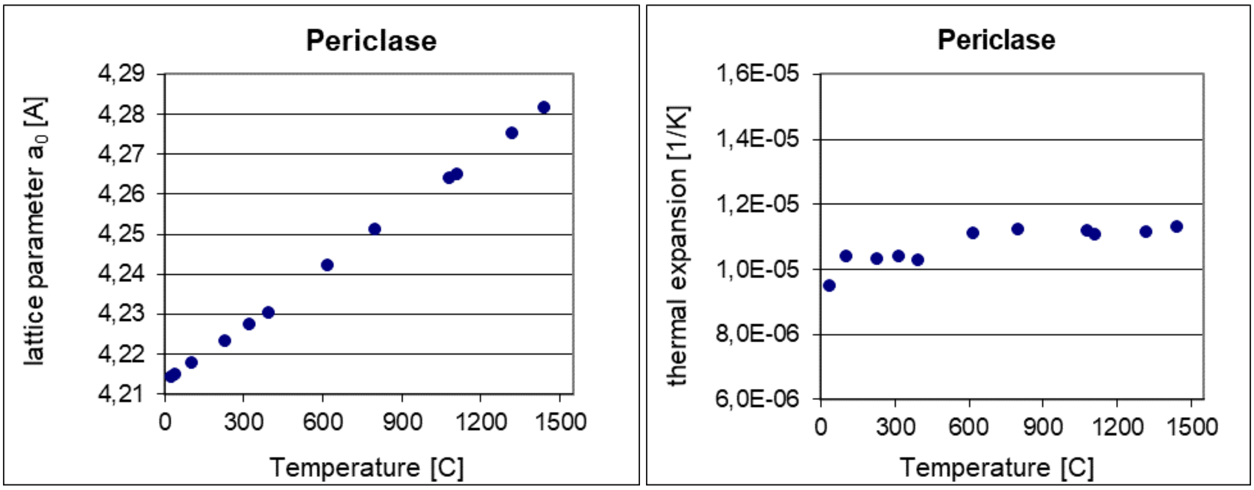

Fig. II.73: Temperature dependency of the periclase crystal lattice parameters a_0 and c_0 (left) and the corresponding thermal expansion (right) determined for the 2FC-S matrix formulation.

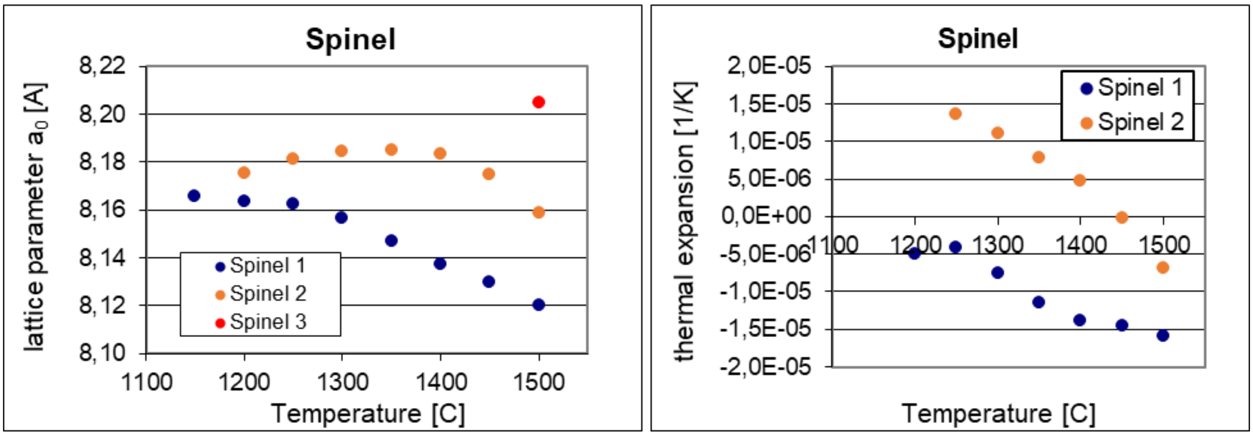

Fig. II.74: Temperature dependency of the spinel crystal lattice parameters a_0 and c_0 (left) and the corresponding thermal expansion (right) determined for the MHA_REF-S matrix formulation.

3.5.8 Microstructural investigation of model castables MHA and MHA-S

Images of the microstructure of the model castables after drying and heat treatment are shown in Figure II.75. In these investigations, changes in the microstructure were observed, mainly related to the formation of microcracks, grain growth and the formation of a bonded microstructure. Microscopic examinations revealed different mechanisms of microcrack formation for different materials: intergranular, trans-crystalline and mixed, accompanying the growth of corundum crystals and other phases in the matrix as well as the evolution of the microstructure more generally. Table II.8 shows a subjective description of the characteristics of the observed microcracks. It was also observed that the introduction of a spinel-forming additive to the material (model castable MHA-S) had a significant impact on the microstructure evolution of the castables. In all cases a significantly smaller number of microcracks were found compared to materials without such an addition.

Subjecting the materials to the thermal treatment also initiated the formation of intergranular bonds, an example of which can be the comparison of the microstructure of the MHA-2NS test piece after drying and after firing (Figures II.76 and II.77). Comparing both of these microstructure images, it can be seen that the fine, uniformly dispersed particles surrounding the finer grains visible in the material after drying disappear as a result of heat treatment. The grains grow and a clearer boundary between individual grains is created. Similar behaviour was also observed for the other materials considered (Fig. II.77).

Model castable	**SEM observation**	
	After drying	**After thermal treatment**
MHA-REF	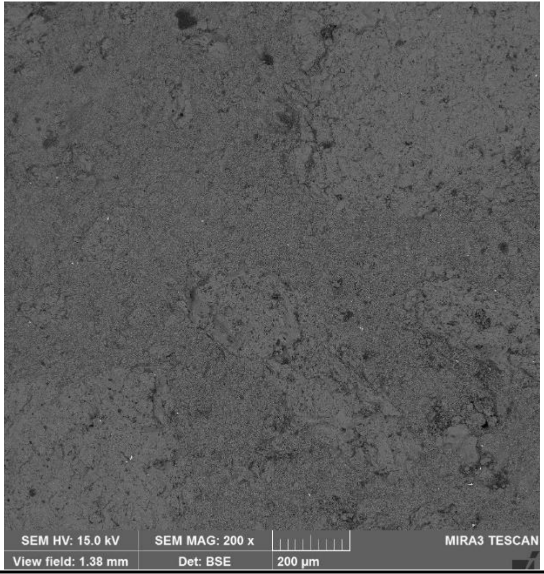	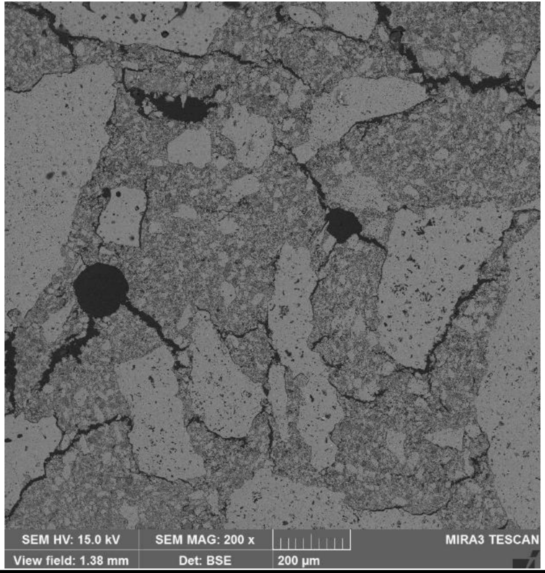
MHA-2CS	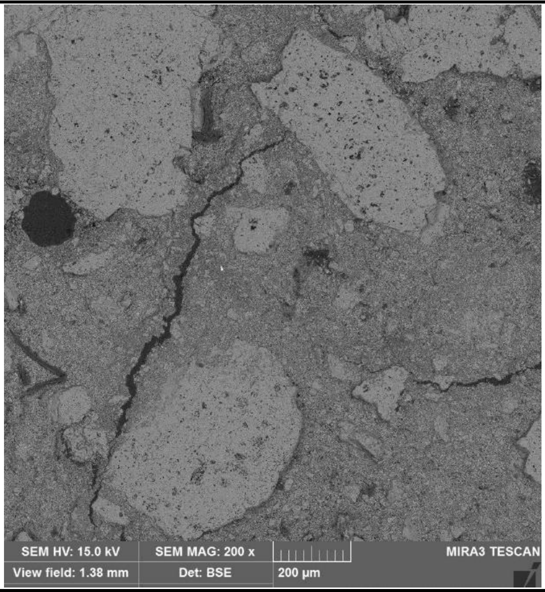	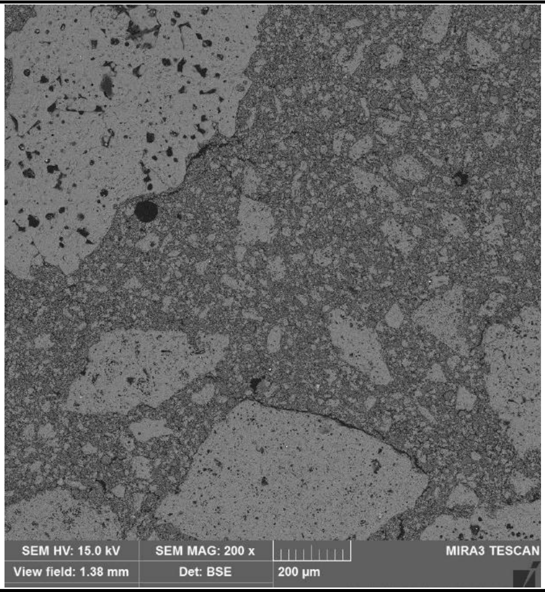
MHA-2NS	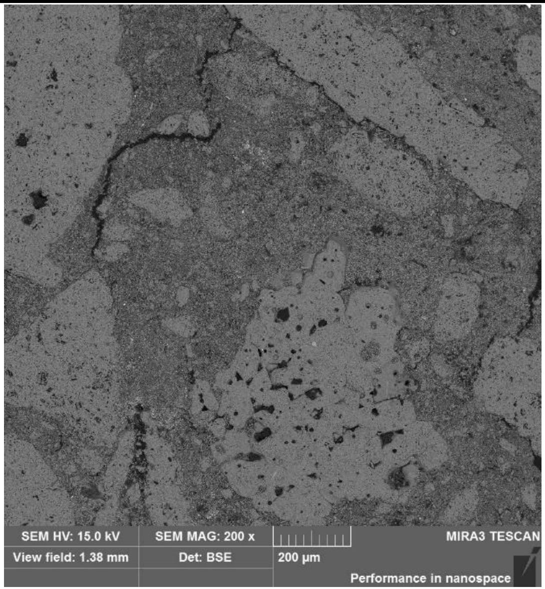	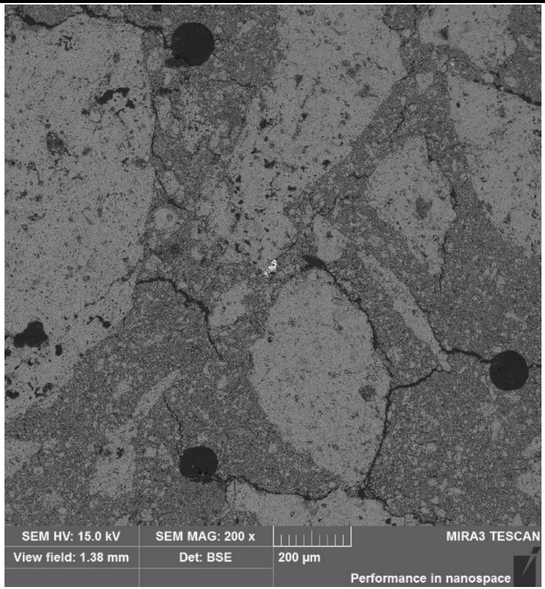

MHA-2FC

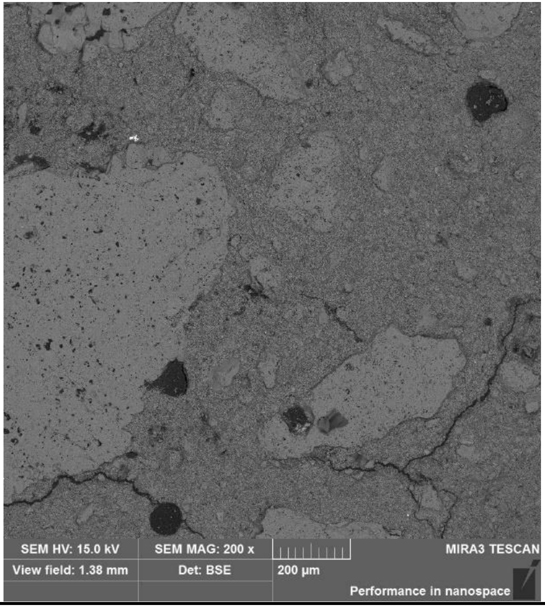

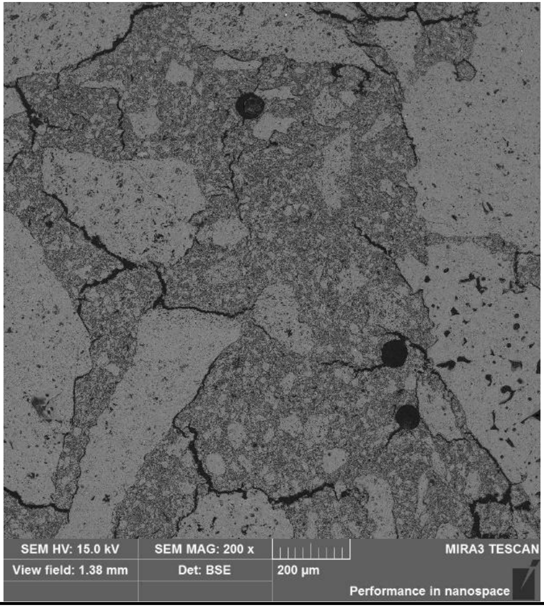

MHA-2FCS

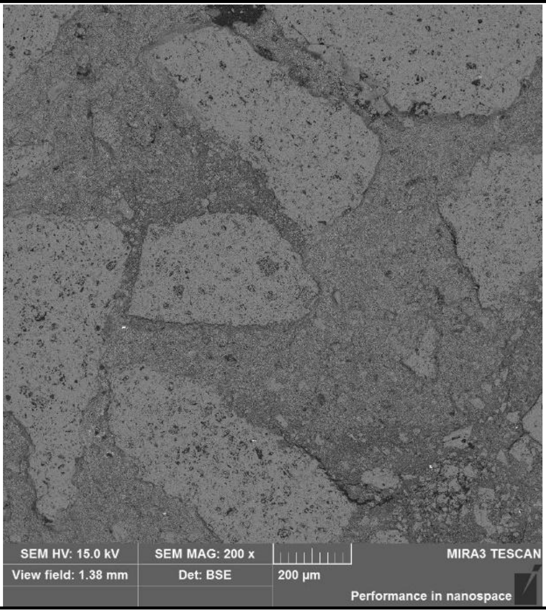

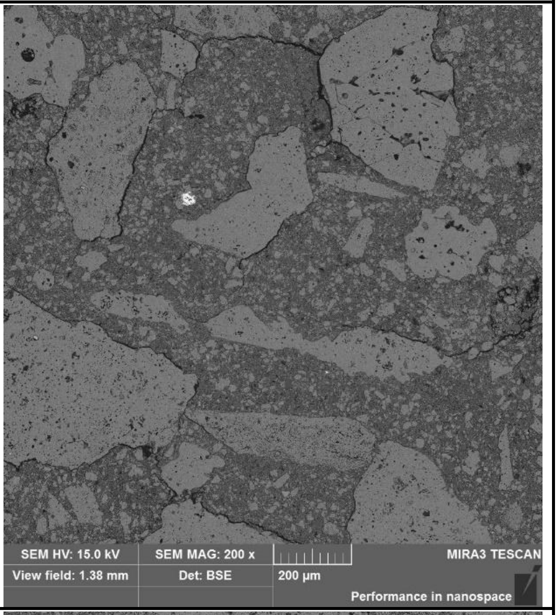

MHA-2TCS

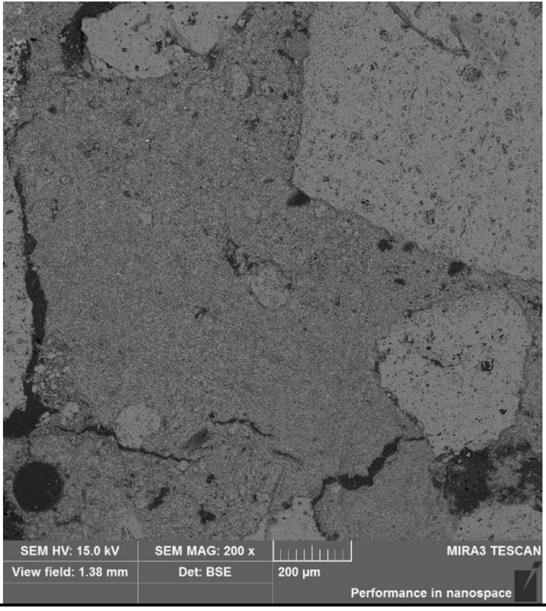

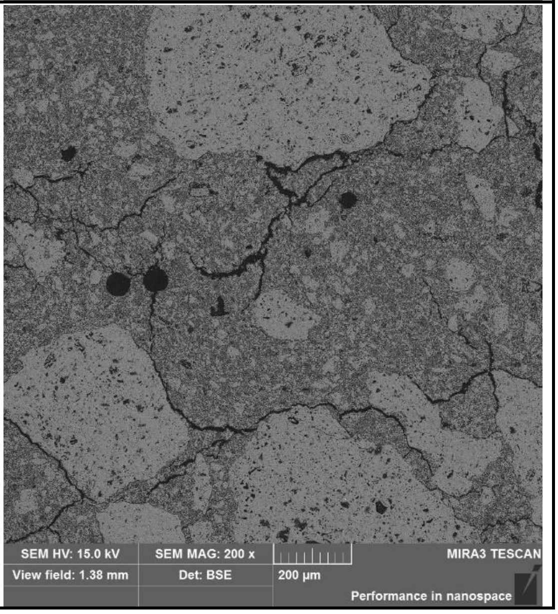

MHA-REF-S

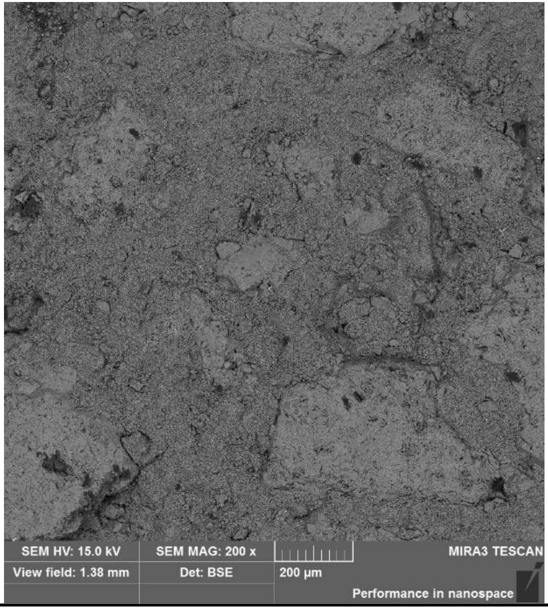

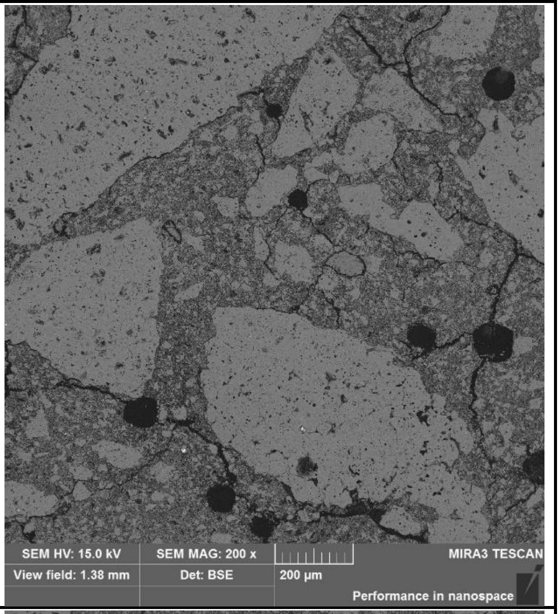

MHA-2CS-S

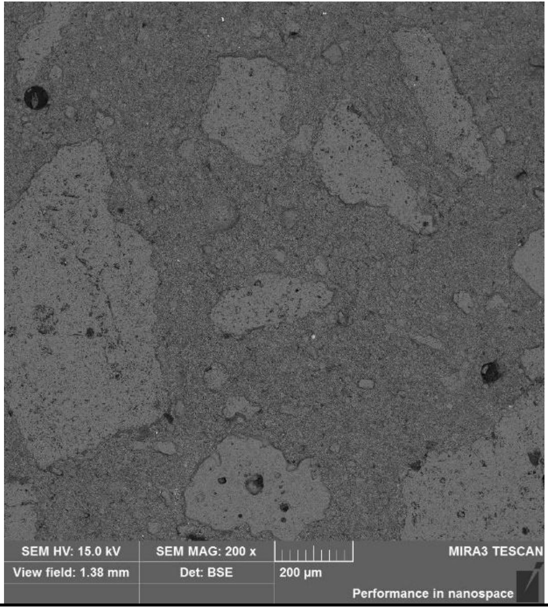

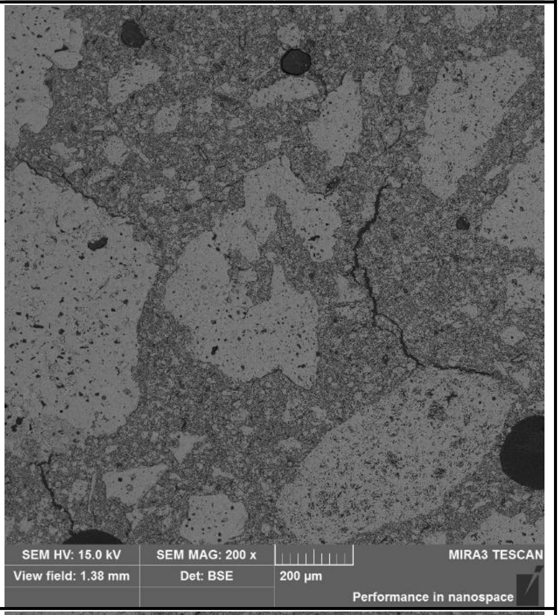

MHA-2NS-S

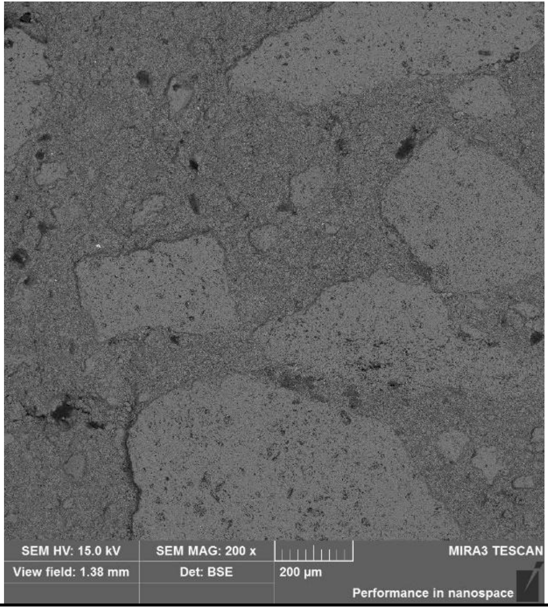

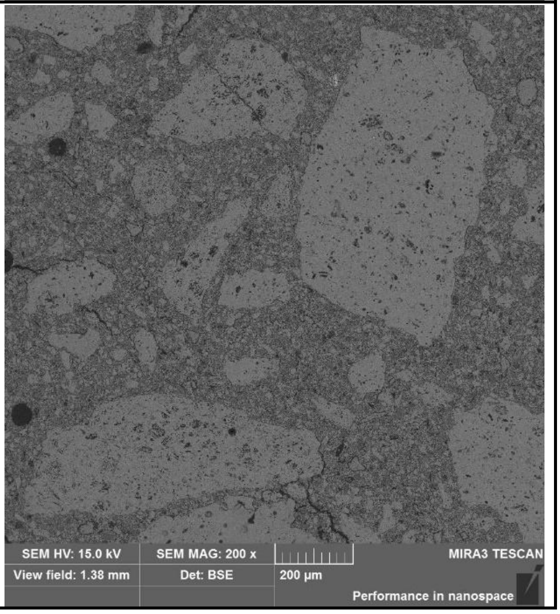

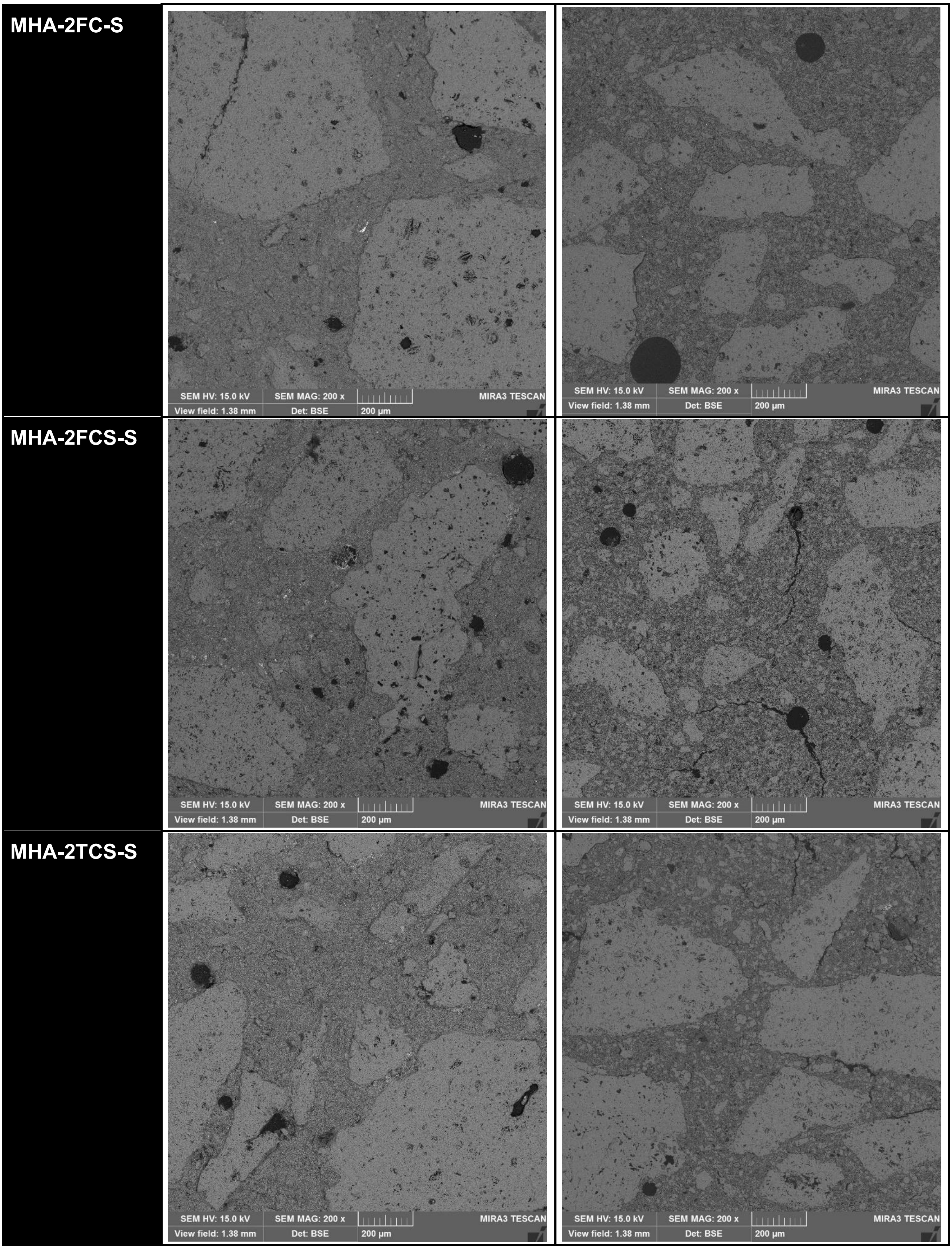

Fig. II.75: SEM images of the investigated model castables, magnification 200x, BSE.

Tab. II.8: Result of a subjective description of micro-cracks formed in the test conditions for castables series MHA and MHA-S.

Model castable	**SEM microcracks observation**	
	After drying	**After RFDA measurement**
MHA-REF	Invisible	Numerous, mostly on the grain/matrix border
MHA-2CS	Numerous, at the grain/matrix interface and through the matrix itself, of various lengths	Single long at the grain/matrix interface and single shorter through the matrix itself
MHA-2NS	Numerous, at the grain/matrix interface and through the matrix itself, of various lengths	Very numerous, on the grain/matrix border and through the matrix itself
MHA-2FC	Numerous, at the grain/matrix interface and through the matrix itself, of various lengths	Very numerous, at the grain/matrix interface and through the matrix itself, often through numerous spherical pores
MHA-2FCS	Single, short	Moderately numerous, mainly at the grain/matrix interface and also visible through the grains themselves
MHA-2TCS	Numerous, at the grain/matrix interface and through the matrix itself, of various lengths	Numerous, mainly through the matrix, sporadically at the grain/matrix boundary
MHA-REF-S	Invisible	Very numerous, at the grain/matrix interface and through the matrix itself, often through numerous
MHA-2CS-S	Invisible	Numerous, on the grain/matrix border and through the matrix itself
MHA-2NS-S	Invisible	Moderately numerous, mainly through the matrix itself
MHA-2FC-S	Invisible	Single, mainly through the matrix itself
MHA-2FCS-S	Single, short	Moderately numerous, mainly at the grain/matrix interface
MHA-2TCS-S	Invisible	Moderately numerous, on the grain/matrix border and through the matrix itself

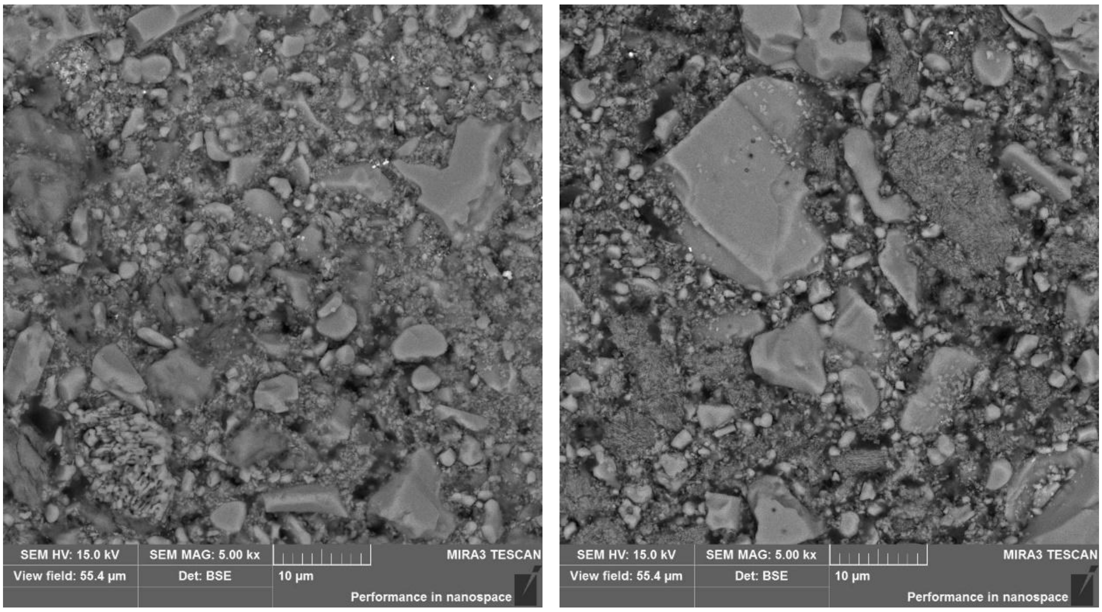

*Fig. II.76: Microstructure of the **MHA-2NS** after drying at 100 °C (left) and microstructure after its firing at 1260 °C (right). Grain growth is clearly visible.*

Model castable	***SEM observation***	
	After drying	***After thermal treatment***
MHA-REF	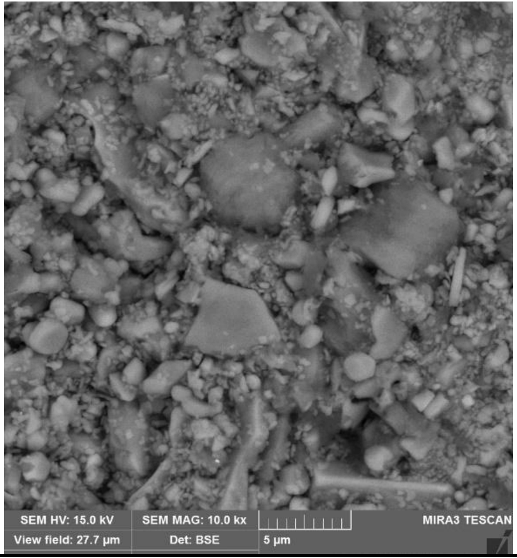	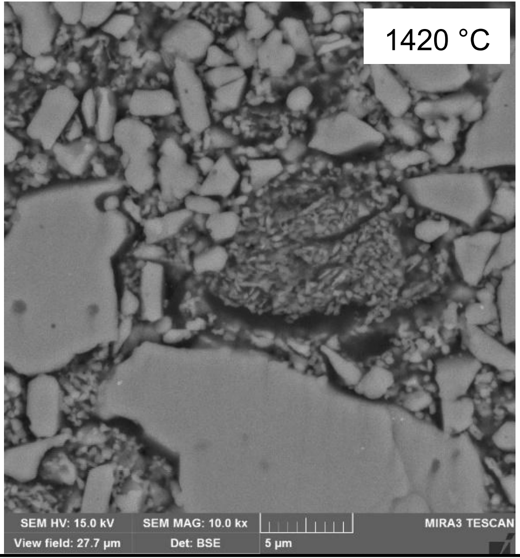
MHA-2CS	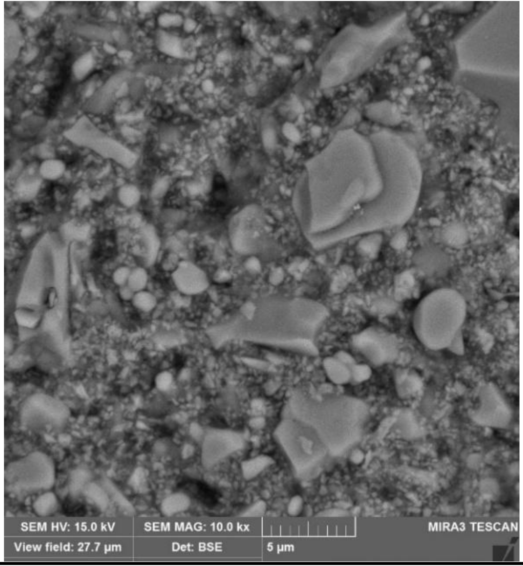	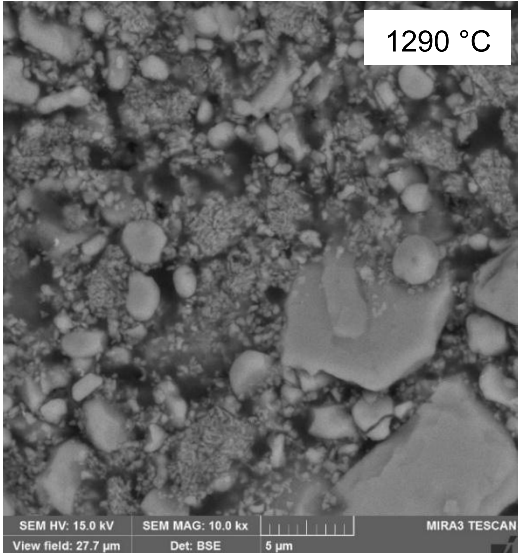
MHA-2NS	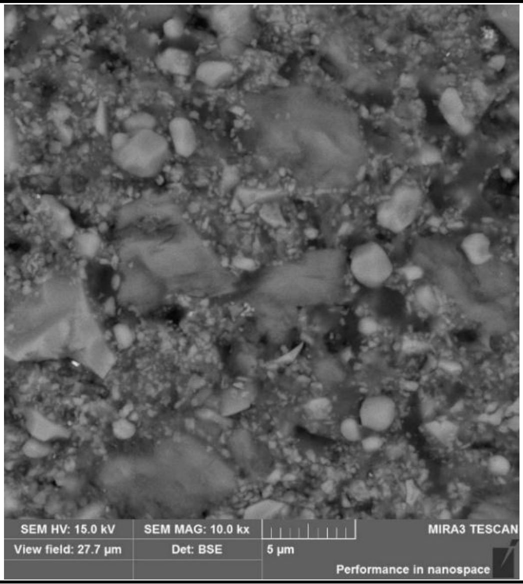	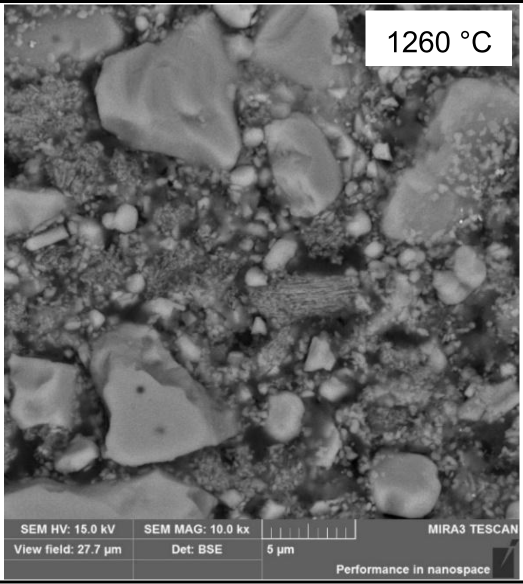

MHA-2FC	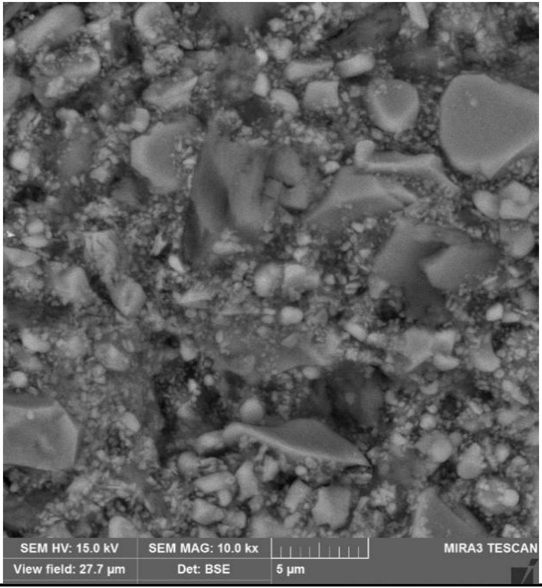	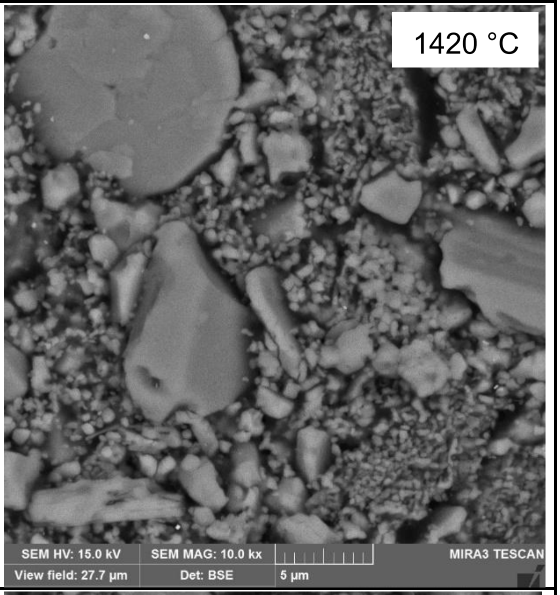
MHA-2FCS	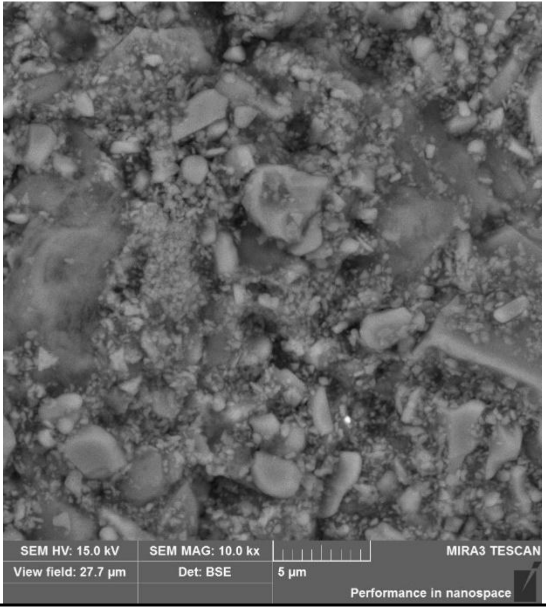	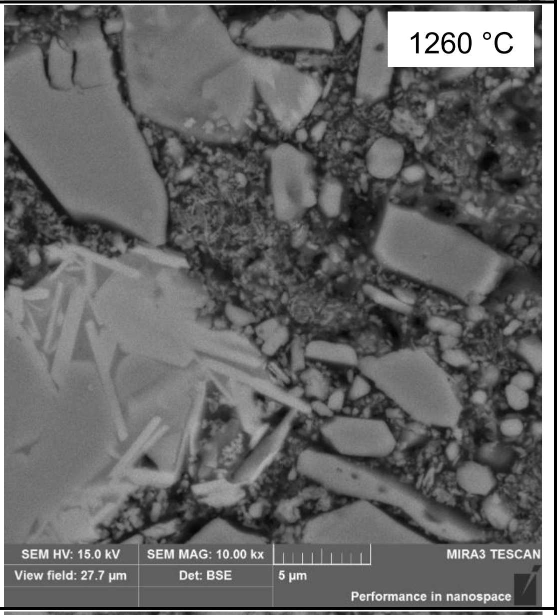
MHA-2TCS	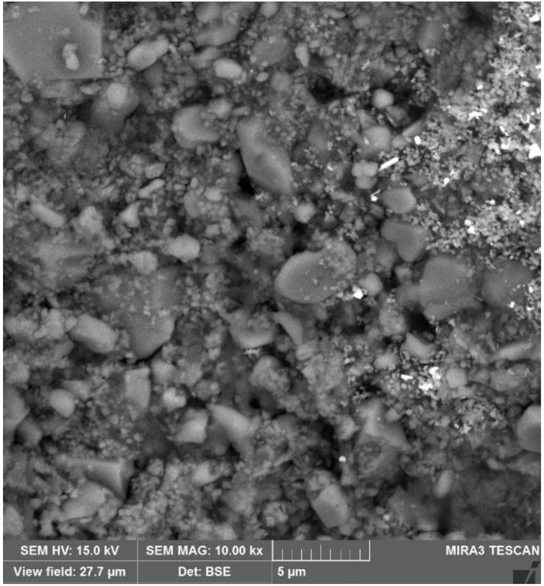	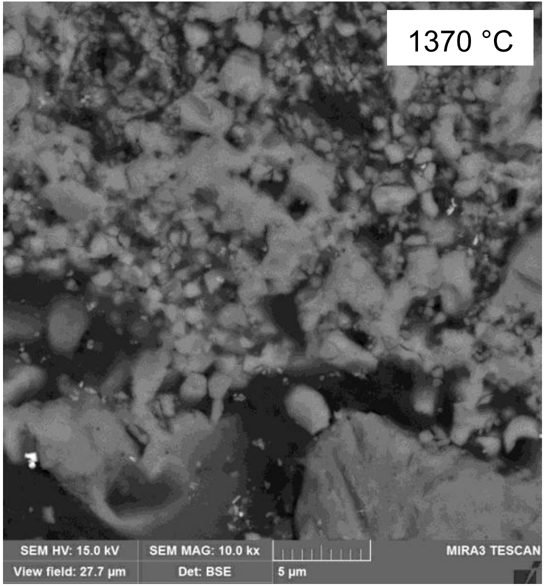

MHA-REF-S	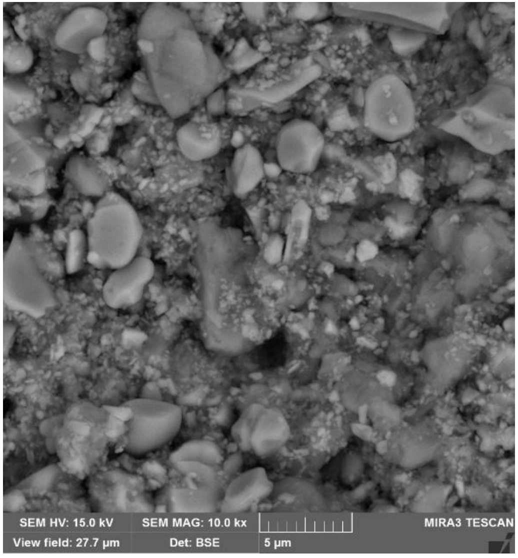	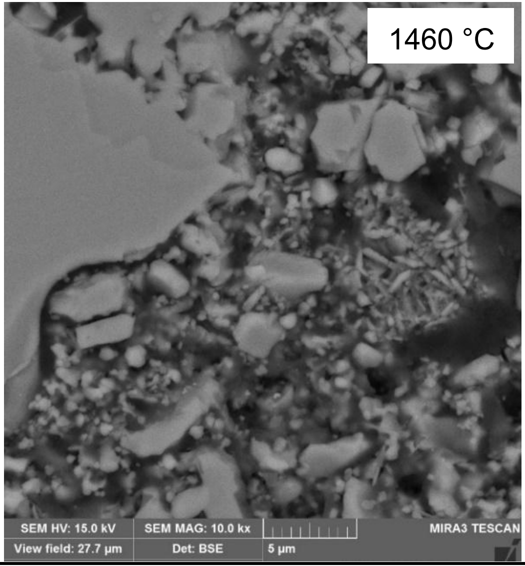
MHA-2CS-S	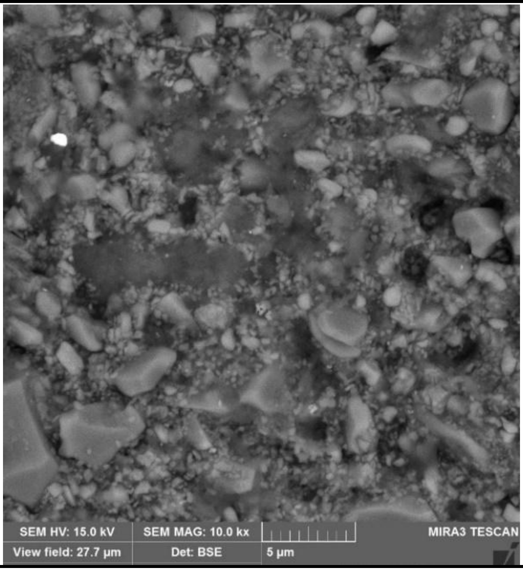	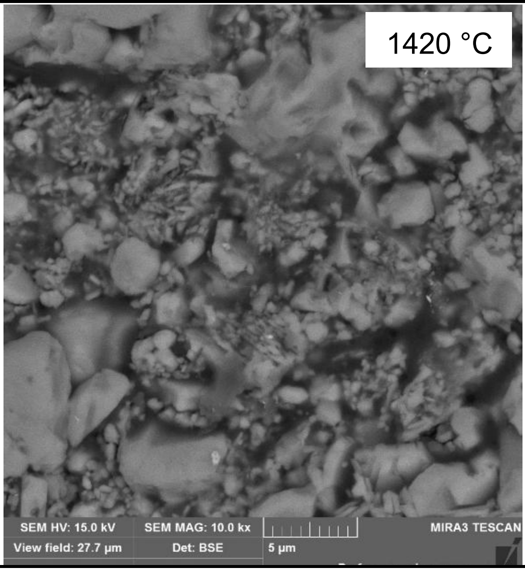
MHA-2NS-S	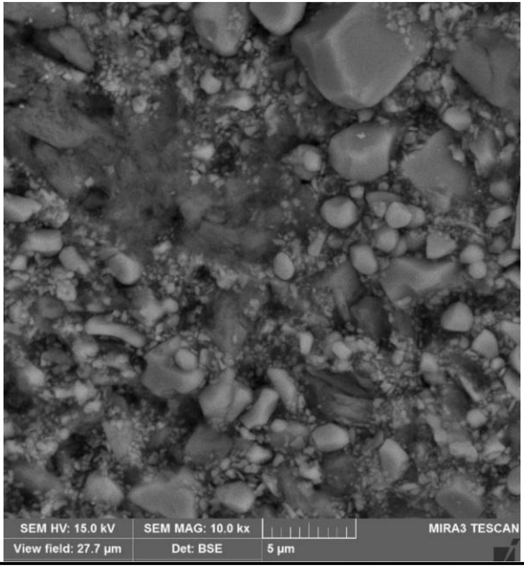	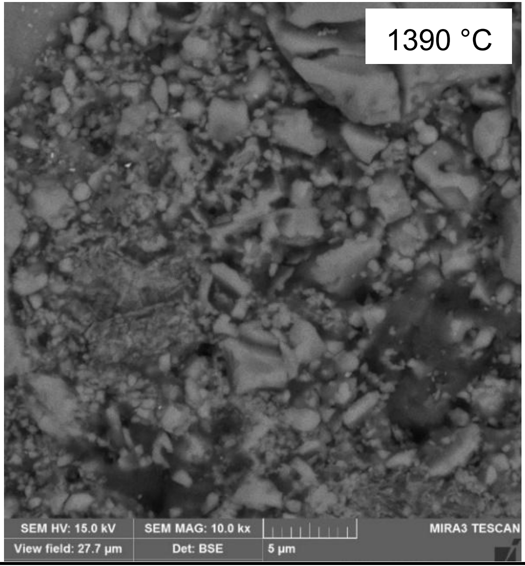

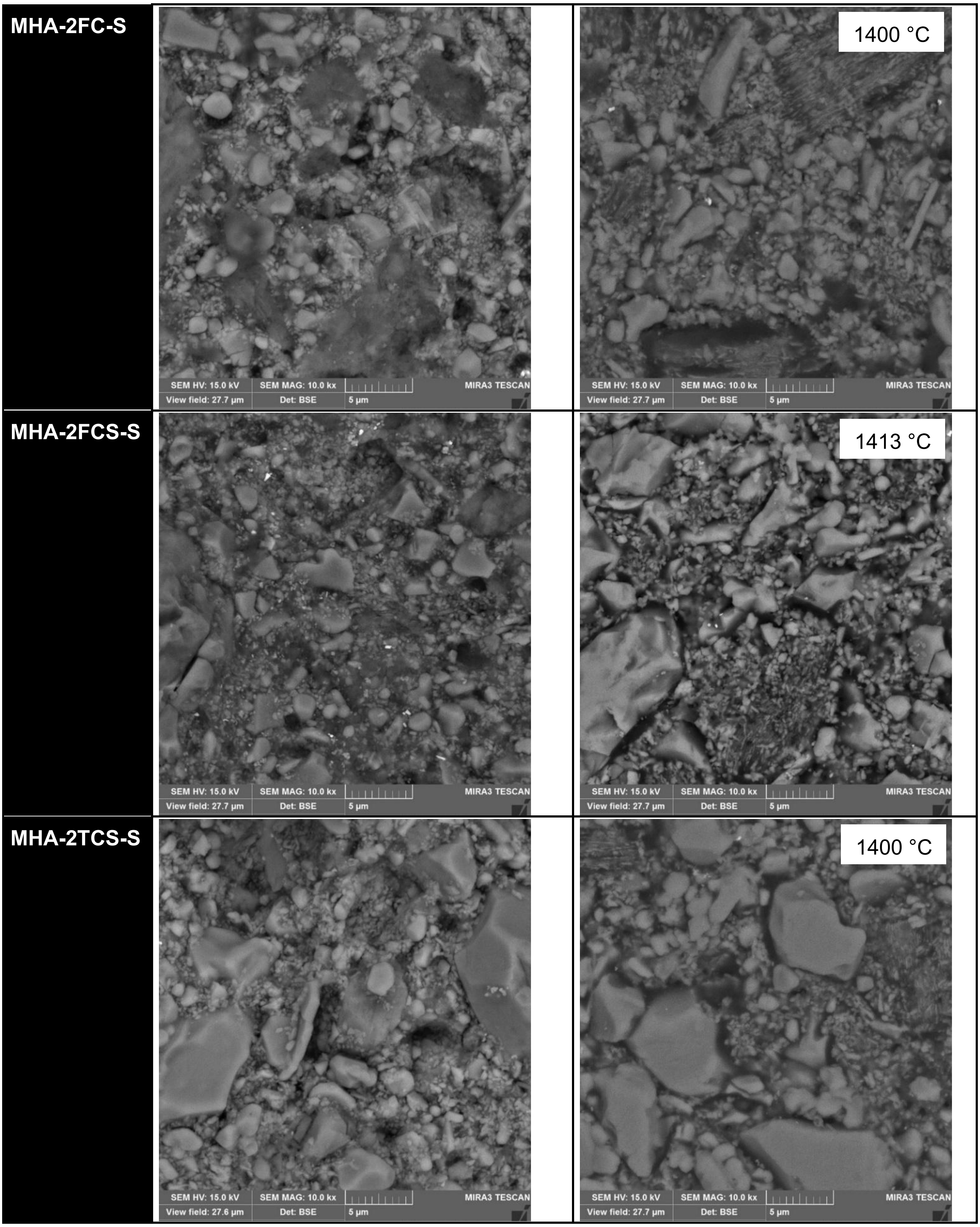

Fig. II.77: SEM images of the investigated model castables, magnification 10000x, BSE.

X-ray maps of the distribution of elements in the model castables after drying are presented in the figures II.78 to II.82. Aluminium and oxygen were identified as the main ingredients, accompanied by other elements - depending on the prepared variant of the model castables - as an additional compound or in trace amounts. In the case of model castables with introduced impurities, their distribution in the examined micro-areas was quite homogeneous, proving that the castables were well prepared. The non-uniform distribution of sodium, similarly to the other cases, can be associated with the presence of larger alumina grains, which indicates the presence of β-Al_2O_3. SEM observations of test pieces after thermal treatment for the model refractory castable without spinel-forming additive showed practically no changes in the distribution of individual elements. This proves that the precursors imitating secondary raw materials prepared in the project were well equilibrated (Figures II.83 to II.91)

In the case of the test piece with spinel-forming additive (model refractory castables MHA-S), micro-areas with regions enriched in magnesium were additionally visible on the EDS maps (Fig. II.87 for instance). In the model refractory castables MHA-S, which were thermally treated at higher temperatures, the appearance of voids (gaps) around larger MgO grains (periclase) and the diffusion of magnesium into the surrounding alumina grains were observed (Figures II.88 to 75). These are places where spinel with disturbed stoichiometry is formed. This is due to the Kirkendall effect, which leads to the inhibition of the spinel formation process as a result of the uneven diffusion flow of aluminium and magnesium ions. The created gap prevents further diffusion and lead to remaining unreacted MgO in the material. This explains the occurrence of periclase in the spinel forming model refractory castables at high temperatures in HT-XRD studies (section 3.5.6.2).

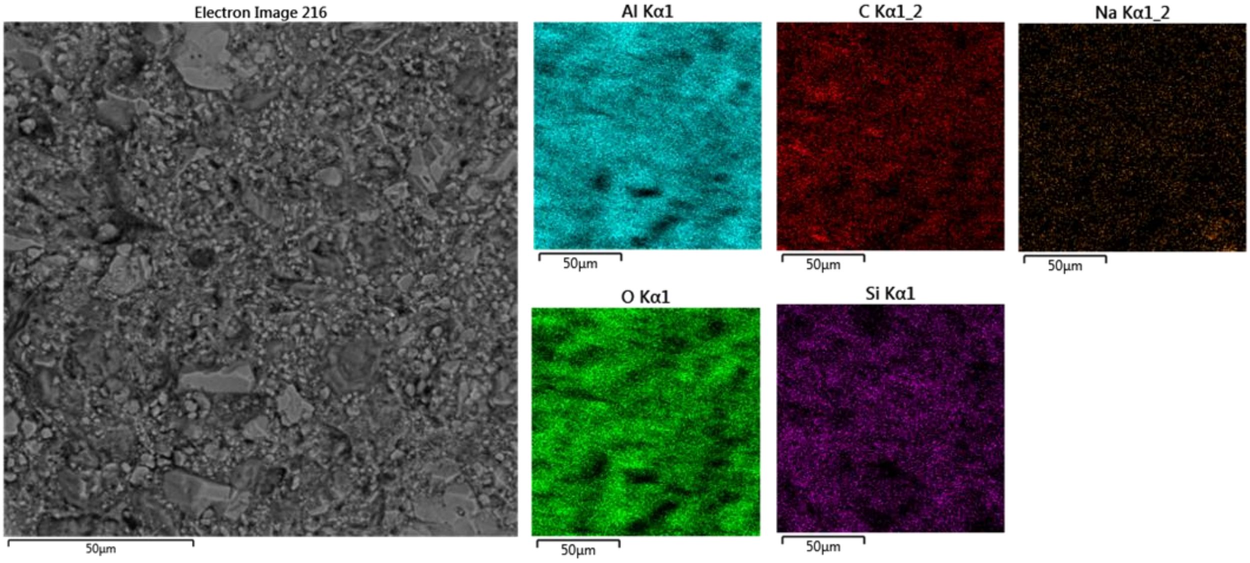

Fig. II.78: EDS element mapping of cross sections of a MHA-2CS test piece after drying (magnification of 2000x).

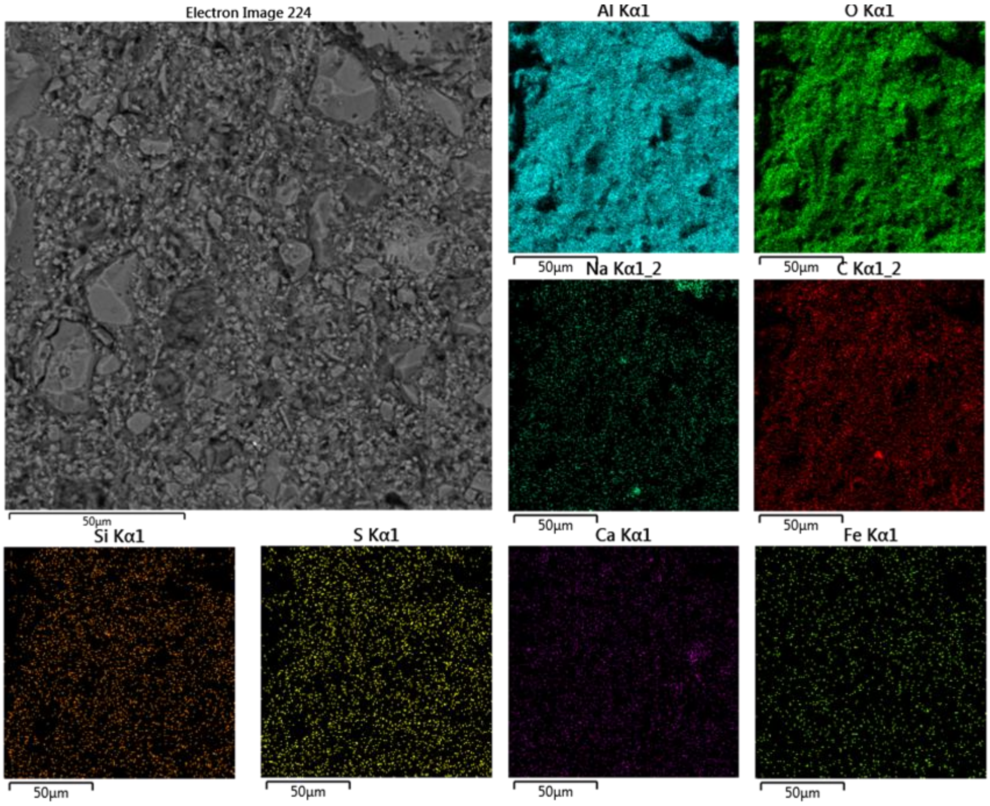

Fig. II.79: EDS element mapping of cross sections of a MHA-2NS test piece after drying (magnification of 2000x).

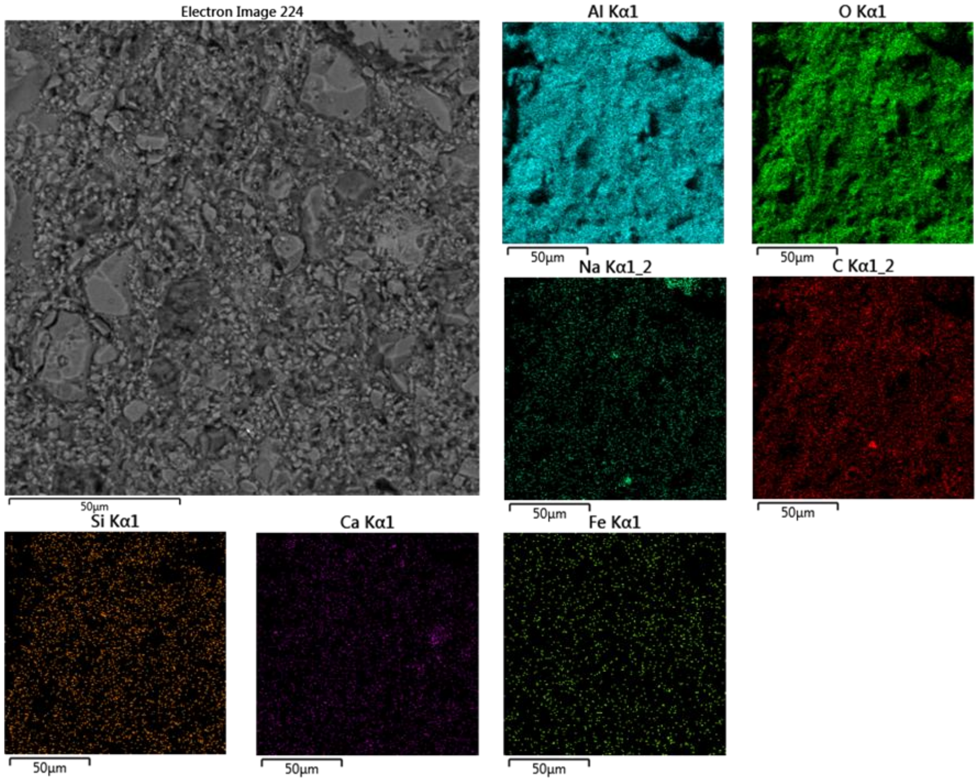

Fig. II.80: EDS element mapping of cross sections of a MHA-2FC test piece after drying (magnification of 2000x).

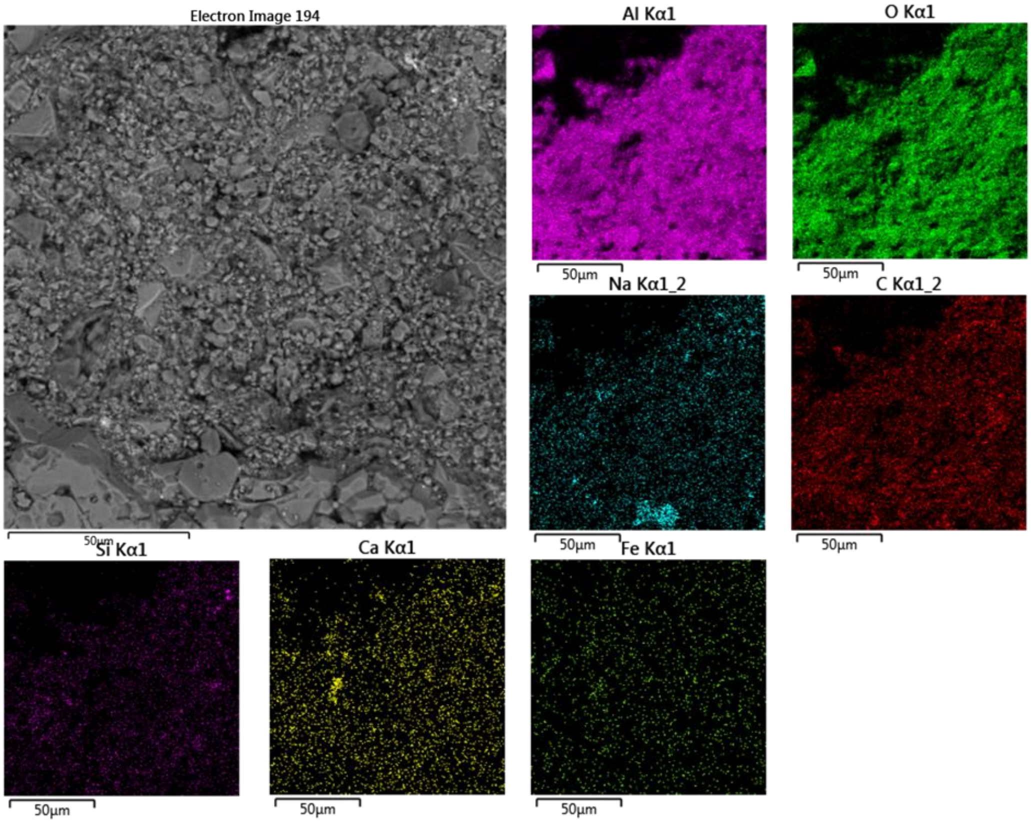

Fig. II.81: EDS element mapping of cross sections of a MHA-2FCS test piece after drying (magnification of 2000x).

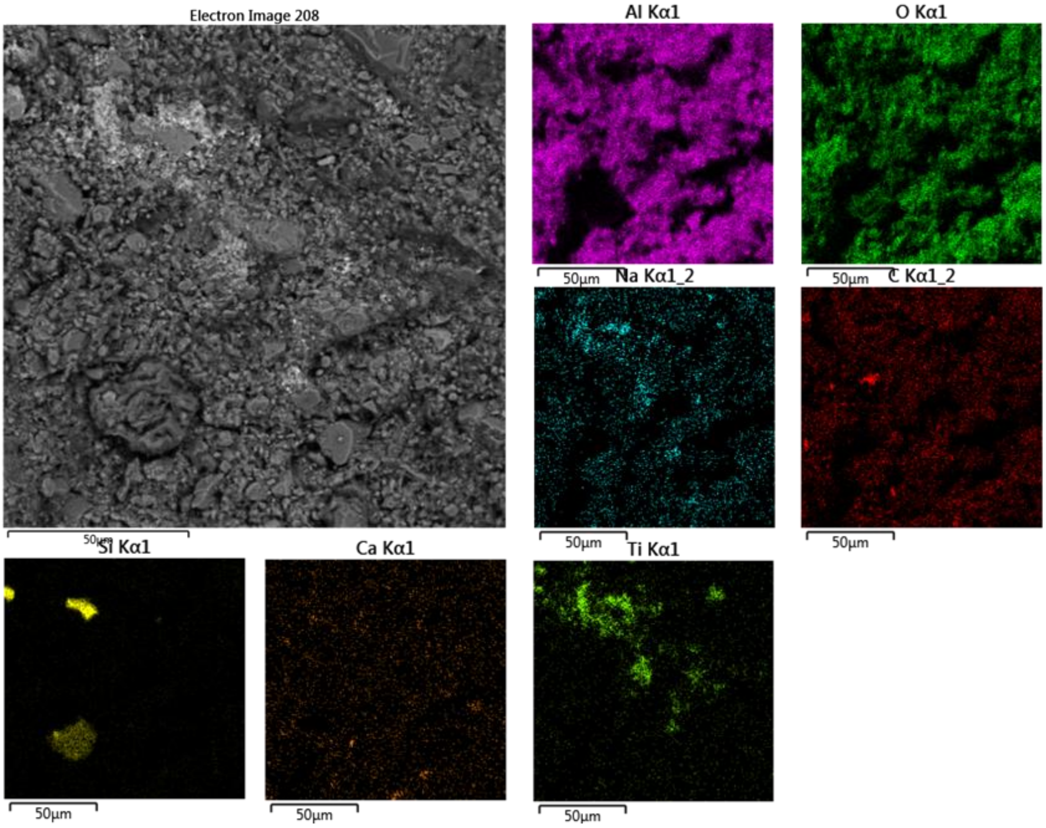

Fig. II.82: EDS element mapping of cross sections of a MHA-2TCS after drying (magnification of 2000x).

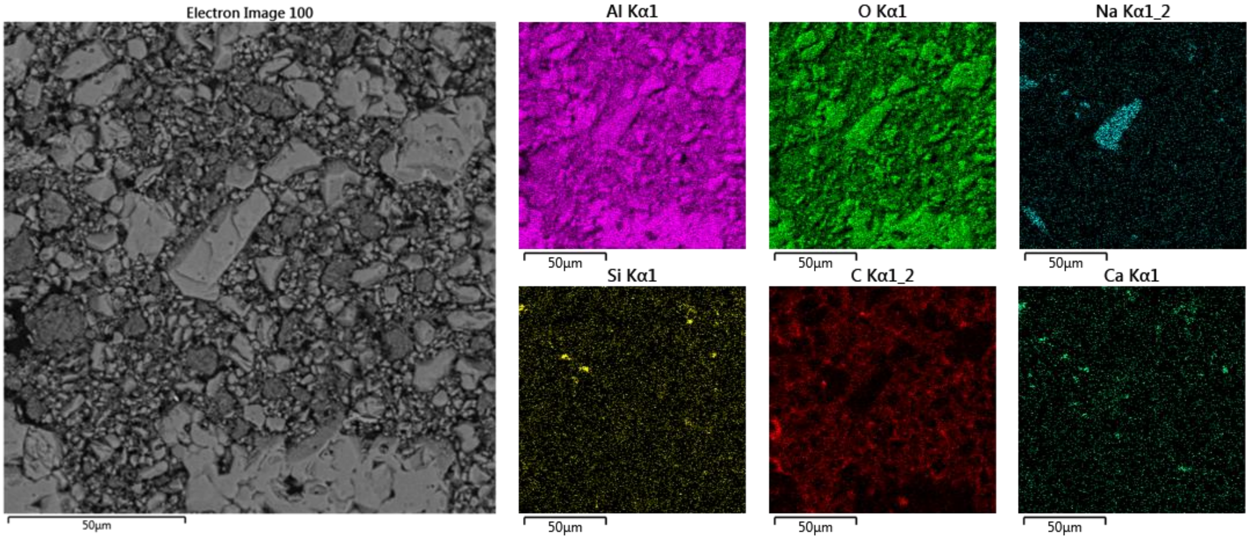

Fig. II.83: EDS element mapping of cross sections of MHA-2CS test piece after firing at 1290°C (magnification of 2000x).

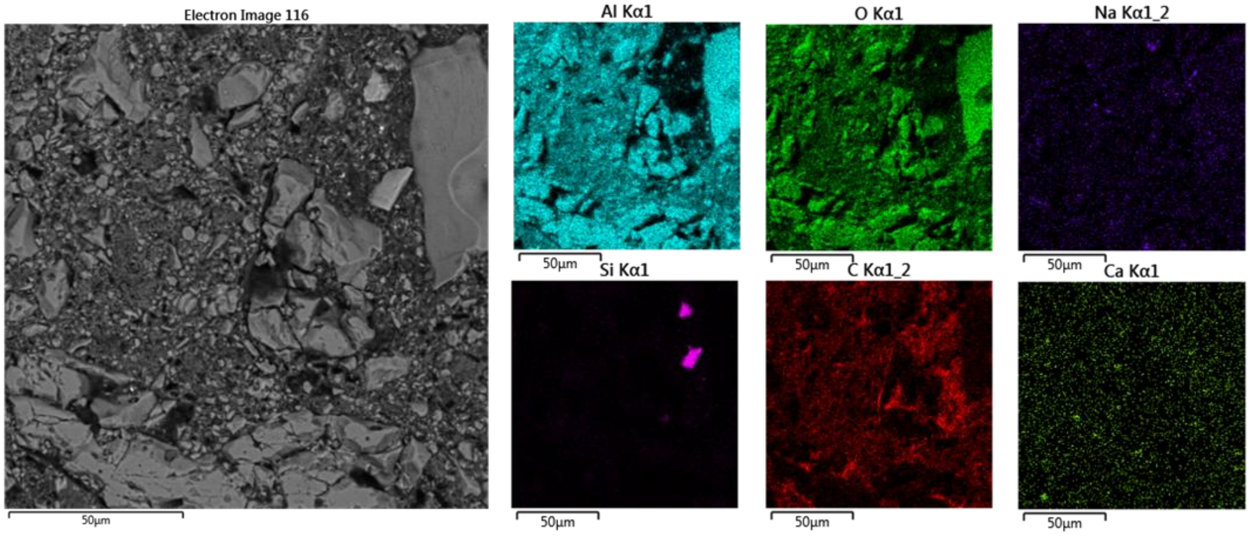

Fig. II.84: EDS element mapping of cross sections of a MHA-2FC test piece after firing at 1320°C (magnification of 2000x).

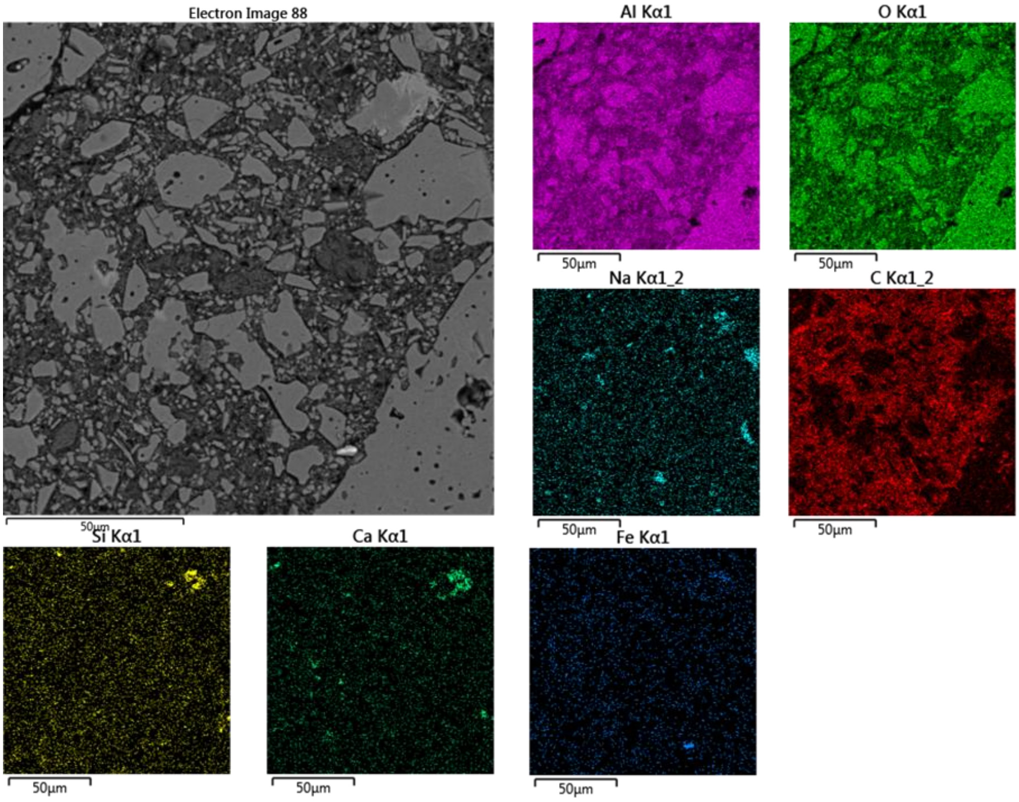

Fig. II.85: *EDS element mapping of cross sections of a MHA-2FCS test piece after firing at 1260°C (magnification of 2000x).*

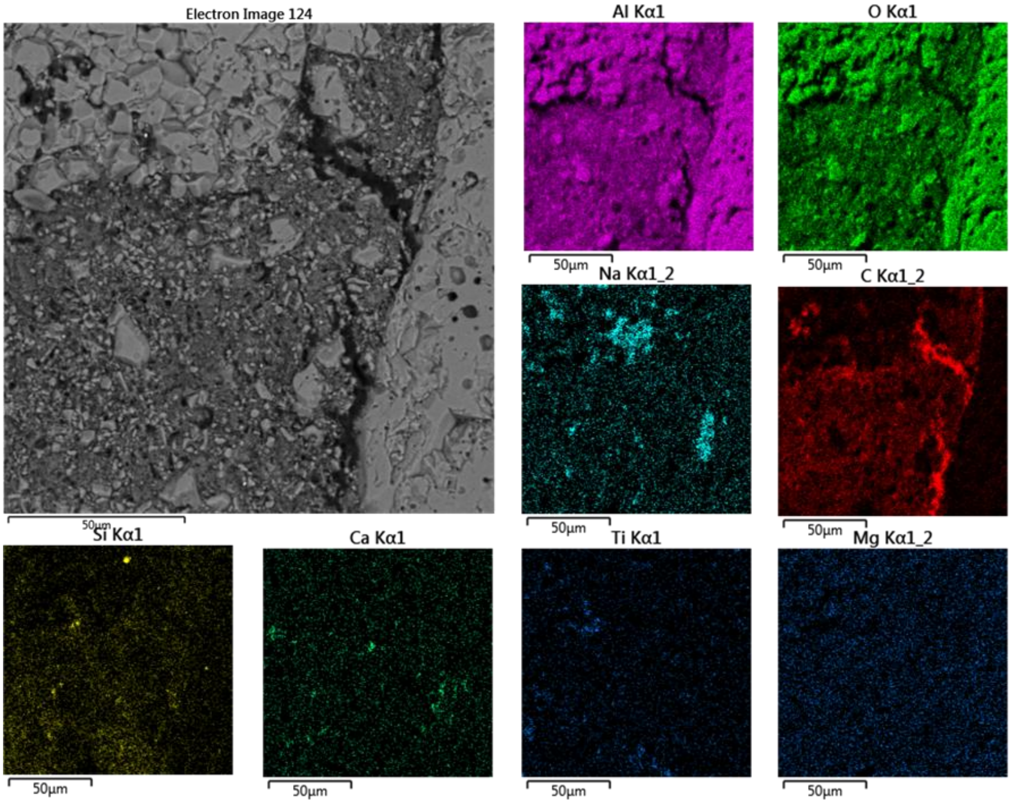

Fig. II.86: *EDS element mapping of cross sections of a MHA-2TCS test piece after firing at 1270°C (magnification of 2000x).*

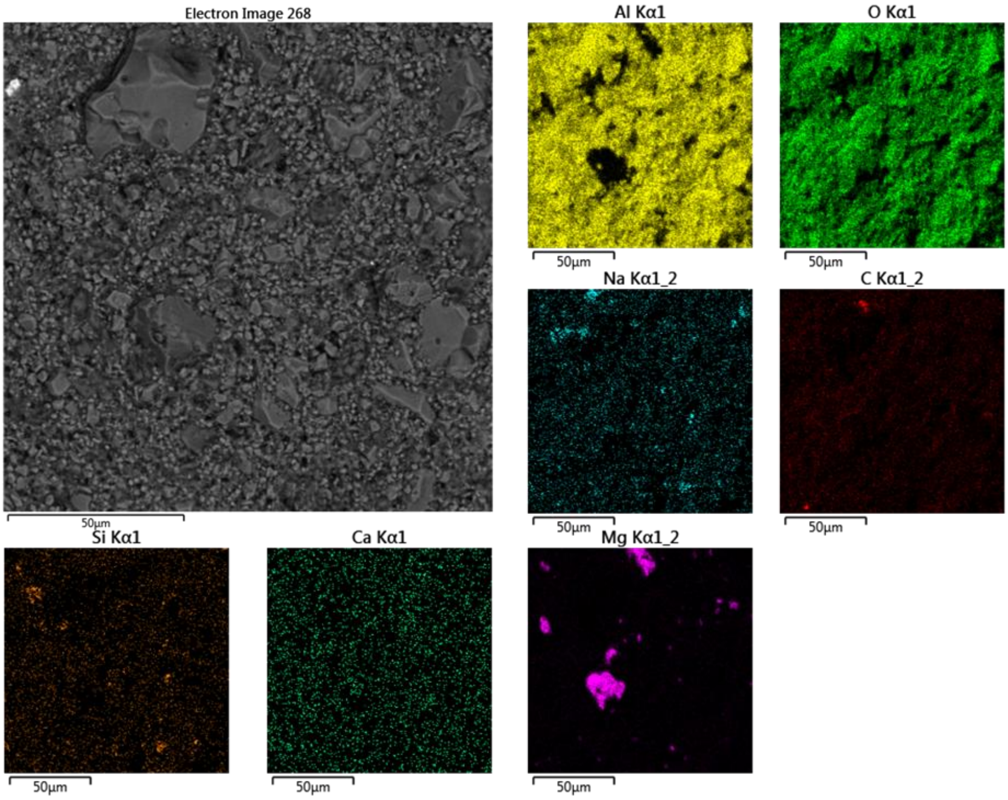

Fig. II.87: EDS element mapping of cross sections of a MHA-S-2NS test piece after drying (magnification of 2000x).

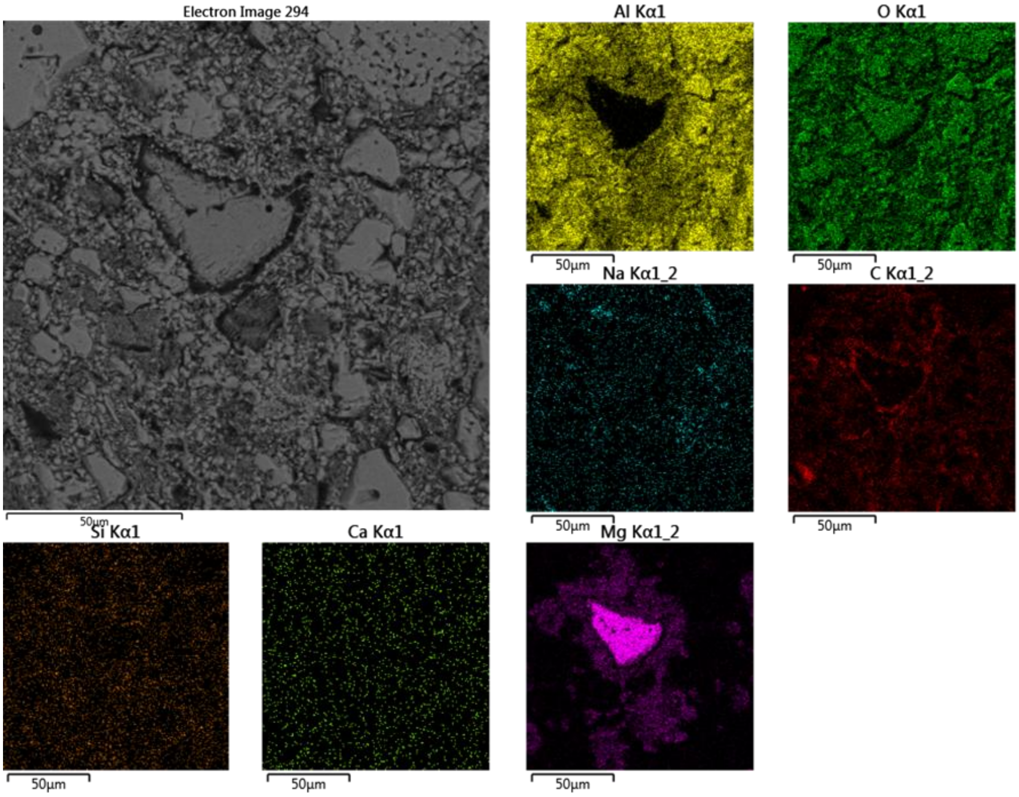

Fig. II.88: EDS element mapping of cross sections of a MHA-2NS-S test piece after firing at 1390°C (magnification of 2000x).

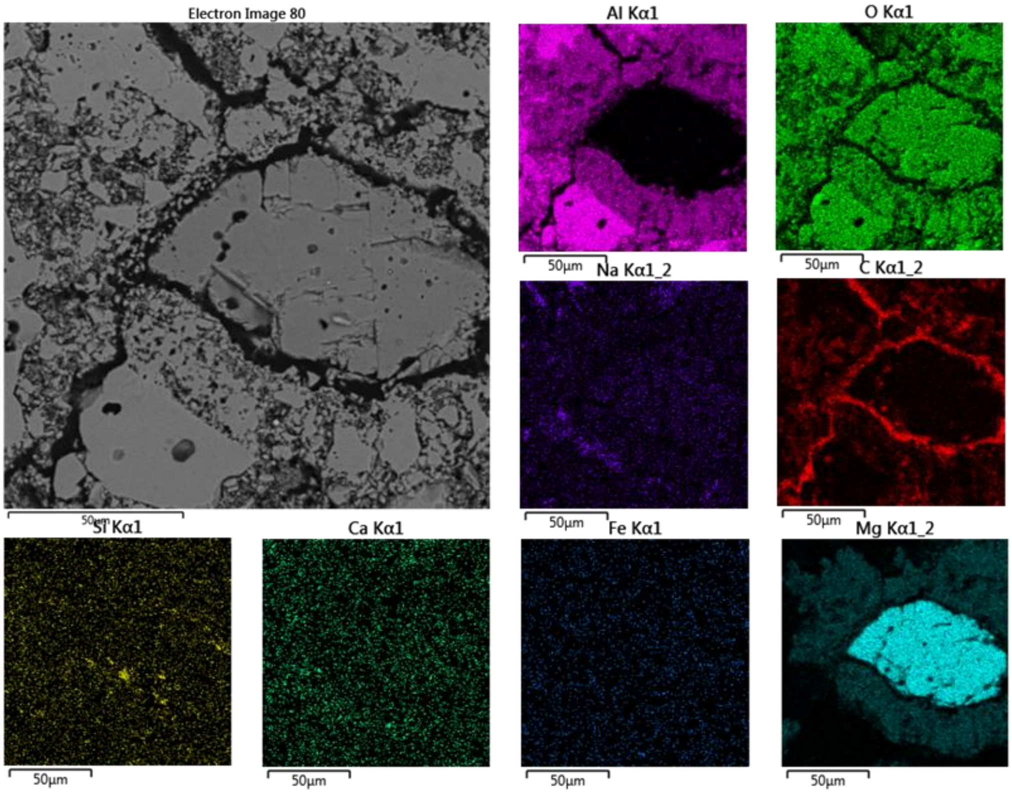

Fig. II.89: EDS element mapping of cross sections of a MHA-REF-S test piece after firing at 1460°C (magnification of 2000x)

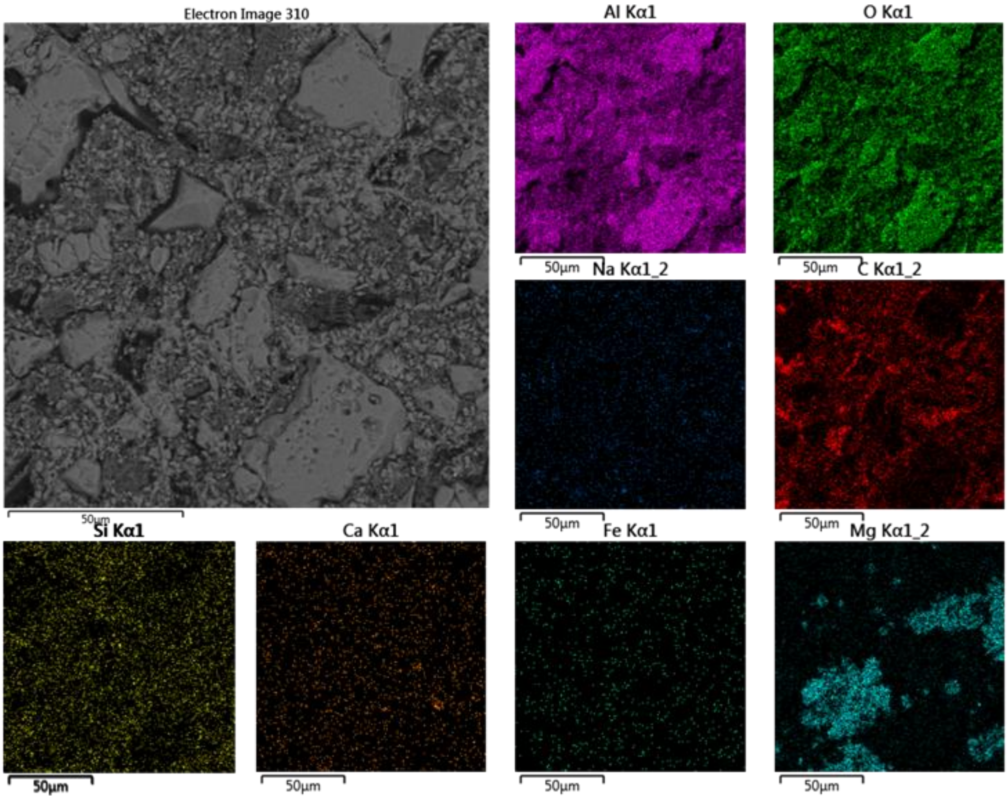

Fig. II.90: EDS element mapping of cross sections of a MHA_2FC-S test piece after firing at 1400°C (magnification of 2000x).

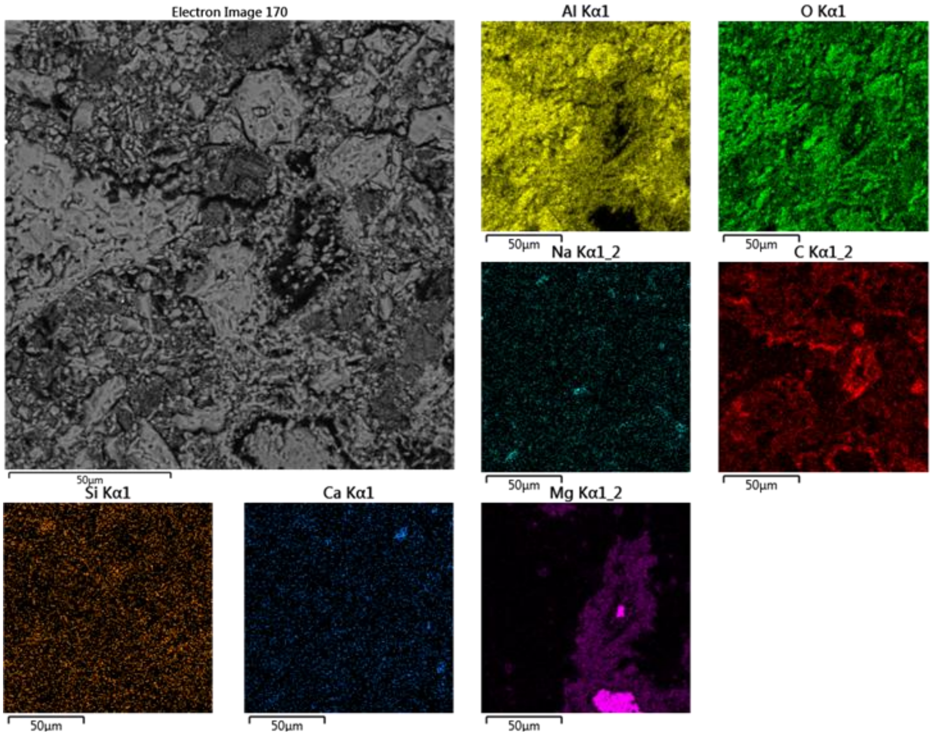

Fig. II.91: EDS element mapping of cross sections of a MHA_2FCS-S test piece after firing at 1413°C (magnification of 2000x)

3.5.9 Elastic properties under cyclic heating and cooling versus temperature by Resonant Frequencies and Damping Analysis (RFDA)

The changes in the elastic properties of the model refractory castables MHA and MHA-S were determined in the temperature range from 25 °C to $T_{0,5}$-100 °C. The temperature $T_{0,5}$-100 °C was taken as upper temperature for the measurements because it was considered that the investigated materials could still behave elastically up to this temperature. In practice, it turned out, by analysing the evolution of the damping with increasing temperature that the model refractory castables could behave thermoplastically already from a temperature of about 900 °C or, at least, significant microstructural changes started at this temperature. The results of the obtained temperature relationships between Young's modulus / flexural resonant frequency and damping are presented in Figures II.92 to II.103.

The evolution of the material microstructure during the first heating is quite well documented in other studies of the thermomechanical properties of corundum refractory castables [21]. The observed changes with temperature, particularly visible in the damping values, are most likely the result of microstructural changes such as sintering, crystal growth, melting and crystallisation from the liquid phase, opening and closing of microcracks. Different mechanisms of cracking during this process were illustrated in chapter 3.5.8 “Microstructural investigation of model castables MHA and MHA-S”, where various mechanisms of crack formation caused by impurities introduced into the model refractory castables were described and discussed.

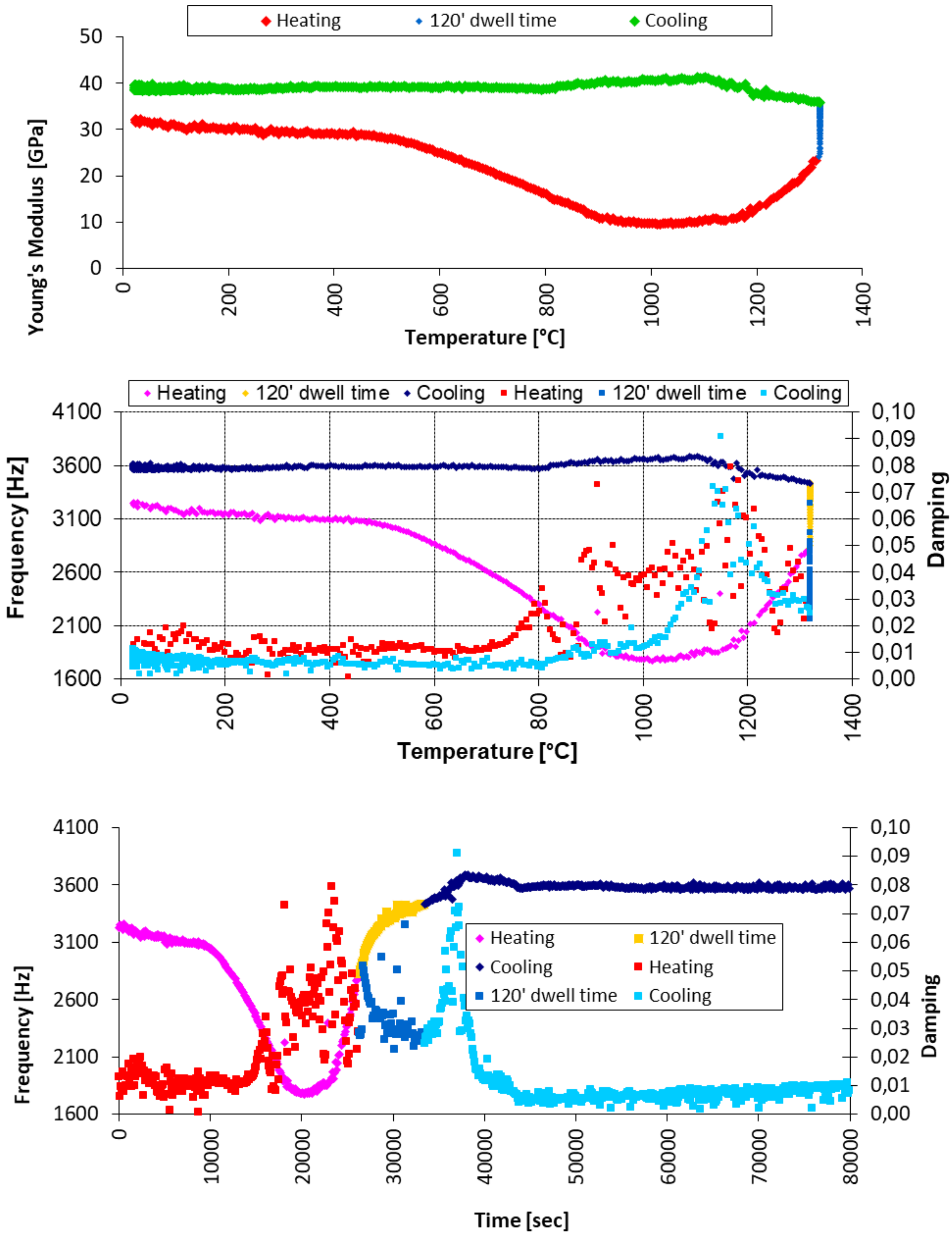

Fig. II.92: Young's modulus versus Temperature (upper), Flexural Frequency & Damping versus Temperature (middle) and Time (bottom). MHA-REF heated up to $T_{0,5\text{-}100\ °C}$ (1320 °C).

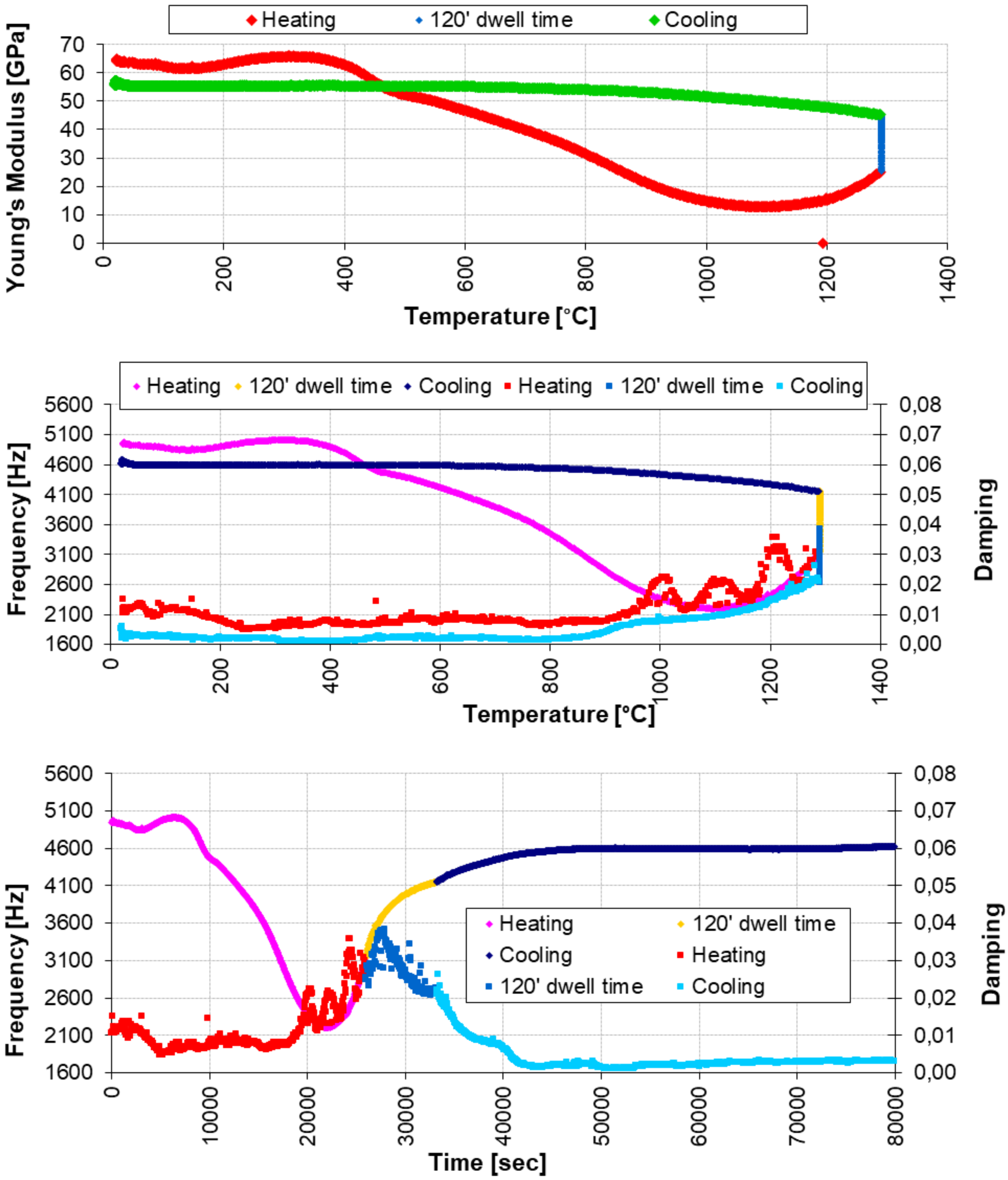

Fig. II.93: Young's modulus versus Temperature (upper), Flexural Frequency & Damping versus Temperature (middle) and Time (bottom). MHA-2CS heated up to $T_{0,5\text{-}100\,°C}$ (1290 °C).

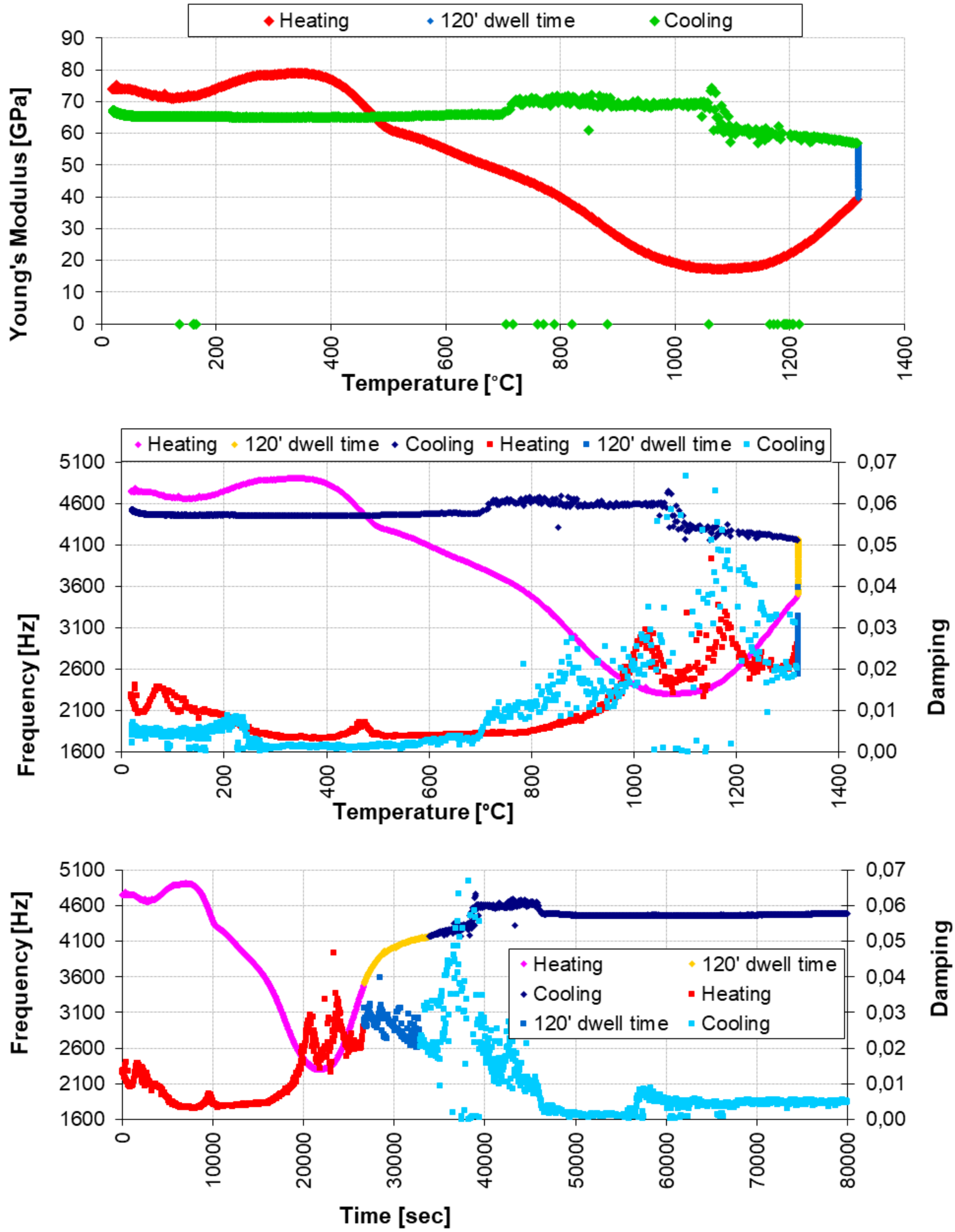

Fig. II.94: Young's modulus versus Temperature (upper), Flexural Frequency & Damping versus Temperature (middle) and Time (bottom). MHA-2FC heated up to $T_{0,5\text{-}100\,°C}$ (1320 °C).

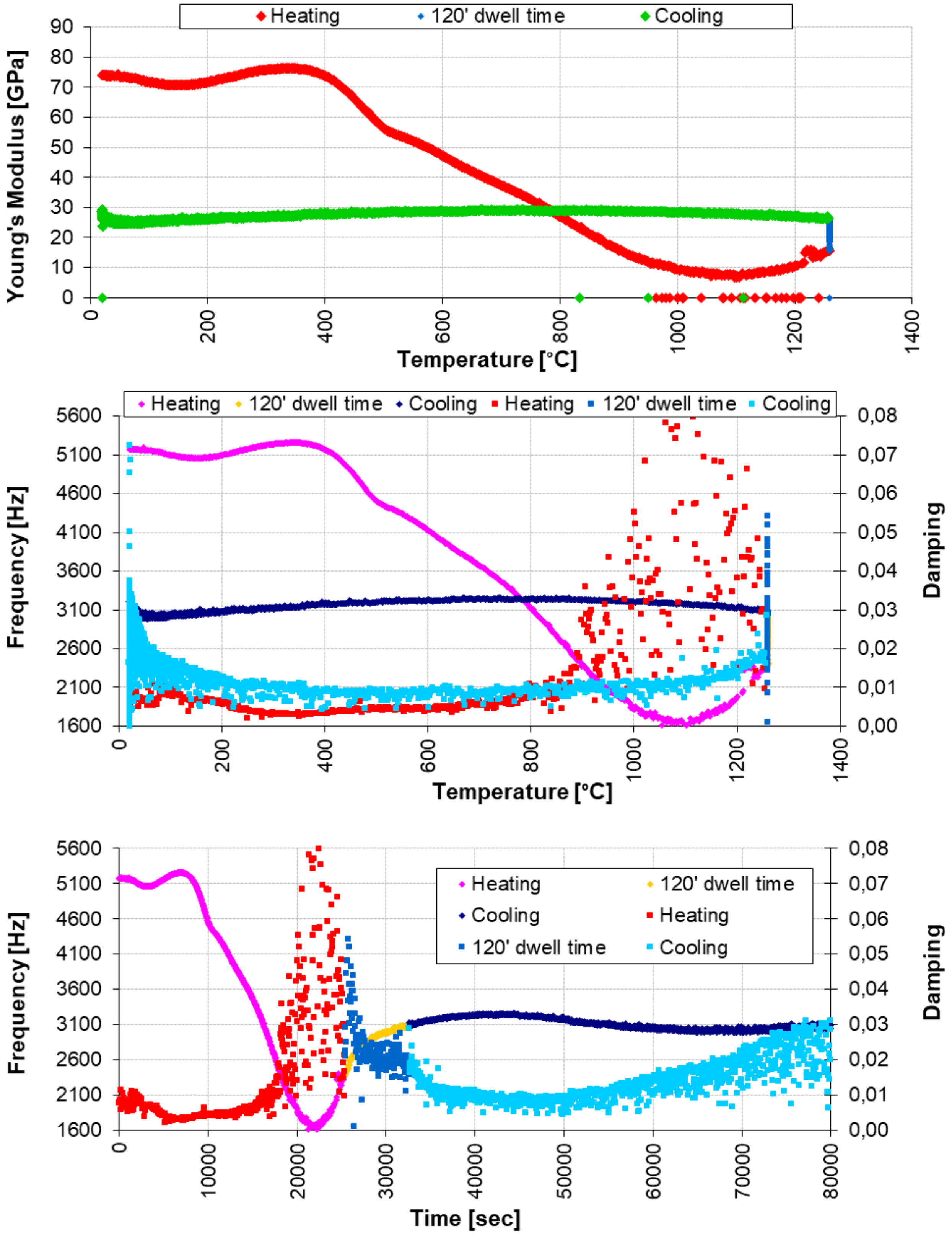

Fig. II.95: Young's modulus versus Temperature (upper), Flexural Frequency & Damping versus Temperature (middle) and Time (bottom). MHA-2FCS heated up to $T_{0,5\text{-}100\,°C}$ *(1260 °C).*

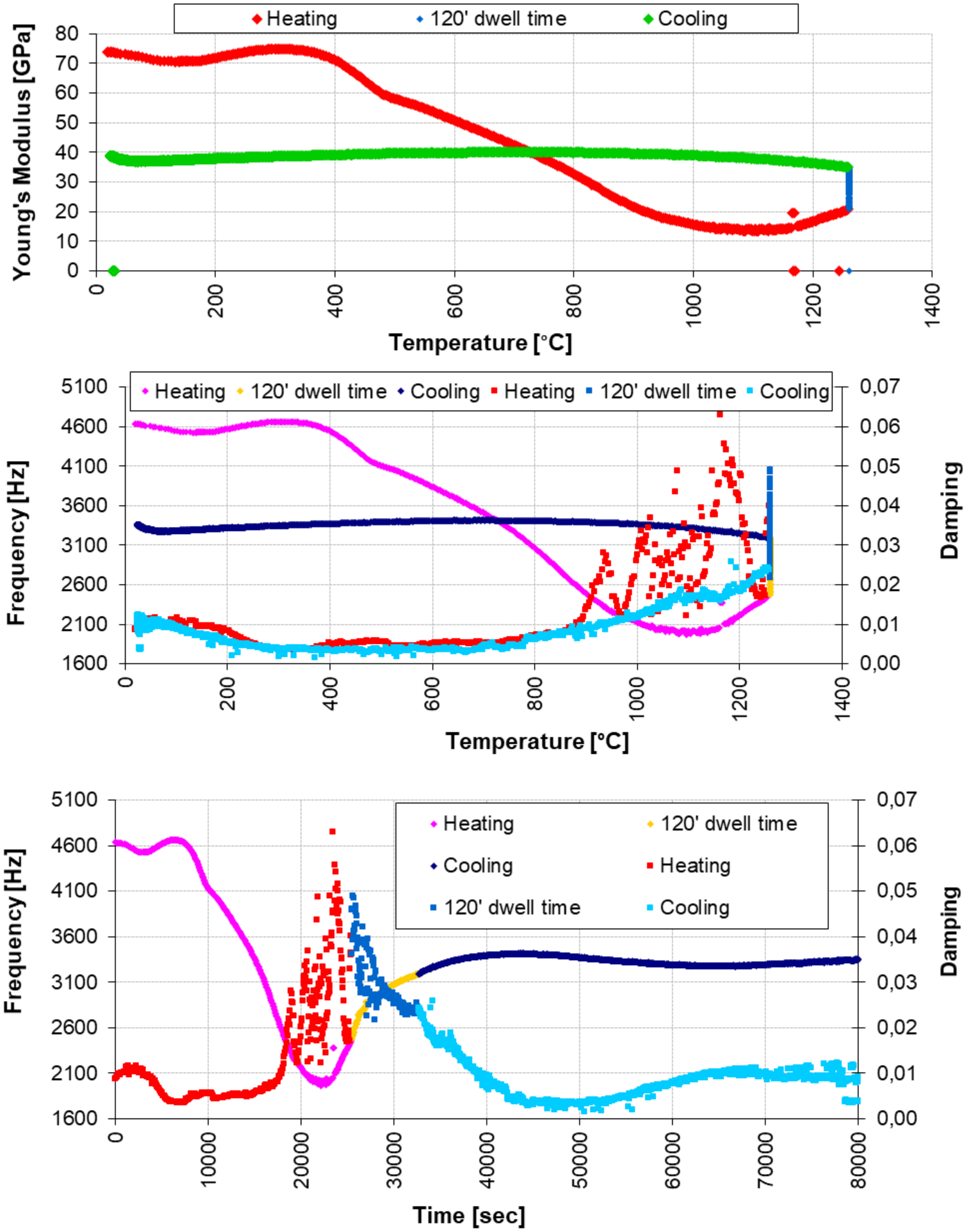

Fig. II.96: Young's modulus versus Temperature (upper), Flexural Frequency & Damping versus Temperature (middle) and Time (bottom). MHA-2NS heated up to $T_{0,5\text{-}100\,°C}$ *(1260 °C).*

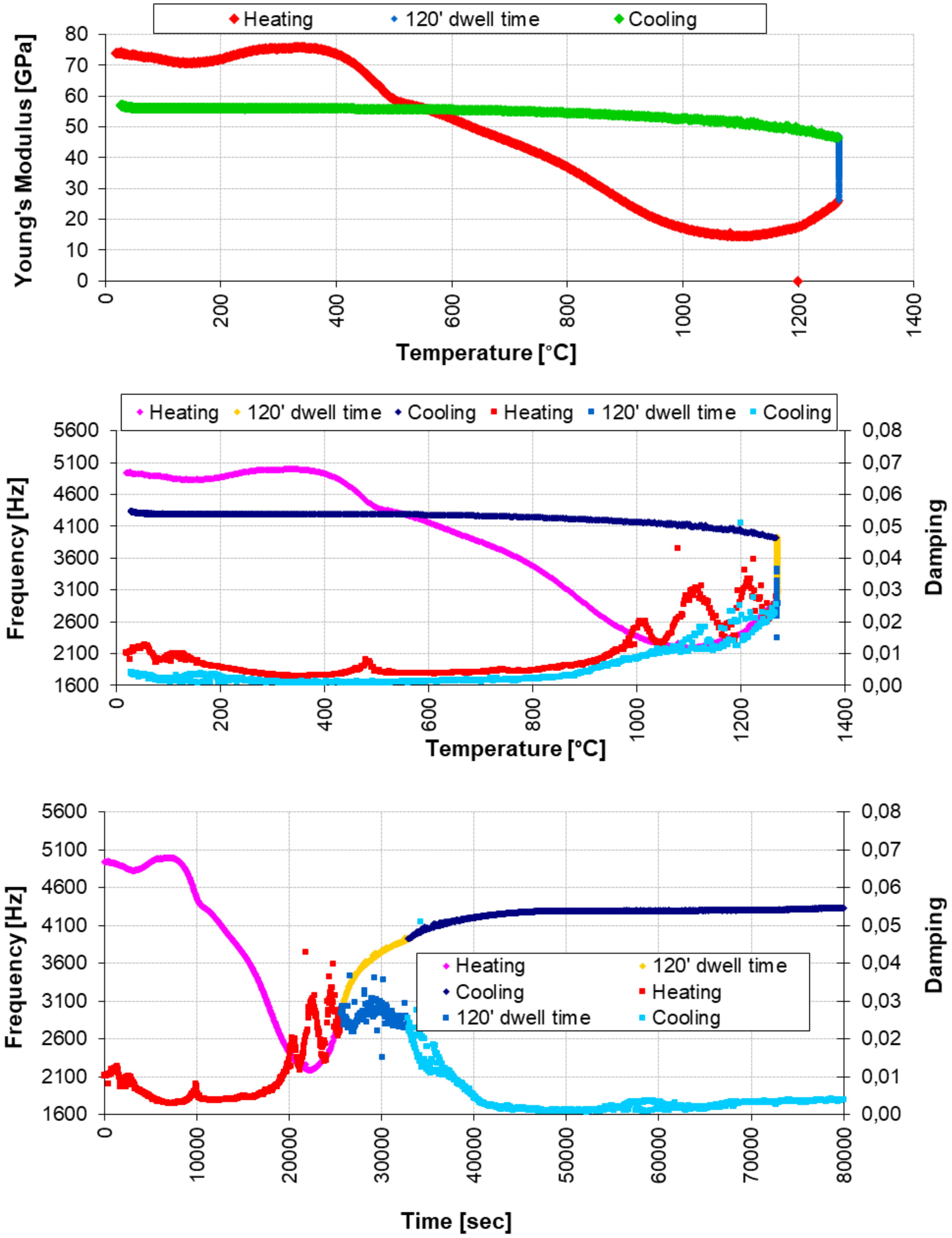

Fig. II.97: Young's modulus versus Temperature (upper), Flexural Frequency & Damping versus Temperature (middle) and Time (bottom). MHA-2TCS heated up to $T_{0,5\text{-}100\,°C}$ (1270 °C).

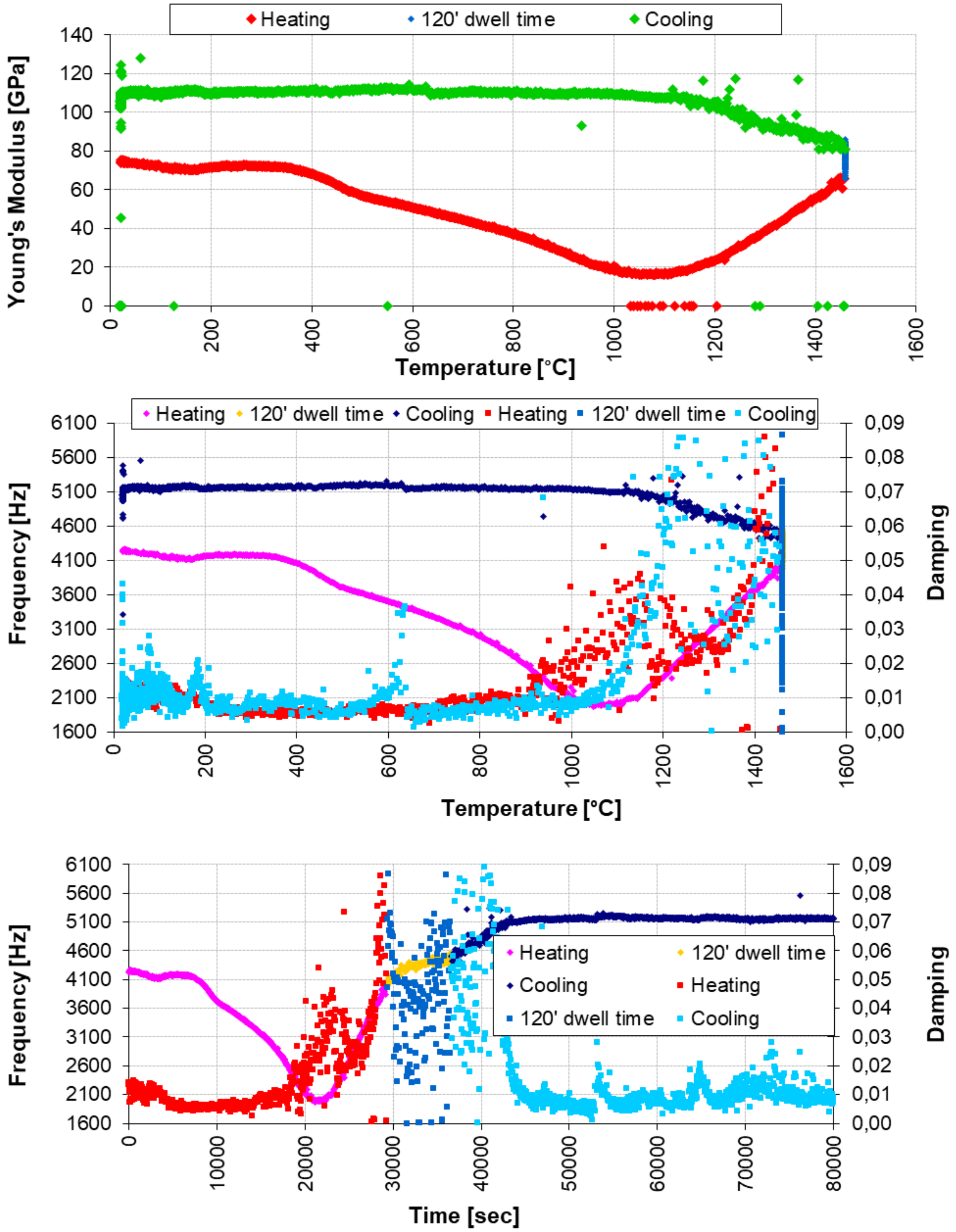

Fig. II.98: Young's modulus versus Temperature (upper), Flexural Frequency & Damping versus Temperature (middle) and Time (bottom). MHA-REF-S heated up to $T_{0,5\text{-}100\ °C}$ (1460 °C).

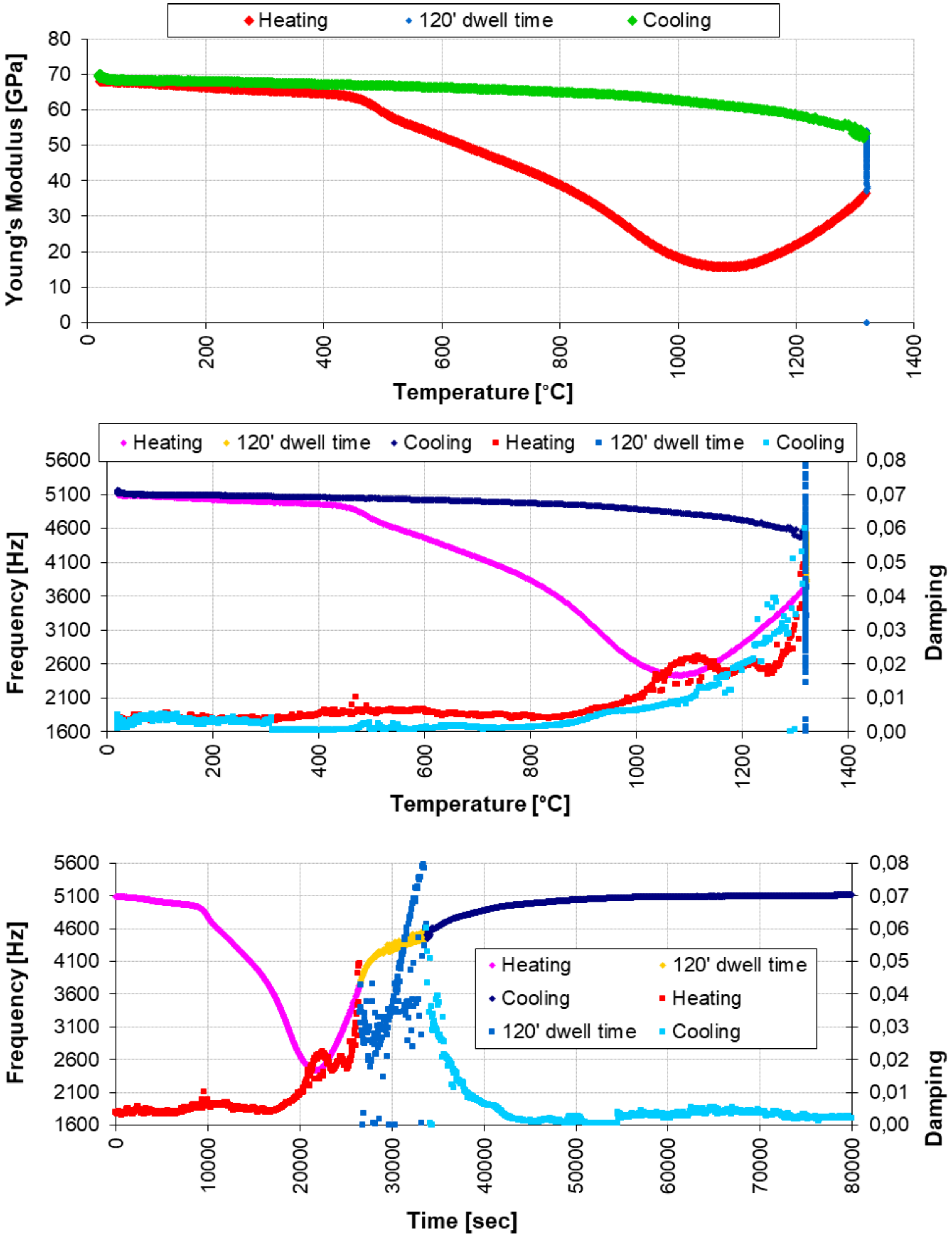

Fig. II.99: Young's modulus versus Temperature (upper), Flexural Frequency & Damping versus Temperature (middle) and Time (bottom). MHA-2CS-S heated up to $T_{0,5\text{-}100\,°C}$ (1320 °C).

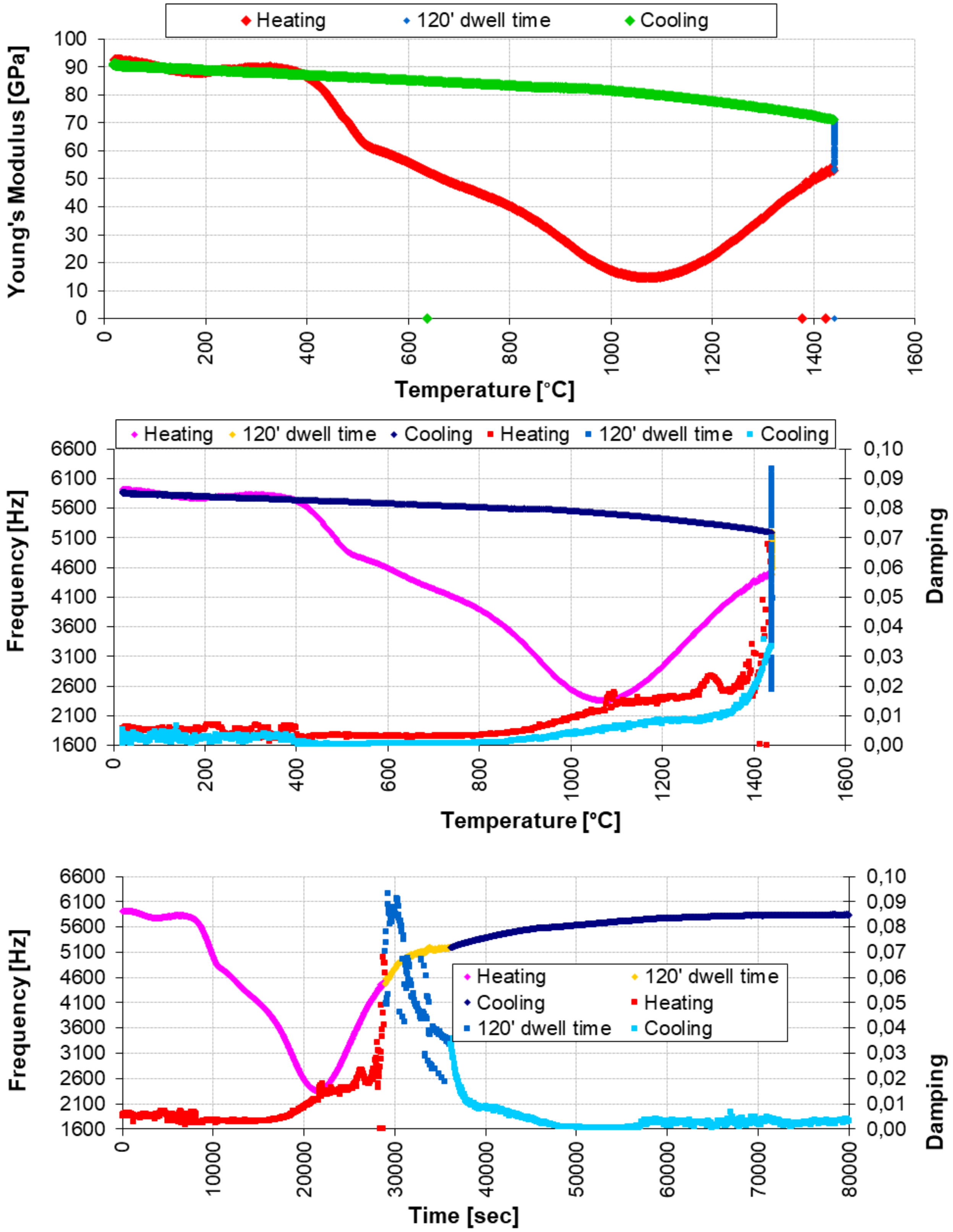

Fig. II.100: Young's modulus versus Temperature (upper), Flexural Frequency & Damping versus Temperature (middle) and Time (bottom). MHA-2FC-S heated up to $T_{0,5\text{-}100\ °C}$ (1440 °C).

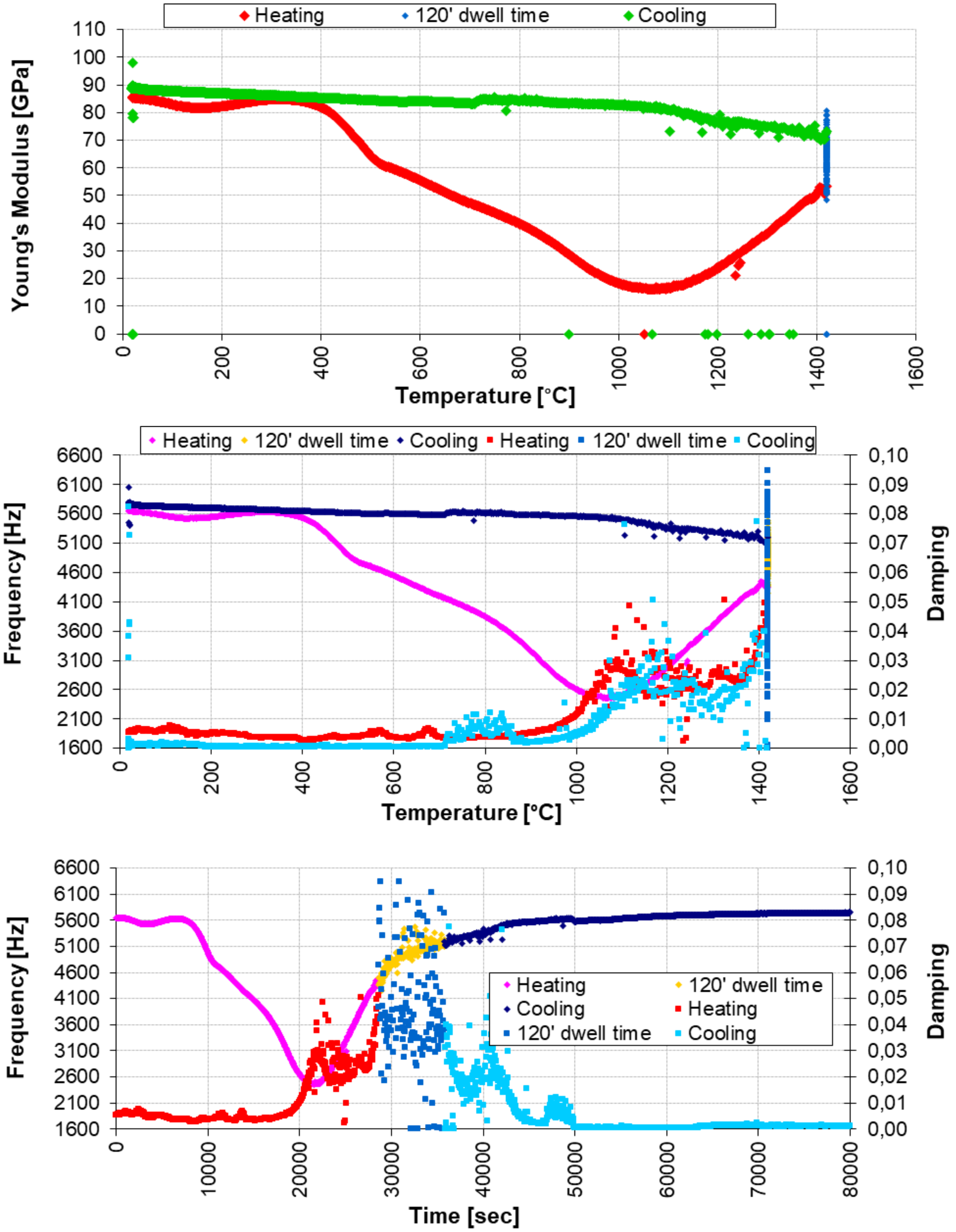

Fig. II.101: Young's modulus versus Temperature (upper), Flexural Frequency & Damping versus Temperature (middle) and Time (bottom). MHA-2FCS-S heated up to $T_{0,5\text{-}100\,°C}$ (1420 °C).

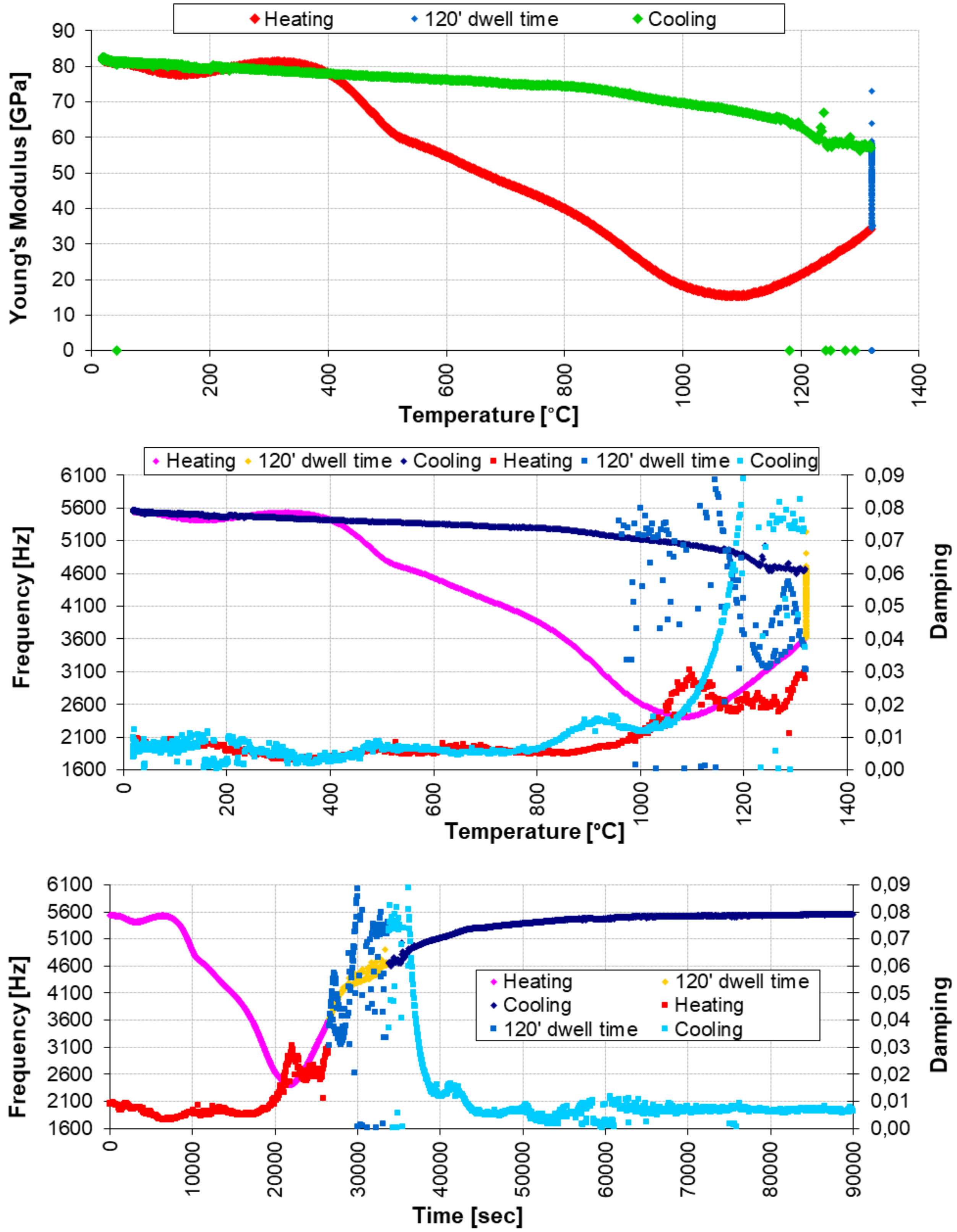

Fig. II.102: Young's modulus versus Temperature (upper), Flexural Frequency & Damping versus Temperature (middle) and Time (bottom). MHA-2NS-S heated up to $T_{0,5\text{-}100\,°C}$ (1390 °C).

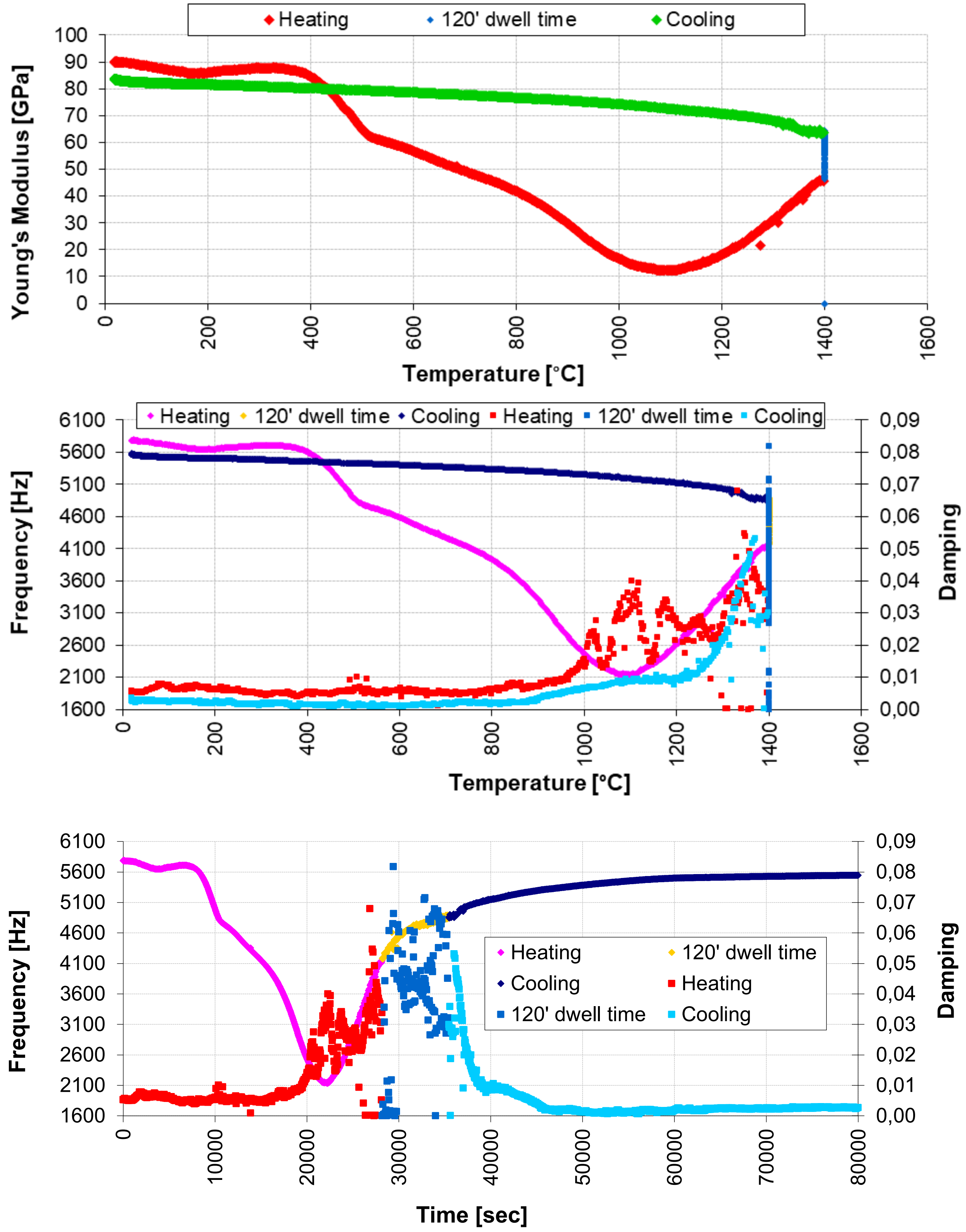

Fig. II.103: Young's modulus versus Temperature (upper), Flexural Frequency & Damping versus Temperature (middle) and Time (bottom). MHA_2TCS-S heated up to $T_{0.5\text{-}100\,°C}$ (1400 °C).

The changes in the Young's modulus obtained in the RFDA measurements performed to the temperature $T_{0.5}$-100 °C for the model refractory castables MHA are summarized in the table II.9.

The results show that only MHA-REF had a higher Young's modulus after the RFDA measurement than at the beginning. The Young's modulus systematically decreased for model refractory castables containing impurities. It was also found that the impurified model castables had a twice as high Young's modulus after setting and drying, suggesting that, in contrast to the findings from Hochschule Koblenz (subproject I – chapter 2), impurities introduced into the material may also play a role in the setting process of the model refractory castables, or at least during their curing.

Tab. II.9: Changes in the Young's modulus measured by RFDA after heating and cooling to the temperature $T_{0,5}$-100 °C for model refractory castables MHA and the results of a subjective description of the micro-cracks formed at the testing conditions.

Castable	**E modulus, GPa** before test	**E modulus, GPa** after $T_{0,5\text{-}100}$ °C	**SEM microcracks observation** Before RFDA	After RFDA
MHA-REF	32	40	Invisible	Numerous. mostly on the grain/matrix border
MHA-2CS	62	53	Numerous. at the grain/matrix interface and through the matrix itself. of various lengths	Single long at the grain/matrix interface and single shorter through the matrix itself
MHA-2NS	74	53	Numerous. at the grain/matrix interface and through the matrix itself. of various lengths	Very numerous. on the grain/matrix border and through the matrix itself
MHA-2FC	74	67	Numerous. at the grain/matrix interface and through the matrix itself. of various lengths	Very numerous. at the grain/matrix interface and through the matrix itself. often through numerous spherical pores
MHA-2FCS	74	53	Single. Short.	Moderately numerous. mainly at the grain/matrix interface and also visible through the grains themselves
MHA-2TCS	74	53	Numerous. at the grain/matrix interface and through the matrix itself. of various lengths	Numerous. mainly through the matrix. sporadically at the grain/matrix boundary

For the model spinel-forming refractory castables MHA-S, the reference castable displayed the lowest value of Young's modulus after curing and drying, but the differences between the reference castable and the impurified castables was much lower as for the non spinel-forming castables. Additionally, almost all model impurified spinel-forming refractory castables have a higher Young's modulus than the reference spinel-forming refractory castable (namely without additional impurities), which indicated that the impurities introduced into the castables could have a beneficial effect on the setting and/or curing process. The only exception was the MHA-2CS-S castable, which had a slightly lower modulus compared to the reference castable MHA-REF-S. In contrast to the model refractory castables, the model spinel-forming refractory castables containing additional impurities retained roughly initial Young's modulus value after heating and holding at a temperature of $T_{0.5}$-100 °C. This is primarily due to higher firing temperatures (higher $T_{0.5}$-100 °C) which promoted the recovery of the Young's modulus after the observed decreased during the first heating mainly due to the decomposition of the hydrate phases (Figures II.99 to II.103).

Tab. II.10: Changes in the Young's modulus measured by RFDA after heating and cooling to the temperature $T_{0,5}$-100 °C for model spinel-forming refractory castables MHA-S and the results of a subjective description of the micro-cracks formed at the testing conditions.

Castable	**E modulus, GPa** before test	**E modulus, GPa** after $T_{0,5-100}$ °C	**SEM microcracks observation**	
			Before RFDA	**After RFDA**
MHA-REF-S	74	105	Invisible	Very numerous, at the grain/matrix interface and through the matrix itself, often through numerous
MHA-2CS-S	68	69	Invisible	Numerous, on the grain/matrix border and through the matrix itself
MHA-2NS-S	82	82	Invisible	Moderately numerous, mainly through the matrix itself
MHA-2FC-S	92	91	Invisible	Single, mainly through the matrix itself
MHA-2FCS-S	86	89	Single, short	Moderately numerous, mainly at the grain/matrix interface
MHA-2TCS-S	90	84	Invisible	Moderately numerous, on the grain/matrix border and through the matrix itself

Tables II.9 and II.10 also list the appearance of microcracks observed on the investigated model refractory castables. This assessment was made on the basis of the microscopic observations described in chapter 3.5.8 “Microstructural investigation of model castables MHA and MHA-S”. The evolution of the Young's modulus / frequency of flexural vibrations and damping with increasing temperature is mainly driven by microstructural changes and differences in the expansion behaviour of phases present in the matrix of the investigated model refractory castables as described and discussed in chapter 3.5.7 “Thermal expansion of corundum. spinel and other identified phases”. Among the possible phase transformations in the investigated model refractory castables, the transformations leading to the formation of spinel solid solutions have obviously the greatest role in shaping the microstructure and influencing the thermomechanical properties.

3.6 Conclusions

The introduction of impurities in the raw materials of model high alumina refractory castables affected the mechanics of cracking and facilitate the sintering at lower temperature by forming of small amounts of liquid phase. This also affects the thermomechanical properties of the investigated materials.

Thanks to high temperature x-ray diffraction investigations, it could be highlighted that the impurified raw materials (precursors) used to produce the model refractory castables were in an equilibrium state, which is probably also the case for secondary raw materials recovered from refractory linings that experienced extended service life. This equilibrium state resulted in the limitation of chemical reactions and phase transformations in the model castable's matrix. Among the identified phase transformations occurring at higher temperatures, the spinel formation in the model refractory castables containing the spinel forming agent (MgO) played the most crucial role in the development of an advantageous microstructure and driven improvements of thermomechanical properties while mitigating the negative effect of the presence of impurities.

The used hydratable alumina binder greatly affected the sintering behaviour of the model refractory castable, allowing them to sinter at relatively low temperatures. The castables were in a viscoplastic state during the sintering process. This had consequences for the thermomechanical properties of this type of castables and was clearly visible, among others, in creep measurements on these model castables. Under the conditions of the experiments, no material destruction stage was observed, even after a hundred-hour test.

Most observed changes of thermomechanical properties are likely to be associated with the appearance of a liquid phase in the model refractory castables and the formation of a microstructure specific to each model castables. The observed microstructural changes of the model refractory castables were related to the sintering of the matrix, grain growth and the formation of microcracks derived by differences in thermal expansion of phases, and in the case of the model spinel forming castables MHA-S, the formation of spinel solid solutions.

One important conclusion is that processes such as grain growth in the material matrix and the formation of ceramic bonds, which increase the thermomechanical strength of the investigated materials, do not keep up with the effects caused by the applied load (i.e. creep). This is a valuable clue that materials of this type, namely bonded with hydratable alumina, should not be use in applications where there is a high mechanical load during initial heating. However, after the first heating, significantly higher resistance to deformation were assessed according to refractoriness under load measurements.

It is important to bear in mind that the combination of impurities selected for the preparation of the impurified raw materials used to prepare the investigated model refractory castables, represented the most unfavourable cases in terms of thermomechanical properties as the formation of liquid phase formation was specifically maximized. This in turn highlighted that these model castables, and, by extension, refractory products using secondary raw materials, could still be used for tailored applications with defined application temperature. Finally, it should be possible to deduce mutual proportions of impurities for which the deterioration of thermomechanical properties should not be that critical, or even beneficial for some applications.

3.7 References

[1] Hart, L.D.; Lense, E.: Alumina Chemicals: Science and Technology Handbook, American Ceramic Society Inc, Westerville, Ohio, 1990.

[2] Schnabel, M.; Buhr, A.; Schmidtmeier, D. et al.: Perceptions and characteristics of fused and sintered refractory aggregates, Refractories WORLDFORUM 7 (4) (2015) 75–81.

[3] Alex, J.; Vandeperre, L.; Touzo, B.; Parr, C.; Lee, W.E.: Effect of sodium impurities on phase and microstructure evolution in calcium aluminate cement bonded castables at high temperatures, Proceeding of UNITECR (2013) 832–837.

[4] Möhmel, S.; Weissenbacher, M.; Kurz, B.; Joubert, O.: The influence of different raw materials on the behaviour of low cement castables, Proceeding of UNITECR (2015).

[5] Da Luz, A.; Gomes, D.; Pandolfelli. V. C.: Maximum working temperature of refractory castables: Do we really know how to evaluate it? CI. 43. 12. p. 9077-9083. (2017)

[6] Rodrigues, J.A.; Santos, S.F.; Pandolfelli, V.C.: Brittle-ductile transition of an Al_2O_3-SiO_2 refractory material, in: Advances in Refractories for the Metallurgical Industry IV, Fourth Intern. Symp., 43rd Annual Conf. Of Metallurgists of CIM, 2004. Hamilton, CA.

[7] Goncalves, L.R.G.; Pandolfelli, V.C.: Hot erosion evaluation of fluid flash calciner refractory castables, Proceedings of UNITECR (2009).

[8] Brochen, E.; Dannert, C.; Holleyn, F.; Krause, O.; Rathaj, M.; Podwórny, J.; Dudek, K.: Matrix design in high alumina refractory castables – Part II: assessment of the brittle-ductile transition temperature and ways to influence it, Proceedings of UNITECR (2019).

[9] Jin, S.; Harmuth, H.; Gruber, D.: Compressive creep testing of refractories at elevated loads—Device. material law and evaluation techniques. Journal of the European Ceramic Society. 34(15). (2014). p. 4037–4042. DOI: 10.1016/j.jeurceramsoc.2014.05.034

[10] Samadi, S.; Jin, S.; Gruber, D.; Harmuth, H.; Schachner, S.: Statistical study of compressive creep parameters of an alumina spinel refractory. Ceramics International 46(10). 2020. p. 14662-14668. DOI: 10.1016/j.ceramint.2020.02.267

[11] Bradt, RC.; Harmuth, H.: The Fracture Resistance of Refractories. Refractories Worldforum. 3 [4] 129-135 (2011).

[12] Swain, MV.: R-curve behavior and thermal shock resistance of ceramics. J. Am. Ceram. Soc.. 73 [3] 621-28 (1990).

[13] Hasselman, DPH.: Unified theory of thermal shock fracture initiation and crack propagation in brittle ceramics. J. Am. Ceram. Soc. 52 [11] 600-604 (1969).

[14] Hasselman, DPH.: Rolle der Bruchzähigkeit bei der Temperaturwechselbeständigkeit feuerfester Erzeugnisse. Proceedings of 19th International colloquium on refractories. Aachen. Germany. 195-201. 1976.

[15] Nakayama, J.: Bending Method for Direct Measurement of Fracture Surface Energy of Brittle Materials. Jap. J. Appl. Phys. 3 [7] 422-423 (1964).

[16] Fryda, H.; Scrivener, KL.; Chanvillard, G.: Relevance of Laboratory Tests to Field Application of Calcium Aluminate Cement Concretes. Calcium Aluminate Cements 2001. Edited by Mangabhai R. J. and Glasser F. P. ISBN 1-86125-142-4. pp.227-246.

[17] Turrillas, X.; Convert, P.; Hansen, T.; De Aza, AH.; Pena, P.; Rodriguez, MA.; De Aza, S.: The Dehydration of calcium Aluminate Hydrates Investigated by Neutron Thermodiffractometry. Calcium Aluminate Cements 2001. Edited by Mangabhai R. J. and Glasser F. P.. ISBN 1-86125-142-4. pp.517-531.

[18] Nakagawa, Z.; Enomoto, N.; Yi, I.S.; Asano, K.: Effect of corundum/periclase sizes on expansion behavior during synthesis of spinel, Proceedings of UNITECR'95, Kyoto, Japan (1995) 1312–1319.

[19] Braulio, M.A.L.; Rigaud, M.; Buhr, A.; Parr, C.; Pandolfelli, V.C.: Spinel-containing alumina-based refractory castables. Ceramics International 37 (2011) 1705-1724, doi:10.1016/j.ceramint.2011.03.049.

[20] Shannon, R.D.: Revised effective ionic radii and systematic studies of interatomic distances in halides and chalcogenides. Acta Crystallographica, A32, (1976) 7 5l:I 67.

[21] Luz, A.P.; Gomes, D.T.; Pandolfelli, V.C.: Maximum working temperature of refractory castables: do we really know how to evaluate it? Ceramics International 43(12), (2017), 9077-9083, DOI: 10.1016/j.ceramint.2017.04.053.

4. Subproject III – Investigation of the high temperature performance of refractories close to service conditions

4.1 Need #3: Innovative testing procedure that allows investigating the high temperature performance of refractories under dynamic, real-life in-use conditions

Refractory linings typically work in a temperature gradient. For monolithic linings this means that the material is composed of a continuous succession of layers in different state, from highly sintered at the hot face to almost green state at the cold face. Over this profile the material behaves heterogeneous. The thermal expansion at the hot face leads to compressive stresses which promote densification of the microstructure, trigger substantial change in the refractory properties and affect its high temperature performance.

At present, standardised testing procedures like “refractoriness under load” or “creep in compression” work under quasi-static and isothermal conditions and do not take into consideration temperature gradients or realistic mechanical load during testing. As a result, the effect of impurities from secondary raw materials on the high temperature behaviour of refractories still cannot be completely understood.

Accordingly, the third need (need #3) that was addressed in this CORNET project was to provide an innovative testing procedure that allows investigating the high temperature behaviour of refractories under dynamic, real-life in-use conditions. With this need fulfilled, the effect of impurities from secondary raw materials on the high-temperature behaviour of refractories under real-life conditions could be investigated to support need #1.

4.2 State of the art

The common denominator for most refractory product applications is that they must withstand high temperatures and substantial loads [1]. In case of refractory linings, only one side of the structure is typically exposed to the process heat, resulting in a steep thermal gradient within the lining. With regards to the mechanical loadings of the refractory linings, these have two main origins. Firstly, individual parts of typical refractory structures support the weight of the parts which are above them. For example, in a brickwork lining, the bricks in the lower part support the weight of all the other bricks above them. Secondly, as temperatures rise in the lining, the hot part of the structure expands and, when at last the expansion joints are closed and/or the cold part of lining cannot follow anymore the thermal expansion of the hot part, the free thermal expansion of the hot part is retrained and significant compressive stresses arise near to the hot face of the lining (Fig. III.1). The combined effect of the thermal gradient and compressive stresses near to the hot face leads to an inhomogeneous evolution of the microstructure and properties of the refractory materials. This is expected to play a critical role and significantly impact the high temperature and long-time performance of refractory linings.

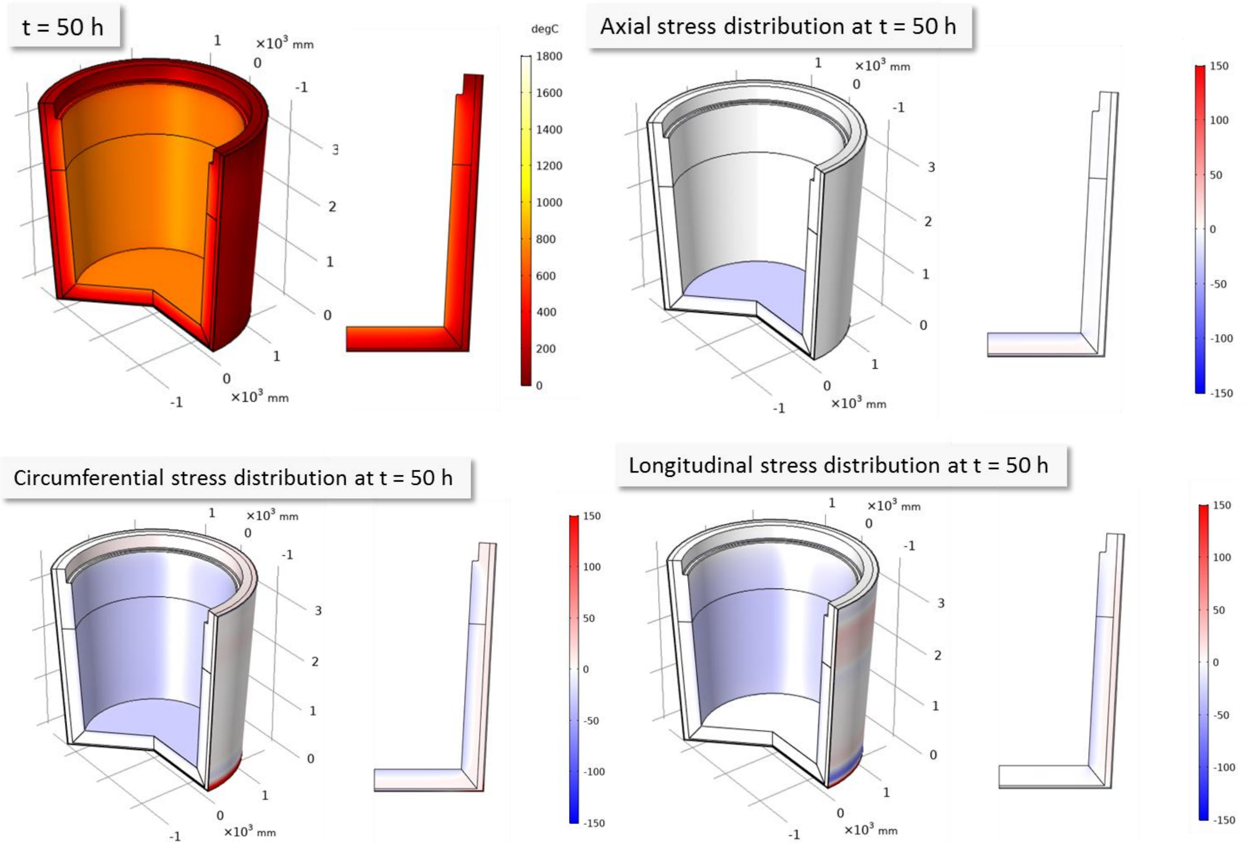

Fig. III.1: Temperature (in °C) and stresses (in MPa) distribution after 50 h of a simulated pre-heating of a steel ladle (material behaviour was assumed to be isotropic linear elastic, neglecting creep effects).

4.2.1 Investigation of the high temperature performance

Besides expensive, time-consuming and risky field tests of monolithic linings, there are virtually two ways to investigate, in laboratory, the behaviour of refractory materials exposed to the basic thermomechanical loading that refractories experience in use:

1) Assess and appraise the material parameters that describe the behaviour of the materials exposed to thermomechanical loading. However, most the usual testing methods tend to focus on a single facet of the material's behaviour under very narrow specified testing conditions, such as its compressive strength at a given temperature. The extrapolation and combination of this material parameters to understand the behaviour on the refractory products in service conditions is a complex task, it usually requires a great deal of empirical experience or well-designed models.
2) Applied close-to-service conditions to test pieces. Regarding the investigation of the behaviour of refractory products as part of an industrial lining and accordingly exposed to a thermal gradient and important compressive load in the plane closed to hot face, there are

no testing devices reported in the scientific literature that allow such investigations, at least of which the involved research performers are aware.

Currently, unless considering the thermal shock resistance, the characterization of refractory materials in the laboratory is mostly limited to test procedures in quasi-isothermal conditions. Some information on the behaviour of refractories experiencing thermal gradient might be obtained from thermal shock tests. However, standardized tests imply a dwell time at elevated temperature, which homogenises the temperature in the test piece and accordingly does not allow for a practice-relevant temperature gradient. The main focus of these tests is, of course, to trigger damage in order to appraise the resistance of the test pieces against thermomechanical stresses, not simulating the behaviour of the test piece as part of refractory lining. In fact, a testing procedure where test pieces are simply heated from one side and experience a thermal gradient comparable to those occurring in service for refractory lining is not challenging to implement, but fails to consider the impact of the compressive stresses at the hot face of a refractory lining. Neither the obtained microstructures, nor the observed deformations, would reflect accurately the evolution of the material as part of a refractory lining. On the other hand, test procedures that apply a compressive load on test pieces, especially the testing standards EN ISO 1893: Determination of refractoriness under load, and EN 993-9: Determination of creep in compression, rely on quasi-isothermal conditions. Both testing standards are carried out with the same testing equipment and similar testing procedure. A cylindrical refractory test piece (50 x 50 mm) is subjected to a constant load (0,2 MPa) while increasing the temperature (5 °C.min^{-1}). The deformation (height) of the test piece is recorded continuously. For the determination of refractoriness under load (RuL), the test is stopped once a prescribe deformation is attained, typically 5 % of its initial length [2]. In contrast, for the determination of creep in compression (CiC), once a specified temperature is reached, the heating is maintained constant for a given time. While both methods are prominently used to investigate the behaviour of refractory materials at high temperature, namely their refractoriness and the creep rate, the exerted load is actually very low and applied in one direction only. In service, much higher levels of stresses are expected and a biaxial loading state in the plane parallel to the hot face of refractory linings prevails [3].

4.2.2 Sintering behaviour of monolithics

In contrast to shaped products, refractory castables are usually not fired before being placed in furnaces, reactors or other processing units. In the best case, a recommended heating up schedule (usually provided by the refractory castable's supplier) is being applied at their hot face during the first heating up before operations start. As temperature increase inside the monolithic linings the progressive dehydration is observed. Physically and chemically bonded water is progressively removed. Most hydrate phases decompose at temperatures below 450 °C [4] [5]. Then, as diffusion processes become gradually activated (above circa 800 °C), calcium cations diffuse in the alumina grains to form calcium aluminates phases with higher and higher alumina contents. In parallel, the matrix gets coarser as smaller grains disappear while larger grains grow and undergo shape accommodation. Especially the intergrain contact zone enlarges (ceramic bond) to enable better packing of the structure. Usually all this leads to a densification of the monolithics, as well as significant changes in the properties of refractory material.

However, as heat is only provided through one side of a refractory lining, only the part of the lining close to the hot face undergoes all the previously described changes and eventually develop a ceramic bond once a sufficient temperature is reached. With increasing distance from the hot face, the temperature in the monolithic lining drops and becomes insufficient to efficiently promote sintering, while still high enough to dehydrate and thus weaken the hydraulic bond. Accordingly, linings made of refractory castables are highly heterogeneous over their thickness, which strongly influences their thermomechanical behaviour, far beyond the simple effect of temperature on a pre-existing (ceramic) bond such as by shaped products.

The sintering behaviour of refractory materials is usually tested in a static manner. That means that refractory materials are exposed to predefined temperatures for a given amount of time. Thereafter technological investigations like the determination of mechanical strength, bulk density/open porosity are accomplished, often at room temperature. This approach is extremely time consuming and implies a large amount of test pieces, since the total amount of measurements is, at least, the number of temperature steps to be investigated multiplied by the number of dwell time to be investigated. Hot stage microscopy is performed as well but delivers only a limited amount of information on a very small, hardly representative, volume of material.

Recent research work however demonstrates that the “method of monotonic heating” (MMH) is a powerful method to understand the sintering behaviour of refractories in detail [6]. MMH was originally developed for the determination of the thermal diffusivity of solid bodies and loose fillings [7] [8]. The principle of the method bases on the continuous measurement of the temperature gradient that occurs from the surface to the centre of a cylindrical or plate shaped test piece during heating with a constant heating rate. Therefore, the method is a dynamic method that enables data acquisition during heating (with any heating rate) and even during cooling with any time-temperature cycle. MMH appeared to be a powerful analytic method to detect, in situ, material changes during heating, for instance cause by sintering.

4.3 Materials and methods

4.3.1 Methods

The key to understanding and predict the behaviour of refractory monolithic products under thermo-mechanical loading in use, lies in the capacity to reproduce and actively monitor the evolution of the material in the laboratory. Two main investigation paths were therefore followed and/or developed to ensure a proper study of the thermo-mechanical loading of refractory monolithics, especially the influence of impurities introduced by secondary raw materials. Firstly, thermomechanical investigations were performed, most of them were carried out as part of subproject II led by the project partner Łukasiewicz - Instytut Ceramiki i Materiałów Budowlanych, but also included the assessment of the fracture behaviour thanks to wedge splitting measurements and the assessment of the sintering behaviour with the method of monotonic heating performed by FGF and described in this part of the report. In parallel, a new testing device was developed to carried out a close-to-service simulation of thermomechanical loading of the refractory products.

Results from both investigation paths were compared to each other including the results obtained by the other two involved research performers.

4.3.2 Thermomechanical investigations

4.3.2.1. Investigation of the fracture behaviour

Able to promote the stable fracture of large test piece, the Wedge Splitting Test (WST) has established itself to investigate the fracture behaviour of coarse grains material such as concretes and refractory materials [9]. Besides, the method can be adapted to be performed by high temperature and therefore investigate the thermomechanical properties of refractory products [10]. The test piece geometry and details of the test principle are displayed in the figure III.2. A cubic test piece (100 x 100 x 75 mm³) is prepared including a starter notch and two guide notches. Besides, a large groove is machined into the test piece to accommodate the mechanism that transmits the load applied on a wedge into the test piece. During a test, the vertical force F_M applied by a press is converted into two horizontal forces F_H by means of a prismatic wedge and the load transmission pieces. The two horizontal forces cause the test piece to split. The main advantage of the method is to promote stable propagation of cracks despite a high fracture area (circa 65 mm x 65 mm), representative of the typical coarse grain structure of refractory products.

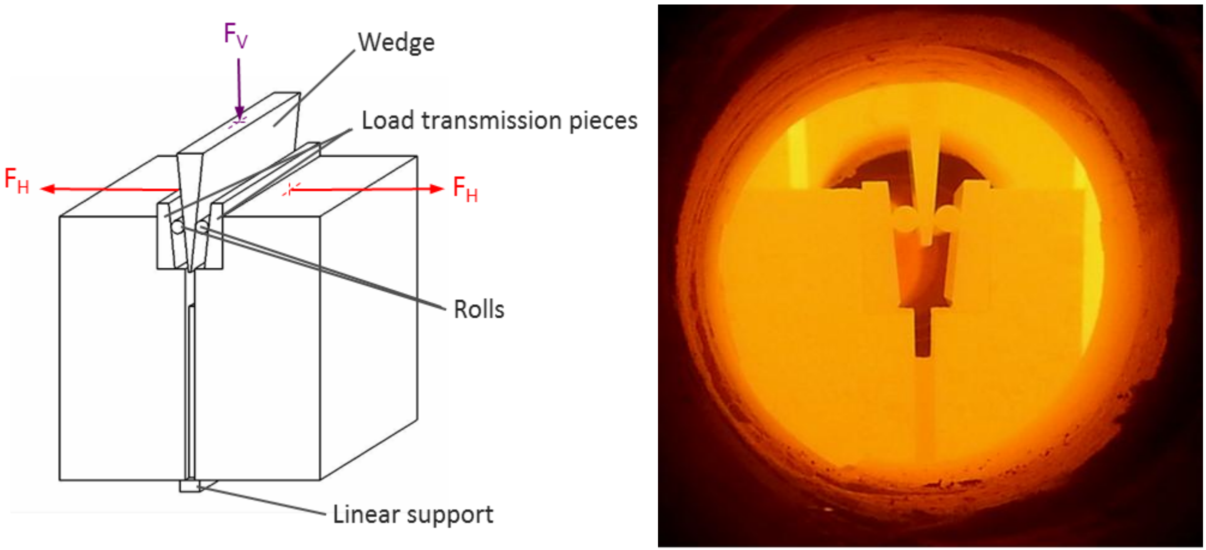

Fig. III.2: (a) Principle of the wedge splitting test, (b) test piece heated to 1200 °C.

During the whole fracture process, the applied force and the opening of the test piece δ are recorded and compiled in a load-displacement diagram.

The specific fracture energy G_f is calculated by integrating the horizontal force on the horizontal displacement δ_H:

$$G_F = \frac{1}{A}\int_0^{\delta_{ult}} F_H \, d\delta_H \qquad \text{(III.1)}$$

δ_{ult} corresponds to the ultimate horizontal displacement (opening) of the test piece during the wedge splitting measurement and A is the fracture surface area. In addition, a nominal notch tensile strength is determined according to the following equation:

$$\sigma_{NT} = \frac{F_{H\max}}{b \cdot h} + \frac{6 \cdot F_{H\max} \cdot y}{b \cdot h^2} \tag{III.2}$$

Here $F_{H\max}$ denotes to the maximum horizontal force measured in the load/displacement diagram, b and h the width and the height of the created fracture surface and y the orthogonal distance of the line of impact of the horizontal force to the centre of gravity of the fracture surface area. With numerical curve fitting, the modulus of elasticity may also be determined.

In order to carry out wedge splitting test at elevated temperatures, a furnace setup with controlled atmospheric conditions is used (Fig. III.2 (b)) and combined with a in-situ optical determination of the opening of the test pieces during testing [11]. Finally, two measurements per tested temperature were performed for each castable formulation in order to check for the reliability of the assessed load-displacement diagrams. If necessary, a third measurement was performed.

4.3.2.2. Investigation of the sintering behaviour of castables with the Method of Monotonic Heating (MMH)

As an alternative to the standardized methods, the “Method of Monotonic Heating” (MMH) allows the investigation of the thermal diffusivity of refractory products above 1250 °C and up to their operating temperature in the most favourable cases [6]. The principle of the measurements is based on the monitoring of the heat distribution in test piece with a defined geometry while being heated up (Fig. III.3**Fehler! Verweisquelle konnte nicht gefunden werden.**). Considering a one-dimensional heat flow during a monotonic heating (i.e. with constant heating rate), the thermal diffusivity is described by the Fourier’s 2nd law:

$$\frac{\delta T}{\delta t} = a\frac{\delta^2 T}{\delta x^2}\left[\frac{K}{s}\right] \tag{III.3}$$

The solution for plate or cylinder of infinite size that is symmetrically warmed from the sides with a constant rate is given by

$$a_{app} = \frac{b \cdot x^2}{n \cdot (T_x - T_0)} \tag{III.4}$$

Where a_{app} is the apparent thermal diffusivity calculated from the measurements, b is the heating rate in the centre of the test piece, x is the distance between the thermocouples in the centre and close to the surface and n is a geometric coefficient (cylinder: n = 4; plate: n = 2).

Should the Method of Monotonic Heating be used to actually determine the thermal diffusivities of ceramics, additional terms for correction in equation III.4 have to be introduced. They are need to consider the temperature dependence of the thermo-physical properties of the test piece materials as well as the non-linear heat flow in the test pieces. However, these additional terms turned out to be small in an optimised experimental setup, as described in [6], and provide no additional information regarding the investigations of the sintering behaviour as described below:

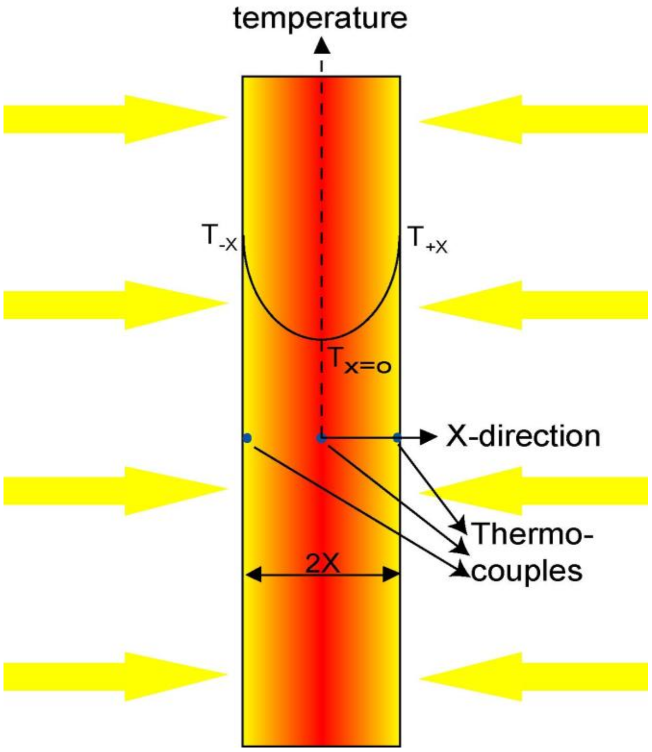

Fig. III.3: Temperature distribution in a Monotonic Heating test piece and position of the thermocouples.

Beside the determination of thermal diffusivities, MMH provides highly valuable information that indicates sintering processes, melting and other phase transformations in the investigated test pieces. This is based on two effects:

1. Changes in the test piece microstructure since sintering modify the apparent thermal diffusivity in an irreversible way.
2. Phase transformations usually release or absorb heat (endothermal or exothermal reactions) and therefore transiently increase or decrease the temperature difference between the surface and the centre of a MMH test piece as well as the heating rate at the centre of the test piece (equation (III.3)). This causes positive or negative peak- like deviations in MMH-curves. Such effects can only be assessed by dynamic methods like MMH.

In the framework of the present investigation, part of the MMH measurements were carried out two times on the same test piece, the second time with increasing the maximal test temperature. Hence the influence of each heating step on the apparent thermal conductivity could be assessed and accordingly an enhanced differentiation between each stage of refractory material's evolution achieved.

4.3.3 New testing device to investigate the simultaneous effect of thermal gradient and high load near to the hot face of refractory linings

4.3.3.1. Experimental setup

In order to simulate the behaviour of refractory products as part of a lining in service, a new testing system has been developed (Fig. III.4). The testing system triggers a realistic thermal gradient in a prismatic test piece (54 x 54 x 230 mm). This has been achieved by heating the test piece through one of its small end faces (54 x 54 mm), later called hot face, thanks to a laboratory furnace with a fitting opening (Fig. III.5).

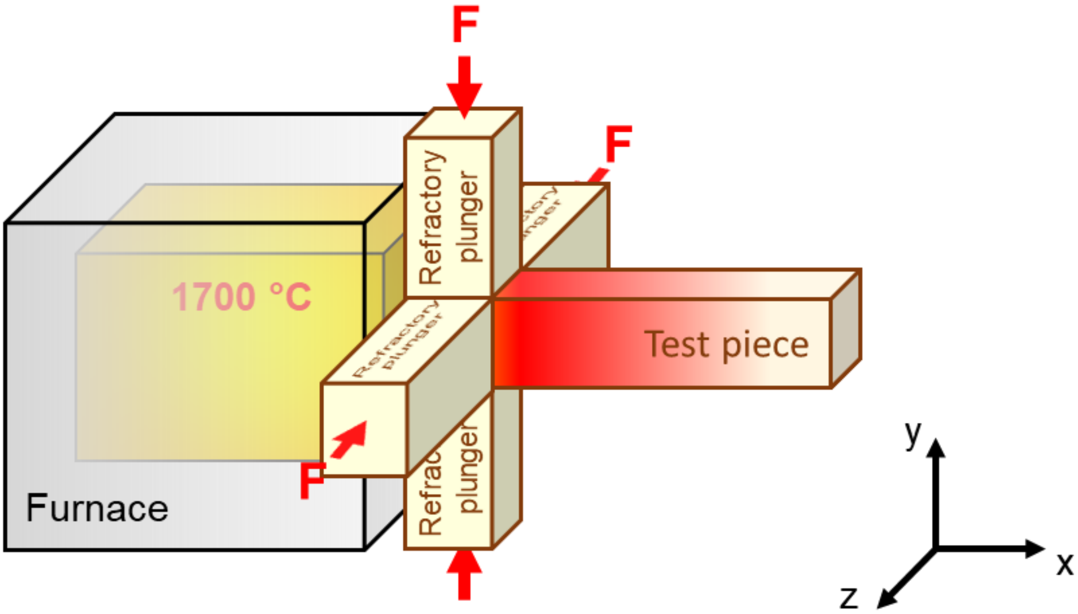

Fig. III.4: Schematic representation of the new testing system and the testing procedure to investigate the combined effect of mechanical loading and thermal gradient.

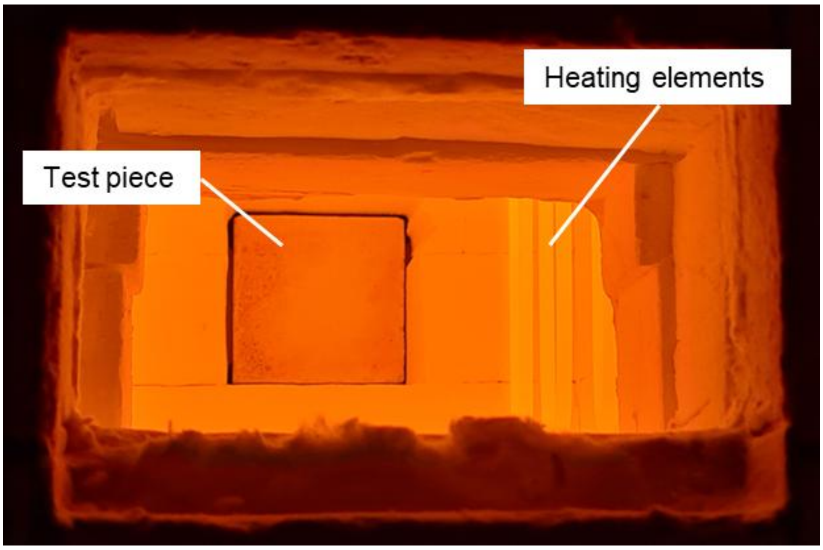

Fig. III.5: Inside of the furnace during heating.

The maximum operating temperature of the laboratory furnace, and accordingly the maximum temperature at the hot face of the test piece, is 1750 °C. During heating, temperature differences of several hundred Kelvin arise between the two small end faces of the test piece (x-direction). Simultaneously, the testing system mimics the thermomechanically induced compressive stresses at the hot face of refractory linings (in the y-z-plane). This was accomplished by applying a load F onto the test piece or constraining the free thermal expansion of the test piece perpendicular to the thermal gradient near to the hot face (Fig. III.4). These loads or constraints are applied to the test piece through four refractory "plungers" (54 x 54 x250 mm), two of those fixed and the other two mobile. Each of the two mobile plungers is connected to a servomotor that is fixed to a robust frame made of high-strength aluminium and can build up compressive forces up to 4 kN (Fig. III.6). The displacements of the mobile plungers are monitored by Linear Variable Differential Transformer (LVDT).

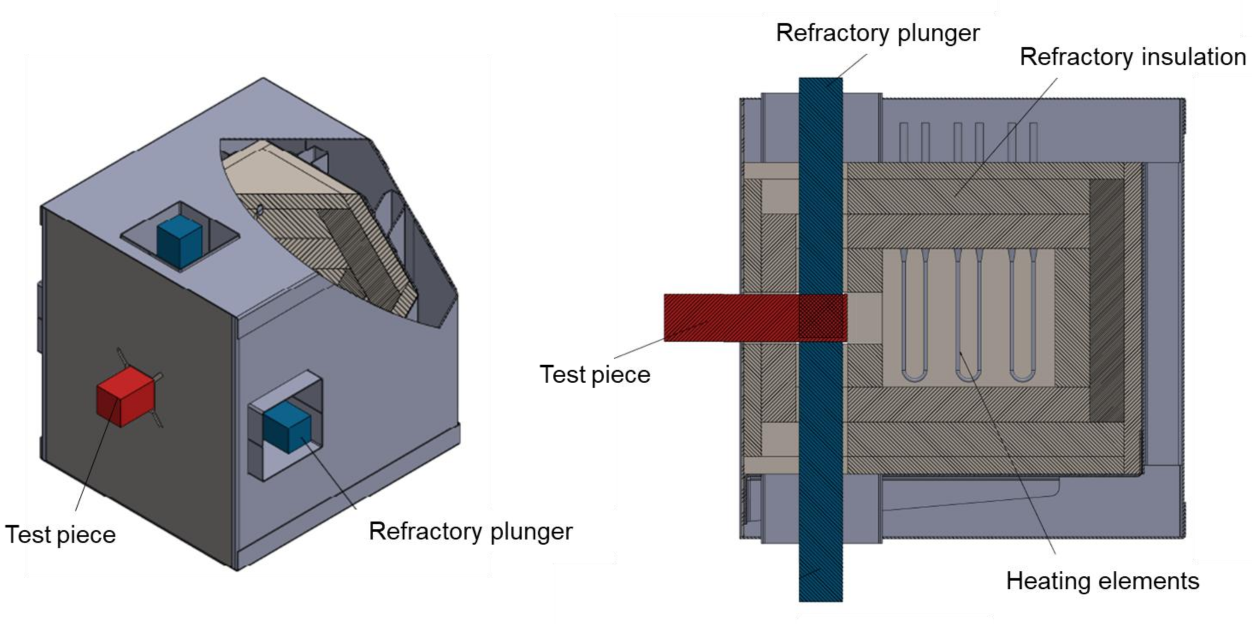

Fig. III.6: Design model of the furnace to heat a test piece through one of its smaller end faces (hot face) and apply load or constraint near to the hot face.

4.3.3.2. Testing strategy

Test pieces made of the investigated materials were heated from one end face with a rate of 5 K.min^{-1}. Two different loading conditions were considered:

- applying a constant load/force near to the hot face of the test piece and following the displacement of the mobile refractory plungers,
- restricting the free thermal expansion of the test piece by blocking the displacement of the mobile refractory plungers and following the evolution of the resulting force.

These two loading configurations can be applied separately on each of the two directions perpendicular to the hot face. Hence, it is possible to just exert a uniaxial loading or perform a biaxial loading. In the case of a biaxial loading, the same configuration can be used in both direction (i.e. constant load or restriction of the free thermal expansion) or a combination of the two different loading combinations (i.e. constant load in one direction and restriction of the free thermal expansion in the other direction) can be applied.

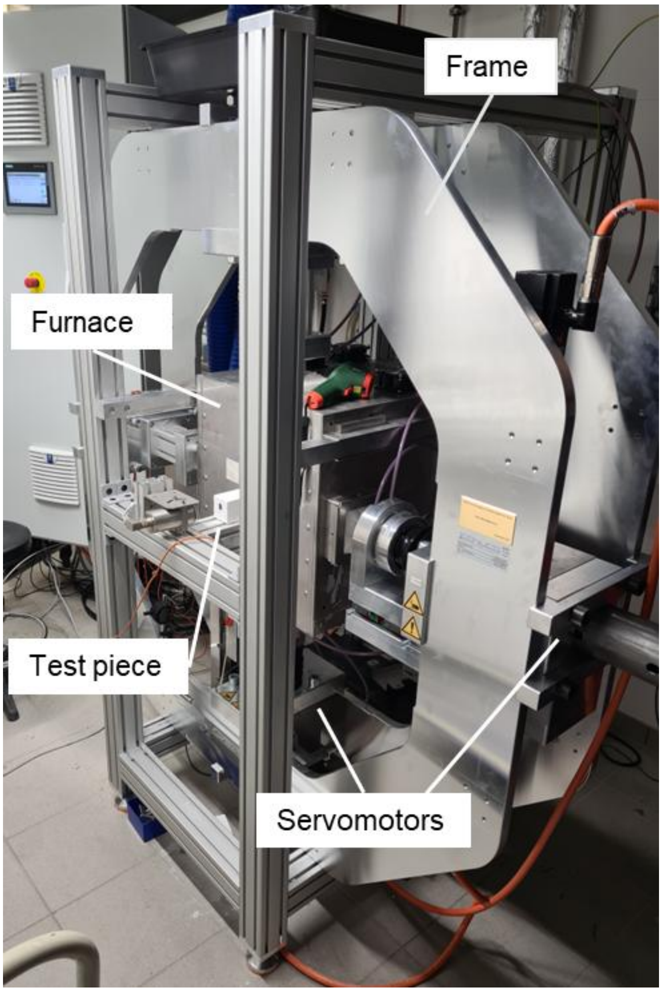

Fig. III.7: New testing system to investigate the combined effect of mechanical loading and thermal gradient.

4.3.4 Materials

4.3.4.1. Formulation

As a base for the investigation, the castable formulations developed and produced by Hochschule Koblenz (subproject I) were used. They are designed to study the influence of impurities typically found in secondary raw materials. As a matter of practicability, a brief description of the model castables provided by Hochschule Koblenz to FGF for the investigations is set forth hereafter.

Tabular alumina (T60/64 from Almatis GmbH, Germany) was spiked with 2 % impurities (SiO_2, Na_2O, CaO, TiO_2, and Fe_2O_3) and used to substitute the grain fraction 0-45 µm of the preparation of the reference model castable (REF_MHA) as listed in the table III.1. The selected impurities are either typically production process-related contaminations, or residue from previous industrial use (secondary raw materials) such as contamination by metallurgical slags. Based on the results from FactSage simulations, five, particularly critical, different combinations of different impurities were selected. The preparation steps for the impurification consisted in 1) Mixing of the tabular alumina with the selected impurities, 2) Pelletizing for a proper connection, 3) Sintering for phase transformation/integration, 4) grinding and screening to fraction of 0-45 µm. The quality of the impurified tabular alumina was then checked with XRF for the concentration of impurities and homogeneity.

After grinding (step 4), all precursors displayed similar particles size distributions, which were quite close to the particles size distribution of the fraction they substitute (0-45 µm), and exhibit the expected chemical composition.

Tab. III.1: Composition of the model reference castable MHA_REF and the impurified formulations MHA_2CS, MHA_2NS, MHA_2FC, MHA_2FCS and MHA_2TCS, where the tabular alumina fraction 0-45 µm has been substituted by the impurified tabulable alumina.

Castable	**MHA_REF**	**MHA_2CS**	**MHA_2NS**	**MHA_2FC**	**MHA_2FCS**	**MHA_2TCS**
Tabular alumina (T60/64)						
0,2-3,0 mm	57	57	57	57	57	57
0,0-0.2 mm	12	12	12	12	12	12
0-45 µm	9	-	-	-	-	-
Impurified tabular alumina						
0-45 µm	-	9	9	9	9	9
Calcined alumina (CTC20)	10	10	10	10	10	10
Reactive alumina (RG4000)	7	7	7	7	7	7
Hydratable alumina (Alphabond 300)	5	5	5	5	5	5
Sum	**100**	**100**	**100**	**100**	**100**	**100**
Dispersing agent (PCE) – Castement FS60	6,3	6,3	6,3	6,3	6,3	6,3
Water	0,15	0,15	0,15	0,15	0,15	0,15

MHA = Monolithic Hydratable Alumina; C = CaO, S = SiO_2, N = Na_2O, CaO, F = Fe_2O_3 and T = TiO_2

High alumina cement-free refractory castables (self-flowing, max. grain size 3 mm) present the decisive advantage to be a relatively simple and convenient model with a well-defined and homogeneous composition, so that the effect of impurification (in the 0-45 µm fraction with the developed precursors) should be easy to spot and investigate. To increase the relevance of the study to the more and more prominent castable using spinel, a high alumina cement-free spinel forming formulation was also developed (

Tab. III.2).

Tab. III.2: Composition of the model reference castable MHA_S_REF and the impurified formulations MHA_S_2CS, MHA_S_2NS, MHA_S_2FC, MHA_S_2FCS and MHA_S_2TCS, where the tabular alumina fraction 0-45 µm has been substituted by the impurified tabulable alumina.

Castable	**MHA_S_REF**	**MHA_S_2CS**	**MHA_S_2NS**	**MHA_S_2FC**	**MHA_S_2FCS**	**MHA_S_2TCS**
Tabular alumina (T60/64)						
0,2-3,0 mm	57	57	57	57	57	57
0,0-0.2 mm	10	10	10	10	10	10
0-45 µm	9	-	-	-	-	-
Impurified tabular alumina						
0-45 µm	-	9	9	9	9	9
Calcined alumina (CTC20)	10	10	10	10	10	10
Reactive alumina (RG4000)	7	7	7	7	7	7
Hydratable alumina (Alphabond 300)	5	5	5	5	5	5
Magnesia (Nedmag DIN70)						
0-0,09 mm	2	2	2	2	2	2
Sum	**100**	**100**	**100**	**100**	**100**	**100**
Dispersing agent (PCE) – Castement FS60	6,3	6,3	6,3	6,3	6,3	6,3
Water	0,15	0,15	0,15	0,15	0,15	0,15

4.3.4.2. Preparation of the test pieces

After mixing in an intensive mixer (type R02E, EIRICH), the model castables were cast into custom-made moulds to produce 100 x 100 x75 mm for the investigation of the fracture behaviour. They were then machined with a precision saw to obtain the wedge splitting test pieces.

A special mould was used to cast test pieces for the method of monotonic heating measurement. It allowed the integration of the thermocouples to the test pieces in a reproducible and effective manner.

Finally, format B alike prismatic test pieces (54 x 54 x 230 mm) were used for the new testing device to investigate the simultaneous effect of thermal gradient and high load. Typically, format B test pieces are cast in a way that the so-called cast skin (i.e. part of the test piece that in not in contact with the mould and accordingly less well-defined) correspond to one of its long side (54 x 230 mm). However, since in order to apply the load in the two perpendicular directions near and parallel to the hot face, the refractory plungers need to come into contact with a well-defined surface so that a homogeneous transmission of the load is ensure. Accordingly, a new mould was produced and used to prepare test pieces with four well-defined long side where the load can be applied, one well-defined small side (54 x 54 mm) exposed to the furnace temperature during test and one small side presenting the cast skin.

All test pieces were stored for 24 h in a climate chamber at 20 °C and a humidity of 95 %. Then they were demoulded to be dried at 100 °C for 24 h.

4.4 Results and discussion

4.4.1 Thermomechanical investigations

4.4.1.1. Investigation of the fracture behaviour

The reference model castable shows a rather low strength, which decreased further with increasing temperature (Tab. III.3, Fig. III.8). This is neither unusual nor problematic for cement-free (hydratable alumina bonded) refractory castables. The specific fracture energy is accordingly moderate, but shows a clear increase at 1250 °C, which coincides with a slowing down or stabilisation of the strength loss. At 1400 °C and above, the strength loss resumes, so that only low values for the specific fracture energy can be determined.

For the subsequent investigations, primarily for the purpose of studying the impact of the impurification on the thermomechanical behaviour on the model castable, the two most relevant temperatures were selected. Since wedge splitting measurements at high temperature are time consuming, this helped to keep the investigation at a reasonable and manageable level. 1000 °C was the first selected temperature as the characterisation of the reference model castable highlighted this temperature as a first minimum of the fracture properties and accordingly a rather critical temperature for the model castables. Provided that the room temperature mechanical properties of the castable with and without impurities were similar (which was the case, see section 2.5.2), it was expected that the impact of the impurities at this temperature should be very moderate (no melt formation expected) while 1000 °C could already be considered as high temperature. The second selected temperature was 1250 °C, since it corresponds to the maximum of the fracture properties at high temperature. The influence of the impurities should be accordingly the most prominent at this temperature.

Tab. III.3: Measured thermomechanical properties for the reference model castable after a dwell time of 1 hour at the testing temperature (two measurements per temperature).

Temperature / °C	**$G_f'^{1)}$ / N/m**	**σ_{NT} / MPa**	**$E^{2)}$ / GPa**
Room Temperature	47	5,0	40,0
450	40	3,6	28,0
700	64	2,4	23,0
1000	26	0,7	5,5
1250	107	0,6	1,8
1400	59	0,2	0,4
1500	7	0,2	0,1

$^{1)}$ G_f': specific fracture energy calculated up to a drop of 90 % in the maximum load

$^{2)}$ Indicative value assessed from the load-displacement diagrams

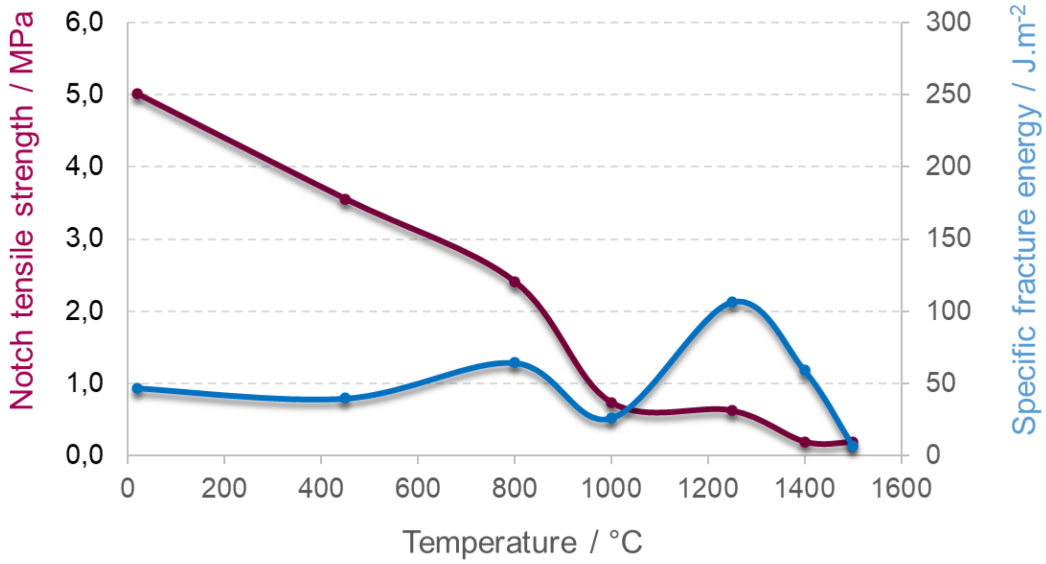

Fig. III.8: Evolution of the notch tensile strength and specific fracture energy after a dwell time of one hour as a function of temperature for the reference cement-free model castable.

As a rather industrial relevant alternative, the spinel-forming model castable was characterised at one additional temperature, namely 1400 °C (Tab. III.4). It displayed improved properties over the reference model castable without additives (Fig. III.9), both the measured strength and specific fracture energy were higher. The reason for higher values for the spinel forming reference model castables already by 1000 °C is not completely clear, but the formation of spinel within the matrix of the castable above circa 1200 °C, toughening the castable, should explain its improved behaviour at high temperatures. It should however be noted that the ratio specific to notch tensile strength increased steadily with increasing temperature for both reference model castables (i.e. without and with spinel forming additives), indicating in both case an increase of the ductility with increasing temperature.

Tab. III.4: Measured thermomechanical properties for the reference spinel forming model castable after a dwell time of 1 hour at the testing temperature (two measurements per temperature).

Temperature / °C	**$G_f'^{1)}$ / N/m**	**σ_{NT} / MPa**	**$E^{2)}$ / GPa**
1000	35,6	1,2	11,0
1250	165,8	1,1	4,8
1400	290	1,0	2

$^{1)}$ G_f': specific fracture energy calculated up to a drop of 90 % in the maximum load

$^{2)}$ Indicative value assessed from the load-displacement diagrams

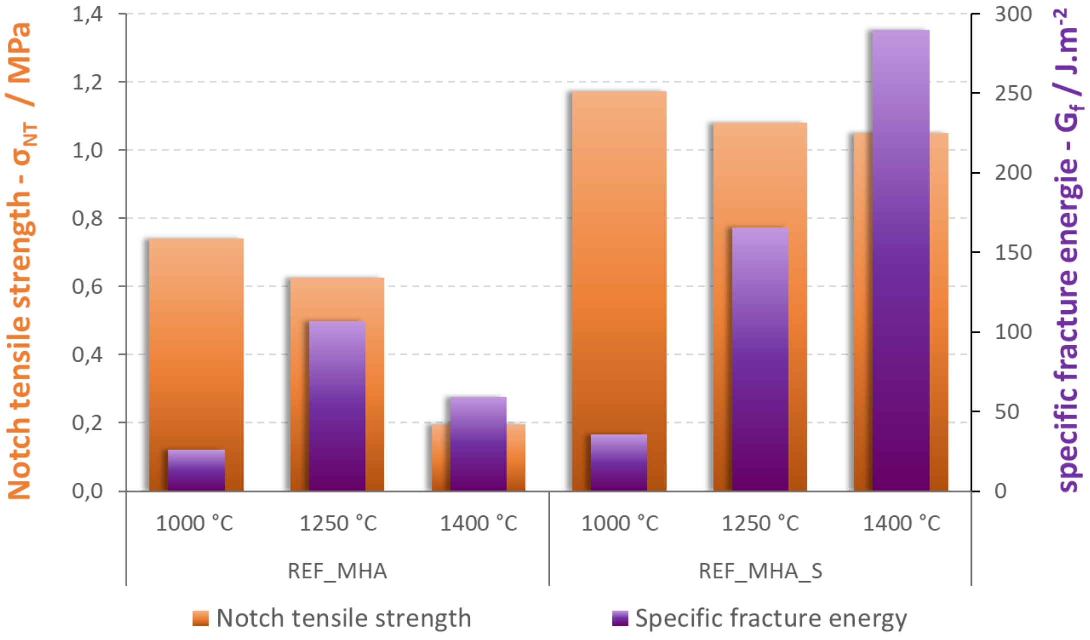

Fig. III.9: Comparison between the high temperature fracture properties of the reference model castable (REF_MHA) and reference model castable with spinel forming additives (REF_MHA_S).

The introduction of impurities into the model castables led almost systematically to a deterioration of the fracture properties compared to the impurity-free reference model castable at high temperature, namely 1200 °C (Tab. III.5, Fig. III.10). The formation of liquid phase in the matrix according to FactSage calculations, which is not expected in the impurity-free reference model castable MHA_REF at this temperature (see chapter 3.3.1 “Thermochemical predictions”), explain in all likelihood this behaviour. Besides and despite all formulations having very similar room temperature mechanical properties, two of the castable formulations containing impurities, MHA_2CS and MHA_2FCS, displayed comparably worse fracture properties already at 1000 °C. This behaviour could not be explained, especially since according to FactSage calculations no liquid phase is expected at this temperature in both cases. Inversely, and equally difficult to explain, the castable formulation containing titanium, calcium and silicon oxide as added impurities, MHA_2TCS, presented improved strength at 1000 °C when compared to the reference model castable MHA_REF. The most surprising result was observed for the model castable where the combination of the impurities iron and calcium was added, namely MHA_2FC. At 1000 °C, MHA_2FC presented similar properties to the reference model castable MHA_REF, but both the strength and specific fracture of the model castable were higher than MHA_REF at 1250 °C. This combination is also the one that, according to FactSage calculations, should lead to the formation of the lowest amount of liquid phase at 1250 °C (Fig. II.3). This may be a hint that a small amount of liquid in the matrix could be beneficial to improve the fracture behaviour of refractory materials, especially improving their ductility, while too large amounts of liquid are, as expected, detrimental.

Tab. III.5: Measured thermomechanical properties for the impurified model castables (two measurements per temperature).

Castable	Temperature / °C	$G_f'^{1)}$ / N/m	σ_{NT} / MPa	$E^{2)}$ / MPa
MHA_2CS	1000	12	0,4	1,5
	1250	3	0,1	0,8
MHA_2FCS	1000	9	0,3	1,5
	1250	17	0,2	0,4
MHA_2NS	1000	19	0,7	3,0
	1250	4	0,2	0,4
MHA_2FC	1000	24	0,8	4,8
	1250	140	0,7	2,4
MHA_2TCS	1000	33	1,2	6,8
	1250	21	0,5	2,7

[1] G_f': specific fracture energy calculated up to a drop of 90 % in the maximum load

[2] Indicative value assessed from the load-displacement diagrams

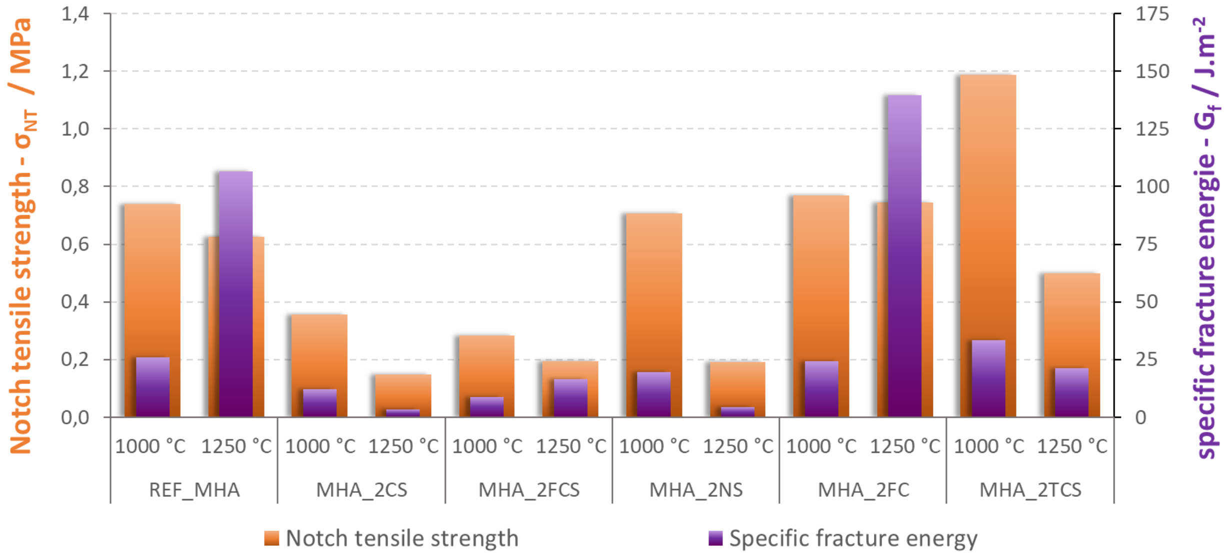

Fig. III.10: Comparison between the high temperature fracture properties of the reference model castable (REF_MHA) and impurified model castables (MHA_2CS, MHA_2FCS, MHA_2NS, MHA_2FC and MHA_2TCS).

The addition of the selected combination of impurities into the spinel-forming model castable was found to have a less marked impact on the fracture properties than for the spinel-free formulations (Tab. III.6, Fig. III.11). The deterioration of the fracture properties was not the quasi-systematic outcomes, and should deterioration have occurred, it was to a lesser extent. Spinel forming formulation proved to be much more tolerant to impurities, which corelates with a tendency to form low amount of liquid at the testing temperature. Spinel is known for its capacity to accommodate foreign species in its structure, which are then not available to form melts or to lower the temperature of apparition of the first liquid and lower its viscosity.

More unexpectedly, two combinations of impurities added to the spinel forming model castables, MHA_S_2CS and MHA_ S_2TCS, led to the explosive spalling of the test pieces during their heating. The reason for this increase sensitivity to explosive spalling remains to be clarified. The simultaneous release of chemically bonded water from the hydrated hydratable alumina (bonding system) and from the hydrated magnesia (brucite formed during the wet mixing and curing of the spinel-forming model castable) is likely to explain why spinel-forming model castables are more prone to explosive spalling, but fail to explain why the combination of calcium and silicon oxide or titanium, calcium and silicon oxide systematically exploded during the heating process and not any of the other combination of impurities or neither the spinel-forming reference model castable.

Tab. III.6: Measured thermomechanical properties for the impurified spinel-forming model castables (two measurements per temperature).

Castable	**Temperature / °C**	**$G_f'^{1)}$ / N/m**	**σ_{NT} / MPa**	**$E^{2)}$ / MPa**
MHA_S_2CS	1000	-	-	-
	1250	-	-	-
MHA_S_2FCS	1000	50	1,6	7,8
	1250	220	1,7	5,8
MHA_S_2NS	1000	49	1,5	8,0
	1250	55	1,0	5,5
MHA_S_2FC	1000	36	0,9	4,8
	1250	193	1,3	4,0
MHA_S_2TCS	1000	-	-	-
	1250	-	-	-

- : no values could be assessed as the test pieces exploded during the heating process before reaching the testing temperature

1) G_f': specific fracture energy calculated up to a drop of 90 % in the maximum load

2) Indicative value assessed from the load-displacement diagrams

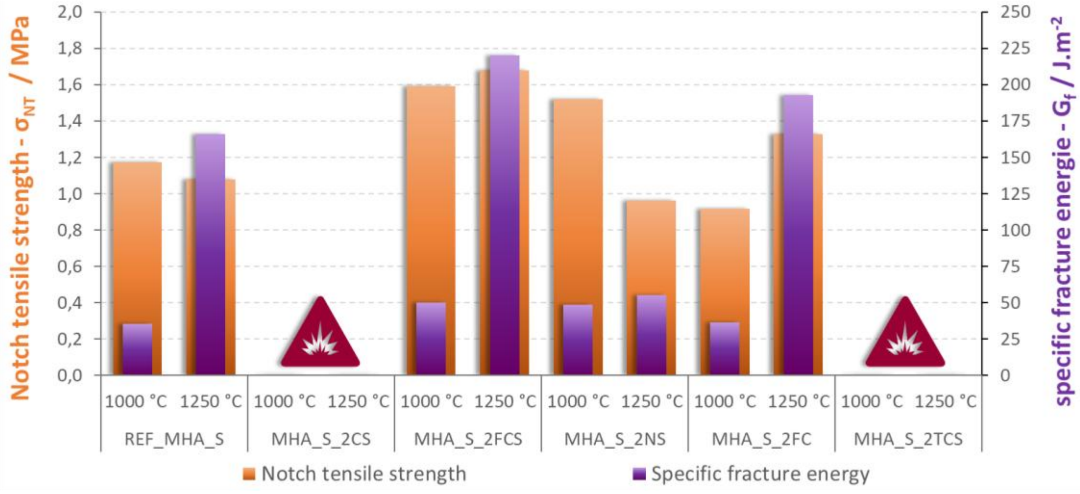

Fig. III.11: Comparison between the high temperature fracture properties of the reference spinel-forming model castable (REF_MHA_S) and impurified spinel-forming model castables (MHA_S_2CS, MHA_ S_2FCS, MHA_ S_2NS, MHA_ S_2FC and MHA_ S_2TCS). The symbol ⚠ means that the test pieces exploded during the heating process.

4.4.1.2. Investigation of the sintering behaviour of castables with the Method of Monotonic Heating (MMH)

Two measurements and accordingly heatings were performed on each test piece. The first measurement/heating was on the test piece which was only dried at 110 °C to remove the free water. This roughly simulated the evolution of test piece during the first heating at the hot face of a refractory lining up to 1250 °C (namely the second temperature used for the wedge splitting investigations). Following this first heating, the test piece, already having experience 1250 °C, stayed in the furnace for a second measurement/heating up to 1600 °C. This procedure allowed discrimination between irreversible transformations/reactions occurring during the initial consolidation of the castable below 1250 °C and reversible transformations prone to take place each time the castable or part of the castable reaches the suitable temperature, for instance the formation of a liquid phase. Previous investigations had shown that if form in a sufficient amount, the formation of a liquid led to a negative peak-like event on the apparent thermal diffusivity curves. By combining the two measurements (e.g. Fig. III.12 (a)), it is also possible to obtain a pseudo curve of the apparent thermal diffusivity simulating a single measurement/heating on simply dried test piece from room temperature to 1600 °C (e.g. Fig. III.12 (b)).

As expected for high alumina refractory products, the apparent thermal diffusivity of the model reference castable decreased with increasing temperature, at least up to circa 1100 °C (Fig. III.12). In this range of temperature, the heat transfer is mainly drive by the mobility of the phonons in the crystal lattice, which decrease with increasing temperature. Above 1100 °C, the contribution of other heat transport mechanisms, especially radiative hear transfer, increase. Additionally, the sintering of the material that improve the connectivity between crystalline grains and accordingly the phonons mobility. Altogether this led to an increase of the apparent thermal diffusivity. Expecting this and because of it very well-defined chemical and mineralogical composition of the reference model castable, no noticeable events or other conspicuous features could be otherwise observed on the apparent thermal diffusivity curves. Accordingly, the said curves served as benchmark curves to identify the influence of the impurities.

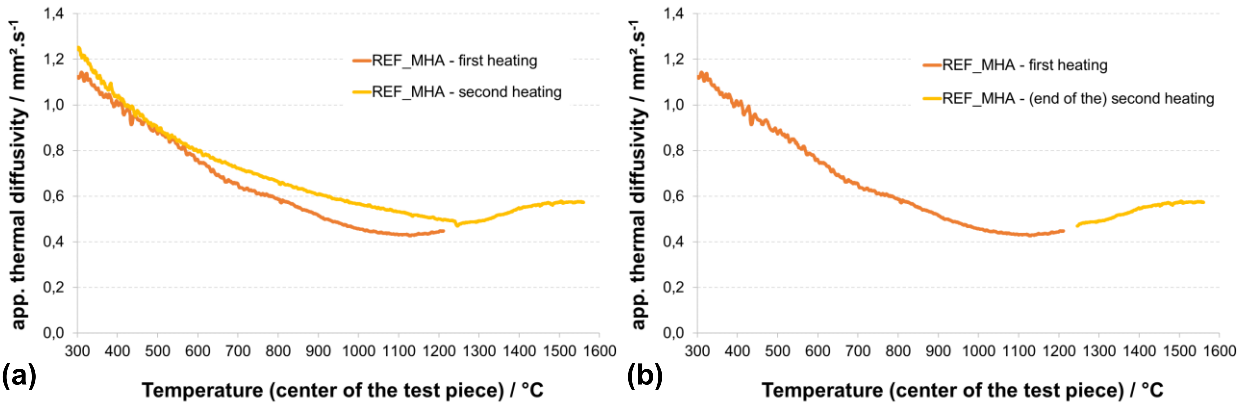

*Fig. III.12: Evolution of the apparent thermal diffusivity for the model reference castable **(a)** comparison between the first heating up to 1250 °C and the second heating up to 1600 °C **(b)** combination of the first and second heating to simulate a first heating up to 1600 °C.*

At first glance, the apparent thermal diffusivity curves of the impurified model castable (Fig. III.13) were not substantially different from the apparent thermal diffusivity curves assessed for the model reference castable (without impurities - Fig. III.12). They follow the same pattern, first decreasing up to circa 1100 °C and then increasing. However, as higher increase of the apparent thermal diffusivity usually means higher sintering of the matrix, it seems that the addition of impurities in the raw material of castable promoted the sintering at high temperature. As expected, and calculated using FactSage, model castable containing impurities tend to form liquids at lower temperatures and in larger amounts than for the reference castable without additional impurities. Liquid phases are well-known to promote the sintering of ceramic material. Additionally, the higher the amount of liquid phase and the lower its viscosity, the higher the sintering kinetic should be. This seems to be consistent with the observed experimental results as impurified model castable that are expected to form more liquid with lower viscosity tend to display a higher increase in their measured apparent thermal diffusivity above 1100 °C (MHA_2CS, MHA_2NS and MHA_2TCS).

Despite the very likely formation of liquid phase in impurified model castable, no negative peak-like event on the apparent thermal diffusivity curves were observed. It is assumed that the formed quantities were too low to significantly affect the measurements. In order to potentially identify the formation of the liquid phase, MMH measurements were performed on the fraction of the castables raw material that were impurified, namely the fraction 0-45 µm (powder).

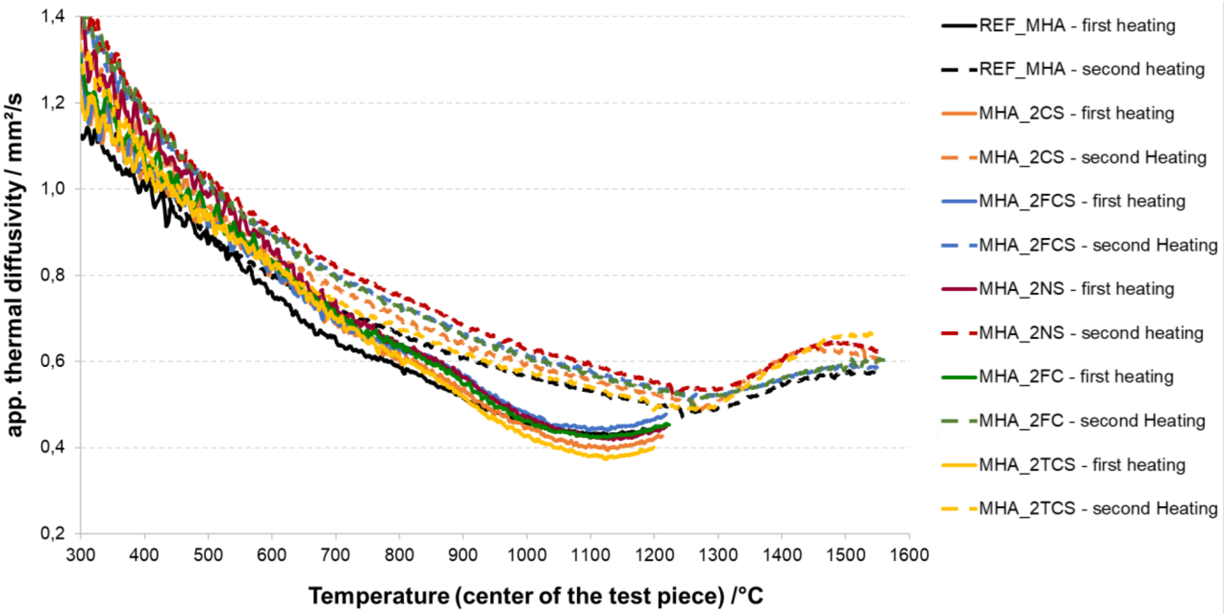

Fig. III.13: Evolution of the apparent thermal diffusivity of the reference model castable (REF_MHA) and impurified model castables (MHA_2CS, MHA_2FCS, MHA_2NS, MHA_2FC and MHA_2TCS).

Powders, as loose material, displayed quite different evolutions of their apparent thermal diffusivity curves. First, their apparent thermal diffusivity is significantly lower than the values observed for the model refractory castable as the absence of physical bonds between particles that form the powder strongly limits the mobility of the phonons, in addition to display a less optimized particles distribution and hence higher porosity acting as insulation. Secondly, at least up to circa 1100 °C, the apparent thermal diffusivity stayed quite constant. With a very limited contribution of the phonons to the overall heat transfer, the share of the other transfer mechanism (convections, radiation) becomes much less marginal and unlike the phonon's mobility, the convective and radiative heat transport tend to increase with increasing temperature.

The tabular alumina powder T60 (as delivered) displayed no special feature, namely the apparent thermal diffusivity stayed relatively constant up to 1300 °C (= reference curve). The impurification of the raw material fraction 0-45 µm led mainly to two changes: 1) the apparition of a more or less pronounced negative peak in the temperature range 1100 °C to 1300 °C. This peak is expected to correlate with the formation of liquid as heat is taken from the system and promote a transient increase of the temperature difference between the thermocouple in the centre of the test piece and the one close to its surface, resulting in a transient decrease of the apparent thermal diffusivity (= a negative peak according to equation III.4. 2) an important increase of the apparent thermal diffusivity, usually directly after the previously mentioned peak, which is assumed to reflect the improvement of the particles connectivity and bonding as a result of presence of a liquid phase. According to the MMH measurements the combination of impurities that should lead to the formation of liquid at the lower temperature should be 2TCS, followed by 2FCS, 2NS, 2FC and finally 2CS. This is rather consistent with the results from the investigations performed at Ł-ICiMB (Subproject II), with the notable exception of the 2FC where the liquid phase seems to appear earlier than indicated by the other investigation methods, but at the same time does not seems to give a rise to an important increase of apparent thermal diffusivity after the negative peak was observed. This could be an indication that, despite being formed the liquid phase does not interact extensively with the system, probably still enough to provide ductility to the model castable as observed during the wedge splitting measurement but with minimal weakening of the model castable.

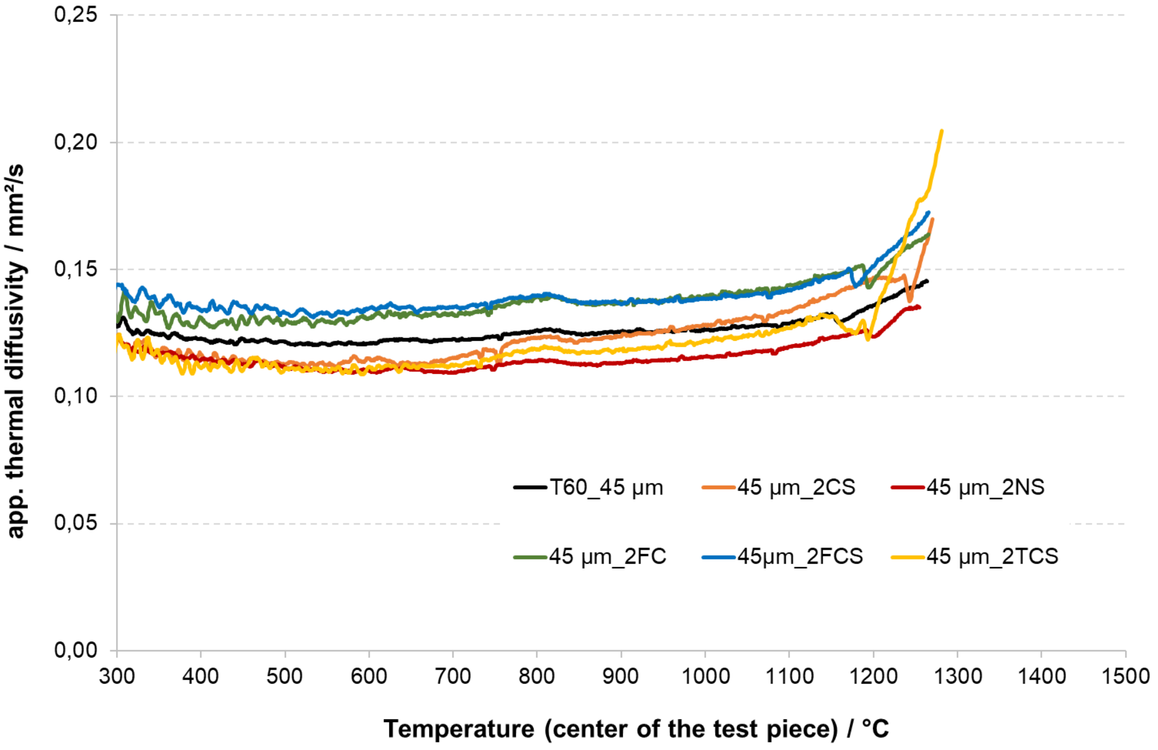

Fig. III.14: Evolution of the apparent thermal diffusivity of the raw material fraction 0-45 µm, either as delivered (T60) or impurified (2CS, 2FCS, 2NS, 2FC, 2TCS).

4.4.2 Investigation of the simultaneous effect of thermal gradient and high load near to the hot face of refractory linings

First investigations were focused on the validation of the newly developed testing system, especially using the reference model castable as simple benchmark material. Only in a last step, a using a reliable testing protocol, the influence of the addition of impurities was investigated.

4.4.2.1. Development of stresses in test pieces with restrained free thermal expansion

To examine the development of stresses in a test piece made of the reference model castable, the laboratory furnace was heated up to 1200 °C while the free thermal expansions in both directions y and z (Fig. III.4) are being restrained. As the temperature increases at the hot face, the heated part of the test piece strives to expand under the fixed refractory plungers and as a result stresses built up. Since the refractory castable is mostly anisotropic, very similar levels of stresses are assessed in the two perpendicular y and z directions, reaching almost 20 MPa (Fig. III.15). The increase of the stresses is not directly proportional to the temperature inside of the furnace, nor linear. The two main reasons for this behaviour are: 1) the part of the test piece in contact with the plungers is not homogenously heated (thermal gradient) and accordingly does not expand linearly, and 2) the refractory plungers themselves heat up as heat from test piece is transferred to the plungers at the contact surfaces. Accordingly, the plungers do also expand, but again not linearly. The second effect also means that the plungers do not only restrain the thermal expansion of the test piece but also compress it further, in a comparable way as neighbouring bricks or parts of a refractory lining would do in service if no expansion joints are present or already closed.

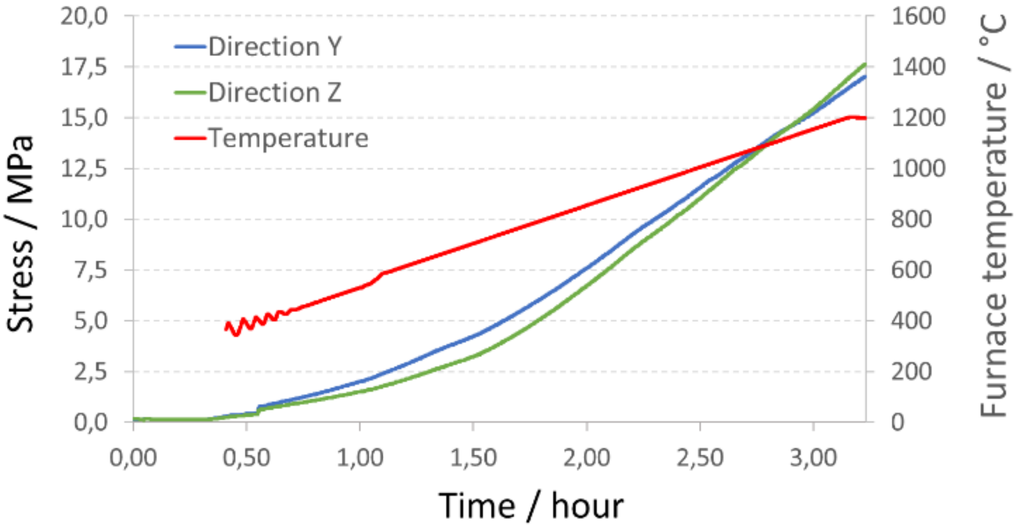

Fig. III.15: Evolution of the furnace temperature and induced stresses for a test piece made of HA bonded high alumina castable with restrained free thermal expansion in the directions y and z near to the hot face.

As a complementary testing configuration, the laboratory furnace was heated to 1700 °C with the displacement of the mobile plunger again blocked in one direction (z), i.e. restraining the free thermal expansion, but the free thermal expansion in the other direction (y) allowed. Actually, a comparably small load of 0,15 MPa is always applied in the y-direction to guarantee the contact between the plunger and the test piece, as well as maintaining the test piece in position, while still allowing the free thermal expansion of the test piece. A stress level of about 23 MPa was assessed in the z-direction and the non-linearity of the expansion of the test piece and plungers confirmed (Fig. III.16). It is also worth noticing that, as the test piece was allowed to expand in the y-direction and because of the Poisson effect, the deformation in the y-direction (perpendicular to the applied load) is slightly higher than the free thermal expansion. This also means that, in case of the restriction of the free thermal expansion in both directions perpendicular to the thermal gradient (y and z-directions), the level of achieved stresses after heating the laboratory furnace to 1700 °C should be significantly higher. By extrapolating the combined results from two experiments (Figures III.15 and III.16), stresses larger than 30 MPa could be expected in the case of the complete restriction of the free thermal expansion in both directions perpendicular to the thermal gradient and accordingly near to the hot face of refractory linings in services.

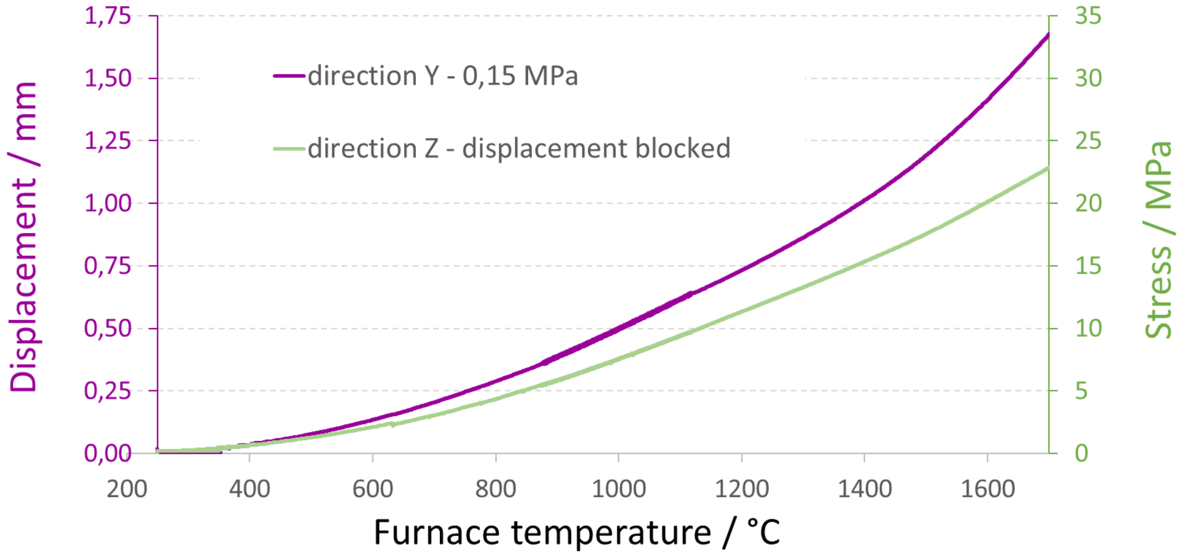

Fig. III.16: Evolution of induced stresses for a test piece made of HA bonded high alumina castable with restrained free thermal expansion in the z-direction and displacement of the refractory plunger in the y-direction near to the hot face.

4.4.2.2. Displacement and creep of test pieces under load: unidirectional loading

Another important aspect of interest is the creep of refractory materials at high temperature. To investigated this, a series of measures was performed in which the laboratory furnace was heated to 1700 °C and the load kept constant in both the y and z-directions. Again, a load of only 0,15 MPa was applied in the y-direction to guarantee a contact between the plungers and the test piece. In the z-direction, the load was first set to 0,15 MPa, but then increased to 10 MPa, 20 MPa or 30 MPa.

Under a load of 0,15 MPa applied in both directions, the displacement of the mobile refractory plungers was found to be almost identical in both directions, which is further evidence of the anisotropic behaviour of the model reference castable. The obtained displacement curve for a load of 0,15 MPa was considered to represent the almost free thermal expansion of the test piece and partially heated refractory plungers. By increasing the load in the z-direction, the corresponding displacement of the plunger in the z-direction followed closely the thermal expansion previously observed for a load of 0,15 MPa, at least up to a furnace temperature of 1200-1300 °C. Above these temperatures, the displacements stay significantly below the displacement previously observed for a load of 0,15 MPa, namely was partially restrained (Fig. III.18). More than just the consequence of a mechanical compression that impedes the free thermal expansion, it is likely that creep occurred near the hot face. Indeed, creep is a function of the temperature and applied load. In the present case, it seems to begin at a furnace temperature of 1200-1300 °C and its contribution increase with increasing temperature and higher applied load, namely the higher the temperature and applied load were, the more limited the displacement in the z-direction was. It is also worth noting that the displacement in the y-direction, in contrast, tended to increase with increasing load in the z-direction (not shown in the figure III.18 to avoid overloading the graph with too much information). This is also likely the result of the creep process. As the test piece is compressed and irreversibly deformed (due to creep) in the z-direction, this deformation is at least partially accommodated by an expansion in the y-direction.

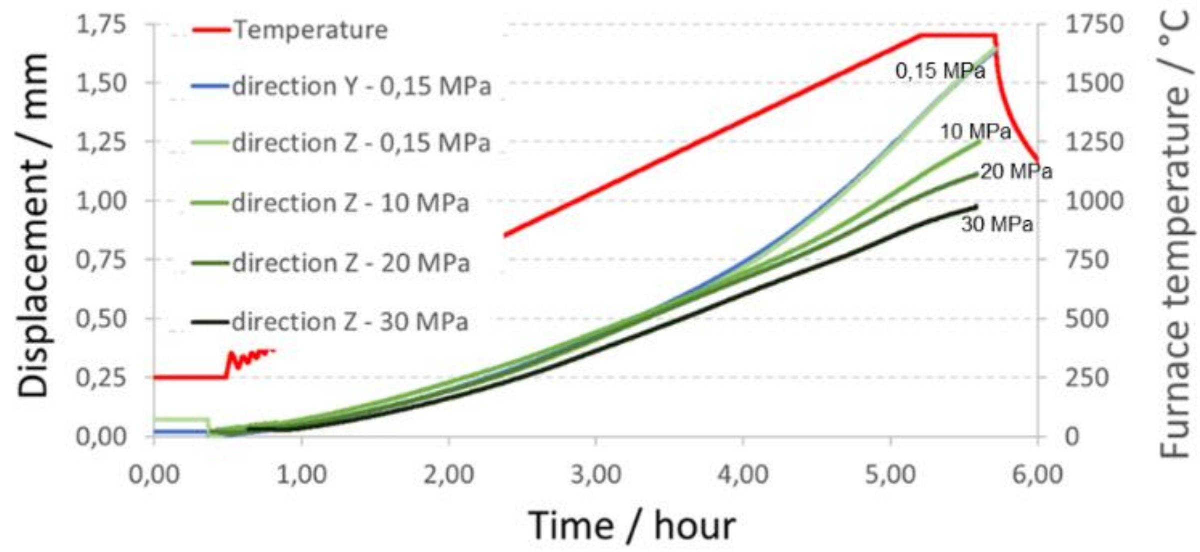

Fig. III.17: Evolution of the furnace temperature and displacement of the mobile refractory plungers applying different load on a test piece made of HA bonded high alumina castable near to the hot face (the displacement in the y-direction corresponds to the measurement where a load of 0,15 MPa was applied in both directions).

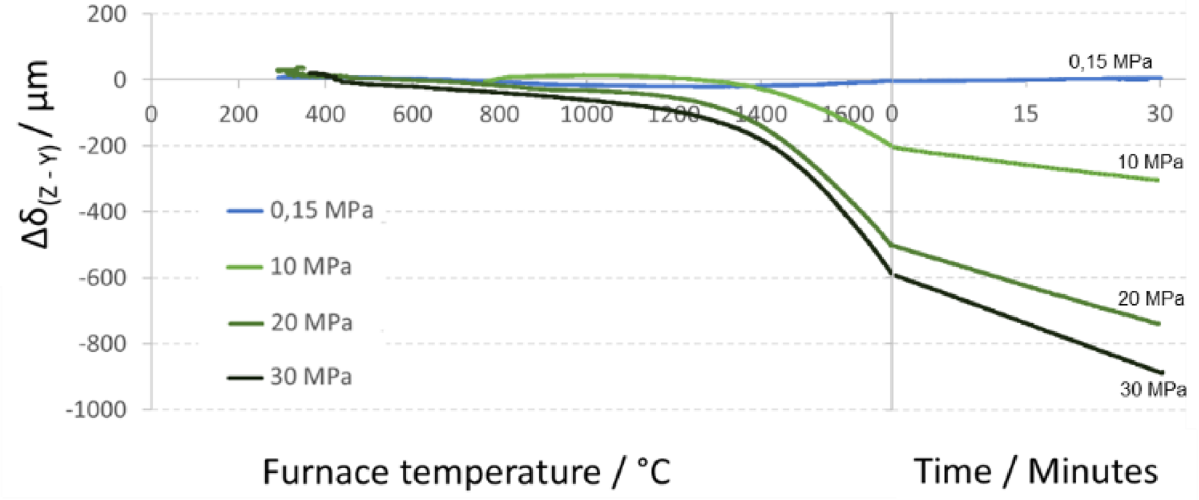

Fig. III.18: Difference between the displacement (Δδ) of the mobile refractory plungers in the z-direction and y-direction as a function of the furnace temperature and time after having reached 1700 °C.

Although not perfectly depicting creep (because of the above-mentioned phenomenon), the difference between the displacement of the mobile refractory plungers in the y-direction and z-direction ($\Delta\delta_{(z-y)}$) provides a valuable information on the creep process (Fig. III.18). Under a load of 0,15 MPa applied in both directions, the displacement of the mobile plungers is almost the same in both directions, and $\Delta\delta_{(z-y)}$ is accordingly almost constant (near to zero). Increasing the load (in the z-direction) resulted in $\Delta\delta_{(z-y)}$ that increases (in terms of absolute value) with increasing furnace temperature. Higher temperatures as well as higher loads in one direction promote the creep process that results in an increased difference between the displacement of the mobile refractory plungers in the y-direction and z-direction. This is also reflected in a higher apparent creep rate (Δδ(z-y)/Δt) with increasing load in the z-direction at a furnace temperature of 1700 °C (Tab. III.7).

Tab. III.7: Deformation rate calculated from the difference between the displacement of the mobile refractory plungers in the y-direction and z-direction over time (Δδ(z-y)/Δt – apparent creep rate) at a furnace temperature of 1700 °C for test pieces made of HA bonded high alumina castable.

Load / MPa	**apparent creep rate / µm.min^{-1}**
0,15	-0,38
10	3,32
20	8,00
30	9,97

Optically and on a macroscopic scale, the application of a load in the z-direction lead to visible deformations of the test piece visible in the form of an imprint on the surface at the contact between the refractory plungers and test piece. This imprint is basically the remanent physical manifestation of the creep (irreversible deformation) under the refractory plungers once the test pieces are cooled down (Fig. III.19). The higher the applied load, the more pronounced the imprint is. Which is coherent with the higher apparent creep rate measured with increasing load applied and discussed previously. Additionally, at the edge of the section of the test piece under load, cracks appear on the surface by load above 20 MPa (Fig. III.19). It is likely due to the presence of high shear stresses in the transition area between the part of the refractory under load and the rest of the refractory. Once again, the higher the load, the more important the cracking is.

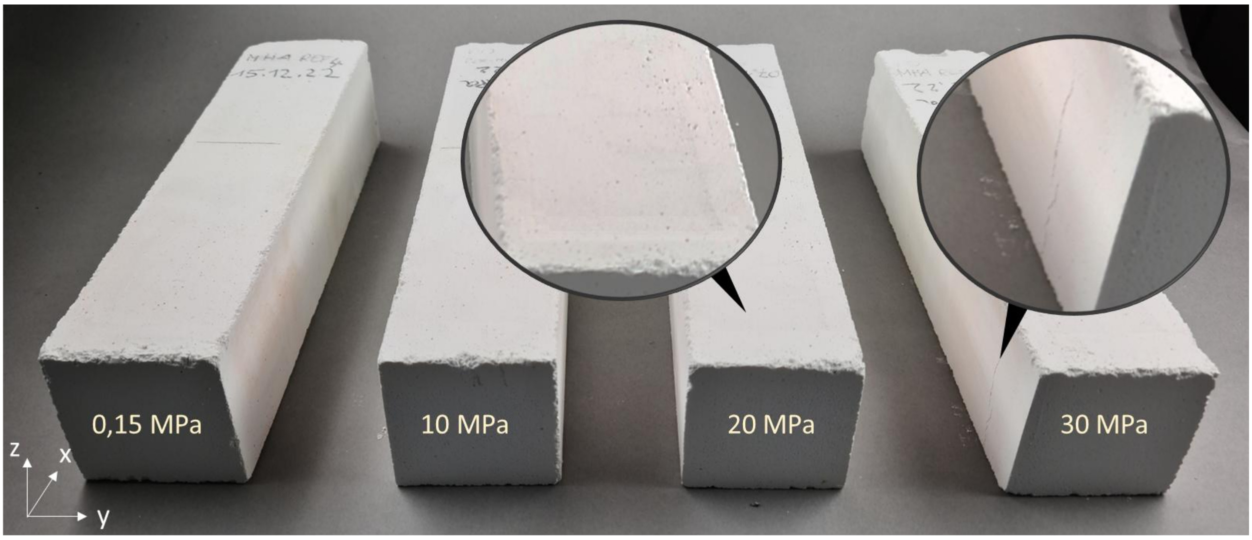

Fig. III.19: Test pieces after being exposed to 1700 °C on one side (hot face) and different loads in the z-direction near to the hot face.

SEM micrographs revealed the manifest influence of the compressive stresses near to the hot face on the microstructure of the test pieces (Fig. III.20). While by modest magnifications (1.000-fold) no clear changes can be observed, higher magnifications (25.000-fold) bring to light an evolution of the microstructure within the reference model castable's matrix. The higher the applied load, the more advanced the coarsening of the matrix is. In light of these results, it is unlikely that simple pre-firing of test pieces or the load imposed by the standards *EN ISO 1893: Determination of refractoriness under load* and *EN 993-9: Determination of creep in compression*, namely 0,2 MPa, are sufficient to promote the formation of the microstructure that can be found near the hot face of refractory linings in service. Furthermore, the observed microstructural changes are expected to impact the properties, behaviour, and performance of the refractory materials at high temperature, such as their strength and resistance to corrosion, erosion and thermal shocks. This aspect can be studied in subsequent investigations on test pieces after being exposed to high temperatures and load in the new testing system.

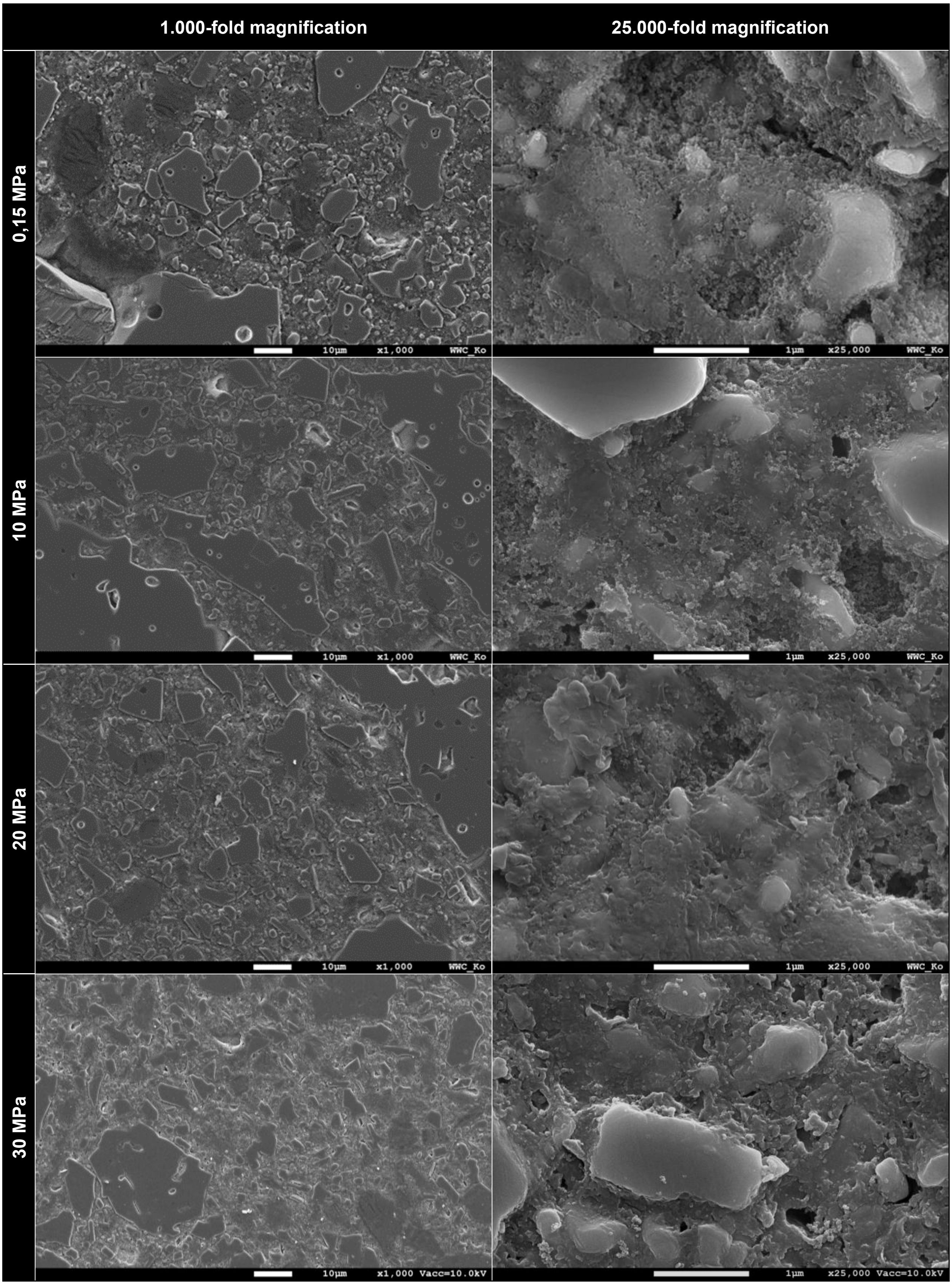

Fig. III.20: Evolution of the microstructure (SEM micrographs, 1.000 and 25.000-fold magnification) of test pieces made of HA bonded high alumina castable near to the hot face and with increasing load applied in the z-direction.

4.4.2.3. Influence of the impurification of the model refractory castable: bidirectional loading

In a first step the laboratory furnace was heated to 1700 °C while the load was kept constant at 0,15 MPa in both the y and z-directions. Once the 1700 °C reached, the load was set to 20 MPa in both the y and z-directions and the laboratory furnace was kept at this temperature for two hours. Since, in this testing configuration both y and z-directions experience a loading and accordingly stress-induced irreversible deformations, an additional measurement was performed on the reference model castable under the same conditions except that the load was set to 0,15 MPa in both directions, namely a loading level that should not induced stress-related irreversible deformations. The stress-induced irreversible deformations of the test piece were hence quantitively assessed by subtracting the measured displacements of the mobile refractory plungers experiencing a load of 0,15 MPa (deemed to correspond only to the thermal expansion of the test piece and refractory plungers) from the measured displacements of the mobile refractory plungers for test piece made of the model castable experiencing a 20 MPa loading (Fig. III.21).

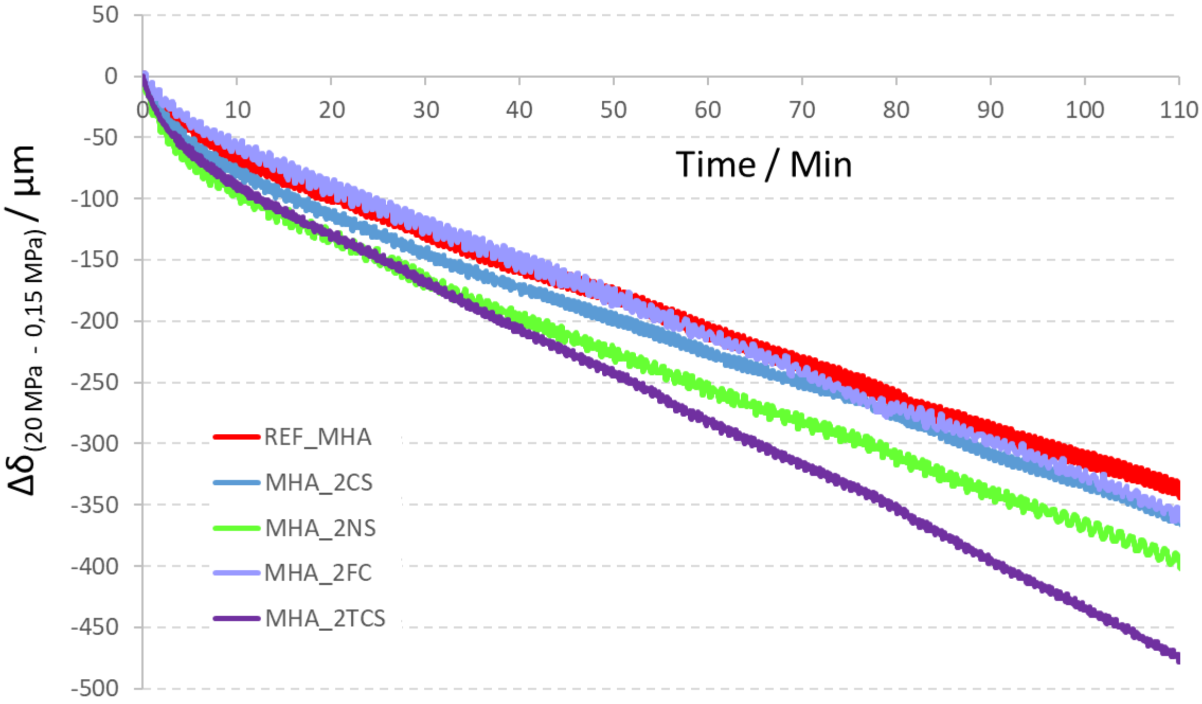

Fig. III.21: Difference between the displacement of the mobile refractory plungers for a test piece loaded with 20 MPa and a test piece made of the reference model castable loaded with 0,15 MPa as a function of time (Δδ(20 MPa-0,15 MPa)) after reaching a furnace temperature of 1700 °C.

The level of deformations and apparent creep rates measured two hours after the furnace reached 1700 °C (Tab. III.8) are significantly lower than those measured previously under unidirectional loading condition (the reference model castable (Fig. III.18 and Tab. III.7). As the test pieces is compressed, and accordingly irreversibly deformed, in two perpendicular directions (y and z), and besides some degree of densification, the test pieces can only accommodate the induced deformations by an expansion in the x-direction, instead of x and y-direction under the previous unidirectional loading condition.

Tab. III.8: Deformation rate calculated from the difference between the displacement of the mobile refractory plungers for a test piece loaded with 20 MPa and a test piece made of the reference model castable loaded with 0,15 MPa over time (Δδ(20 MPa-0,15 MPa)/Δt – apparent creep rate in stage II) at a furnace temperature of 1700 °C.

Model refractory castable	apparent creep rate / µm.min^{-1}
REF_MHA	2,69
MHA_2CS	2,76
MHA_2NS	2,95
MHA_2FC	2,93
MHA_2TCS	3,81

Overall, the addition of impurities in the model refractory castable led to increase of the level of deformations and apparent creep rates (Fig. III.21 and Tab. III.8), in all likelihood promoted by the formation of liquid phase earlier than in the impurity-free reference model castable. A direct comparison with the creep rate measured by the partner research institute L-ICiMB (section 3.4.2) cannot be performed since the section of the test piece under compression experience 1) bidirectional loading (instead of unidirectional), 2) at much higher loading (20 MPa instead of up to 1,2 MPa) and 3) in a thermal gradient (instead of at a well-defined temperature). However, the classification of the observed level of deformations and creep rates stay roughly the same with the lower level of deformations and creep rates for the model castables that tend to form lower amounts of liquid phases at higher temperature and/or presenting high viscosity (REF_MHA and MHA_2FC). Conversely model castables that tend to form higher amounts of liquid phases at lower temperature and/or presenting low viscosity (MHA_2NS and MHA_2TCS) displayed the highest level of deformations and creep rates.

Once again, optically and on a macroscopic scale, the application of a load in the y and z-direction lead to visible deformations of the test piece visible in the form of an imprint on the surface at the contact between the refractory plungers and test piece, as well as cracks at the edge of the section of the test piece under load. Longitudinally cut test pieces (Fig. III.22) seems to highlight to antagonistic processes happening during the measurements. First the high temperatures induced an embrittlement of the hydratable alumina bonded castable so that the surface that experienced sufficiently high temperature near to the face, tend to erode during the cutting process at room temperature. This is particularly visible for the test piece made of the reference model castable (Fig. III.22 - REF_MHA 0,15 MPa) and having experiencing only a loading of 0,15 MPa, which displayed an eroded cut surface from the hot face to a deep of circa 50 mm. In contrast, the very same material having experiencing a loading of 20 MPa (Fig. III.22 - REF_MHA_20 MPa) still displayed an eroded cut surface up to a deep of circa 50 mm, but the section experiencing the highest temperature (namely directly adjoining the hot face surface) and the loading appear to be much more resistant and do suffer less from erosion during the cutting process. This correspond to the part of the test piece that is expected to display the largest thermal expansion and accordingly undergo the highest compressive stresses. As expected, high temperatures and high compressive stresses promote the densification of the material and strengthen it, counteracting the embrittling effect of the temperature on the hydratable alumina bonded castables. By promoting the creep process and hence the densification, the presence of impurities should further strengthen the material and reduced the erosion phenomenon near to the hot during the cutting process. While this is not unequivocal for the test piece MHA_2CS, MHA_2NS and MHA_2FC, the test piece MHA_2TCS, which displayed the highest level of deformations and apparent creep rates (Fig. III.21 and Tab. III.8), clearly present a smaller eroded section and a larger intact (in all likelihood densified) zone near to the hot face. Since all model castables were able to withstand the testing conditions without failing (at least under the refractory plunger and besides cracks in the sheared transition zone between loaded and load-free part of the test pieces), the presence of a moderate amount of impurities seems to even strengthen the material as long as only (bi-directional) compressive loading prevail. The material and especially induced microstructure should be further investigated, for instance “new” test pieces cut out the section under the refractory plungers could be used for hight temperature compressive strength measurements and thermal shock resistance investigations. Hence the impact of the microstructural changes could be more specifically assessed.

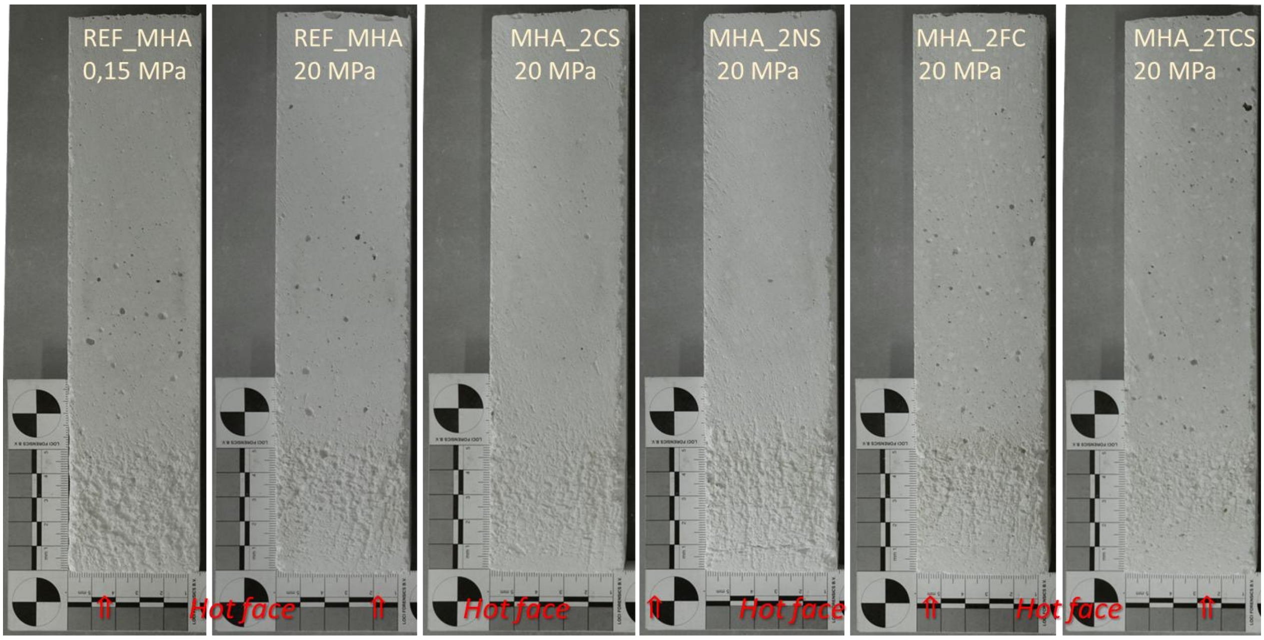

Fig. III.22: Longitudinally cut test pieces.

SEM microscopy on thin section was performed to investigate the impact of the combination of impurities on the microstructure of the refractory model castables (figures III.23 to 25). Except a higher density of the cracks near to the hot face, in all likelihood because of the shear stresses occurring in the zone between the part under the refractory plungers (loaded) and the immediate vicinity of the hot face (not loaded), all investigated microstructures were very similar. Either between the different refractory model castables (without and with different combinations of impurities) or as a function of the distance from the hot face, no significant change in the microstructures could be observed. Eventually and in line with the previous observation on a macroscopic scale

(Fig. III.22), the model refractory castable MHA_2TCS might appear a little bit more densified throughout all the investigated distance to the hot face.

Finally, the mapping of the elements (EDS analysis) could not highlight any specific concentration or diffusion’s process of the impurities in the investigated test pieces.

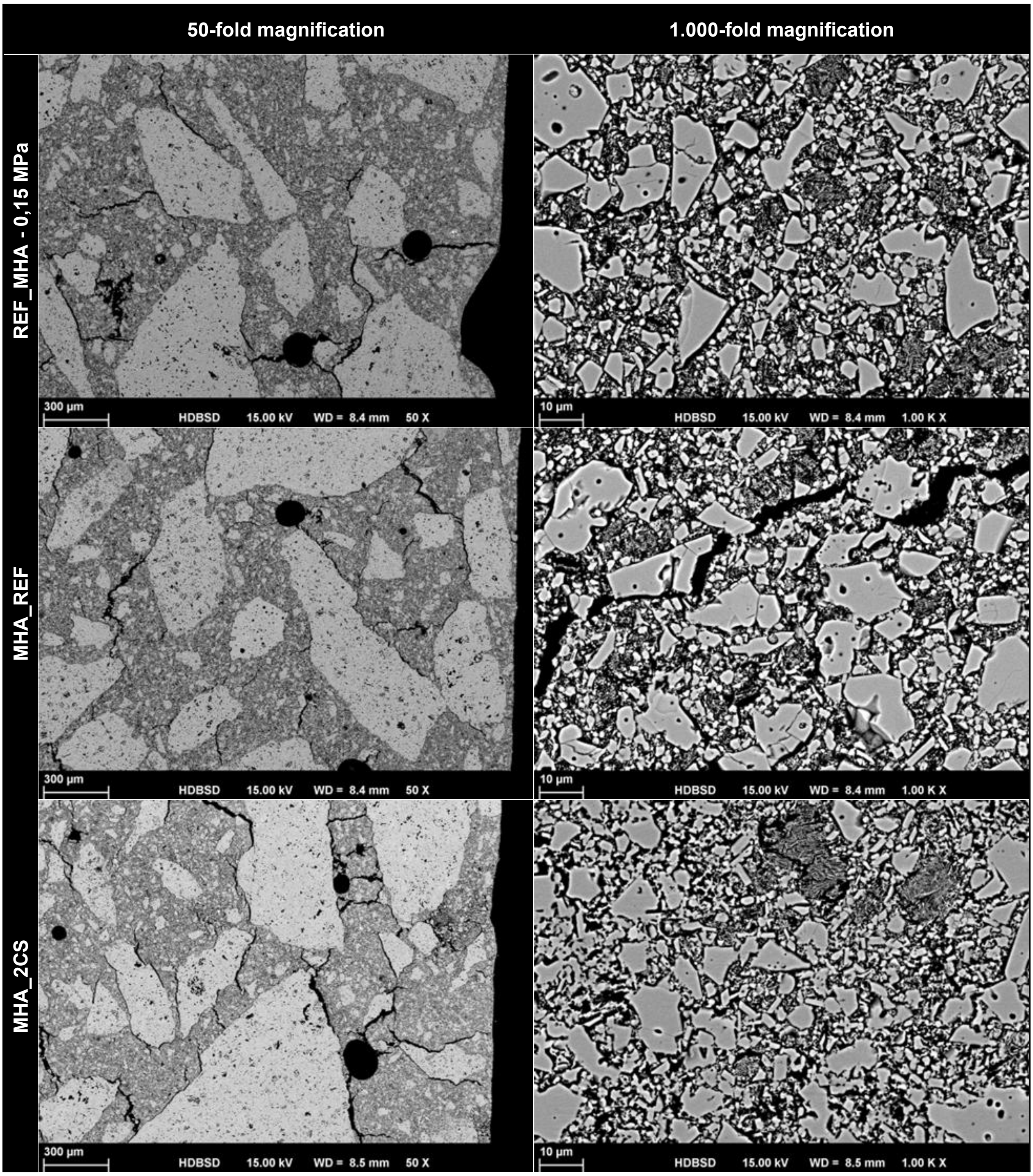

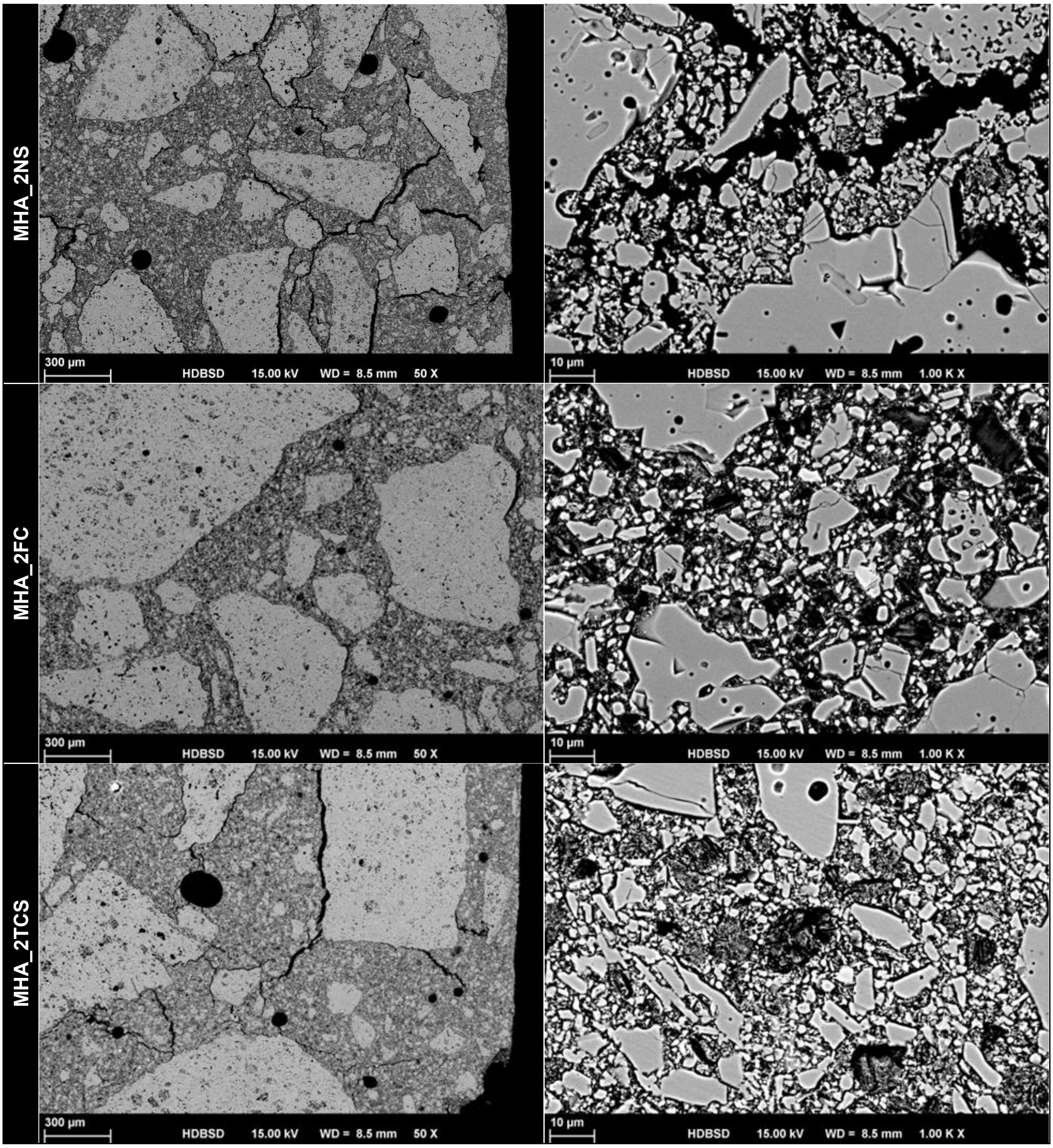

Fig. III.23: Evolution of the microstructure (SEM micrographs, 50 and 1.000-fold magnification) of test pieces made of HA bonded high alumina castable in the immediate vicinity of the hot for a load of 20 MPa applied in in both the y and z-directions (except, as indicated, for one reference castable).

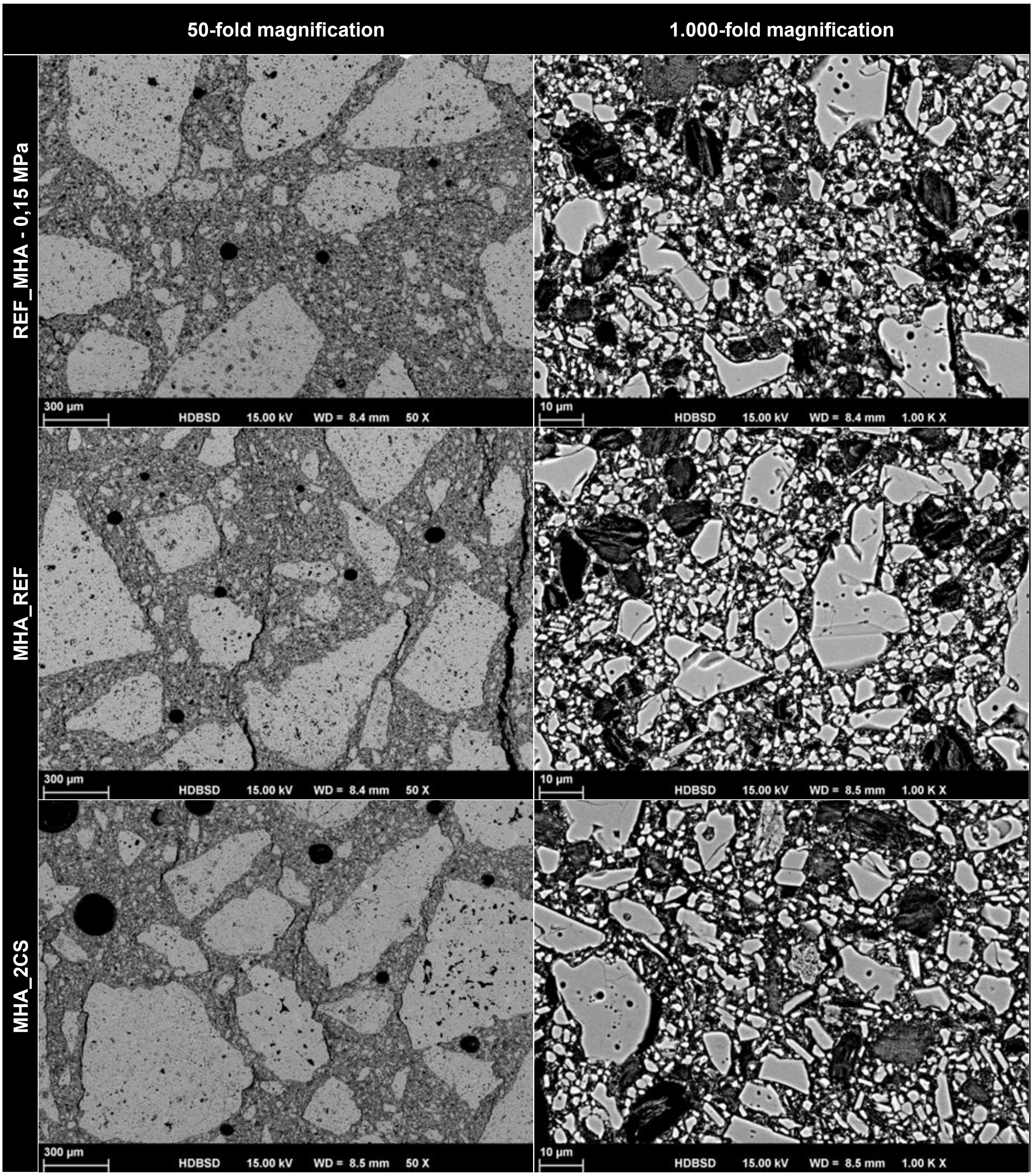
50-fold magnification
1.000-fold magnification
REF_MHA - 0,15 MPa
MHA_REF
MHA_2CS
300 µm HDBSD 15.00 kV WD = 8.4 mm 50 X
10 µm HDBSD 15.00 kV WD = 8.4 mm 1.00 K X
300 µm HDBSD 15.00 kV WD = 8.4 mm 50 X
10 µm HDBSD 15.00 kV WD = 8.5 mm 1.00 K X
300 µm HDBSD 15.00 kV WD = 8.5 mm 50 X
10 µm HDBSD 15.00 kV WD = 8.5 mm 1.00 K X

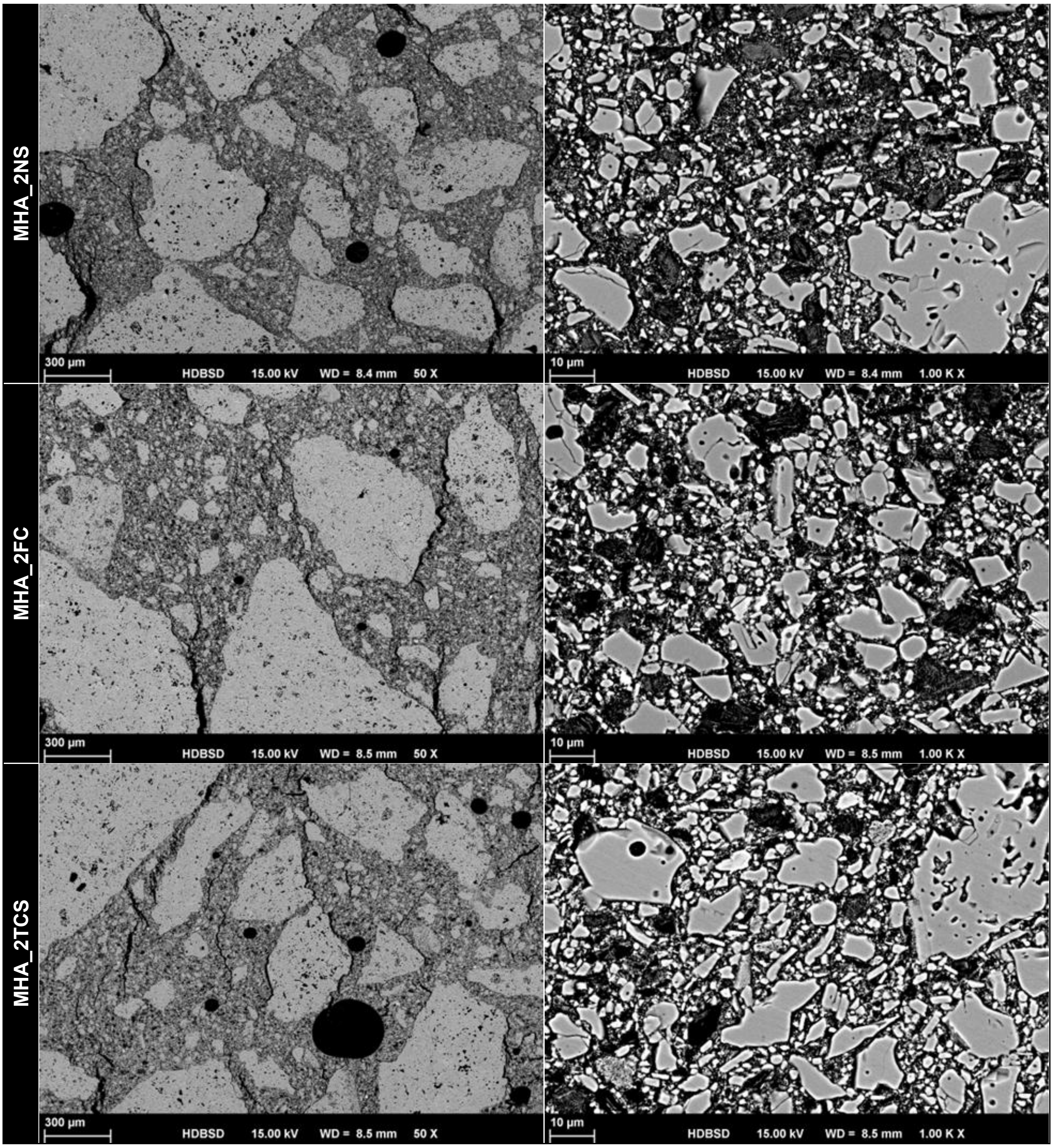

Fig. III.24: Evolution of the microstructure (SEM micrographs, 50 and 1.000-fold magnification) of test pieces made of HA bonded high alumina castable 15 mm away from the hot for a load of 20 MPa applied in in both the y and z-directions (except, as indicated, for one reference castable).

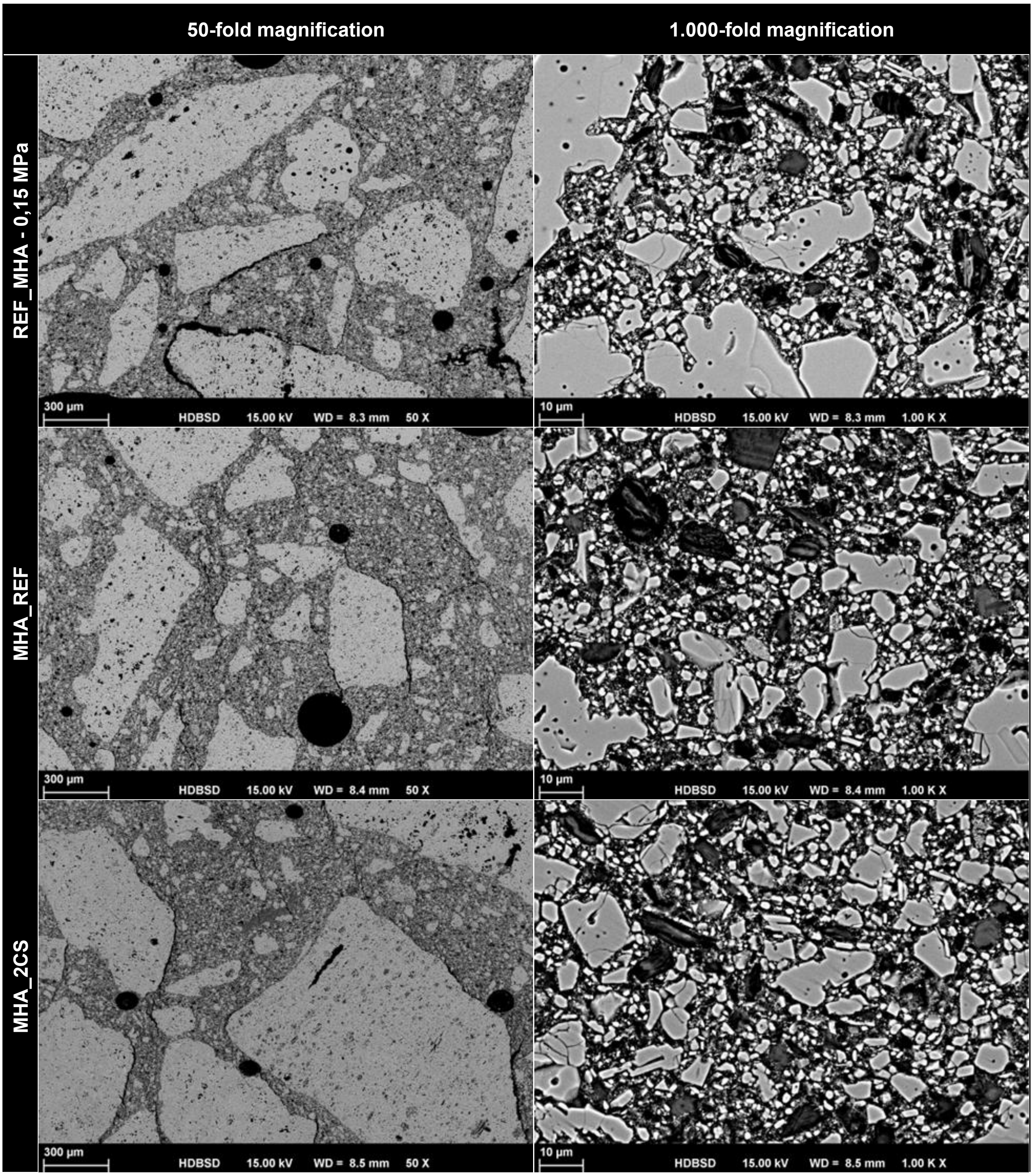
50-fold magnification
1.000-fold magnification
REF_MHA - 0,15 MPa
300 µm HDBSD 15.00 kV WD = 8.3 mm 50 X
10 µm HDBSD 15.00 kV WD = 8.3 mm 1.00 K X
MHA_REF
300 µm HDBSD 15.00 kV WD = 8.4 mm 50 X
10 µm HDBSD 15.00 kV WD = 8.4 mm 1.00 K X
MHA_2CS
300 µm HDBSD 15.00 kV WD = 8.5 mm 50 X
10 µm HDBSD 15.00 kV WD = 8.5 mm 1.00 K X

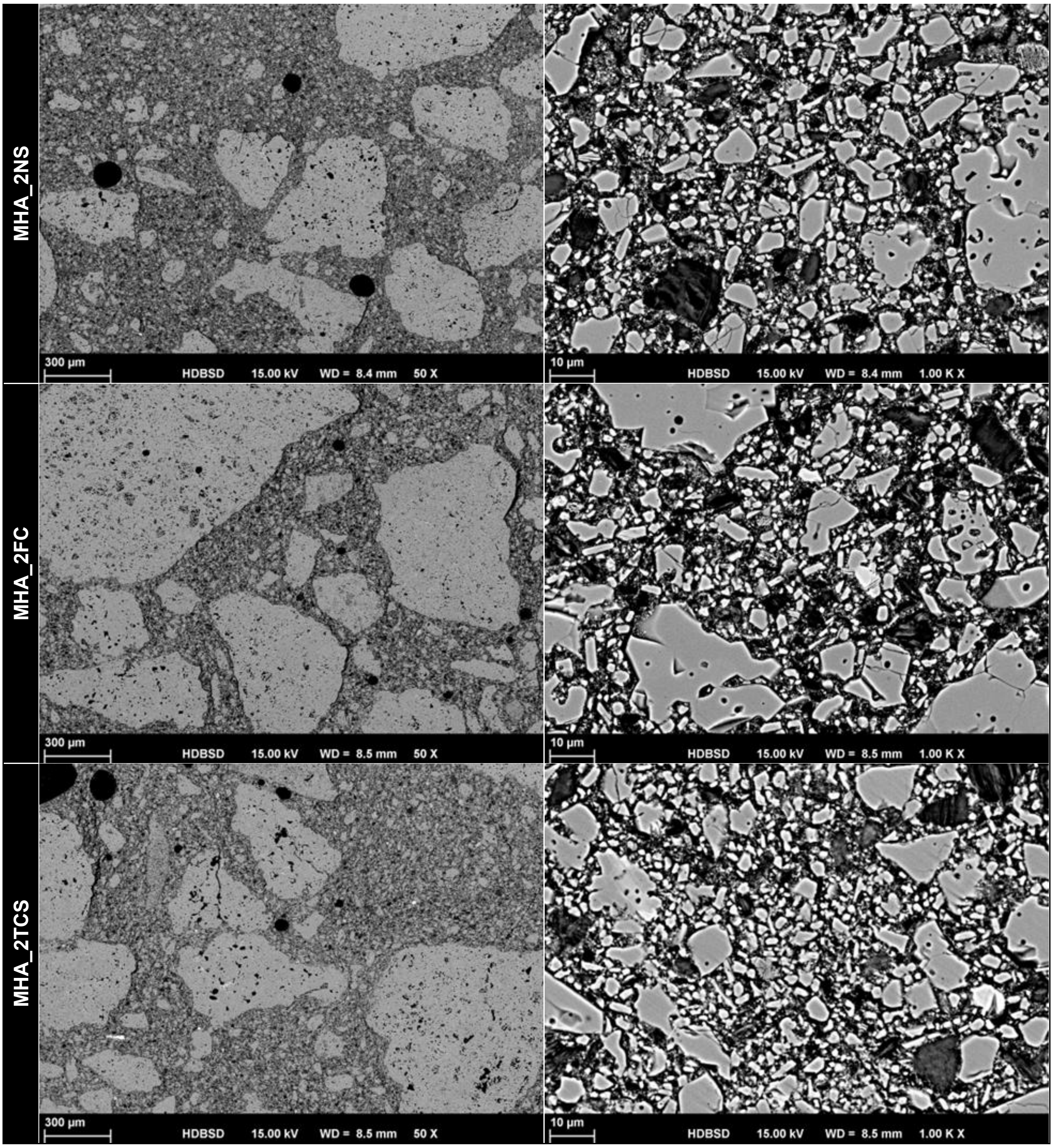

Fig. III.25: Evolution of the microstructure (SEM micrographs, 50 and 1.000-fold magnification) of test pieces made of HA bonded high alumina castable 30 mm away from the hot for a load of 20 MPa applied in in both the y and z-directions (except, as indicated, for one reference castable).

4.5 Conclusions

Typically, refractory linings operate in a temperature gradient. For monolithic linings, which are directly installed on site at room temperature and experience extensive changes in their microstructure with increasing temperature, this led to an inhomogeneous evolution of the microstructure and the properties within the thickness of the refractory lining. The material consists then of a continuous succession of layers in different states, from highly sintered at the hot face to almost green at the cold face. Added to that, the free thermal expansion, especially at the hot face, is restrained by the neighbouring parts of the linings that strive to expand as well, and by the colder part of the linings that experiences much lower thermal expansion. As a result, substantial load/stresses develop at the hot face impacting directly the microstructure evolution of the refractory linings. Finally, the presence of impurities in the raw materials, for instance resulting from the production process or in the case of recycled raw materials, promotes the formation of liquid phases at high temperature that impact the behaviour of the refractory lining in service.

Thanks to wedge splitting tests (WST), the stabile fracture process of test pieces was monitored and quantified, hence their ability to resist damaging assessed. The reference model castable (high alumina cement-free model refractory castables) display a relative moderate strength and specific fracture energy that get weakened by increasing temperature. The addition of spinel precursors to the castable promote an increase of the material strength and specific fracture energy as well as reduction of its brittleness. The impurification of the raw materials (2 % additional impurities in the fraction 0-45 µm) almost systematically resulted in the deterioration of the mechanical properties of the model castable and enhancement of their brittleness. One notable exception in the spinel free formulations was the combination of Fe and Ca that apparently toughen the material and reduce its brittleness, which corelates with the combination of impurities that is expected to form the lowest amount of liquid at the testing temperature. Spinel forming formulation were much more tolerant to impurities, which corelates with their tendency to form low amount of liquid at the testing temperature. This indicates that a small amount of liquid phase is beneficial, increasing the ductility of the material without impacting its mechanical strength extensively.

Despite its ability to detect different microstructural changes, such phase transformation, the method of the monotonic heating (MMH) was not sensitive enough to detect the formation of the liquid in the model castables with impurified raw materials. However, MMH measurements on the impurified raw materials helped to classify the raw materials by identifying at which temperature should the formation occurred.

A new testing system was developed to simulate the thermal gradient and compressive loading that refractory materials experience as a part of linings in industry furnaces and vessels in service. The thermal gradient resulted from the heating of a prismatic test piece from one side (hot face). The loading was applied through refractory plungers connected with servomotors, either by restricting the free thermal expansion or applying a constant load. Stress levels of up to 30 MPa were assessed or applied near to the hot face, in either one or two directions perpendicular to the thermal gradient. Such levels of stress should be expected near the hot face of refractory linings.

High load and high temperatures promoted specific microstructural changes in the test piece near to the hot face, especially a densification of the matrix that cannot be achieved by a simple prefiring or moderate load as prescribed in the standards *EN ISO 1893: Determination of refractoriness under load* and *EN 993-9: Determination of creep in compression*. Similarly, the addition of impurities in the model refractory castable led to increase of the level of deformations and apparent creep rates under bi-directional loading condition. In combination with high load and high temperature, impurified raw materials that tend to form liquid phases earlier and in higher amount promoted microstructural changes that make the material more resistance to erosion during cutting at room temperature. The high temperature properties of materials with these microstructural changes should now be investigated to improve our understanding on the behaviour of the hot face of refractory linings as well as to push forward our ability to predict its performance.

Overall, a better insight into the behaviour of refractory materials exposed to thermal gradient and high compressive stresses as occurring in refractory linings was gained.

4.6 References

[1] S. CA, Refractories Handbook, Boca Raton: Taylor & Francis Inc, 2004.

[2] G. Routschka and O. Krause, Normen-Handbuch: Feuerfest Werkstoffe und Feuerfestbau, 2. Auflage, Vulkan Verlag, 2010.

[3] R. Oliveira, J. Rodrigues and J. Pereira, “Numerical simulations on refractory linings for steel casting vessels,” *Fire Safety Journal,* vol. 138, p. 103794, 2023.

[4] H. Fryda, K. Scrivener and G. Chanvillard, “Relevance of Laboratory Tests to Field Application of Calcium Aluminate Cement Concretes,” in *Calcium Aluminate Cements 2001*, 2001.

[5] X. Turrillas, P. Convert, T. Hansen, A. De Aza and F. Pena, “The Dehydration of calcium Aluminate Hydrates Investigated by Neutron Thermodiffractometry,” in *Calcium Aluminate Cements 2001*.

[6] R. Simmat, E. Brochen, C. Dannert, O. Krause and M. Rathaj, “In-situ determination of sintering processes in refractory materials by the method of monotonic heating (MMH)”, in *Proceedings 14th Unified International Technical Conference on Refractories*, Wien, 2015.

[7] E. Litovsky, Thermal Physical Properties of Refractories in the Wide Range of Temperature and Gas Pressure, Moscow: DSc. Th., IVTAN of USSR Ac. Of Sc., 1982.

[8] K. Maglic, A. Cezairlina and V. Peletsky, Compendium of Thermophysical Properties Meas-ure-ment Methods. Recommended Measurement Techniques and Practices, New York and London: Plenum Press, 1989.

[9] E. K. Tschegg, “Prüfeinrichtung zur Ermittlung von bruchmechanischen Kennwerten”. Austrian Patent AT 390328B, 1986.

[10] H. Harmuth and E. K. Tschegg, “A fracture mechanics approach for the development of refractory materials with reduced brittleness,” *Fatigue Fract. Eng. Mater. Struct.,* vol. 11, no. 20, p. 1585–1603, 1997.

[11] E. Brochen, C. Dannert and P. Quirmbach, “Thermo-Mechanical Characterisation of Magnesia-Carbon Refractories by Means of Wedge Splitting Test under Controlled Atmosphere at High-Temperature,” in *Proceedings of the 13th Unified International Technical Conference on Refractories (UNITECR)*, Victoria, 2013.